

Sustainable Aviation

T. Hikmet Karakoc · Soledad Le Clainche ·
Xin Chen · Alper Dalkiran ·
Ali Haydar Ercan *Editors*

New Technologies and Developments in Unmanned Systems

Proceedings of the International
Symposium on Unmanned Systems and
The Defense Industry 2022

 **SARES**
INTERNATIONAL SUSTAINABLE AVIATION
AND ENERGY RESEARCH SOCIETY





Springer

Sustainable Aviation

Series Editors

T. Hikmet Karakoc , Eskisehir Technical University, Eskisehir, Türkiye

C Ozgur Colpan , Department of Mechanical Engineering, Dokuz Eylöl University, Buca, Izmir, Türkiye

Alper Dalkiran , School of Aviation, Süleyman Demirel University, Isparta, Türkiye

The Sustainable Aviation book series focuses on sustainability in aviation, considering all aspects of the field. The books are developed in partnership with the International Sustainable Aviation Research Society (SARES). They include contributed volumes comprising select contributions to international symposiums and conferences, monographs, and professional books focused on all aspects of sustainable aviation. The series aims at publishing state-of-the-art research and development in areas including, but not limited to:

- Green and renewable energy resources and aviation technologies
- Aircraft engine, control systems, production, storage, efficiency, and planning
- Exploring the potential of integrating renewables within airports
- Sustainable infrastructure development under a changing climate
- Training and awareness facilities with aviation sector and social levels
- Teaching and professional development in renewable energy technologies and sustainability

* * *


T. Hikmet Karakoc • Soledad Le Clainche
Xin Chen • Alper Dalkiran • Ali Haydar Ercan
Editors

New Technologies and Developments in Unmanned Systems


Proceedings of the International Symposium
on Unmanned Systems and The Defense
Industry 2022


 Springer

Editors


T. Hikmet Karakoc 
Faculty of Aeronautics and Astronautics
Eskisehir Technical University
Eskisehir, Türkiye

Information Technology Research
and Application Center
Istanbul Ticaret University
Istanbul, Türkiye

Xin Chen 
Telecommunications Engineering School
King Juan Carlos University
Madrid, Spain

Ali Haydar Ercan 
Porsuk Vocational School
Eskisehir Technical University
Eskisehir, Türkiye

Soledad Le Clainche 
School of Aerospace Engineering
Universidad Politécnica de Madrid
Madrid, Spain

Alper Dalkiran 
School of Aviation
Süleyman Demirel University
Keciborlu, Isparta, Türkiye

ISSN 2730-7778

Sustainable Aviation

ISBN 978-3-031-37159-2

<https://doi.org/10.1007/978-3-031-37160-8>

ISSN 2730-7786 (electronic)

ISBN 978-3-031-37160-8 (eBook)

© The Editor(s) (if applicable) and The Author(s), under exclusive license to Springer Nature Switzerland AG 2023

This work is subject to copyright. All rights are solely and exclusively licensed by the Publisher, whether the whole or part of the material is concerned, specifically the rights of translation, reprinting, reuse of illustrations, recitation, broadcasting, reproduction on microfilms or in any other physical way, and transmission or information storage and retrieval, electronic adaptation, computer software, or by similar or dissimilar methodology now known or hereafter developed.

The use of general descriptive names, registered names, trademarks, service marks, etc. in this publication does not imply, even in the absence of a specific statement, that such names are exempt from the relevant protective laws and regulations and therefore free for general use.

The publisher, the authors, and the editors are safe to assume that the advice and information in this book are believed to be true and accurate at the date of publication. Neither the publisher nor the authors or the editors give a warranty, expressed or implied, with respect to the material contained herein or for any errors or omissions that may have been made. The publisher remains neutral with regard to jurisdictional claims in published maps and institutional affiliations.

This Springer imprint is published by the registered company Springer Nature Switzerland AG
The registered company address is: Gewerbestrasse 11, 6330 Cham, Switzerland

Paper in this product is recyclable.

Preface

Autonomous unmanned air vehicles (UAVs), more commonly referred to as drones, are undergoing fast development. The number of use cases that may be helpful is growing as technology progresses that can be grouped under agriculture, infrastructure, cargo, security, and entertainment areas. Also, the future possibilities for upcoming advances can be summarized as increased autonomy, more adaptation with artificial intelligence (AI) applications, swarm power of multiple drones, advantages of urban mobility, improved delivery solutions, and better environmental monitoring capabilities.

Increased autonomy UAVs will grow more independent in their navigation and control functions, requiring less human assistance. Because of this, they will be able to carry out increasingly complicated duties, such as checking infrastructure or transporting commodities, without the need for ongoing human supervision. AI-supported UAVs will dominate the skies and be equipped with cutting-edge AI technology, allowing them to learn and adjust to the conditions of their surroundings in real time. This development might lead to drone operations that are both more efficient and effective, as well as the potential to do complicated tasks that are now outside the capability of drones.

The following step will be expected as the “Swarms of Drones” age in the next decade. In the not-too-distant future, swarms of drones may be employed for many purposes, including environmental monitoring, military activities, and search and rescue efforts. These swarms can collaborate to accomplish a shared objective by employing complex algorithms to coordinate their motions and activities.

UAVs can become a popular means of transportation, which has already enabled the pre-evident results of this service of moving people and products across urban areas quicker and more efficiently. This futuristic approach is referred to as urban air mobility. This evolution may lead to a decrease in traffic and an improvement in productivity in the transportation sector. As the pioneering applications of urban mobility can be stated, the use of UAVs to provide delivery services is now undergoing testing, and it is possible that this technology may be widely used in

the near future. UAVs can potentially reduce both the amount of time needed for delivery and the associated expenses. Additionally, UAVs can be used as “Monitoring agents of Environmental Abuses” simultaneously. Researchers might utilize UAVs to monitor and study the environment, providing them with vital data on climate change, air quality, and natural catastrophes.

In general, the future of autonomous UAVs looks bright since numerous possible uses and technological developments are on the horizon. We may anticipate the development of unmanned aerial vehicles that are more effective, dependable, and adaptable as the state of technology continues to improve. ISUDEF '22, an international and multi-disciplinary symposium, was held online between May 30–June 1, 2022, to address current issues in the field of research developments in UAVs and other unmanned autonomous vehicles. We have kindly invited academics, scientists, engineers, practitioners, policymakers, and students to attend the ISUDEF symposium to share knowledge, explain new technologies and discoveries, and consider the future direction, strategies, and goals in the autonomy, AI, and swarm power of distributed actions. This conference featured keynote presentations by invited speakers and general papers in oral and poster sessions.

We want to thank Springer’s editorial team for their support toward the preparation of this book and the chapter authors and reviewers for their outstanding efforts.

On the other hand, we would like to give special thanks to the SARES Editorial office members for gathering these chapters, who are the heroes behind the veil of the stage. Dilara Kılıc played a significant role in sharing the load and managing the chapters with Sinem Can. Also, we thank Kemal Keles for his efforts in the long run for symposium author communications.

Eskisehir, Türkiye
Istanbul, Türkiye
Madrid, Spain
Madrid, Spain
Keciborlu, Türkiye
Eskisehir, Türkiye

T. Hikmet Karakoc
Soledad Le Clainche
Xin Chen
Alper Dalkiran
Ali Haydar Ercan

Contents

Energy Storage Technologies in Aircraft Hybrid-Electric Propulsion Systems	1
Murat Ayar, Selcuk Ekici, and T. Hikmet Karakoc	
Use of (PET-G) Material in Mini-scale Unmanned Surface Vehicle (USV) for Additive Manufacturing	9
Alperen Doğru, Ayberk Sözen, and M. Özgür Seydibeyoğlu	
The Use of State Feedback Control Based on LMI to Suppress Oscillations of Payload Carried by UAV	15
Renan S. Geronel, Ruxandra M. Botez, and Douglas D. Bueno	
Impact of Free-Form Deformation Control Points on the Optimization of the UAS-S45	21
Mir Hossein Negahban, Musavir Bashir, and Ruxandra Mihaela Botez	
Unmanned Aerial Vehicle Propeller Design and Production by Fused Filament Fabrication	29
Mesut Pehlivan, Eren Özen, and Alperen Doğru	
An Aerodynamic Model for Gliding Snake-Bots	37
Harshini Aich, Shanmukha Preetham Akella, Balajee Ramakrishnananda, and T. Rajesh Senthil Kumar	
Effect of Aerodynamic Loads on Wing Deformation of Insect-Mimicking Flapping-Wing Micro Air Vehicles	43
Vu Dan Thanh Le, Anh Tuan Nguyen, Ngoc Thanh Dang, and Utku Kale	
Influence of Gyroscopes on the Accuracy of a Nanosatellite Attitude Estimation	49
Hasan Kinatas and Chingiz Hajiyev	

Insertion of Shape Memory Alloy Wire with 3D Printed Thermoplastic Polyurethane Structure for Flexural Application	55
Leong Shii Jang, Dayang Laila Majid, Ermira Junita Abdullah, Faisal Abdul Hamid, and Husam Yahya Imrana	
Coherence in Turbulent Canopy Flows: A Study of the Flow Patterns	61
Christian Amor, Alessandro Monti, Marco Edoardo Rosti, and Soledad Le Clainche	
PD Controller with Particle Swarm Optimization for Satellite Attitude Control	67
Mehmet Fatih Erturk and Chingiz Hajiyev	
A Predictive Physics-Aware Machine Learning Model for Reacting Flows	75
Adrián Corrochano, Rodolfo S. M. Freitas, Alessandro Parente, and Soledad Le Clainche	
Rendezvous and Docking for Space Vehicles	81
Mert Sever and Tuncay Yunus Erkeç	
Effect of the Grid Span on a Biomimetic UAV	93
Rafael Bardera, Ángel Rodríguez-Sevillano, Estela Barroso, and Juan Carlos Matías	
Shallow Neural Networks and Turbulent Flows	99
Rodrigo Abadía-Heredia, Marco Crialesi-Esposito, Luca Brandt, and Soledad Le Clainche	
Data-Driven Methods Beyond Aerospace Field	105
Nourelhouda Groun, Beka Begiashvili, Eusebio Valero, Jesús Garicano-Mena, and Soledad Le Clainche	
Modeling and Simulation of Double-Acting Hydropneumatic Suspension System for 6×6 Terrain Vehicle with Different Performance Parameters	111
Kaan Berke Ulusoy, Bensus Değirmenci, Derin Türedi, Erkin Filiz, Mustafa Karaman, and Erhan İlhan Konukseven	
Inspection of Welding Joints Using Topological Derivative Methods	119
Sergio Muñoz and María-Luisa Rapún	
Machine Learning to Reconstruct Aeronautical Databases with Deep Neural Networks	125
Paula Díaz, Adrián Corrochano, Manuel López-Martín, and Soledad Le Clainche	

Reduced-Order Models Using Clustering-Based Methods in Synthetic Jets 131
 Eva Muñoz, Himanshu Dave, Giuseppe D’Alessio, Alessandro Parente, and Soledad Le Clainche

Ethics and Autonomous Systems: An Ethical Landscape of Autonomous Weapons 137
 Aysegul Ozerdem

The Analysis of Collision Avoidance in Honeybee Flights 143
 Shreyansh Singh, Rishabh Desai, Mandyam Veerambudi Srinivasan, and Sridhar Ravi

Numerical Investigation of a Uniform Viscous Transonic Flow Past a Rotating Circular Cylinder 151
 Inés Arauzo and José Miguel Pérez

Design and Analysis of Rocket Launch Vehicle for CubeSats 157
 Alper Şanlı, Tuncay Yunus Erkeç, Melih Beceren, and Mehmet Furkan Kemalli

Aeroelastic Flutter Detection by Higher Order Dynamic Mode Decomposition (HODMD)-Based Techniques and Convolutional Neural Networks (CNN) 163
 Joseba López, Rubén Moreno-Ramos, and Soledad Le Clainche

An Invariant Feature Space for Flow Region Identification Using Machine Learning 169
 Kheir-eddine Otmani, Esteban Ferrer, and Gerasimos Ntoukas

Smart Disaster Management Using Big Data Analytics 175
 Ali Burak Can, İsmail Burak Parlak, and Tankut Acarman

A Critical Review of Deployable Truss Masts and Proposal of a New Mast: HiDAM 181
 Yunus Cebeci, Murat Demirel, and Gökhan Kiper

Implementation of Trajectory Propagator for Artillery Projectiles Based on Artificial Neural Networks 187
 Alejandro Céniz Bragado, Alberto Solera-Rico, and M. A. Gómez

Manufacturing of a Hybrid VTOL UAV Using Rapid Prototyping Techniques 193
 Sinan Alnıpak, Turan Konyalıođlu, İbrahim Halil Şahin, and Erdinç Altuđ

Efficient Data-Driven Algorithms to Identify Patterns in Aeronautical Industrial Problems	201
Eneko Lazpita, Beka Begiashvili, Jesús Garicano, Soledad Le Clainche, and Eusebio Valero	
The Use of Tethered Unmanned Aerial Vehicles in the Field of Defense and Current Developments	207
Alpaslan Durmus, Erol Duymaz, and Mehmet Baran	
Optimal Thermal Sensor Placement for Accurate Heat Transfer Measurements	215
Jorge Saavedra and Agustín Villa Ortiz	
Time-Varying Consensus Formation Control of a Group of Quadrotor System with Collision Avoidance	221
Kaan Can and Abdullah Başçi	
Aerodynamic Effects of Airfoil Shape on Tandem Airfoil Configuration in Low-Reynolds-Number Transonic Flows	229
Nitin Vinodh, Ashwin Sridhar, Pavan Asha Sreekanth, Nivetha Srinivasan, Sanjiv Krishna Vetrivel, Balajee Ramakrishnananda, and T. Rajesh Senthil Kumar	
Neural Networks to Speed Up Multiphase Flow Numerical Simulations	235
León Mata, Rodrigo Abadía-Heredia, José Miguel Pérez, and Soledad Le Clainche	
Installation of a Ram Air Turbine in a Fixed-Wing UAV	241
María Expósito Turbak, Xin Chen, and Andreu Carbó Molina	
Assessment of UAV Operators by Human Factor Analysis and Classification System (HFACS) Based on AHP	249
Omar Alharasees and Utku Kale	
WMLES of a Small-Scale Hovering Propeller	259
Jelena Svorcan and Christopher Ivey	
A Review on Fishbone Active Camber Morphing Wing Surfaces	265
Emre Özbek, Selcuk Ekici, and T. Hikmet Karakoc	
Reliable Aircraft Trajectory Prediction Using Autoencoder Secured with P2P Blockchain	271
Seyed Mohammad Hashemi, Seyed Ali Hashemi, and Ruxandra Mihaela Botez	
Sensor Hybridization Through Neural Networks for Terminal Guidance	277
Raul de Celis, P. Solano-Lopez, and Luis Cadarso	

**Performance Improvement of a Fixed-Wing UAV
Using Model Predictive Control 283**
Abdurrahman Talha Yildiz and Kemal Keskin

**Deep Q Network-Based Controller for Vertical Takeoff
and Landing System 291**
Şerefcan Helvacıoğlu, Mehmet Uğur Soydemir,
Alkım Gökçen, and Savaş Şahin

**Process and Measurement Noise Covariance Tuning
in Kalman-Based Estimator Aided by SVD 297**
Chingiz Hajiyev and Demet Cilden-Guler


**Fault-Tolerant Attitude Estimation for a Nanosatellite
Using Adaptive Fading Kalman Filter 303**
Hasan Kinatas and Chingiz Hajiyev

On the Number of Monte Carlo Runs for Stochastic Processes 311
Alvaro Arroyo Cebeira and Mariano Asensio Vicente

Index 317

Energy Storage Technologies in Aircraft Hybrid-Electric Propulsion Systems



Murat Ayar, Selcuk Ekici, and T. Hikmet Karakoc 

1 Introduction

Air transportation is more and more in our lives today. The increase in the risk of depletion of conventional fuels in aircraft, its adverse effects on sustainability, and the gradual increase in greenhouse gas emissions have led to efforts to make the propulsion systems of new-generation aircraft environmentally friendly. Studies have shown that air traffic doubles every 15 years (De Neufville et al., 2013). Accordingly, it is obvious that CO₂ emission, which is one of the main causes of global warming due to aircraft, will increase at the same rate. As an alternative to propulsion systems in conventional aircraft, hybrid and electric aircraft technologies, which have almost zero environmental pollution and reduce side factors such as noise, have become a very important goal (Varyukhin et al., 2019).

Today, most aircraft use internal combustion engines. The interest in electric aircraft is increasing day by day due to their superior features such as low noise, vibration, emissions, and high efficiency (Baroutaji et al., 2019). Depending on their energy source, electric aircraft are classified as all electric aircraft (AEA) and more electric aircraft (MEA) (Zhang et al., 2008). AEA class aircraft are powered entirely by electricity, while MEA class aircraft are powered by internal combustion engines fuelled to a certain extent by conventional fuels (Boglietti et al., 2009). Hybrid-

M. Ayar (✉)

Faculty of Aeronautics and Astronautics, Eskişehir Technical University, Eskişehir, Türkiye
e-mail: muratayar@eskisehir.edu.tr

S. Ekici

Faculty of Economics and Administrative Sciences, Iğdir University, Iğdir, Türkiye

T. H. Karakoc

Faculty of Aeronautics and Astronautics, Eskişehir Technical University, Eskişehir, Türkiye
Information Technology Research and Application Center, Istanbul Ticaret University,
Istanbul, Türkiye

electric propulsion is used for situations where the aircraft receives the energy required for the electric motor from more than one different energy source.

Since electric aircraft do not use fossil fuels as an energy source, operational costs related to fuels and maintenance are significantly reduced. Moreover, the maneuverability and performance of the aircraft are improved, and the aircraft can achieve a lower level of vibration (Silva et al., 2022). However, despite these benefits, there are still a number of obstacles to the application of electric aircraft. These obstacles generally stem from the fact that battery technology is still not at an adequate level (Dorn-Gomba et al., 2020). Very large batteries are needed to provide propulsion with electrical energy. Nevertheless, the energy density of Li-ion batteries, which are most preferred in electric vehicles, is insufficient compared to the energy density obtained from fossil fuels (Kasimalla & Velisala, 2018).

2 Literature Review

In today's aircraft, electrical energy storage systems, which are used only in certain situations, have become the main source of energy in aircraft where the propulsion system is also converted into electrical energy (Emadi & Ehsani, 2000). For this reason, the importance of energy storage devices such as batteries, fuel cells, solar cells, and supercapacitors has increased considerably (Çınar & Kandemir, 2021). The energy density parameter, which refers to the energy delivered per unit kilogram in energy storage systems, stands out as the most critical element as it is directly related to the range of the aircraft (Koochi-Fayegh & Rosen, 2020). In addition to this, power density is another important parameter, which is particularly important during the takeoff and climb phases (Canders et al., 2019). Batteries have high energy density and moderate power density (Li et al., 2017). The energy density of fuel cells is better than batteries, and their power density is competitive with batteries (Han et al., 2020) (Fig. 1).

In the propulsion systems of electric aircraft, the energy density, defined in watt-hours per kilogram, has a direct impact on determining the range and payload capacity of the aircraft (Gray et al., 2021). While conventional Li-ion batteries can provide an energy density of about 150–200 Wh/kg (Dubal et al., 2019), a fuel cell system provides higher specific energy (Depcik et al., 2020). Energy density affects the flight time that can be achieved with a full tank of fuel (Arat & Süner, 2020), while power density has an impact on characteristics such as maximum speed, payload capacity, achievable flight altitude, and rate of climb (Luo et al., 2021). Batteries have higher power density, while fuel cells provide better energy density than batteries (Collins & McLarty, 2020). Therefore, the combination of fuel cells and batteries is often the ideal solution for better flight.

Fuel cells, which generate electricity through an electrochemical reaction, consist of two electrodes made of a porous material, called anode and cathode, and an electrolyte sandwiched between them (Singh et al., 2021). The structure consisting of each anode-electrolyte-cathode element where the basic electrochemical reactions

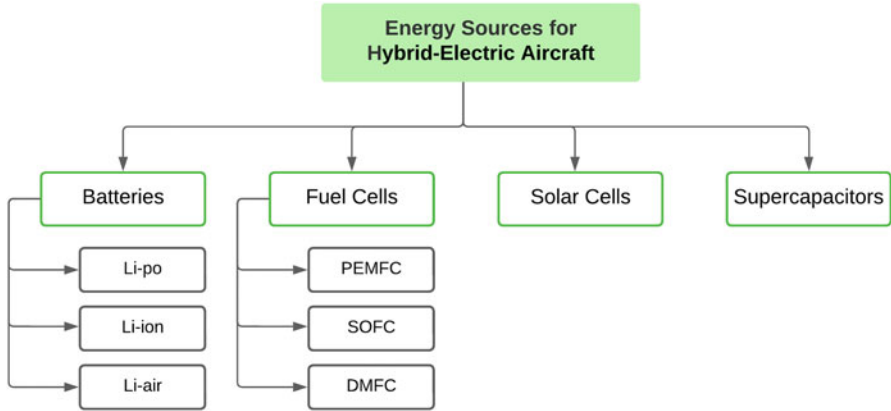
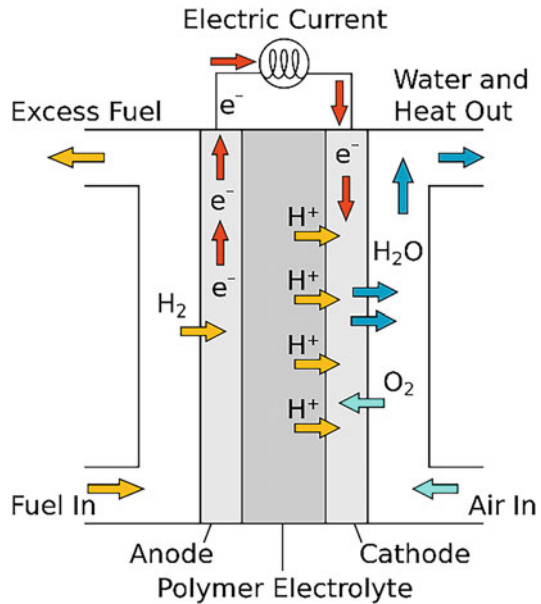


Fig. 1 Energy sources for hybrid electric aircraft

Fig. 2 Basic structure of fuel cell. (Sakurambo, 2023)



in a fuel cell take place is called the membrane electrode assembly. A simple schematic representation of a fuel cell is given in Fig. 2 (Nsour et al., 2019). Since the potential of a single unit cell is between 0.5 and 0.8 V, it is necessary to connect several unit cells in series to form a fuel cell stack to obtain higher voltages (Zhang et al., 2020).

Fuel cells are divided into various classes according to operating temperature, electrolyte type, and fuel type. Fuel cells, if the operating temperature is lower than 150 °C, are called “low-temperature fuel cell,” fuel cells operating between 150 °C and 500 °C are called “medium-temperature fuel cell,” and fuel cells operating

between 500 °C and 1000 °C are called “high-temperature fuel cell” (Xing et al., 2021). According to the type of electrolyte used in fuel cells, they are classified as follows (Peighambardoust et al., 2010):

- Proton exchange membrane fuel cells, PEMFC
- Direct methanol fuel cells, DMFC
- Solid oxide fuel cells, SOFC
- Alkaline fuel cells, AFC
- Phosphoric acid fuel cells, PAFC
- Molten carbonate fuel cells, MCFC

PEMFC-, DMFC-, and SOFC-type fuel cells are more suitable for use in electric aircraft today due to their high power density and high energy conversion efficiency, small footprint, lightness, and low operating temperature (Ellis et al., 2001).

In solar-powered aircraft, an energy storage system is needed to meet the intense power demand during takeoff, landing, and some maneuvers and to provide energy to continue uninterrupted flight at night or in conditions of insufficient solar radiation (Gang & Kwon, 2018). In solar hybrid systems, batteries or fuel cells are usually used as auxiliary energy storage systems (Mane et al., 2016). Lithium polymer (Li-Po), lithium ion (Li-ion), and lithium-sulfur (Li-S) batteries and fuel cells are the most preferred energy storage systems in solar-powered air vehicles (Elouarouar & Medromi, 2022). Li-ion batteries with an energy density of approximately 200 Wh/kg are highly preferred for electric ground and air vehicles and solar vehicle applications (Ranjan & Bodkhe, 2022). Li-Po batteries are similar to Li-ion batteries, but their electrolyte is polymer. Li-S batteries stand out with their high energy density and light weight (Zhang et al., 2018).

Especially during takeoff, climb, landing, and maneuvers during cruise, supercapacitors provide support to the power system as a hybrid with fuel cells in situations where intensive power use is required (Boukoberine et al., 2019). It is considered that supercapacitors for aircraft will be independently applicable in the future when they reach a density in the range of 50–100 Wh/kg (Misra, 2018). Capacitors are circuit elements that store energy by separating positive and negative electrostatic charges (Shukla et al., 2012). In the structure of a capacitor, there are two conductive plates and dielectric material separating these plates. The dielectric material prevents arcing between the two plates, allowing the device to charge more (Kaiser, 2012). Capacitors are divided into two categories: electrochemical capacitors and supercapacitors. Supercapacitors are practically an improved version of electrochemical capacitors (Zhao & Burke, 2021). Although the power density of electrochemical capacitors is very high, their energy density is very low. With their high power density, cyclic stability, and fast charge/discharge, they are a technology that brings solutions to environmental and energy-related issues (El-Kady et al., 2012). While supercapacitors have 10 times higher energy density than electrochemical capacitors (Shukla et al., 2012), they have shorter charge-discharge time, higher power density, higher charge-discharge efficiency, and longer cycle life than batteries (Yi et al., 2014).

3 Conclusion

As the demand for air transportation increases, more and more flights will be made, and more emissions will be released. Aware of this situation, authorities are implementing programs such as zero emission targets. Electric aircraft are seen as the shortest way forward to reach the desired targets. Unfortunately, we cannot yet talk about fully electric vehicles for air passenger transportation. But land transportation has come a long way in this regard. For this reason, there is a need for more academic studies and initiatives on electrification, especially in aircraft propulsion.

References

- Arat, H. T., & Sürer, M. G. (2020). Experimental investigation of fuel cell usage on an air vehicle's hybrid propulsion system. *International Journal of Hydrogen Energy*, 45(49), 26370–26378.
- Baroutaji, A., Wilberforce, T., Ramadan, M., & Olabi, A. G. (2019). Comprehensive investigation on hydrogen and fuel cell technology in the aviation and aerospace sectors. *Renewable and Sustainable Energy Reviews*, 106, 31–40.
- Boglietti, A., Cavagnino, A., Tenconi, A., Vaschetto, S., & di Torino, P. (2009). *The safety critical electric machines and drives in the more electric aircraft: A survey*. 2009 35th annual conference of IEEE industrial electronics.
- Boukoberine, M. N., Zhou, Z., & Benbouzid, M. (2019). A critical review on unmanned aerial vehicles power supply and energy management: Solutions, strategies, and prospects. *Applied Energy*, 255, 113823.
- Canders, W.-R., Hoffmann, J., & Henke, M. (2019). Cooling technologies for high power density electrical machines for aviation applications. *Energies*, 12(23), 4579.
- Çınar, H., & Kandemir, I. (2021). Active energy management based on meta-heuristic algorithms of fuel cell/battery/supercapacitor energy storage system for aircraft. *Aerospace*, 8(3), 85.
- Collins, J. M., & McLarty, D. (2020). All-electric commercial aviation with solid oxide fuel cell-gas turbine-battery hybrids. *Applied Energy*, 265, 114787.
- De Neufville, R., Odoni, A. R., Belobaba, P. P., & Reynolds, T. G. (2013). *Airport systems: Planning, design, and management*. McGraw-Hill Education.
- Depcik, C., Cassady, T., Collicott, B., Burugupally, S. P., Li, X., Alam, S. S., Arandia, J. R., & Hobeck, J. (2020). Comparison of lithium ion batteries, hydrogen fueled combustion engines, and a hydrogen fuel cell in powering a small unmanned aerial vehicle. *Energy Conversion and Management*, 207, 112514.
- Dorn-Gomba, L., Ramoul, J., Reimers, J., & Emadi, A. (2020). Power electronic converters in electric aircraft: Current status, challenges, and emerging technologies. *IEEE Transactions on Transportation Electrification*, 6(4), 1648–1664.
- Dubal, D., Jagadale, A., Chodankar, N. R., Kim, D. H., Gomez-Romero, P., & Holze, R. (2019). Polypyrrole nanotubes as a promising cathode material for Li-ion batteries and Li-ion capacitors: Two-in-one approach. *Energy Technology*, 7(2), 193–200.
- El-Kady, M. F., Strong, V., Dubin, S., & Kaner, R. B. (2012). Laser scribing of high-performance and flexible graphene-based electrochemical capacitors. *Science*, 335(6074), 1326–1330.
- Ellis, M. W., Von Spakovsky, M. R., & Nelson, D. J. (2001). Fuel cell systems: Efficient, flexible energy conversion for the 21st century. *Proceedings of the IEEE*, 89(12), 1808–1818.
- Elouarouar, S., & Medromi, H. (2022). *Multi-rotors unmanned aerial vehicles power supply and energy management*. E3S web of conferences.

- Emadi, K., & Ehsani, M. (2000). Aircraft power systems: Technology, state of the art, and future trends. *IEEE Aerospace and Electronic Systems Magazine*, 15(1), 28–32.
- Gang, B. G., & Kwon, S. (2018). Design of an energy management technique for high endurance unmanned aerial vehicles powered by fuel and solar cell systems. *International Journal of Hydrogen Energy*, 43(20), 9787–9796.
- Gray, N., McDonagh, S., O’Shea, R., Smyth, B., & Murphy, J. D. (2021). Decarbonising ships, planes and trucks: An analysis of suitable low-carbon fuels for the maritime, aviation and haulage sectors. *Advances in Applied Energy*, 1, 100008.
- Han, G., Kwon, Y., Kim, J. B., Lee, S., Bae, J., Cho, E., Lee, B. J., Cho, S., & Park, J. (2020). Development of a high-energy-density portable/mobile hydrogen energy storage system incorporating an electrolyzer, a metal hydride and a fuel cell. *Applied Energy*, 259, 114175.
- Kaiser, C. J. (2012). *The capacitor handbook*. Springer.
- Kasimalla, V. K., & Velisala, V. (2018). A review on energy allocation of fuel cell/battery/ultracapacitor for hybrid electric vehicles. *International Journal of Energy Research*, 42(14), 4263–4283.
- Koohi-Fayegh, S., & Rosen, M. A. (2020). A review of energy storage types, applications and recent developments. *Journal of Energy Storage*, 27, 101047.
- Li, J., Du, Z., Ruther, R. E., An, S. J., David, L. A., Hays, K., Wood, M., Phillip, N. D., Sheng, Y., & Mao, C. (2017). Toward low-cost, high-energy density, and high-power density lithium-ion batteries. *JOM*, 69, 1484–1496.
- Luo, Y., Qian, Y., Zeng, Z., & Zhang, Y. (2021). Simulation and analysis of operating characteristics of power battery for flying car utilization. *eTransportation*, 8, 100111.
- Mane, S., Kadam, P., Lahoti, G., Kazi, F., & Singh, N. (2016). *Optimal load balancing strategy for hybrid energy management system in DC microgrid with PV, fuel cell and battery storage*. 2016 IEEE international conference on renewable energy research and applications (ICRERA).
- Misra, A. (2018). Energy storage for electrified aircraft: The need for better batteries, fuel cells, and supercapacitors. *IEEE Electrification Magazine*, 6(3), 54–61.
- Nsour, W., Taa’mneh, T., Ayadi, O., & Al Asfar, J. (2019). Design of Stand-Alone Proton Exchange Membrane Fuel Cell Hybrid System under Amman climate [journal article]. *Journal of Ecological Engineering*, 20(9), 1–10. <https://doi.org/10.12911/22998993/111800>
- Peighambaroust, S. J., Rowshanzamir, S., & Amjadi, M. (2010). Review of the proton exchange membranes for fuel cell applications. *International Journal of Hydrogen Energy*, 35(17), 9349–9384.
- Ranjan, A., & Bodkhe, S. B. (2022). Energy management strategy for hybrid energy storage systems in electric vehicle—A review. *International Journal of Electrical and Electronic Engineering & Telecommunications*, 11(2).
- Sakurambo. (2023). Solid oxide fuel cell. In *Wikipedia*. https://commons.wikimedia.org/wiki/File:Solid_oxide_fuel_cell.svg
- Shukla, A., Banerjee, A., Ravikumar, M., & Jalajakshi, A. (2012). Electrochemical capacitors: Technical challenges and prognosis for future markets. *Electrochimica Acta*, 84, 165–173.
- Silva, H. L., Guimarães, T. A. M., & Ziberov, M. (2022). Hybrid-electric airplane design optimization considering climb and cruise phases. *Journal of the Brazilian Society of Mechanical Sciences and Engineering*, 44(1), 41.
- Singh, M., Zappa, D., & Comini, E. (2021). Solid oxide fuel cell: Decade of progress, future perspectives and challenges. *International Journal of Hydrogen Energy*, 46(54), 27643–27674.
- Varyukhin, A., Zakharchenko, V., Vlasov, A., Gordin, M., & Ovdienko, M. (2019). *Roadmap for the technological development of hybrid electric and full-electric propulsion systems of aircrafts*. 2019 international conference on electrotechnical complexes and systems (ICOECS).
- Xing, H., Stuart, C., Spence, S., & Chen, H. (2021). Fuel cell power systems for maritime applications: Progress and perspectives. *Sustainability*, 13(3), 1213.
- Yi, R., Chen, S., Song, J., Gordin, M. L., Manivannan, A., & Wang, D. (2014). High-performance hybrid supercapacitor enabled by a high-rate Si-based anode. *Advanced Functional Materials*, 24(47), 7433–7439.

- Zhang, H., Saudemont, C., Robyns, B., & Petit, M. (2008). *Comparison of technical features between a more electric aircraft and a hybrid electric vehicle*. 2008 IEEE vehicle power and propulsion conference.
- Zhang, Z. W., Peng, H. J., Zhao, M., & Huang, J. Q. (2018). Heterogeneous/homogeneous mediators for high-energy-density lithium–sulfur batteries: Progress and prospects. *Advanced Functional Materials*, 28(38), 1707536.
- Zhang, Q., Tong, Z., & Tong, S. (2020). Effect of cathode recirculation on high potential limitation and self-humidification of hydrogen fuel cell system. *Journal of Power Sources*, 468, 228388.
- Zhao, J., & Burke, A. F. (2021). Electrochemical capacitors: Performance metrics and evaluation by testing and analysis. *Advanced Energy Materials*, 11(1), 2002192.

Use of (PET-G) Material in Mini-scale Unmanned Surface Vehicle (USV) for Additive Manufacturing



Alperen Dođru, Ayberk Sözen, and M. Özgür Seydibeyođlu

Nomenclature

ABS	Acrylonitrile butadiene styrene
CFD	Computer fluid dynamics
FFF	Fused filament fabrication
PET-G	Polyethylene terephthalate glycol
PLA	Polylactic acid
USV	Unmanned surface vehicle

1 Introduction

The defense expenditures of the countries constitute an important part of the world economy. A report by SIPRI (an independent international institute conducting research on conflicts, armaments, disarmament, and arms control) shows that, in 2021, expenses in the defense industry in the USA (\$801 billion, accounting for

A. Dođru

Aviation HVS, Aircraft Technology, Ege University, İzmir, Türkiye

Mechanical Engineering, University of Alberta, Edmonton, AB, Canada

e-mail: alperen.dogru@ege.edu.tr

A. Sözen (✉)

Institute of Marine Sciences and Technology, Dokuz Eylul University, İzmir, Türkiye

e-mail: ayberk.sozen@deu.edu.tr

M. Ö. Seydibeyođlu

Material Sciences, and Engineering, İzmir Katip Çelebi University, İzmir, Türkiye

Advanced Structures & Composites Center, Maine University, Orono, ME, USA

e-mail: ozgur.seydibeyoglu@ikcu.edu.tr

30%), China (\$292 billion, accounting for 14%), India (\$76.6 billion, accounting for 3.6%), the UK (\$68.4 billion, accounting for 3.2%), and Russia (\$65.9 billion, accounting for 3.1%) (Yearbook, 2021). In addition, the defense expenditures of the countries are increasing daily, and the effort to establish technological superiority leads to the use of many resources, mainly research and development, in these areas (Ledesma et al., 2022). The importance of efficient use of resources, development of products suitable for the purpose, and the emergence of projects with high cost/benefit ratio can be seen from the unpredictable budget increases of the past defense industry projects (Hanefi Topal et al., 2014). Integrating the gains in defense technologies into our daily lives increases the standard of living of human beings. The benefits of location systems in finding direction and address, the use of existing communication systems for information and information purposes, and the achievements in materials science leading to new products can be given as examples.

Although additive manufacturing technologies were first used in the 1980s, after the patent restrictions remained, they quickly became widespread in the 2010s and started to be used in many different sectors and application areas. Additive manufacturing has advantages such as meeting the rapidly changing market needs with a high cost/benefit ratio, producing personalized and/or customized products, and providing design flexibility. These methods, which were used for trial production in the past, are now able to produce final products. Although we do not have high production speeds, advantages such as freedom of design, on-site manufacturing, and low cost in low-volume production have made additive manufacturing methods today's focus production method and research topic. Additive manufacturing methods produce in layers by slicing the 3D drawing data of the part in layers and processing the solid regions in each slice. Today, it is possible to shape all kinds of materials, including metal, polymer, and even ceramic, with these methods. The parts are processed in layers, and these processes involve different techniques such as laser joining or material extrusion. Among these methods, fused filament fabrication (FFF) is the most cost-effective and widely used method (Cole et al., 2020). In the FFF method, polymer materials are used as raw materials.

More than 51% of the materials produced by additive manufacturing are polymer materials. In the FFF method, a heated nozzle moving in the Cartesian coordinate system melts and extrudes the polymer. It is mostly fed in polymer filament form. Equipped with a heated nozzle, the head can move on the X- and Y-axis. The movement in the Z-axis is very precise, and this determines the layer height. Parts are produced layer by layer in this method (Fig. 1).

In today's small craft industry, the use of polymer composite materials is becoming widespread and replacing metals. Thermoplastic materials are preferred more, and their use is supported due to the recycling problems of thermosettings (Fig. 2).

Even though thermoplastic or thermosetting matrix composite boats have size limits compared to metal hull boats, it can be said that polymer materials are ideal to produce small-sized unmanned surface vehicles (USVs) (Yan et al., 2010). In addition, considering that the products we use today are the garbage of tomorrow, the recycling of thermosetting composite boats and synthetic fiber reinforcements is an important problem (Backman & Lidgren, 1986). Humanity is facing this problem

Fig. 1 FFF method in additive manufacturing

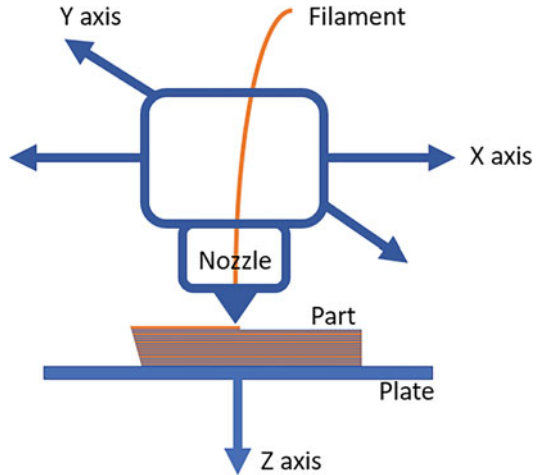


Fig. 2 A small craft example for patrol boats. (ribandhsc.com, 2022)

more and more every day. The recycling advantages of thermoplastic materials are critical to sustainability. The use of thermoplastic materials with the FFF method creates significant opportunities. Many different thermoplastic materials can be processed with the FFF method: PLA, ABS, PE, PA, PET, etc. One of these thermoplastic polymers is polyethylene terephthalate glycol (PETG). Developed from PET material, PETG copolymer has increasing importance in the FFF method, thanks to its properties. It has durability, flexibility, high impact resistance, high chemical resistance, ultraviolet and weather resistance, low moisture absorption and gas permeability, no odor, and recyclability (Bhandari et al., 2019; Latko-Duralek et al., 2019). PETG material is easy to produce with the FFF method, and stable



Fig. 3 USV boats. (Unmanned Surface Vehicles (USV), [n.d.](#))

products can be produced (Szykiedans et al., 2017). In addition, because PETG is an amorphous and linear polymer, it is an excellent material for extrusion, injection molding, blow molding, and thermoforming (Latko-Durałek et al., 2019) (Fig. 3).

PETG's low crystalline phase content, good mechanical properties, and good chemical resistance make it a good alternative for marine applications (Barrios & Romero, 2019; Srinivasan et al., 2020). Intercalarily, when the advantages of additive manufacturing and thermoplastic materials are combined, mini-scale USV has opportunities for the maritime industry due to their low production and operating costs. Mini-scale USVs are used for underwater mapping, underwater imaging, minefield detection, combating irregular migrants, territorial water security, etc., can be used for purposes.

2 Method

Resistance analysis was carried out using finite element methods of boat forms with different principles, such as planing, displacement, and catamaran. The hull form, which exhibits the lowest resistance value, was produced with the FFF method using PETG copolymer developed from environmentally friendly PET material, and 40-cm-long mini-scale USV sea trials were performed. In numerical analyses, the turbulent flow around the boundary condition is modeled by the Reynolds-averaged Navier-Stokes (RANS) model and the SST Menter $k-\epsilon$ turbulence model.

A 1.75-mm-diameter PETG (copolyester) filament of the AzureFilm brand was used. AzureFilm PETG (copolyester) filament is a filament that combines the properties of ABS filament (strong, temperature resistant, extremely durable,

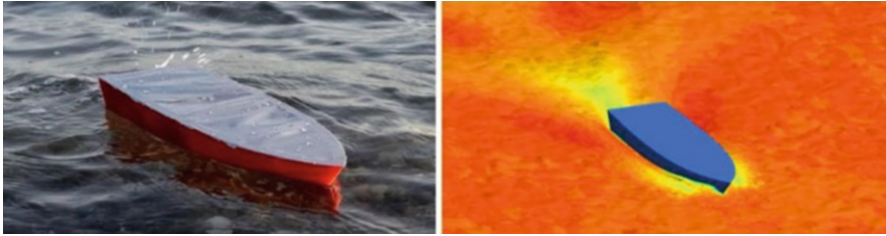


Fig. 4 USV built by additive manufacturing on PET-G material and CFD

Table 1 Resistance results for three different boat types

Velocity (m/s)	Resistance (Newton)		
	Planing hull	Displacement hull	Catamaran hull
1	0,3	0,4	0,45
3	1,7	2,32	2,57
5	5,12	6,38	7,2

flexible) and PLA filament (easy to print). It has a density of 1.29 g/cm^3 , 51 MPa tensile yield stress, and 68 MPa flexural strength. The red-colored filament was preferred to make a visual inspection and photographing clearer and easier.

The production of the mini-scale USV design selected by comparing the data obtained as a result of the numerical analysis was carried out with the Creality CR-200b brand model FFF device, using a 0.6-mm-diameter nozzle. Printing parameters were obtained as infill rate 25%, layer height 0.2 mm, nozzle temperature $230 \text{ }^\circ\text{C}$ and printing table temperature $80 \text{ }^\circ\text{C}$ and printing speed 40 mm/s (Fig. 4).

3 Results and Discussion

This study shows the numerical prediction of resistance characteristics of three hull models, for different velocity conditions. The resistance characteristics of the hull models were compared in terms of total resistance. For the same hydrodynamic conditions and investigated velocity range, the total resistance values of the catamaran hull model are higher than the others. Planing hull performs the best results. Consequently, this study shows that CFD can be used as a practicable and feasible tool in gaining insight into the various hydrodynamic problems and generating new designs.

PET-G provides superior layer adhesion. It is much more resistant to layer shifting. This feature makes this material very attractive for marine uses. Sea tests prove this situation. Although the outer layer wall thickness is 2 mm, waterproofing has been achieved successfully. In addition, the hull was printed in two pieces, and the welding points of the hull are quite strong and waterproof (Table 1).

4 Conclusion

In this study, the processes of determining the material performance of PET-G material and producing a small-scale USV resistant to sea conditions with additive manufacturing were carried out to emphasize effective benefits. PETG material has great potential for marine use in additive manufacturing with its superior waterproofing. USV produced by additive manufacturing is expected to become widespread soon due to increasing cost concerns and design freedom in the defense industry.

References

- Backman, M., & Lidgren, K. (1986). Recovery of old plastic small craft. *Resources and Conservation*, 12(3–4), 215–224. [https://doi.org/10.1016/0166-3097\(86\)90012-X](https://doi.org/10.1016/0166-3097(86)90012-X)
- Barrios, J., & Romero, P. (2019). Improvement of surface roughness and hydrophobicity in PETG parts manufactured via fused deposition modeling (FDM): An application in 3D printed self-cleaning parts. *Materials*, 12. <https://doi.org/10.3390/ma12152499>
- Bhandari, S., Lopez-Anido, R. A., & Gardner, D. J. (2019, June). Enhancing the interlayer tensile strength of 3D printed short carbon fiber reinforced PETG and PLA composites via annealing. *Additive Manufacturing*, 30, 100922. <https://doi.org/10.1016/j.addma.2019.100922>
- Cole, D. P., Gardea, F., Henry, T. C., Seppala, J. E., Garboczi, E. J., Migler, K. D., Shumeiko, C. M., Westrich, J. R., Orski, S. V., & Gair, J. L. (2020). AMB2018-03: Benchmark physical property measurements for material extrusion additive manufacturing of polycarbonate. *Integrating Materials and Manufacturing Innovation*, 9(4), 358–375. <https://doi.org/10.1007/s40192-020-00188-y>
- Hanefi Topal, M., Unver, M., & Türed, S. (2014). *The military expenditures and economic growth nexus: Panel bootstrap granger causality evidence from NATO countries*. Paper Knowledge. Toward a Media History of Documents.
- Latko-Durafek, P., Dydek, K., & Boczkowska, A. (2019). Thermal, rheological and mechanical properties of PETG/rPETG blends. *Journal of Polymers and the Environment*, 27(11), 2600–2606. <https://doi.org/10.1007/s10924-019-01544-6>
- Ledesma, C. I. O., Quetua, S. M. S., & Rosete, M. A. L. (2022). Analyzing the economic effects of military expenditures in ASEAN countries. *International Journal of Social and Management Studies*, 3(5), 20–36.
- ribandhsc.com. (2022). http://ribandhsc.com/media/images/earticles/16_earticle.jpg
- Srinivasan, R., Nirmal Kumar, K., Jenish Ibrahim, A., Anandu, K. V., & Gurudhevan, R. (2020). Impact of fused deposition process parameter (infill pattern) on the strength of PETG part. *Materials Today: Proceedings*, 27, 1801–1805. <https://doi.org/10.1016/j.matpr.2020.03.777>
- Szykiedans, K., Credo, W., & Osinski, D. (2017). *Selected mechanical properties of PETG 3-D prints*. XXI international Polish-Slovak conference “machine modeling and simulations 2016,” pp. 455–461.
- Unmanned Surface Vehicles (USV). (n.d.). Retrieved April 29, 2022, from <https://www.unmannedsystemstechnology.com/company/seafloor-systems/>
- Yan, R. J., Pang, S., Sun, H. B., & Pang, Y. J. (2010). Development and missions of unmanned surface vehicle. *Journal of Marine Science and Application*, 9(4), 451–457. <https://doi.org/10.1007/s11804-010-1033-2>
- Yearbook, S. (2021). *Armaments, disarmament and international security*. www.sipriyearbook.org

The Use of State Feedback Control Based on LMI to Suppress Oscillations of Payload Carried by UAV



Renan S. Geronel, Ruxandra M. Botez, and Douglas D. Bueno

1 Introduction

Unmanned aerial vehicles (UAVs) have gained rapid attention as a potential solution to overcome geographical and logistic challenges in medical transportation. Nowadays, UAVs are used to assist health-care services in the transportation of medical goods and organs and in the delivery of blood stocks and pharmacies to clinics and hospitals. On the other hand, some medicines are sensitive to vibration, which can decrease the therapeutic efficacy of the transported load. Thus, UAVs represent a low-cost and feasible solution to be used in remote areas and low-income countries and therefore to overpass critical demand in the medical field.

Several controllers have been developed to enhance the UAV performance (Kammegne et al., 2017, 2019) at LARCASE laboratory (Botez, 2018). Two types of UAVs (fixed and rotary wings) and a traditional road vehicle were used to assess the vibration intensities on medical cargoes (Oakey et al., 2021). The insulin was chosen as a medical cargo, since its sensibility to vibration can induce its precipitation and then its loss of efficacy. The results have shown that the overall vibration intensities obtained from UAVs were more significant than those from road transportation, which makes the frequency evaluation a prerequisite to planning new missions of medical goods not previously transported by UAVs.

This paper introduces a vibrating payload attenuation trajectory control. A 7-degree-of-freedom UAV and an elastic attachment (between the UAV and its payload) are considered for the system modeling. Then, proportional derivative

R. S. Geronel (✉) · D. D. Bueno
Mechanical Engineering department, UNESP, São Paulo, Brazil
e-mail: renan.sanches@unesp.br; douglas.bueno@unesp.br

R. M. Botez
École de technologie supérieure (ÉTS), Montreal, QC, Canada
e-mail: Ruxandra.Botez@etsmtl.ca

(PD) is combined with the state feedback control based on linear matrix inequality (LMI) methodology to generate a desired trajectory with payload oscillation suppression.

2 Methodology

A UAV with a vibrating payload is modeled using 7 degrees of freedom, as depicted in Fig. 1. Two coordinate reference frames are used to describe the motion of the system: the inertial reference frame and the body-fixed reference frame.

where x, y, z and ϕ, θ, ψ are the linear and angular UAV positions, while v_{xB}, v_{yB}, v_{zB} and $\omega_x, \omega_y, \omega_z$ are the linear and angular velocities of the UAV. The terms z_p and m_p correspond to the payload vertical position and the payload mass, respectively. In addition, m is the UAV mass and k_p is the vertical stiffness between the UAV and its payload. The equation of motion of the UAV carrying a payload is expressed as:

$$\mathbf{M}_I \ddot{\boldsymbol{\eta}}_p + \mathbf{C}_I \dot{\boldsymbol{\eta}}_p + \mathbf{K}_I \boldsymbol{\eta}_p + \mathbf{g}_I = \boldsymbol{\tau}_I + \mathbf{F}_{cI} - \mathbf{F}_o \quad (1)$$

where \mathbf{M}_I is the inertial matrix, \mathbf{C}_I is the Coriolis matrix, \mathbf{K}_I is the stiffness matrix, \mathbf{g}_I is the gravitational vector, $\boldsymbol{\tau}_I$ is the control input vector, \mathbf{F}_{cI} is the constraint vector, and \mathbf{F}_o is the state feedback control. The matrices can also be written in body frame as $\mathbf{M}_I = \mathbf{I}_{7 \times 7}$, $\mathbf{C}_I = \mathbf{J}_b \mathbf{M}_b^{-1} \mathbf{C}_b \mathbf{J}_b - \dot{\mathbf{J}}_b \mathbf{J}_b^{-1}$, and $\mathbf{T}_I = \mathbf{J}_b \mathbf{M}_b^{-1} \mathbf{T}_b$, where $\mathbf{I}_{7 \times 7}$ is an identity matrix, \mathbf{M}_b is the inertial matrix, \mathbf{C}_b is the Coriolis matrix, \mathbf{T}_I is used to represent the terms \mathbf{g}_I , \mathbf{K}_I , and $\boldsymbol{\tau}_I$ (similarly to \mathbf{T}_b), and \mathbf{J}_b and $\dot{\mathbf{J}}_b$ are the transformation matrix and its time derivative. The elastic representation $\mathbf{K}_I - \mathbf{B}_1 k_p \mathbf{l}_d$ is divided into two terms. The first term (\mathbf{K}_I) is placed in the stiffness matrix, while the second ($\mathbf{B}_1 k_p \mathbf{l}_d$) represents the constraint force vector \mathbf{F}_{cI} . The stiffness is then defined as:

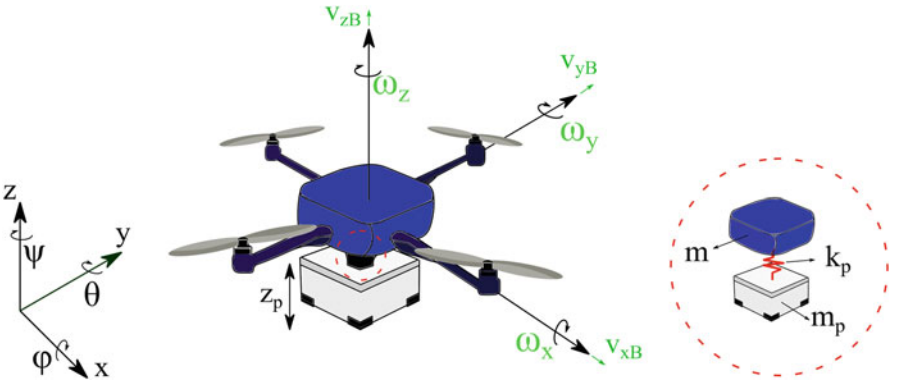


Fig. 1 Schematic illustration of the UAV

$$\mathbf{K}_b = [\mathbf{0}_{2 \times 7} \quad \mathbf{k}_{sp} \quad \mathbf{0}_{3 \times 7} \quad -\mathbf{k}_{sp}]^T \tag{2}$$

where $\mathbf{k}_{sp} = \{0 \ 0 \ k_p \ 0 \ 0 \ 0 \ -k_p\}$, and $\mathbf{B}_I = \{\mathbf{J}_b \mathbf{M}_b^{-1} \mathbf{B}_{Ia} \ \mathbf{0}_{7 \times 1}\}$, such that $\mathbf{B}_{Ia} = \{0 \ 0 \ 1 \ 0 \ 0 \ 0 \ -1\}^T$. The generalized coordinate vector of the UAV and its payload is given by $\boldsymbol{\eta}_p = \{x \ y \ z \ \phi \ \theta \ \psi \ z_p\}^T$. The second-order differential equation (Eq. (1)) can also be represented in its state form as $\dot{\mathbf{x}} = \mathbf{A}\mathbf{x} + \mathbf{B}\mathbf{u} + \mathbf{X}_g + \mathbf{F}_{ci} - \mathbf{B}\mathbf{F}_o$, where the dynamic (\mathbf{A}) and input (\mathbf{B}) matrices are defined as follows:

$$\mathbf{A} = \begin{bmatrix} -\mathbf{M}_I^{-1} \mathbf{C}_I & -\mathbf{M}_I^{-1} \mathbf{K}_I \\ \mathbf{I}_{7 \times 7} & \mathbf{0}_{7 \times 7} \end{bmatrix}, \quad \mathbf{B} = \begin{bmatrix} -\mathbf{M}_I^{-1} \\ \mathbf{0}_{7 \times 7} \end{bmatrix} \tag{3}$$

Further details regarding the equation of motion development and its matrices can be found in Geronel et al. (2023).

2.1 Controller Design

The controller is divided into two stages. The first stage (PD controller) generates the UAV desired trajectory, and the state feedback based on LMI is used to suppress the payload residual oscillations (second stage). Figure 2 shows the schematic illustration of the controller design.

The controller inputs, generated from the PD controller, can be defined such as:

$$U_1 = \tilde{m}(g + k_{pz}(z_{des} - z) + k_{dz}(\dot{z}_{des} - \dot{z}))/c\phi c\theta \tag{4}$$

where $c(\cdot)$ is the cosine function and $\tilde{m} = m + m_p$. In addition, the attitude controller inputs are expressed by the following expressions: $U_2 = I_x [k_{p\phi}(\phi_{des} - \phi) + k_{d\phi}(\dot{\phi}_{des} - \dot{\phi})]$, $U_3 = I_y [k_{p\theta}(\theta_{des} - \theta) + k_{d\theta}(\dot{\theta}_{des} - \dot{\theta})]$, and $U_4 = I_z [k_{p\psi}(\psi_{des} - \psi) + k_{d\psi}(\dot{\psi}_{des} - \dot{\psi})]$, where I_j are the moments of inertia along x , y and z axes and k_{pj} and k_{dj} are the PD controller gains (Castillo-Zamora et al., 2018). Next, the linearized equations of motion are calculated at the hovering

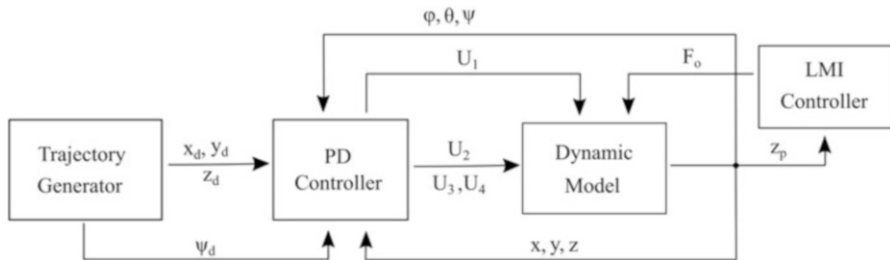


Fig. 2 Schematic illustration of the controller design

state of the UAV (where ϕ and θ are small and ψ is stabilized close to zero), leading to the linearized dynamic matrix (\mathbf{A}_1), expressed as follows:

$$\mathbf{A}_1 = \begin{bmatrix} \mathbf{0}_{7 \times 7} & \mathbf{A}_{1a} \\ \mathbf{I}_{7 \times 7} & \mathbf{0}_{7 \times 7} \end{bmatrix}, \quad \text{where } \mathbf{A}_{1a} = [\mathbf{A}_a \quad \mathbf{A}_b \quad \mathbf{A}_c/m \quad \mathbf{0}_{7 \times 3} \quad -\mathbf{A}_c/m_p]^T \quad (5)$$

where $\mathbf{A}_a = \{0 \ 0 \ 0 \ 0 \ g \ 0 \ 0\}^T$, $\mathbf{A}_b = \{0 \ 0 \ 0 \ -g \ 0 \ 0 \ 0\}^T$, $\mathbf{A}_c = \{0 \ 0 \ -k_p \ 0 \ 0 \ 0 \ k_p\}^T$. Since the controller aims to suppress the vertical direction, only the vertical states (z and z_p) are used to design the state feedback control based on the LMI, as follows:

$$\mathbf{A}_s = \begin{bmatrix} \mathbf{0}_{2 \times 2} & \mathbf{A}_a \\ \mathbf{I}_{2 \times 2} & \mathbf{0}_{2 \times 2} \end{bmatrix}, \quad \text{where } \mathbf{A}_a = \begin{bmatrix} k_p/m & -k_p/m \\ -k_p/m_p & k_p/m_p \end{bmatrix} \quad (6)$$

and they are also represented in the state form as $\dot{\mathbf{x}} = \mathbf{A}_s \mathbf{x}_s + \mathbf{B}_s F_o$, where \mathbf{A}_s is dynamic matrix, \mathbf{B}_s is the control input ($\mathbf{B}_s = \{0 \ 1/m_p\}^T$) and \mathbf{x}_s is the state vector. Assuming that the feedback control is given as $F_o = -\mathbf{K}_h \mathbf{x}_s$ where \mathbf{K}_h is the gain matrix, the generic LMI equation is defined using $\mathbf{W} \mathbf{A}_s^T + \mathbf{A}_s \mathbf{W} - \mathbf{Z}^T \mathbf{B}_s^T - \mathbf{B}_s \mathbf{Z} + 2\alpha \mathbf{W} < 0$. In addition, to ensure a minimum decay ratio (α), damping ratio ($\xi = c(\theta_h)$), and a minimum undamped natural frequency ($\omega_d = r s(\theta_h)$), the LMI poles must be calculated in a region of interest $S(\alpha, r, \theta_h)$, as seen in Chilali and Gahinet (1996):

$$\begin{bmatrix} -r\mathbf{W} & \mathbf{A}_s \mathbf{W} - \mathbf{B}_s \mathbf{Z} \\ \mathbf{W} \mathbf{A}_s - \mathbf{Z}^T \mathbf{B}_s^T & -r\mathbf{W} \end{bmatrix} < 0$$

$$\begin{bmatrix} s\theta_h (\mathbf{W} \mathbf{A}_s^T + \mathbf{A}_s \mathbf{W} - \mathbf{Z}^T \mathbf{B}_s^T - \mathbf{B}_s \mathbf{Z}) & c\theta_h (-\mathbf{W} \mathbf{A}_s^T + \mathbf{A}_s \mathbf{W} + \mathbf{Z}^T \mathbf{B}_s^T - \mathbf{B}_s \mathbf{Z}) \\ c\theta_h (\mathbf{W} \mathbf{A}_s^T - \mathbf{A}_s \mathbf{W} - \mathbf{Z}^T \mathbf{B}_s^T + \mathbf{B}_s \mathbf{Z}) & s\theta_h (\mathbf{W} \mathbf{A}_s^T + \mathbf{A}_s \mathbf{W} - \mathbf{Z}^T \mathbf{B}_s^T - \mathbf{B}_s \mathbf{Z}) \end{bmatrix} < 0 \quad (7)$$

The poles are calculated by combining these three LMI expressions (the generic LMI equation and Eq. 7). Following these assumptions, the gain matrix is calculated as $\mathbf{K}_h = \mathbf{Z} \mathbf{W}^{-1}$, and it is used to attenuate the payload oscillations.

3 Results and Discussion

For numerical simulations, m and m_p are 2.2 kg and 0.44 kg, l_d is 0.2 m and $I_x = I_y = 0.0167 \text{ kgm}^3$, and $I_z = 0.0231 \text{ kgm}^3$. Figure 3 shows the three-dimensional trajectory and the vertical displacement of the UAV and its payload.

The presence of a vibrating payload impacts on the UAV trajectory, by creating residual oscillations (as seen in Fig. 3b). In this sense, the use of the state feedback based on LMI results in significant undesired oscillation reduction (as seen in

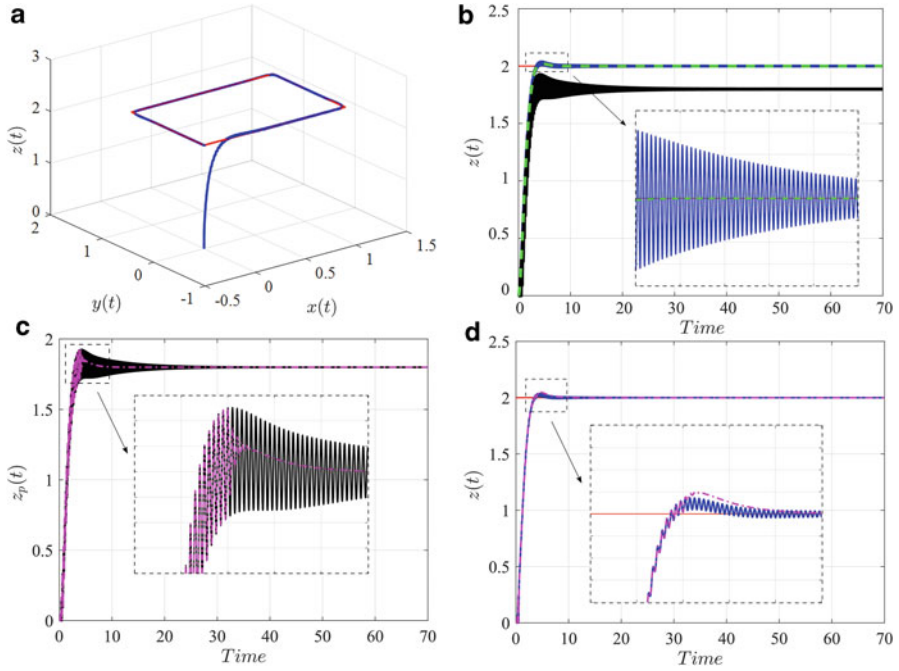


Fig. 3 Flight (a) Three dimensional trajectory and (b) UAV and its payload trajectory with no control, (c) payload trajectory, and (d) UAV trajectory in the presence of controller. The lines represent the desired (—), UAV (—), payload (—), and UAV with no load (- -) trajectories in the absence of the controller and in the presence of controller (-.)

Fig. 3c, d). Therefore, besides guaranteeing a safe transportation of fragile loads, a significant increase of flight performance (for both UAV and its payload) is obtained.

4 Conclusion

The presence of an attached payload can alter the UAV dynamics, by creating residual oscillations on the system. Since, in medical applications, some products are sensitive to vibrations, these oscillations can damage the cargo efficacy. Then, the combination of proportional derivative and state feedback control based on the LMI is designed to attenuate residual oscillations and to consequently increase the UAV flight performance. Therefore, low payload oscillations guarantee a rapid spread and use of commercial UAVs in low-income countries with high transportation reliability.

Funding The authors thank the Brazilian Coordination for the Improvement of Higher Education Personnel – Finance Code 001 (and PDSE 88881.622726/2021–01), NSERC for the Canada Research Chair Holder Tier 1 in Aircraft Mod. and Sim. Tech. Program, and the National Council for Scientific and Technological Development – Grant no. 406328/2021-8.

References

- Botez, R. M. (2018). Morphing wing, UAV and aircraft multidisciplinary studies at the laboratory of applied research in active controls, avionics and AeroServoElasticity LARCASE. *AerospaceLab Journal, ONERA*, 1–11. <https://doi.org/10.12762/2018.AL14-02>
- Castillo-Zamora, J. J., Camarillo-Gomez, K. A., Perez-Soto, G. I., & Rodriguez-Resendiz, J. (2018). Comparison of PD, PID and sliding-mode position controllers for V-tail quadcopter stability. *IEEE Access*, 6, 38086–38096.
- Chilali, M., & Gahinet, P. (1996). H_∞ design with pole placement constraints: An LMI approach. *IEEE Transactions on Automatic Control*, 41, 1–10.
- Geronel, R. S., Botez, R. M., & Bueno, D. D. (2023). Dynamic responses due to the Dryden gust of an autonomous quadrotor UAV carrying a payload. *The Aeronautical Journal*, 127, 116–138.
- Kammegne, M. J. T., Botez, R. M., Grigorie, L. T., Mamou, M., & Mébarki, Y. (2017). Proportional fuzzy feed-forward architecture control validation by wind tunnel tests of a morphing wing. *Chinese Journal of Aeronautics*, 30, 561–576.
- Kammegne, M. J. T., Botez, R. M., Grigorie, L. T., Mamou, M., & Mébarki, Y. (2019). A new hybrid control methodology for a morphing aircraft wing-tip actuation mechanism. *The Aeronautical Journal*, 123, 1757–1787.
- Oakey, A., Waters, T., Zhu, W., Royall, P. G., Cherrett, T., Courtney, P., Majoe, D., & Jelev, N. (2021). Quantifying the effects of vibration on medicines in transit caused by fixed-wing and multi-copter drones. *Drones*, 5, 1–22.

Impact of Free-Form Deformation Control Points on the Optimization of the UAS-S45



Mir Hossein Negahban, Musavir Bashir, and Ruxandra Mihaela Botez

1 Introduction

Aerodynamic shape optimization has recently been the focus of many researchers in the field of aeronautics, thanks to its significant contribution in the improvement of aircraft and unmanned aerial vehicle (UAV) performance. In the aerodynamic optimization, the choice of an adequate parametrization method to adapt the wing shape is the crucial part in the choice of an optimization algorithm, which means that the more realistically the wing shape could be parameterized, the more accurate and robust the optimization results will be. A successful parameterization method is characterized by its capability to cover a large design space using a limited set of design variables (Masters & Taylor, 2015). Shape parameterization methodology is divided into two categories: constructive and deformative. In “constructive” methods, the generation of an airfoil is done using a series of specified parameters, while in “deformative” methods, such as free-form deformation, the wing is generated by changing its initial shape. In a comparative study (Sripawadkul et al., 2010), five constructive parametrization methods are compared. Several desired characteristics, namely, parsimony, intuitiveness, orthogonality, completeness, and flawlessness, are applied as criteria to find the best method. In the morphing wing design, numerous aerodynamic shape optimizations have been carried out at the LARCASE (Botez 2018, 2022). Using constructive parametrization, Bashir et al. (2021a, b) performed two aerodynamic shape optimizations for morphing leading edge using Bezier-PARSEC parametrization method, taking advantage of Bezier and PARSEC. In another study (Bashir et al., 2022), the CST parametrization was implemented on

M. H. Negahban (✉) · M. Bashir · R. M. Botez
Research Laboratory in Active Controls, Avionics and Aeroservoelasticity (LARCASE), École de technologie supérieure (ÉTS), Université du Québec, Montreal, QC, Canada
e-mail: mir-hossein.negahban-alvar.1@ens.etsmtl.ca;
musavir-bashir.musavir-bashir.1@ens.etsmtl.ca; Ruxandra.botez@etsmtl.ca

morphing leading edge (drooped nose leading edge) by adding local shape changes. Nonetheless, in the optimization of the whole wing section or the whole aircraft or UAV, the constructive parametrization methods may lose their efficiency since the number of design variables could not be met; therefore, it is better to use the free-form deformation (FFD) technique because of its flexibility in problems with high number of design variables of order of 10^2 . In the literature, there are many available optimization problems that use the FFD technique in the optimization of the whole wing and aircraft. FFD parametrization technique was applied to the UAV and common research model (CRM) wings with the number of design variables being 127 and 201, respectively (He et al., 2019). In another study (He et al., 2018), FFD parametrization method was applied for the optimization of Ahmed body and a full model car. Also, He et al. (2020) parameterized CRM wing-body-tail (whole aircraft) with a total design variable of 227, blended tube, and turbine blade with FFD technique. It is obvious that due to higher number of design variables for three-dimensional body optimization, the FFD technique is the most feasible methodology.

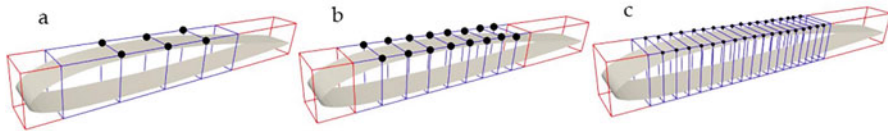
In this study, our aim is to use the FFD technique for the deformation of the wing upper surface, for which some studies have been performed at the LARCASE (Koreanschi et al., 2016; Kammegne et al., 2014; Botez et al., 2018) as part of CRIAQ 7.1 and CRIAQ MDO 505 projects. In the FFD parametrization, the choice of the number of control points is done using trial and error process as there is no direct way to find the exact number. A case study is performed to show the flexibility of FFD control points and to compare the results obtained for a different number of control points to their influences on the optimization results. In this way, airfoil shape optimization with upper surface morphing has been performed for the UAS-S45 using gradient-based optimization method and the FFD as the parametrization technique. OpenFOAM is used as flow solver in this optimization, while the generation of the FFD block is done using the PyGeo module.

2 Method

In the present study, the FFD block has been created for the UAS-S45 airfoil design using the PyGeo module in Python with different control points. Using the gradient-based optimization, the upper surface of the airfoil is optimized. The objective function is the drag minimization with a constant lift as constraint and other constraints, as summarized in Table 1. Figure 1a, c shows the FFD block with a different number of control points for the airfoil design. As depicted in these figures, the blue blocks are the deforming blocks (only the upper surface of the airfoil, specified with black dots which are displaced), and the red blocks are the constant blocks. In the deforming blocks, the specified control points (represented in black colors) move in the vertical direction, while the rest of the control points, including the control points belonging to the interface of the deforming and static blocks, are constrained. The location of the interface between the static and flexible upper

Table 1 Optimization setup for the morphing upper surface of the UAS-S45

Function/ variable	Description	Quantity		
		Case1	Case2	Case3
Minimization of				
C_d	Drag coefficient			
with respect to:				
y	Morphing surface (FFD)	6	16	36
α	Angle of attack	1	1	1
	Total design variables	7	17	37
Subject to:				
$C_l = 0.38514$	Lift coefficient constraint			
$V \geq V_{\text{baseline}}$	Volume constraint			
Δy	Design variable bounds	$0 \leq \Delta y \leq 0.5$	$0 \leq \Delta y \leq 0.01$	$0 \leq \Delta y \leq 0.008$
$\Delta y_{z=0}^{\text{upper}} = \Delta y_{z=1}^{\text{upper}}$	Linear constraint	6	16	36

**Fig. 1** UAS-S45 airfoil with (a) 5 control points, (b) 10 control points, and (c) 20 control points in the chord-wise direction

surface is determined with the methodology described in the previous CRIAQ 7.1 project (Botez et al., 2007); their location is between 7% and 65% of chord length.

2.1 FFD Parametrization Technique

The FFD parametrization technique was first proposed by Sederberg and Parry (1986), in which they introduced a new way to modify a solid model so that its volume remains the same. Their scheme was based on trivariate Bernstein polynomials with control points being the coefficients of polynomials. In this technique, the geometry of any size or configuration is embedded inside a lattice, called FFD block, with its corresponding control points. The lattice consists of B-spline control points, in which, when altered, the embedded body is deformed, and by establishing Newton search, the parameter space is mapped to a physical space. The number of control points, as well as their displacements, is dependent on the geometry and the deformation zone. FFD blocks parametrize the geometry change rather than the geometry itself; it is therefore only necessary to use a set of design variables that span the desired modification rather than the geometry itself (Kenway et al., 2010).

Based on the fact that the FFD blocks are trivariate B-spline volumes, the sensitivity of any point inside the volume is calculated as follows:

$$\frac{\partial X_{pt}}{\partial x_{dv}} = \frac{\partial X_{coef}}{\partial x_{dv}} \frac{\partial X_{pt}}{\partial X_{coef}} \quad (1)$$

where X_{pt} are the spatial coordinates of the embedded points, x_{dv} are the design variables, and X_{coef} are the spatial coordinates of the FFD block control points. In Eq. (1), $\frac{\partial X_{coef}}{\partial x_{dv}}$ shows the relationship of control point motion with respect to the actual design variables, and $\frac{\partial X_{pt}}{\partial X_{coef}}$ is the shape function.

2.2 Optimization Framework

Optimization is performed on the upper surface of the airfoil with the objective function of drag minimization. Gradient-based optimization has been established, using interior point optimizer (IPOPT). The setup of the morphing upper surface optimization of the UAS-S45 has been summarized in Table 1.

3 Results and Discussion

The optimization process was completed for the three cases for three computing systems of the same type (8-core CPUs with 2.9 GHz and 16 GB of memory). The accuracy of optimization is evaluated by two criteria, optimality and feasibility, where feasibility concerns with the degree of which the optimization constrains are satisfied and optimality shows the how well the objective function could be minimized or maximized, which in this study it is the drag minimization. The final results are shown in Table 2.

Table 2 Comparison of the results for the three cases

	Case 1	Case 2	Case3
Control points	5	10	20
Runtime (s)	20,605	16,224	39,602
Upper limit (m)	0.5	0.01	0.008
Number of iterations	50	50	50
Baseline C_d	0.009392	0.009392	0.009392
Objective function (C_d)	0.009380	0.009351	0.009544
Target angle of attack	2.525°	2.502°	2.5560°
Feasibility	1.51×10^{-6}	2.88×10^{-3}	4.12×10^{-2}
Optimality	2.29×10^{-8}	2.34×10^{-5}	1.66×10^{-4}

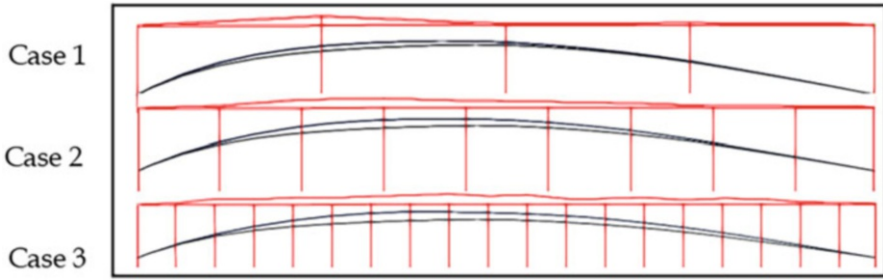


Fig. 2 Illustration of morphing upper surface for different control points in FFD block: case 1, five control points; case 2, ten control points; case 3, 20 control points

As shown in Table 2, as the number of control points increases, the accuracy of the optimization results is lost in terms of optimality and feasibility, and even in case 3, the objective function is not optimized as expected. However, for cases 1 and 2, the drag is reduced by 0.13% and 0.43%, respectively. By considering the runtime, for case 3, having lost the accuracy, has the maximum runtime and, therefore, it is not recommended. Firstly, the displacement limit was set to 0.5 m for all of the cases; however, higher numbers of control points (10 and 20) led to unprecedented deformations for cases 2 and 3, and the solution was stopped due to mesh distortion as a result of irregular deformations. Thus, the upper limit of the deformation was reduced to 0.01 m and 0.008 m for cases 2 and 3, respectively, and the deformation was controlled by reducing the upper limit. Figure 2 shows the morphing of the upper surface for the three cases.

4 Conclusion

As mentioned above, there is not a straightforward way to compute the FFD control points, and the methodology used here is geometry-based and is found by trial and error. In this study, a comparative analysis was performed to show how the number of control points impacts the final optimization results from using parameters such as different points of views like objective function, feasibility and optimality, etc. It was shown that the increase of the control point number has the penalty of reducing the accuracy of the optimization results (optimality and feasibility) and of increasing the runtime. It was also shown that there is an infinitesimal difference in the value of objective functions as calculated in cases 1 and 2 and there should be a trade-off between the accuracy of the optimization results and the objective function value to find the optimum number of control points. By increasing the number of control points, as shown in case 3 does, it actually limits the displacements (case 2, case 3), but for case 1, the solution was completed without any mesh distortion; thus, no restriction in upper bound was required. By considering the results summarized in Table 2, case 2 is chosen for the UAS-S45 airfoil design following its optimization

accuracy and overall runtime. In the continuation of this study, the topology analysis of the FFD blocks will be presented in future work with the aim of finding the relationship between the FFD topology and the optimization results to analyze the way in which the topology influences the derivative computation of the block.

References

- Bashir, M., Longtin Martel, S., & Botez, R. M. (2021a). Numerical study of the boundary layer behavior on morphing trailing edge wing using intermittency transition model. In *AIAA AVIATION 2021 FORUM* (p. 2567).
- Bashir, M., Longtin-Martel, S., Botez, R. M., & Wong, T. (2021b). Aerodynamic design optimization of a morphing leading edge and trailing edge airfoil – Application on the UAS-S45. *Applied Sciences*, *11*(4), 1664.
- Bashir, M., Longtin-Martel, S., Botez, R. M., & Wong, T. (2022). Optimization and design of a flexible droop-nose leading-edge morphing wing based on a novel black widow optimization algorithm—Part I. *Designs*, *6*(1), 10.
- Botez, R. M. (2018). Morphing wing, UAV and aircraft multidisciplinary studies at the laboratory of applied research in active controls, avionics and AeroServoElasticity LARCASE. *Aerospace Lab*, *14*, 1–11.
- Botez, R. M. (2022). Overview of morphing aircraft and unmanned aerial systems methodologies and results – Application on the Cessna Citation X, CRJ-700, UAS-S4 and UAS-S45. In *AIAA SCITECH 2022 Forum* (p. 1038).
- Botez, R. M., Molaret, P., & Laurendeau, E. (2007). Laminar flow control on a research wing project presentation covering a three-year period. In *Canadian aeronautics and space institute annual general meeting* (Vol. 2007).
- Botez, R. M., Koreanschi, A., Gabor, O. S., Tondji, Y., Guezguez, M., Kammegne, J. T., Grigorie, L. T., Sandu, D., Mebarki, Y., Mamou, M., & Amoroso, F. (2018). Numerical and experimental transition results evaluation for a morphing wing and aileron system. *The Aeronautical Journal*, *122*(1251), 747–784.
- He, P., Mader, C. A., Martins, J. R., & Maki, K. J. (2018). An aerodynamic design optimization framework using a discrete adjoint approach with OpenFOAM. *Computers & Fluids*, *168*, 285–303.
- He, P., Mader, C. A., Martins, J. R., & Maki, K. (2019). An object-oriented framework for rapid discrete adjoint development using OpenFOAM. In *AIAA Scitech 2019 Forum* (p. 1210).
- He, P., Mader, C. A., Martins, J. R., & Maki, K. J. (2020). Dafoam: An open-source adjoint framework for multidisciplinary design optimization with openfoam. *AIAA Journal*, *58*(3), 1304–1319.
- Kammegne, M. J. T., Grigorie, T. L., Botez, R. M., & Koreanschi, A. (2014). Design and validation of a position controller in the Price-Paidoussis wind tunnel. In *IATED Modeling, Simulation and Control Conference, Innsbruck, Austria* (pp. 17–19).
- Kenway, G., Kennedy, G., & Martins, J. R. (2010). A CAD-free approach to high-fidelity aerostructural optimization. In *13th AIAA/ISSMO multidisciplinary analysis optimization conference* (p. 9231).
- Koreanschi, A., Gabor, O. S., Acotto, J., Brianchon, G., Portier, G., Botez, R. M., Mamou, M., & Mebarki, Y. (2016). Optimization and design of a morphing wing tip aircraft demonstrator for drag reduction at low speeds, Part II – Experimental validation using infra-red transition measurements during wind tunnel tests, *30*, 164.
- Masters, D., & Taylor, N. (2015). *Review of aerofoil parameterisation methods for aerodynamic shape optimisation*. 53rd AIAA aerospace sciences meeting.

Sederberg, T. W., & Parry, S. R. (1986). Free-form deformation of solid geometric models. In *Proceedings of the 13th annual conference on computer graphics and interactive techniques* (pp. 151–160).

Sripawadkul, V., Padulo, M., & Guenov, M. (2010). A comparison of airfoil shape parameterization techniques for early design optimization. In *13th AIAA/ISSMO multidisciplinary analysis optimization conference* (p. 9050).

Unmanned Aerial Vehicle Propeller Design and Production by Fused Filament Fabrication



Mesut Pehlivan, Eren Özen, and Alperen Doğru

Nomenclature

CAD	Computer-aided design
CW	Clockwise
CWW	Counterclockwise
FFF	Fused filament fabrication
PLA	Polylactic acid
UAV	Unmanned aerial vehicle

1 Introduction

Today, it is much easier to produce more durable and more complex geometries than in the past. We provide this convenience with additive manufacturing methods. This method, which is an alternative to traditional manufacturing methods, has many advantages. Many constraints created by the complexity of the geometric shape of the product to be produced have become history with this manufacturing method. No matter how difficult the shape of the product we want to obtain, we can easily produce the product we want with CAD data and gain from the workforce.

The initial goal of additive manufacturing technology was to be able to produce prototypes flexibly and quickly. For this reason, the method taken under the name of rapid prototyping has become able to produce the final product with new developments over time. With the improvement of processes and the increase in material diversity, additive manufacturing has become a powerful tool for small batch

M. Pehlivan · E. Özen (✉) · A. Doğru
Ege University Aviation HVS, Aircraft Technology, İzmir, Türkiye
e-mail: alperen.dogru@ege.edu.tr

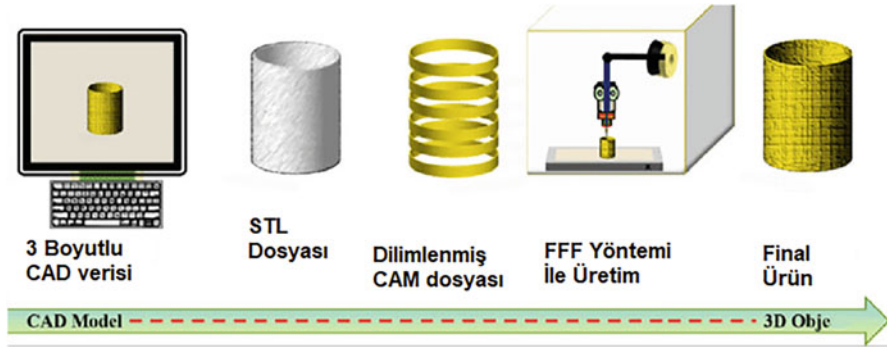


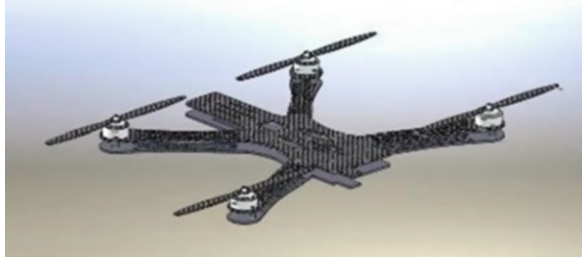
Fig. 1 Additive manufacturing processes

production and tool manufacturing and, more recently, for flexibility in production, complex parts, and cost-effectively (Gibson et al., 2015). Although additive manufacturing cannot meet all applications and industry requirements such as dimensional stability, structural strength, and surface treatments, research and development activities in this field have made significant progress since the 1980s, when the method began (Wohlers & Caffrey, 2014).

Additive manufacturing is an economically promising technology. Additive manufacturing production processes are shown in Fig. 1. This technology is used to attach the parts of the mass production parts together. Although it is not possible to obtain superior mechanical properties when comparing plastic parts produced by additive manufacturing with their equivalents produced by injection molding, similar properties can be obtained (De Leon et al., 2016). On the other hand, the flexibility of additive manufacturing methods and increasing material diversity create new opportunities. It has great opportunities, especially in areas where there is a lot of design change, personalized production, and few mass productions (Ning et al., 2017). Applications of additive manufacturing methods are found in fields such as art, architecture, jewelry, entertainment, education, energy, electronics, scientific visualization, nanotechnology, automotive, aerospace, defense, medicine, dentistry, and equipment manufacturing. Additive manufacturing is particularly beneficial for the aerospace and defense industries in terms of shortening lead times and reducing the cost of manufacturing a small number of parts (Wohlers, 2019). Additive manufacturing methods enable lightweight designs, assembly-free parts, on-site manufacturing, anisotropic materials, in-structure supports, and personalized products (Huang et al., 2013; Parandoush & Lin, 2017). Additive manufacturing methods create significant opportunities in the aerospace and defense industries where the number of production is low and parts with complex geometry and topology optimization are intense.

The most innovative technology in the aerospace and defense industry is UAV. UAV sector, although it developed after World War II, became widespread with the demands of model airplane clubs and hobbyists (Toleos et al., 2020). However, the use of UAVs for the problems of daily life started in the 2000s. After the studies led

Fig. 2 Four-engine UAV (drone) with a take-off weight of 2 kg



by academic researchers, especially NASA, UAVs have found many applications such as environment, security, surveillance, urbanism, and earth science with a wider scope. UAVs numbers are expected to increase and their widespread use in the future. Studies in this field are important for the continuation of this sectoral success.

UAVs are sought to be lightened to achieve shorter take-off range and longer flight time without sacrificing performance and durability (Ferro et al., 2016). Lattice structures are preferred to achieve lightness, and these lightweight structures with complex internal properties are difficult to manufacture using traditional fabrication methods. The increase in the variety of materials that can be used in additive manufacturing methods and the latest developments in production technologies provide opportunities for the easy production of light structures, industrial products, and new platforms (Gibson et al., 2015) (Fig. 2).

Multi-rotor aircraft (drones), which is one of the UAV technologies, have become an inevitable reality in modern aerospace. Drones consist of a body that creates lift by a series of fixed-pitch propellers, each powered by an electric motor. These air vehicles have great potential for different uses, and research on this topic is focused on reducing structure weight to maximize flight time, range, and payload (Biswas et al., 2018). Structural parts and components for drones have different challenges for 3D modeling, optimization, and manufacturing (Goh et al., 2017). The most important feature among these parameters is to obtain strength and lightness in complex geometries (Germanischer Lloyd, 2009; Kabir et al., 2020). In the production of these complex geometries, additive manufacturing methods enable the production of lattice structures to provide lightness.

FFF, which is included in the additive manufacturing classification with material extrusion among additive manufacturing technologies, refers to the process of bringing together the materials heated to the melting temperature in layers in the production of the physical model (Ryan et al., 2018). With the FFF method, small mass production prototypes are obtained for special parts in many application areas, and drone technology is one of the areas where this method can be used most effectively.

PLA material was used for propeller production in this research study. PLA material was preferred due to its tensile strength, toughness, and wear resistance. UAV propellers were produced with the FFF method, which is an innovative production method and provides design freedom. The mechanical properties and application performances of the produced propellers were tested.

2 Method

In the study, propellers that were designed allow a UAV with a 2 kg take-off weight to be used in different missions. These were produced by the FFF Fused filament fabrication (FFF) method using pure polymer. The propellers produced by the FFF method have different manufacturing parameters and materials. The mechanical properties and force generation performances of the produced propellers were tested.

By using the propCalc program, the propeller dimensions required for the flight of a four-engine UAV (drone) with a take-off weight of 2 kg were determined. In the preliminary study, it was calculated that the propeller dimensions should be approximately 11 inches in length and should have 4.7 pitch characteristics. The propeller design and conceptual drawings of the propeller were made using the AutoCAD Fusion 360 program.

A 2.85 mm diameter black-colored PLA filament of the BASF brand was used to produce propellers by FFF. BASF PLA filament has a density of 1.248 g/cm³, 34.7 MPa ultimate tensile strength, and 3.3 kJ/m² Izod impact strength.

The propellers were produced by Ultimaker S3 FFF device and by using different diameter nozzles. The 0.4 and 0.8 mm diameter nozzles were used for melting PLA, and the propellers were positioned at two different angles on the building plate. Because the propellers will be used in the drone, it was produced as CW and CWW (Table 1).

Propeller drawings made in the AutoCAD Fusion 360 program are saved in “.stl” (stereolithography) format. Two different propeller drawings, CW and CWW, were made, and the Cura CAM program was used to produce the propeller with the FFF method. With the CURA program, the positioning of the propeller on the build plate, nozzle temperature, layer thickness, support structures, lattice geometry, infill density, printing speed, and other parameters have been entered (Table 2).

Propellers were produced by FFF methods with two different positionings on the build plate. These positionings are seeming in Fig. 3.

The performance tests of the produced propeller were tested with the Mayatech MT5 50 N Engine Thrust Tester. This test device measured the tension and power of the propeller.

Table 1 Propeller production differences

Rotation	Nozzle	Angle
CW	0.4, 0.8 mm	75 and 90°
CWW	0.4, 0.8 mm	75 and 90°

Table 2 FFF manufacturing parameters

Parameters	Value
Infill density	50%
Layer height	0.2 mm
Nozzle temp.	210° C
Printing speed	70 mm/s

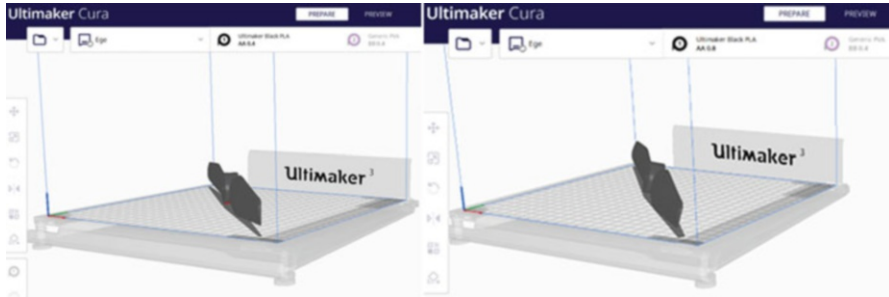


Fig. 3 Propeller positioning on build plate

3 Results and Discussion

In this study, propeller groups with different rotation directions, CW and CWW, were produced. The thrust values produced by each propeller in response to the engine power consumption were measured. Figure 4 shows the amp–thrust graphics of the propellers produced.

When the maximum thrust values reached by the propellers are compared, the CW propeller, which is produced by being positioned at an angle of 75° with a 0.8 mm diameter nozzle with a value of 81.5 N, has reached the highest thrust value. Produced at an angle of 75° and with a 0.8 mm diameter nozzle, this propeller can produce the thrust needed for a drone with a take-off weight of 2 kg.

The maximum thrust values that the produced propellers can reach before they are damaged and the amperage values they consume at that moment are shown in Fig. 5. The propellers produced with 0.8 mm diameter nozzles produced high thrust at low amperage values. This situation can be interpreted as melting and extruding the material from nozzles that have larger diameters reduces the hollow structure in the material and the resonance-induced resistance may be reduced. Vibration analysis can be done for more detailed examinations (Fig. 6).

Among the propellers that produce thrust in the CW direction, the propeller that produces 50 N thrust at the lowest amperage is the propeller labeled 0.8 mm/ 90° /CW. Among the propellers that produce thrust in the CWW direction, the one that produces 50 N thrust at the lowest amperage is labeled 0.8 mm/ 75° /CWW.

It has been observed that the production time of the propeller produced with a large diameter nozzle is short and the nozzle movement pattern is shorter, the effect of increasing the impeller strengths. It has been determined that these propellers reach higher thrust values by maintaining their integrity. The same is true for both CW and CWW redirects. In addition, it has been observed that 75° positioning instead of 90° gives better results in the production of 4.7 pitch and 11 inch length propellers with FFF. It is thought that the 75° positioning provides a better combination of the layers for the pitch orientation of the propeller. Examination of damaged parts by optical microscope analysis will be useful to support this statement.

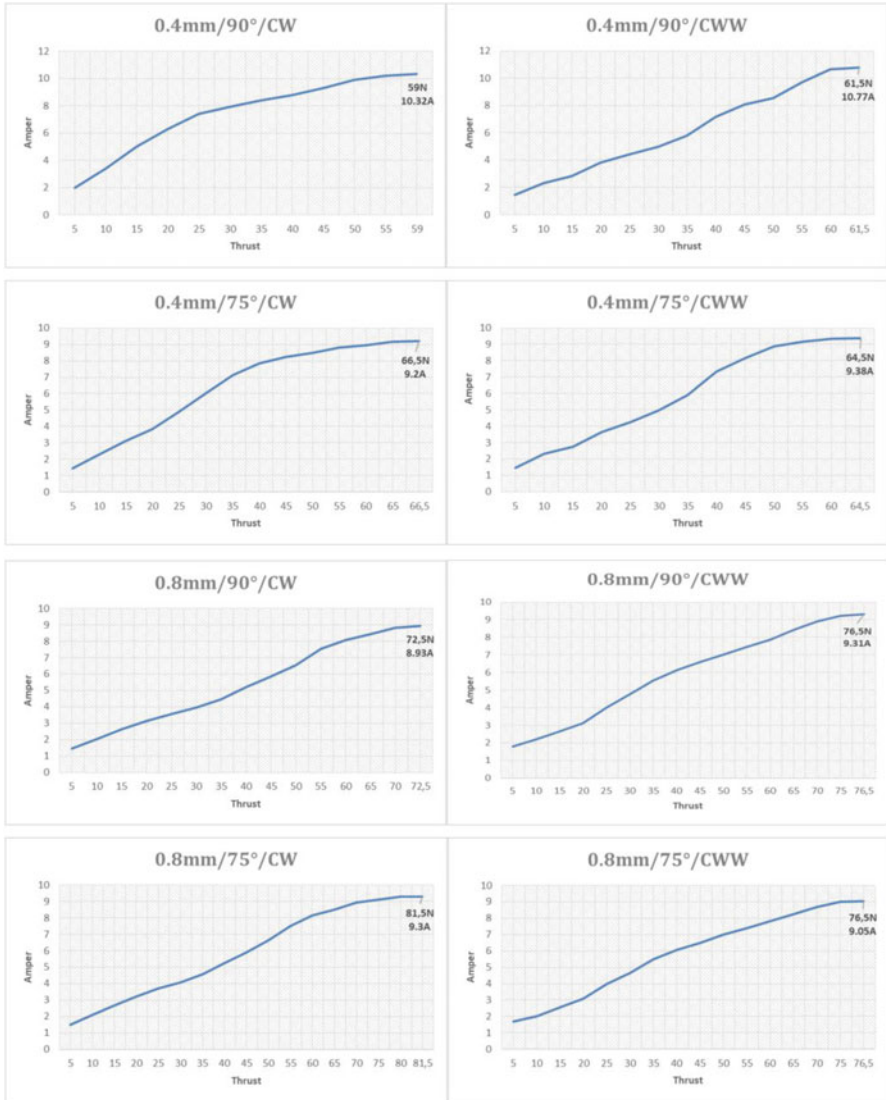


Fig. 4 Amper–thrust chart for all propellers

When the amperage consumed while producing 50 N lift force is compared, it has been determined that the propellers produced with 0.8 mm nozzle produce 50 N thrust with a lower amperage value. This means longer flight times for drones. There is a gain of 24% when compared to the average values of the propellers produced with the 0.4 mm diameter nozzle.

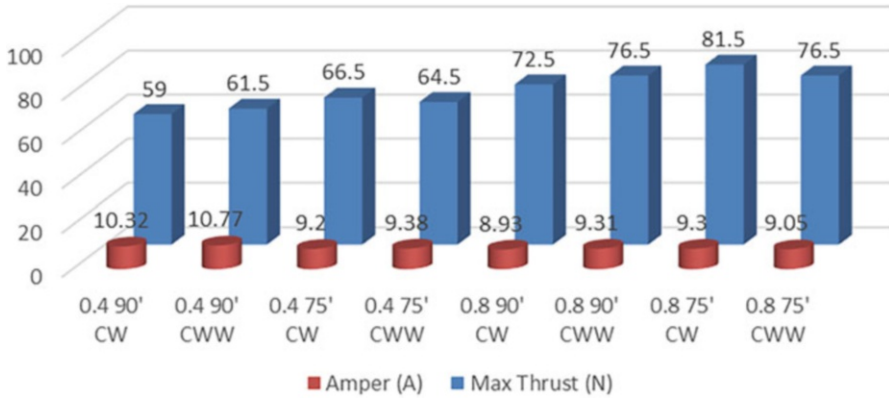


Fig. 5 Max. thrust and ampere values

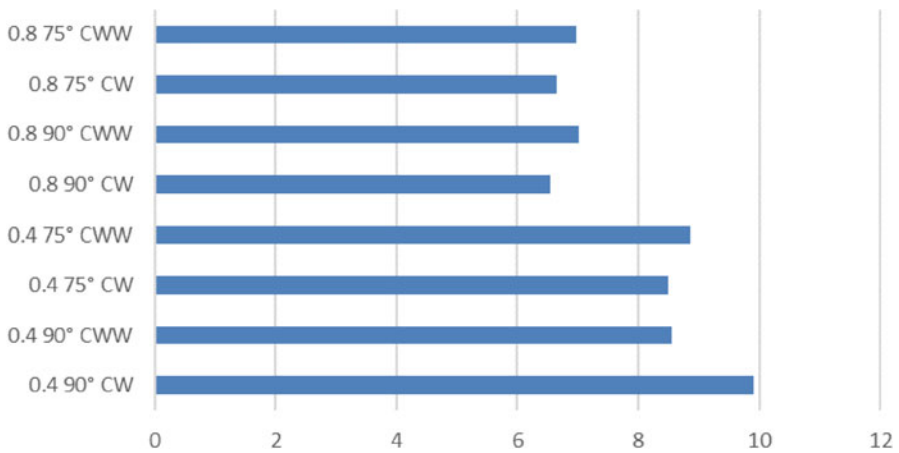


Fig. 6 Ampere ratings at 50 N thrust

4 Conclusion

One of the most important parts affecting flight performance among drone components is the drone propeller. The propeller directly affects the lift, weight, and propulsion system. On the other hand, the propeller of small drones is very prone to breakage during operation and often crashes into bushes and small trees. Therefore, it is often necessary to replace the propeller. The FFF method is one of the ideal methods for producing drone propellers. The fact that this method is used by many users, properties about freedom of design, and extending the material portfolio are improving usability.

The mechanical properties and force generation performances of the produced propellers were tested in this study. The tests of the propeller groups produced with a

fixed layer thickness of 0.2 mm and 50% occupancy were carried out. In future studies, examining the effects of different layer thicknesses, occupancy rates, and infill patterns will provide useful results. In addition, it may be the subject of new research to examine the properties exhibited by other polymers.

Acknowledgments This research was supported by the 1919B012100470 numbered project within the scope of Tübitak 2209A. We would like to thank Tübitak for supporting young researchers in this way and the 3Dörtgen company for providing spare parts for our FFF devices.

References

- Biswas, P., et al. (2018, October). Prediction of printing failure of a 3D printed drone propeller using fused deposition modeling. *Science in the Age of Experience*, pp. 531–540. Available at: https://www.3ds.com/fileadmin/PRODUCTS-SERVICES/SIMULIA/Resources-center/PDF/2018-SAoE-Prediction_of_Printing_Failure_of_a_3D_Printed_Drone_Propeller_using_Fused_Deposition_Modeling.pdf
- De Leon, A. C., et al. (2016). High performance polymer nanocomposites for additive manufacturing applications. *Reactive and Functional Polymers*, 103, 141–155. <https://doi.org/10.1016/j.reactfunctpolym.2016.04.010>
- Ferro, C., et al. (2016). Additive manufacturing offers new opportunities in UAV research. *Procedia CIRP*. Elsevier B.V., 1004–1010. <https://doi.org/10.1016/j.procir.2015.12.104>
- Germanischer Lloyd. (2009). *Materials for propeller fabrication*. Germanischer Lloyd Aktiengesellschaft.
- Gibson, I., Rosen, D., & Stucker, B. (2015). *Additive manufacturing technologies 3D printing, rapid prototyping, and direct digital manufacturing*. Springer.
- Goh, G. D., et al. (2017). Additive manufacturing in unmanned aerial vehicles (UAVs): Challenges and potential. *Aerospace Science and Technology*, 63, 140–151. <https://doi.org/10.1016/j.ast.2016.12.019>
- Huang, S. H., et al. (2013). Additive manufacturing and its societal impact: A literature review. *International Journal of Advanced Manufacturing Technology*, 67(5–8), 1191–1203. <https://doi.org/10.1007/s00170-012-4558-5>
- Kabir, S. M. F., Mathur, K., & Seyam, A. F. M. (2020). A critical review on 3D printed continuous fiber-reinforced composites: History, mechanism, materials and properties. *Composite Structures*, 232(August 2019), 111476. <https://doi.org/10.1016/j.compstruct.2019.111476>
- Ning, F., et al. (2017). Additive manufacturing of carbon fiber-reinforced plastic composites using fused deposition modeling: Effects of process parameters on tensile properties. *Journal of Composite Materials*, 51(4), 451–462. <https://doi.org/10.1177/0021998316646169>
- Parandoush, P., & Lin, D. (2017). A review on additive manufacturing of polymer-fiber composites. *Composite Structures*, 182, 36–53. <https://doi.org/10.1016/j.compstruct.2017.08.088>
- Ryan, J., et al. (2018). Mechanical characterization of 3D-printed polymers. *Additive Manufacturing*, 20, 44–67. <https://doi.org/10.1016/j.addma.2017.12.002>
- Toleos, L. R., et al. (2020). Feasibility study for fused deposition modeling (FDM) 3D-printed propellers for unmanned aerial vehicles. *International Journal of Mechanical Engineering and Robotics Research*, 9(4), 548–558. <https://doi.org/10.18178/ijmerr.9.4.548-558>
- Wohlers, T. (2019). *Wohlers report 2019: 3D printing and additive manufacturing state of the industry annual worldwide progress report*. Wohlers Associates. Available at: <https://wohlersassociates.com/2019report.htm>
- Wohlers, T., & Caffrey, T. (2014). *Wohlers report 2014: 3D printing and additive manufacturing state of the industry annual worldwide progress report*, Wohlers Associates. <https://doi.org/10.1017/CBO9781107415324.004>

An Aerodynamic Model for Gliding Snake-Bots



Harshini Aich, Shanmukha Preetham Akella, Balajee Ramakrishnananda,
and T. Rajesh Senthil Kumar

Nomenclature

CG Center of gravity
SVL Snout-to-vent length

1 Introduction

Most vertebrate gliders, such as flying squirrels, generate lift via symmetrically coupled “wings” during their flight. The *Chrysopelea* genus of snakes is remarkable because of its ability to fly without the structures we conventionally associate with flight (Socha, 2002). These snakes create a lifting surface by morphing their body surfaces during a glide. They achieve the aerodynamic efficiency needed for good glide performance by using an irregular cross section of their body and undulations in their body shape (Socha & LaBarbera, 2005). The snake body’s cross-sectional shape during glide is comparable to that of an airfoil and is found to be an effective source of lift to facilitate gliding across short distances (Miklasz et al., 2010).

The snake undulates in a plane oriented upward toward the head at approximately 20–40° to the direction of forward motion during this steepening period of the glide (Socha & LaBarbera, 2005).

H. Aich

Aerospace Engineering Department, ISAE SUPAERO, Toulouse, France

S. P. Akella · B. Ramakrishnananda (✉) · T. R. S. Kumar

Department of Aerospace Engineering, Amrita School of Engineering, Amrita Vishwa Vidyapeetham, Coimbatore, India

e-mail: r_balajee@cb.amrita.edu; t_rajesh@cb.amrita.edu

The most surprising aspect of these snakes is their ability to achieve control during their short glides (Socha, 2002). The landing spot is actively chosen by the snake, and the undulation pattern it follows during the glide enables it to reach this chosen destination. Seeing how this creature is able to utilize the closely spaced trees of its natural habitat to move across distances, an idea of a robot that could mimic this movement and provide surveillance in such terrain is one that holds much potential. Such a robot would move from tree to tree via short glides and provide audio, visual, or other data of the surrounding area. This would fill surveillance gaps in dense forests where aerial drones cannot easily penetrate.

The three-dimensional kinematic analysis of gliding snakes was performed in Socha et al. (2005), where experiments were performed on snakes ranging from 3.0 to 82.7 g in mass and from 31.0 to 86.5 cm in SVL. Parameters pertinent to the trajectory and behavior of the snake such as total horizontal distance travelled, glide angle, undulation frequency, wave length, and wave speed range were observed.

The undulation pattern of such snakes has been modeled in earlier works (Balaramraja et al., 2016; Gopi et al., 2017; Parameswaran et al., 2019). The aerodynamic forces acting on the undulating body at an instant of time were obtained (Gopi et al., 2017) by utilizing the n-chain model used in Gopi et al. (2017) coupled with thin airfoil theory (Anderson, 2017) for evaluating two-dimensional sectional lift and blade element theory assumption (Seddon & Newman, 2017) to integrate the sectional lift and obtain the total lift. However, the effects of the moments of aerodynamic forces around the CG were neglected in the work of Gopi et al. (2017).

Jafari et al. (2017) investigated the control of gliding in such shapes. Turn control in 2D for such shapes was shown to be possible by Parameswaran et al. (2019), utilizing the aerodynamic model deployed in Gopi et al. (2017). To achieve control in three-dimensional space, an improved aerodynamic model which accounts for the moments produced by the body during flight would be necessary. It is the objective of the present work to develop such an aerodynamic model and compare it with the earlier model against the experimental results of Socha et al. (2010).

2 Method

First, an undulation model is created to create a replica of the actual snake's motion in 3D. Later, the model is broken into n-sections in which aerodynamic properties of the snake cross section are used to calculate the sectional lift forces from thin airfoil theory. These are summed up vectorially to determine the total aerodynamic force on the body. Blade element theory approximation is used here. These were already implemented in the work of Gopi et al. (2017). Figure 1 shows the snapshot of the undulating shape of the n-chain model at an instant of time.

Figure 2 shows the process adopted for the present work, and Fig. 3 shows the moment caused by a sectional force around CG.

Subsequently, in the present work, the location of center of gravity is computed for a given time step from the shape of the undulating body at that instant of time.

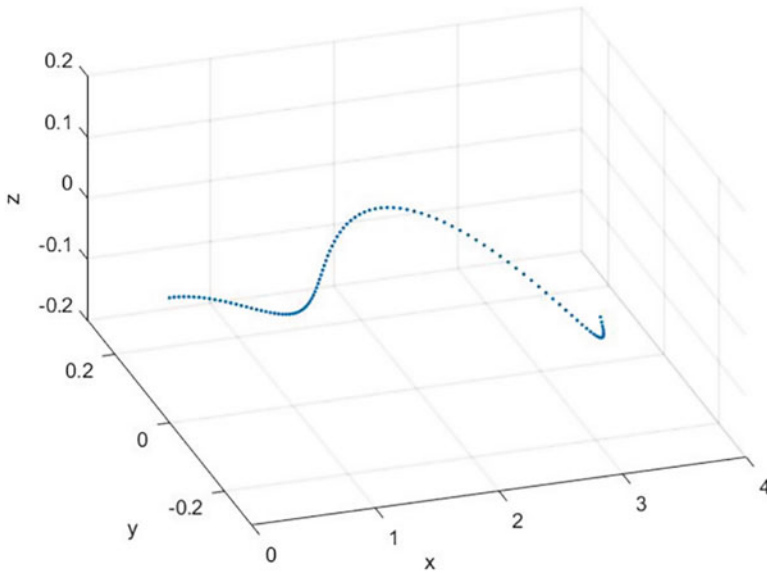


Fig. 1 Undulating shape at an instant of time

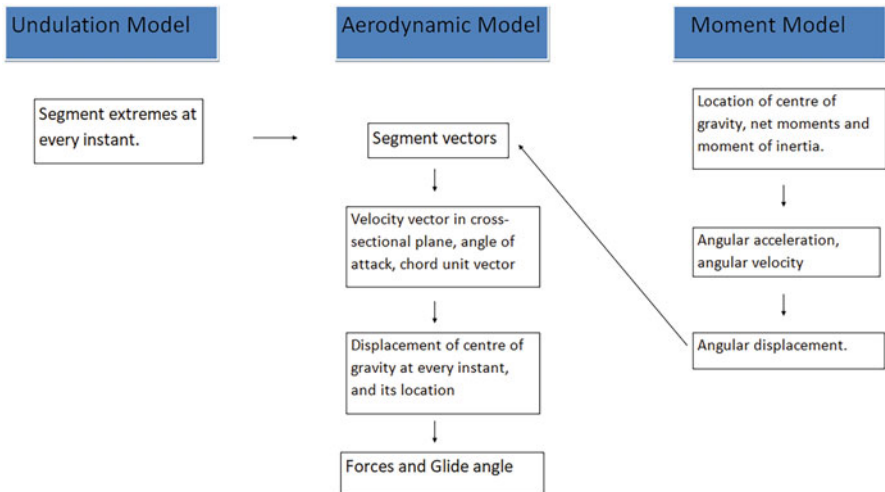


Fig. 2 Process flowchart

Since the locations of the sections, their distances from CG, and the lift force acting on the various sections are known, the moments of these forces around CG can be calculated and summed up. The location of CG is updated for each time step.

Moments about CG are calculated from the mass moment of inertia matrix I_{seg} for each segment, approximating each segment as a point mass. The segmental moment

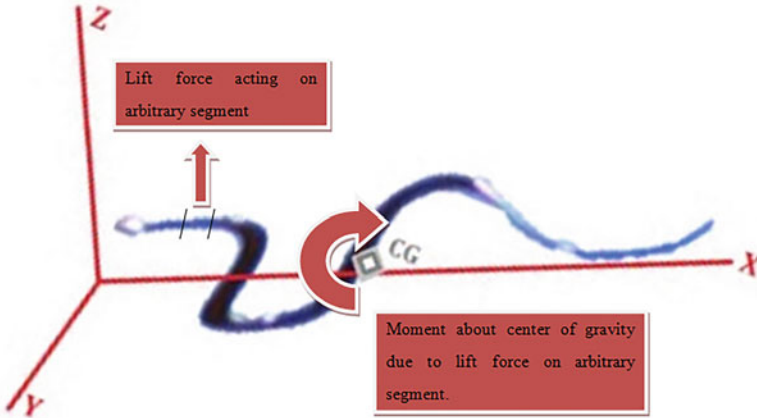


Fig. 3 Moment around CG

vectors are then added vectorially to get the net moment (\vec{M}). Moment of inertia I is recomputed about CG at each time step since the shape of undulation would change with time. The angular acceleration vector ($\vec{\theta}$) of the model at an instant of time is found in Eq. (1):

$$\vec{M} = [I] \cdot \vec{\theta} \quad (1)$$

Using change in angular acceleration vector ($\vec{\theta}$) and change in time step (dt), change in angular velocity ($\vec{\omega}$) and angular displacement ($\vec{\theta}$) of the model are computed.

The angular displacement components calculated in the moment model are passed to rotate the orientation of the snake-like shape at that instant using the methodology detailed in any standard flight dynamics textbook (Etkin & Lloyd, 1996).

3 Results and Discussion

Glide angle, and free-stream velocity are plotted versus time to verify the closeness with the experimental values of Socha et al., (2010), and check whether the agreement is better than the earlier model. The comparison is made for Case 6 in Socha et al. (2010), which corresponds to the average values over the many field trials conducted as part of the referenced study.

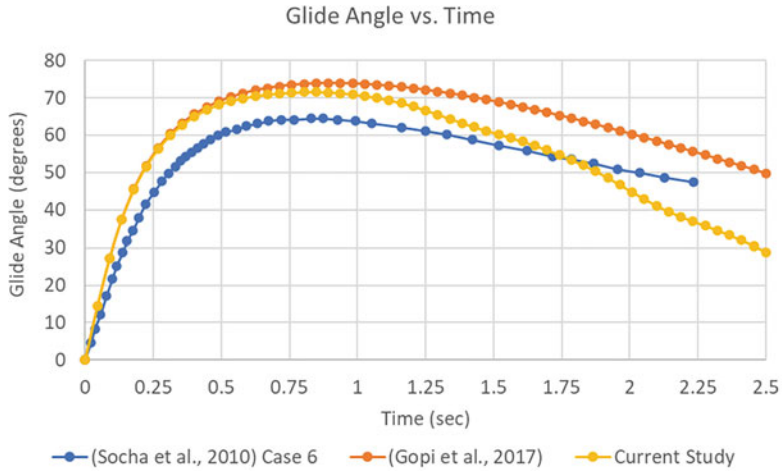


Fig. 4 Glide angle comparison with experiment (Socha et al., 2010): Case 6

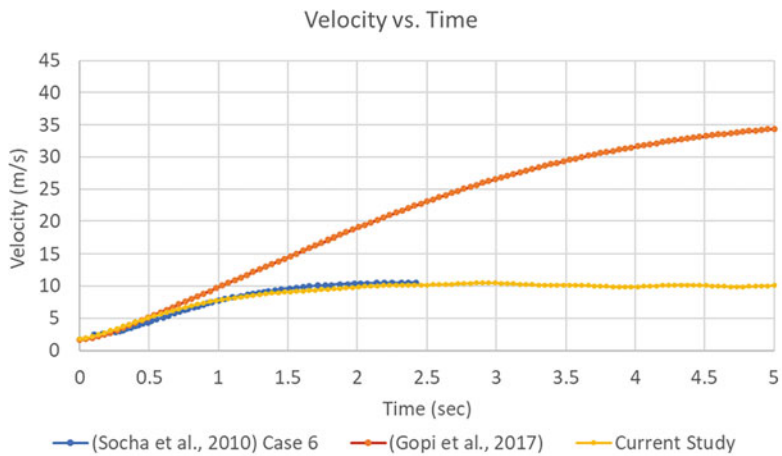


Fig. 5 Velocity with time – comparison with experiment (Socha et al., 2010): Case 6

The results show that including the moment, although only an approximate model, results in a better qualitative and quantitative agreement with experimental results, as seen from Figs. 4 and 5.

4 Conclusion and Future Work

An improved aerodynamic model has been formulated for deployment in control algorithms for snake-bots in flight. Although relatively simple, this model accounts for the rotation of the body due to the aerodynamic moments produced during the gliding motion. Comparing the results of this model with the earlier model of Gopi et al. (2017) against experimental values of Socha et al. (2010) shows the improved prediction of this model.

Acknowledgments This work is part of a final year B.Tech dissertation project of the first two authors. The authors would like to thank all the faculty of Department of Aerospace Engineering Department, Amrita Vishwa Vidyapeetham, Ettimadai, for their constructive suggestions and fruitful discussions at various stages of this work.

References

- Anderson, J. D., Jr. (2017). *Fundamentals of aerodynamics*. McGraw-Hill.
- Balaramraja, V. S., Sankrityayan, S. E., Sivagurunathan, S. C., Ramakrishnananda, B., & Kumar, T. R. S. (2016). *Modelling the undulation pattern of flying snakes*. 2016 international conference on advances in computing, communications and informatics, IEEE Xplore. <https://ieeexplore.ieee.org/xpl/conhome/7592392/proceeding>
- Etkin, B., & Lloyd, D. R. (1996). *Dynamics of flight: Stability and control*. Wiley.
- Gopi, S. H., Valappil, D. K., Ramakrishnananda, B., Kumar, T. R. S., & Balaramraja, V. S. (2017). *Modeling non-equilibrium glides in flying snakes*. 2017 international conference on advances in computing, communications and informatics, IEEE Xplore.
- Jafari, F., Tahmasian, S., Ross, S. D., & Socha, J. J. (2017). Control of gliding in a flying snake-inspired n-chain model. *Bioinspiration & Biomimetics*, 12(6). <https://doi.org/10.1088/1748-3190/aa8c2f>
- Miklasz, K., LaBarbera, M., Chen, X., & Socha, J. J. (2010). Effects of body cross-sectional shape on flying snake aerodynamics. *Experimental Mechanics*, 50(9), 1335–1348.
- Parameswaran, S., Rajaguru, K. R., Gopi, S. H., Ramakrishnananda, B., & Thangeswaran, R. S. K. (2019). Turn control in wings inspired by flying snakes. *AIP Conference Proceedings*, 2134(1), 020005. AIP Publishing LLC.
- Seddon, J. M., & Newman, S. (2017). *Basic helicopter aerodynamics*. Wiley.
- Socha, J. J. (2002). Gliding flight in the paradise tree snake. *Nature*, 418(6898), 603–604.
- Socha, J. J., & LaBarbera, M. (2005). Effects of size and behavior on aerial performance of two species of flying snakes (Chrysopeleae). *Journal of Experimental Biology*, 208(10), 1835–1847.
- Socha, J. J., Miklasz, K., Jafari, F., & Vlachos, P. P. (2010). Non-equilibrium trajectory dynamics and the kinematics of gliding in a flying snake. *Bioinspiration & Biomimetics*, 5. <https://doi.org/10.1088/1748-3182/5/4/045002>

Effect of Aerodynamic Loads on Wing Deformation of Insect-Mimicking Flapping-Wing Micro Air Vehicles



Vu Dan Thanh Le, Anh Tuan Nguyen, Ngoc Thanh Dang, and Utku Kale

1 Introduction

Insect-mimicking flapping-wing micro air vehicles (FWMAVs) are presently being researched and developed with many different sizes, shapes, and operating principles (Phan & Park, 2019). Insect wings are flexible structures consisting of veins and membranes, usually deforming greatly when flapping in the air (Combes & Daniel, 2003; Willmott & Ellington, 1997). Many studies have shown that wing deformation has a great influence on the aerodynamic characteristics of insect-like wings (Nguyen & Han, 2018; Nakata & Liu, 2012). However, the effect of aerodynamic loads on wing deformation has not been fully studied. A pioneering experimental study (Daniel & Combes, 2002) showed that wing deformation is mainly due to inertial-elastic forces. Based on this result, many researchers used a one-way approach to study the fluid–structure interaction (FSI) problem of insect-like wings. However, another experiment (Norris, 2013) showed that the effect of aerodynamic loads on wing deformation cannot be ignored, and it is necessary to perform a two-dimensional FSI analysis.

In this paper, the insect-like wing structure is modeled by a body–spring system. This multibody dynamics (MBD) model is combined with an aerodynamic model based on the unsteady vortex-lattice method (UVLM). The wing deformations when

V. D. T. Le (✉) · A. T. Nguyen
Faculty of Aerospace Engineering, Le Quy Don Technical University, Hanoi, Vietnam
e-mail: danthanh@lqdtu.edu.vn; atnguyen@lqdtu.edu.vn

N. T. Dang
Post-Graduate Department, Le Quy Don Technical University, Hanoi, Vietnam
e-mail: thanhdn@lqdtu.edu.vn

U. Kale
Faculty of Transportation Engineering and Vehicle Engineering, Budapest University of
Technology and Economics, Budapest, Hungary

flapping in the vacuum and the air are compared to evaluate the effect of aerodynamic forces.

2 Method

2.1 Co-simulation Framework

The wing structure is approximated by a system of N rigid bodies connected by bending and torsion springs (Fig. 1a). The inertia and stiffness properties of the system are determined based on a finite element model built from the experimental data (Le et al., 2020).

The system's motion is activated at the wing base, equivalent to the motion of the first body, which is determined by three Euler angles $\phi_1, \theta_1, \alpha_1$ relative to the stroke plane. The relative position and direction of the k th body ($k > 1$) relative to the $(k - 1)$ th body is determined by the bending θ_k and torsion angles α_k of the $(k - 1)$ th spring. The generalized coordinate vector used to determine the state of the system is $\Phi = [\theta_2, \alpha_2, \theta_3, \alpha_3, \dots, \theta_N, \alpha_N]^T$.

Using the Lagrangian method, the equations of motion of the multibody dynamics system can be obtained as follows (Le et al., 2022):

$$\mathbf{M}(\Phi, \dot{\Phi}, t)\ddot{\Phi} + \mathbf{H}(\Phi, \dot{\Phi}, t) = \mathbf{Q}(\Phi, \dot{\Phi}, t) \quad (1)$$

where \mathbf{M} , \mathbf{H} , and \mathbf{Q} are the generalized mass matrix, generalized stiffness matrix, and generalized force matrix, respectively.

The extended UVLM is used to compute the aerodynamic load of the wing. In this method, the wing is discretized into panels (Fig. 1b), and on each a vortex ring consisting of bound-vortex segments with equal circulation is placed. The circulation on each panel is determined by solving a system of algebraic equations, obtaining from the Neumann (no-penetration) boundary condition. The pressure difference between the lower and upper surfaces at each panel is estimated using the unsteady Bernoulli equation (Nguyen et al., 2016).

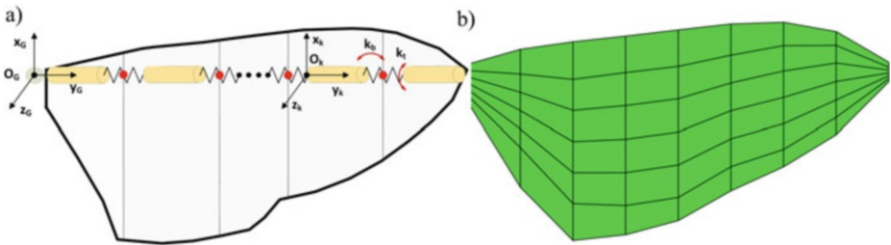
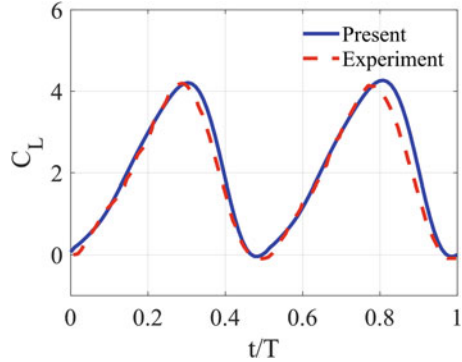


Fig. 1 (a) Body-spring system; (b) aerodynamic mesh

Fig. 2 Comparison of lift coefficient between the simulation and experiment



There is a bidirectional information exchange between the dynamic and aerodynamic models. At each iteration, the wing deformation from the MBD solver is used to interpolate the updated position of the nodes on the aerodynamic mesh and therefore to determine the aerodynamic load. In turn, the aerodynamic load on the wing surface from the aerodynamic solver is converted to concentrated forces and moment on the MBD solver, which is used to determine the new deformation state of the wing.

2.2 Validation

The simulation program is validated by comparing the simulated lift coefficient of a hawkmoth-like wing with Lua et al. (2014). It can be seen that the simulation and experimental results are quite close (Fig. 2), which proves the accuracy of the present model.

3 Results and Discussion

The suggested model is used to study the FSI problem of a hawkmoth *Manduca sexta* wing. The wing structure model is built based on the experimental data (O'Hara & Palazotto, 2012). The simulation is performed for hovering flight in the air and in vacuum. The motions at the wing base are described by periodic functions with the flapping frequency of $f = 26.1$ Hz (Willmott & Ellington, 1997).

The wing deformation is evaluated through the bending and twist angle at the wingtip region. Figure 3 shows the variation of these angles in a flapping cycle. The amplitudes of bending and twist angle when flapping in the air are greater than in vacuum by 36.7% and 127.8%, respectively. Thus, the bending deformation of the wing is mainly due to the inertia force, but the twist deformation due to the aerodynamic force is even greater than that of the inertia force. It should be noted

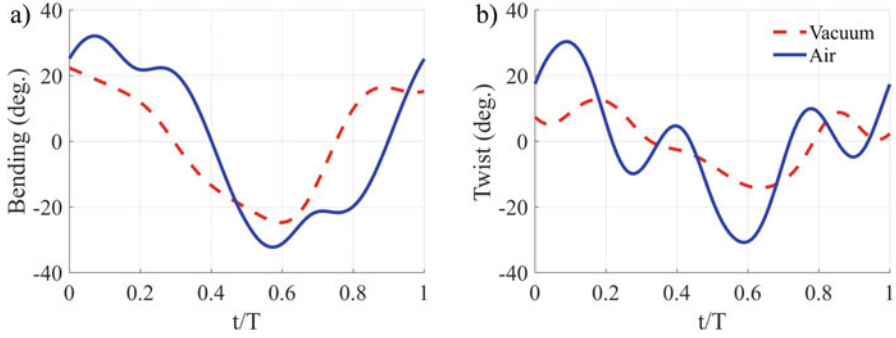


Fig. 3 Comparison of the wing deformation: (a) bending angle and (b) twist

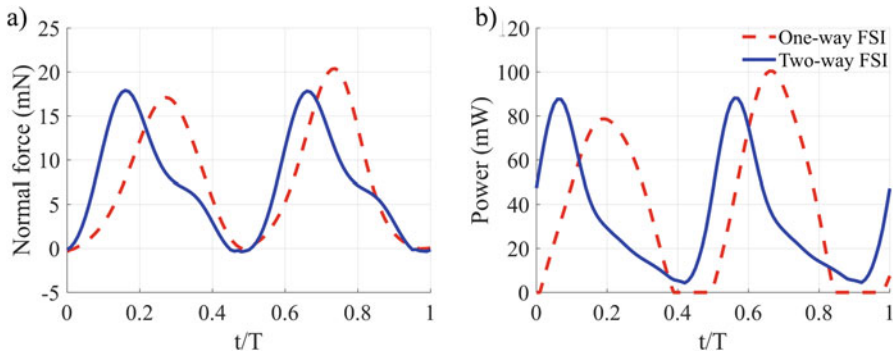


Fig. 4 The change of normal force (a) and (b) power in time

that the aerodynamic load causes a phase advance in the twist deformation, which is also observed in other simulations (Nakata & Liu, 2012).

Next, the normal force and mechanical power are determined for hovering flight, using both one-way and two-way FSI approaches (Fig. 4). There is a phase advance in both force and power variation for the two-way approach, corresponding to the phase advance of the twist angle due to the aerodynamic force mentioned above. However, it should be noted that there are no significant differences in the mean values of the normal force and power between those approaches.

4 Conclusion

In this paper, a co-simulation framework combined from an MBD model and a UVLM-based aerodynamic solver is used to study the FSI problem of an insect-like flapping wing. The results show that the aerodynamic load has a great influence on the deformation of the wing, especially on the twist angle. The normal force and

mechanical power are calculated for hovering flight using both one-way and two-way FSI approaches. There is a significant phase difference between the results obtained for the two models.

References

- Combes, S. A., & Daniel, T. L. (2003). Into thin air: Contributions of aerodynamic and inertial-elastic forces to wing bending in the hawkmoth *Manduca sexta*. *The Journal of Experimental Biology*, *206*, 2999–3006.
- Daniel, T. L., & Combes, S. A. (2002). Flexible wings and fins: Bending by inertial or fluid-dynamic forces? *Integrative and Comparative Biology*, *42*, 1044–1049.
- Le, V. D. T., Nguyen, A. T., Phung, V. B., Pham, T. D., & Han, J.-H. (2020). *The beam modelling of the hawkmoth wing structure*. Bioinspiration, biomimetics, and bioreplication X.
- Le, V. D. T., Nguyen, A. T., Dang, N. T., & Phung, B. V. (2022). A multibody dynamics approach to study an insect-wing structure. In *Modern mechanics and applications*. Springer.
- Lua, K. B., Lim, T. T., & Yeo, K. S. (2014). Scaling of aerodynamic forces of three-dimensional flapping wings. *AIAA Journal*, *52*, 1095–1101.
- Nakata, T., & Liu, H. (2012). A fluid–structure interaction model of insect flight with flexible wings. *Journal of Computational Physics*, *231*, 1822–1847.
- Nguyen, A. T., & Han, J.-H. (2018). Wing flexibility effects on the flight performance of an insect-like flapping-wing micro-air vehicle. *Aerospace Science and Technology*, *79*, 468–481.
- Nguyen, A. T., Kim, J.-K., Han, J.-S., & Han, J.-H. (2016). Extended unsteady vortex-lattice method for insect flapping wings. *Journal of Aircraft*, *53*, 1709–1718.
- Norris, A. G. 2013. *Experimental characterization of the structural dynamics and aero-structural sensitivity of a hawkmoth wing toward the development of design rules for flapping-wing micro air vehicles*. Ph.D. Air Force Institute of Technology.
- O’Hara, R. P., & Palazotto, A. N. (2012). The morphological characterization of the forewing of the *Manduca sexta* species for the application of biomimetic flapping wing micro air vehicles. *Bioinspiration & Biomimetics*, *7*, 046011.
- Phan, H. V., & Park, H. C. (2019). Insect-inspired, tailless, hover-capable flapping-wing robots: Recent progress, challenges, and future directions. *Progress in Aerospace Sciences*, *111*, 100573.
- Willmott, A. P., & Ellington, C. P. (1997). The mechanics of flight in the hawkmoth *Manduca sexta*. I. Kinematics of hovering and forward flight. *Journal of Experimental Biology*, *200*, 2705–2722.

Influence of Gyroscopes on the Accuracy of a Nanosatellite Attitude Estimation



Hasan Kinatas and Chingiz Hajiyev

Nomenclature

ADCS	Attitude determination and control subsystem/system
EKF	Extended Kalman filter
PRA	Principal rotation angle
RMSE	Root-mean-square error

1 Introduction

Small satellites, especially nanosatellites, offer an economical and relatively faster way to access space, leading more institutions and people to engage with the space technologies. However, being strictly limited in size, mass and cost brings some challenges during the design process. When designing subsystems, priority should be given to the use of only the components essential for the system to work at the desired level in order not to exceed the predetermined size, mass, and cost. Designing the Attitude Determination and Control Subsystem (ADCS) is especially important since achieving the desired accuracy for this subsystem is crucial. Having a poor attitude estimation accuracy can cause wrong control actions to be taken which may eventually lead to fatal consequences for the mission.

It is well known that for a three-axis attitude determination, at least two independent reference directions are needed. For these directions, the basic attitude sensor package for a nanosatellite generally consists of magnetometers and Sun sensors (Hajiyev & Soken, 2021). Using reference directions (Earth's magnetic field and Sun

H. Kinatas (✉) · C. Hajiyev
Istanbul Technical University, Istanbul, Türkiye
e-mail: kinatas16@itu.edu.tr; cingiz@itu.edu.tr

direction) and measurements of these directions, three-axis attitude information can be obtained via single-frame attitude determination methods or filtering methods. Single-frame methods aim to find the transformation matrix between the satellite body frame and reference frame of interest. These methods are heavily dependent on measurements and continue to give an attitude estimate as long as measurements are available. Various single-frame algorithms have been developed to date (TRIAD, q-method, QUEST, SVD, etc.). A study explaining and comparing these methods can be found in Cilden and Hajiyev (2014). On the other hand, filtering methods use satellite's mathematical model as well as vector measurements. Therefore, it is possible to estimate the attitude even if there is no measurement available. One of the most popular filtering techniques for spacecraft attitude estimation is known to be Kalman filtering, and it is possible to find many studies in the literature regarding this (Lefferts et al., 1982). However, the attitude estimation system requires nonlinear filtering since satellite's mathematical model and attitude sensor measurement models (e.g., magnetometer) are nonlinear. This is an undesirable situation, especially for nanosatellites, as it will increase the computational load. Integrating single-frame and filtering methods can be offered as a solution to this problem (Hajiyev & Bahar, 2003). In integrated algorithms, an initial attitude estimation is obtained using one of the single-frame methods, and then this initial estimation is given as input to the Kalman filter. This process partly reduces the computational load since the measurement model becomes linear. Integrated methods are also known as nontraditional methods since unlike traditional Kalman filtering, they do not use sensor measurements directly as input.

Gyroscope usage in satellite attitude estimation systems is optional. For single-frame methods, angular rate measurements are clearly not required. On the other hand, Kalman filters (also integrated methods) require angular rates in order to propagate the satellite's kinematic equations. Angular rate information can be obtained via satellite's dynamic equations or gyroscopes. Considering that dynamic equations are not exact and gyroscopes suffer from sensor errors such as drift and noise, estimating also angular rates during Kalman filtering along with the attitude may improve the overall attitude estimation accuracy. In Mimasu et al. (2008), authors investigate the effect of the use of gyroscopes on the accuracy where traditional Kalman filtering methods are used for the attitude estimation system, in which Sun sensors and magnetometers are the main attitude sensors, and conclude that gyro rate sensor does not bring a significant benefit. In this study, the situation is investigated for a nontraditional (integrated) attitude estimation system. An integrated TRIAD/extended Kalman filter (EKF) approach is used where a Sun direction-Earth's magnetic field-based single-frame algorithm (TRIAD) and a filtering algorithm (EKF) are integrated. In the first step of the algorithm, the TRIAD produces an initial attitude estimation using Sun sensor and magnetometer measurements. In the second step, this estimation is given to the EKF as input, and after the filtering process, final estimation is obtained. The integrated algorithm is simulated with and without gyroscope measurements, and attitude estimation accuracies are compared.

2 Method

The dimensions of the state vector \mathbf{x} are 7×1 and composed as

$$\mathbf{x} = [\bar{\mathbf{q}} \quad \boldsymbol{\omega}_{br}]^T \tag{1}$$

where $\bar{\mathbf{q}}$ is the quaternion set and $\boldsymbol{\omega}_{br}$ is the body angular velocity vector with respect to the reference frame of interest. General flow of the integrated TRIAD/EKF algorithm for nanosatellite attitude estimation is given in Fig. 1.

The estimation algorithm starts with an initial quaternion set and angular velocity vector. States are propagated using the satellite’s mathematical model of attitude motion in the prediction step, and the next quaternion set, angular velocity vector, and estimation error covariance matrix are predicted. Then, the TRIAD algorithm and onboard gyroscopes give quaternion and angular velocity measurements to the filter. Following that, the predicted state vector and given measurements are used to calculate the filter innovation and Kalman gain. Finally, using this information, the predicted state vector is updated, and final attitude and angular velocity estimations are obtained. Satellite’s mathematical model of attitude motion (Wertz, 1978), the TRIAD (Shuster & Oh, 1981), and standard EKF (Lefferts et al., 1982) algorithms are well explained in other studies and will not be repeated here for the sake of brevity.

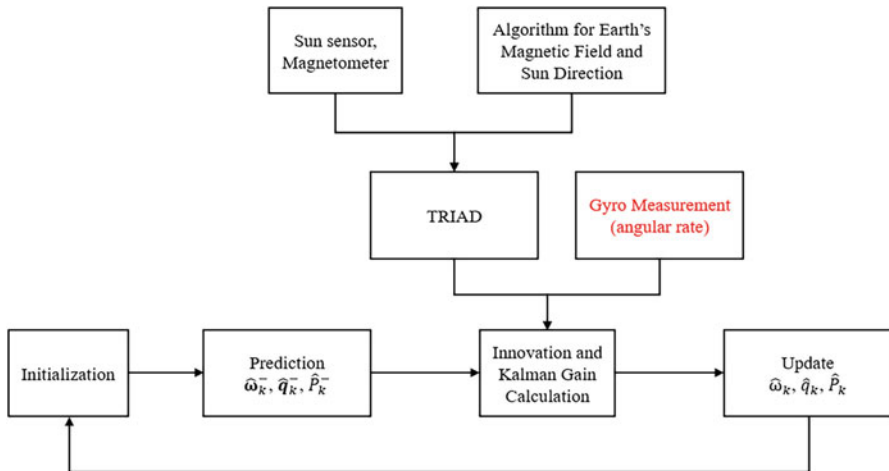


Fig. 1 General flow of the integrated TRIAD/EKF algorithm for attitude estimation

3 Results and Discussion

In order to understand the usefulness of the gyroscope measurements, the integrated TRIAD/EKF algorithm shown in Fig. 1 is simulated with and without gyroscope measurements (the box shown in red). Simulations are performed in a circular LEO, assuming an environment where only the gravity gradient torque exists as the disturbance torque. The simulated orbit has an altitude of 626 km, and its inclination and longitude of the ascending node are chosen to be 111.5° and 15° , respectively. The simulation time is determined as 5833.7 s, which is a full orbital period. Magnetometer, Sun sensor, and gyroscope noise standard deviations are chosen to be 0.08, 0.02, and 0.001, respectively. Since direction cosines are used, units are not available for noise standard deviations. It is also assumed that the satellite never enters eclipse throughout the orbit so that measurements from the Sun sensor can be taken continuously.

Figure 2 shows attitude estimation errors of integrated TRIAD/EKF algorithm with and without gyroscope measurements in terms of Euler angles. In order to see the difference better, Table 1 shows root-mean-square errors (RMSE) for each attitude angle. Converting Euler angles to the principal rotation angle (PRA), overall

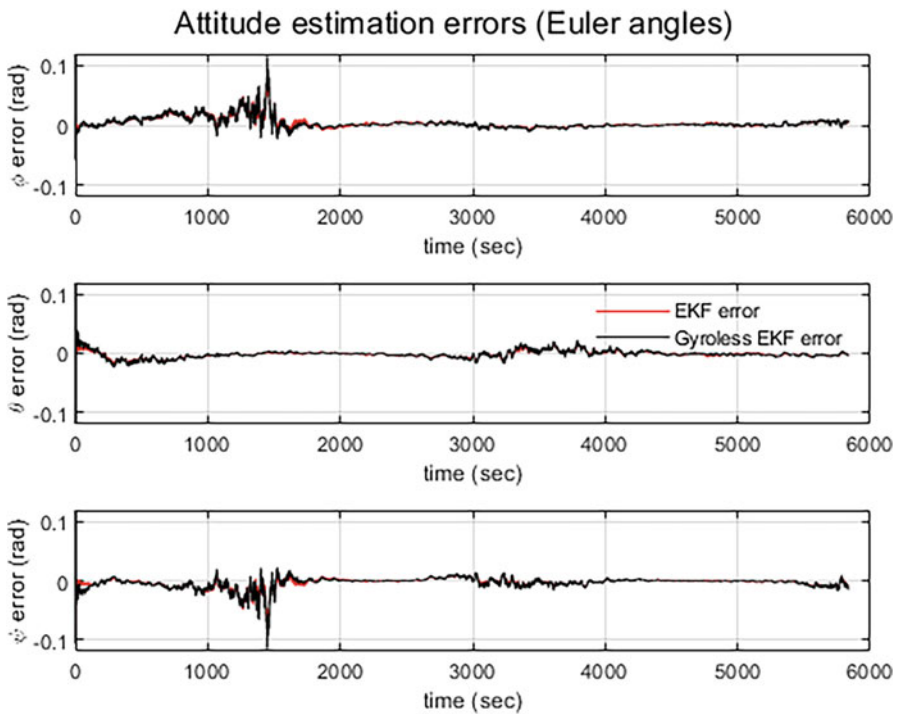


Fig. 2 Attitude estimation errors of integrated TRIAD/EKF algorithm with and without gyroscope measurements

Table 1 RMSE values of integrated TRIAD/EKF algorithm with and without gyroscope measurements

Euler Angle (deg.)	With gyroscope measurements	Without gyroscope measurements
ϕ (roll)	0.5709°	0.6144°
θ (pitch)	0.3177°	0.3811°
ψ (yaw)	0.8773°	0.9206°

attitude estimation errors for integrated TRIAD/EKF algorithm with and without gyroscope measurements are obtained as 0.4476° and 0.5344°, respectively. This result indicates an improvement of approximately 16% in case gyroscope measurements are used.

4 Conclusion

In this study, the effect of gyroscope usage on the accuracy of a nanosatellite attitude estimation system is investigated. A nontraditional satellite attitude estimation algorithm based on the TRIAD algorithm and EKF is proposed where the TRIAD algorithm uses Sun direction and Earth's magnetic field information to provide attitude information before the filtering process. The simulation results show that attitude estimation errors are reduced by up to 16% if gyroscope measurements are used.

References

- Cilden, D., & Hajiyev, C. (2014). Small satellite attitude determination methods with vector observations. *Journal of Astronautical Sciences*, 7(2), 35–43.
- Hajiyev, C., & Bahar, M. (2003). Attitude determination and control system design of the ITU-UUBF LEO1 satellite. *Acta Astronautica*, 52, 493–499. [https://doi.org/10.1016/S0094-5765\(02\)00192-3](https://doi.org/10.1016/S0094-5765(02)00192-3)
- Hajiyev, C., & Soken, H. E. (2021). Fault tolerant attitude estimation for small satellites. In *Boca Raton (Fla.)*. CRC Press Taylor & Francis Group.
- Lefferts, E. J., Markley, F. L., & Shuster, M. D. (1982). Kalman filtering for spacecraft attitude estimation. *Journal of Guidance, Control, and Dynamics*, 5(5), 417–429. <https://doi.org/10.2514/3.56190>
- Mimasu, Y., van der Ha, J. C., & Narumi, T. (2008). Attitude determination by magnetometer and gyros during eclipse. In *AIAA/AAS astrodynamics specialist conference and exhibit, Honolulu, HI, 18–21 August 2008*. <https://doi.org/10.2514/6.2008-6932>
- Shuster, M. D., & Oh, S. D. (1981). Three-axis attitude determination from vector observations. *Journal of Guidance and Control*, 4(1), 70–77. <https://doi.org/10.2514/3.19717>
- Wertz, J. R. (Ed.). (1978). *Spacecraft attitude determination and control* (pp. 510–557). Kluwer Academic Publishers.

Insertion of Shape Memory Alloy Wire with 3D Printed Thermoplastic Polyurethane Structure for Flexural Application



Leong Shii Jang, Dayang Laila Majid, Ermira Junita Abdullah, Faisal Abdul Hamid, and Husam Yahya Imrana

1 Introduction

Shape memory alloy (SMA) wire is one of the shape memory materials that are able to change its shape and return to previous shape when exposed to heat. Its strain ranging in 5–8% and high force-to-weight ratio have progressed SMA in many actuator and morphing wing applications. However, the actuation performance of SMA-based actuator highly depends on the material properties, type of bonding between SMA and host material, and SMA arrangements in the structure. A perfect bonding relation ensures the superior actuation performance and consistent recovery of SMA-based actuator. However, composite material is not an ideal matrix for SMA embedded internally to achieve high deflection or morphing application. Delamination of SMA wire from the composite due to high in-plane contraction forces has been reported. The bonding of two materials of different thermal expansion coefficient (CTE) will cause delamination, crack, and structure failure.

Instead of embedding into matrix and relying on the interface for mechanical performance, 3D printed TPU with aperture for SMA wire insertion prevents the issues. Although various studies have demonstrated the successful deformation of SMA-based soft actuator, they did not sustain large perpendicular load (Khalili et al. 2020; Rodrigue et al. 2015). Thus, the combination of soft material and SMA actuator will ensure shape deformation while resisting the external applied perpendicular load. In this paper, the effect of three-point bending load to the flexure properties of 3D printed TPU insertion with SMA wire is investigated. Since shape deformation is affected by flexural rigidity, the area moment of inertia of each infill pattern of TPU is evaluated. The parameters to be explored are TPU

L. S. Jang (✉) · D. L. Majid · E. J. Abdullah · F. A. Hamid · H. Y. Imrana
Aerospace Engineering, Universiti Putra Malaysia, Serdang, Selangor, Malaysia
e-mail: dlaila@upm.edu.my

sample: without SMA, with inactive SMA, and with active SMA inserted at top, middle, and bottom eccentric from sectional neutral axis, respectively.

2 Material and Method

In this research, SMA wire with 0.3 mm diameter manufactured by DYNALLOY Inc. is used. The phase transformation temperatures of the SMA wires (austenite start temperature, 74.59 °C, and martensite start temperature, 36.12 °C) are established through ASTM F2004-05 experiment by Baitab (2020). An infill percentage of 20% is defined for the sample's density. Various infill pattern selections available by default from CURA printing software are shown in Fig. 3. As infill pattern controls the part's strength and flexibility, its geometry property is first evaluated. Since the testing part is fabricated by repetitive infill unit cells, the single unit cell in longitudinal is discrete into multiple small area for the area moment of inertia (AMOI) analysis.

The flexure experiment is carried out using UTM machine INSTRON 3365 with 5 kN load capacity and installed with three-point loading assembly system as shown in Fig. 1. TPU samples are sized according to ASTM D790 with 48 mm × 12.7 mm × 3 mm (length × width × thickness) (Mahmood 2020). SMA wire insertion at top, middle, and bottom from the sectional neutral axis of TPU is illustrated in Fig. 2, left. SMA wire are crimped at the two ends followed the established work of John Corven (2013). For flexural test of SMA wire, the default three-point bending flexure fixture is removed to replace with two M8 hardened screw as fixture knotted over the SMA wire and tightened with upper nuts locked near the screw cap as shown in Fig. 2b. The length between the screws is adjusted to 48 mm to follow previous test configuration.

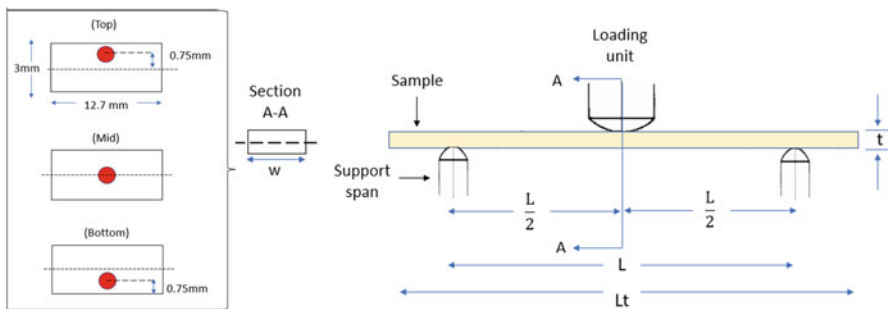


Fig. 1 schematic diagram of three-point bending test of TPU sample insertion with SMA wire (red circle) at top, middle, and bottom eccentric from sectional neutral axis

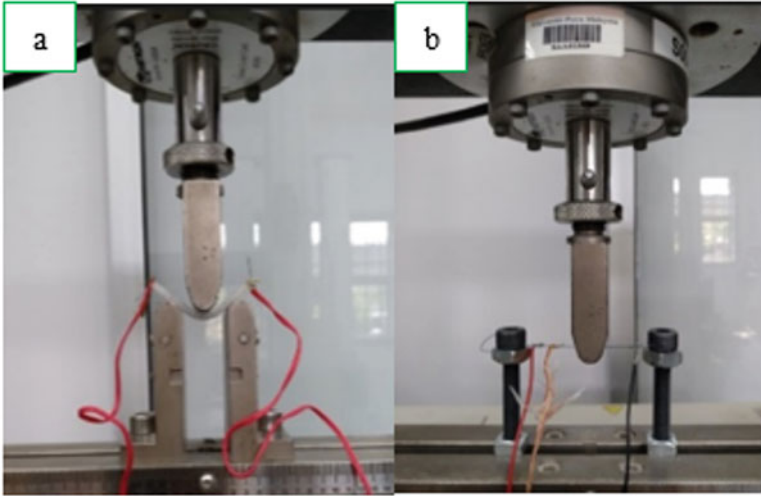


Fig. 2 Three-point bending test of (a) TPU sample integrated with inactive and activated SMA wire and (b) fixed-fixed SMA wire

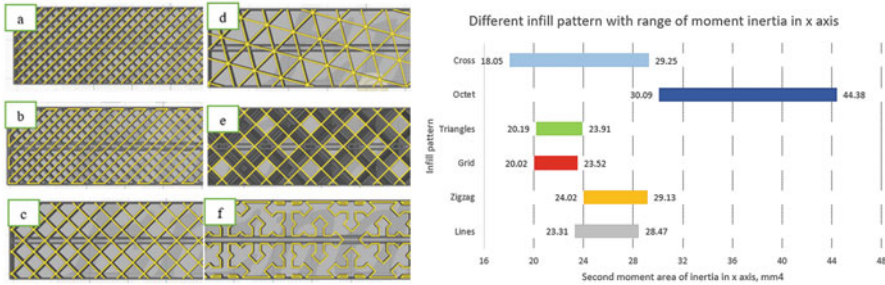


Fig. 3 (Left) Top view of infill pattern: (a) lines, (b) zigzag, (c) grid, (d) triangle, (e) octet, and (f) cross (right), AMOI of each infill pattern

3 Results and Discussion

The result of AMOI of different infill patterns is compiled and presented in Fig. 3 (right). Based on the result, the AMOI of octet infill pattern has the highest magnitude in range of 30–44 mm⁴, while the cross-infill pattern has the lowest magnitude in range of 18–29 mm⁴. Thus, cross-infill pattern is selected for three-point bending test sample as it delivers lowest strength and highest flexibility for SMA actuator.

Next, the three-point bending result of TPU without SMA has shown flexure modulus of 184.5 MPa. However, the inactive SMA wire insertion has increased the flexural stiffness. Figure 4 has shown that TPU with inactive SMA wire insertion at

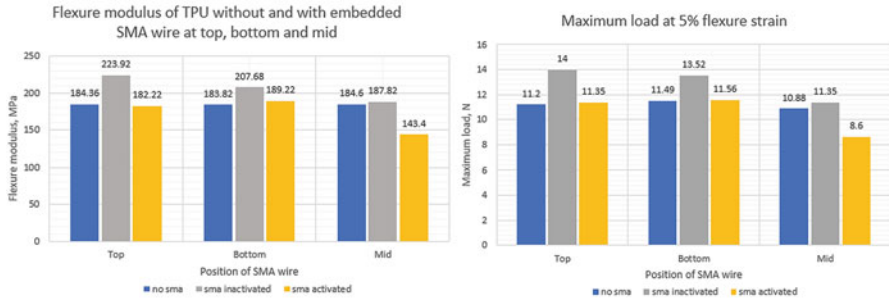


Fig. 4 (Left) Flexure modulus and (right) maximum load of TPU plate with and without SMA wire at the top, bottom, and mid placement in active and inactive condition

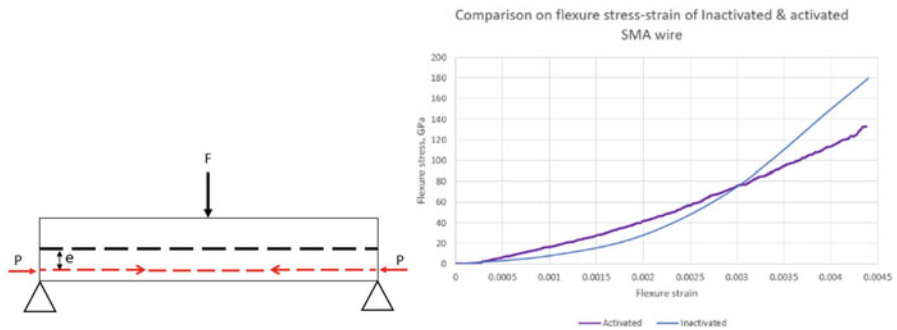


Fig. 5 (Left) Schematic diagram of axial contraction force (red) by SMA wire at the bottom eccentric from neutral axis “black” and (right) flexure stress-strain behavior of active and inactive SMA wire

the top eccentric from neutral axis has 19.6%, while the bottom has 12.6% increase in flexure modulus compared to TPU without SMA. The inactive SMA wire has also increased maximum load of 20% and 14% when inserted at the top and bottom position. When SMA is fixed at the top or bottom, the top or bottom section of TPU experienced both compression from the TPU structure and also the compression induced by the prestressing of inactive SMA. The tension from external load will first need to cancel the compression induced by the prestressing due to fixation of inactive SMA before bending the structure. However, TPU with SMA inserted at the mid has lowest flexure modulus because bending stress is absence at the neutral axis.

For activated SMA wire, axially contraction force is produced at both ends and acting over the length of the structure as shown in Fig. 5 (left). This compressive stress due to SMA eccentric from sectional neutral axis is similar to the design of prestress concrete with eccentric tensioned steel. It indicated that the stress due to SMA eccentric position has caused nonuniform stress distribution at different cross section when SMA is actuated. TPU with activated SMA has led to the decrease of flexure modulus compared with inactive SMA. Besides, the top and bottom activated SMA samples have about the same flexure modulus compared to the sample without

SMA wire. However, TPU with mid-activated SMA has significant drop about 23% in flexure modulus because moment of force is zero when SMA is inserted at the neutral axis of TPU (Banerjee 2010).

Lastly, the result of flexural stress of SMA wire in both active and inactive are seen to cross over at about flexure strain of 3% as shown in Fig. 5 (right). At higher strain, inactive SMA has higher flexure modulus than active SMA to resist the same amount of bending load. Thus, this SMA wire bending deformation result has supported the previous finding in which SMA activation led to direct contraction stress and decreased the flexure modulus of TPU structure.

4 Conclusion

In the present paper, a detached insertion of SMA wire actuator into 3D printed TPU elastomer is successfully tested instead of directly embedded into the material. Based on the cross sectional area property result obtained, the cross-infill pattern has exhibited lowest AMOI to maximize flexure ability of SMA-based actuator. The three-point bending result has revealed TPU with inactive SMA insertion at the top eccentric from sectional neutral axis has the highest flexure modulus and maximum load with 19.6% and 20% increase compared to TPU without SMA, whereas activated SMA insertion has decreased the flexure modulus of the structure about 21% compared to TPU without SMA wire. Thus, it increased the elastic symmetric bending deformation of the sample with applied load, not to mention the limitations in this research that are restricted to small SMA slot sectional area of 1.3% over TPU sectional area, symmetrical infill pattern, and thin plate structure.

Acknowledgments The work is ostensibly supported by grant no. FRGS/1/2019/STG07/UPM/02/10 and VOT No. 5540209.

References

- Baitab, D. M., Majid, D. L., Abdullah, E. J., & Hamid, M. F. A. (2020). Tensile behavior of multilayer 3D smart woven composites embedded with shape memory alloy (SMA) wires. *Journal of Materials Research and Technology*, 9(5), 10876–10885. <https://doi.org/10.1016/j.jmrt.2020.07.035>
- Banerjee, A., Bhattacharya, B., & Mallik, A. K. (2010). Optimum discrete location of shape memory alloy wire for enhanced actuation of a compliant link, May 2014. <https://doi.org/10.1115/1.4000643>
- John Corven, P. E., & Moreton, A. (2013). *Post-tensioning tendon installation and grouting manual*. American Segmental Bridge Institute.
- Khalili, S., Khalili, S. M. R., Farsani, R. E., & Mahajan, P. (2020). Flexural properties of sandwich composite panels with glass laminate aluminum reinforced epoxy facesheets strengthened by SMA wires. *Polymer Testing*, 89(September 2019), 106641. <https://doi.org/10.1016/j.polymeresting.2020.106641>

- Mahmood, D., Laila, D., & Junita, E. (2020). Tensile behavior of multilayer 3D smart woven composites embedded with shape memory alloy (SMA) wires. *Integrative Medicine Research*, 9(5), 10876–10885. <https://doi.org/10.1016/j.jmrt.2020.07.035>
- Rodrigue, H., Wei, W., Bhandari, B., & Ahn, S. (2015, December). Fabrication of wrist-like SMA-based actuator by double smart soft composite casting. <https://doi.org/10.1088/0964-1726/24/12/125003>

Coherence in Turbulent Canopy Flows: A Study of the Flow Patterns



Christian Amor, Alessandro Monti, Marco Edoardo Rosti,
and Soledad Le Clainche 

1 Introduction

The recent goals in sustainability, proposed by the governments to face the climate change threat, have motivated the research of new surface-related technologies, such as thin-filamentous canopies, for industrial applications, for instance, the aerospace industry.

Canopy flows play an important role in nature (i.e., assist in vital processes in living microorganisms, transport and deposition of nutrients in submerged vegetative populations, etc.) and industrial applications (transport of pollutants). The flow physics in canopy flows are well known throughout recent years (see Nepf, 2012; Monti et al., 2019), where their feasibility for flight control in aerodynamics has been deeply studied (Favier et al., 2009; Venkataraman & Bottaro, 2012). Therefore, the need to fully understand the flow structures and physical principles present in these kinds of complex flows suggests the application of modern data-analysis tools.

In this work, we characterize the flow structures in a submerged canopy flow (Nepf, 2012) with filaments mounted wall-normally on the bed of the domain.

C. Amor (✉) · A. Monti · M. E. Rosti
Okinawa Institute of Science and Technology Graduate University, Okinawa, Japan
e-mail: christian.amor@oist.jp; alessandro.monti@oist.jp; marco.rosti@oist.jp

S. Le Clainche
School of Aerospace Engineering, Universidad Politécnica de Madrid, Madrid, Spain
e-mail: soledad.leclainche@upm.es

2 Numerical Simulation

This section introduces the database corresponding to the scenario analyzed by Monti et al. (2019).

The three-dimensional velocity field is solved by means of high-fidelity simulations that tackle the full Navier-Stokes equations (see Monti et al., 2019, 2020 for more details). The canopy is modeled as a set of rigid, solid, and slender cylindrical stems normally resolved one by one using an immersed-boundary method (Pinelli et al., 2010). Finally, each canopy stem is randomly distributed within one of the squared tiles used to uniformly partition the bottom wall (see Monti et al., 2019). The choices of the size of the tile and the length of filament set the solidity of the canopy to $\lambda = 0.35$, therefore classifying the regime of this particular case as dense (Nepf, 2012).

The flow is simulated within a Cartesian computational box ($2\pi H$ long and $1.5\pi H$ wide, with H being the open-channel depth) with periodic boundary conditions in the streamwise and spanwise directions, free-slip at the top and no-slip at the bottom walls, respectively. The Reynolds number based on the bulk velocity is $\text{Re}_b = U_b H / \nu = 6.000$. The database analyzed in this article includes 353 flow realizations equidistant in time with time step $\Delta t = 0,1 H U_b^{-1}$, and the number of grid points is $144 \times 230 \times 144$ in the streamwise, wall-normal, and spanwise directions, respectively.

3 Higher-Order Dynamic Mode Decomposition

Higher-order dynamic mode decomposition (HODMD) (Le Clainche & Vega, 2017a) is an extension of the dynamic mode decomposition (DMD) (Schmid, 2010) method, recently introduced to study flow structures in turbulent fluid flow data (Amor et al., 2022; Le Clainche et al., 2020). This algorithm decomposes spatiotemporal information organized in matrix form as

$$\mathbf{X} = [\mathbf{v}_1, \mathbf{v}_2, \dots, \mathbf{v}_k, \mathbf{v}_{k+1}, \dots, \mathbf{v}_{K+1}, \mathbf{v}_K] \quad (1)$$

collected equidistant in time, where $\mathbf{v}_1, \dots, \mathbf{v}_k$ are snapshots collected at time instant t_k for $k = 1, \dots, K$ with K the number of snapshots in the database, as an expansion of M modes in a Fourier-like fashion:

$$\mathbf{v}(x, y, z, t_k) \cong \sum_{m=1}^M a_m \mathbf{u}_{m(x,y,z)} e^{(\delta_m + i\omega_m)t_k} \quad (2)$$

where the DMD modes \mathbf{u}_m are weighted by an amplitude a_m , and they oscillate with frequency ω_m growing, decaying, or remaining neutral in time with growth rate δ_m .

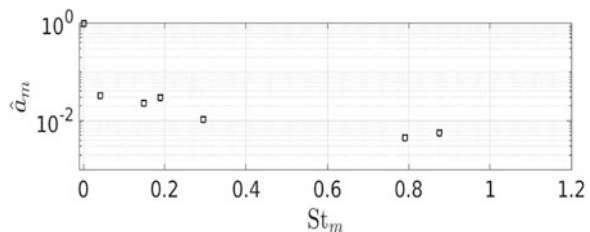
The HODMD methodology can be summarized in two main steps. First of all, the algorithm performs the singular value decomposition (SVD) to (1), reducing the spatial complexity from the total number of grid points J to a few N singular values, with $J \gg N$, by means of a tunable tolerance ε_1 , so $\sigma_i/\sigma_1 \geq \varepsilon_1$ for $i = 1, \dots, N$ (and $\sigma_{N+1}/\sigma_1 < \varepsilon_1$). This step removes spatial redundances in the data, such as noise in experimental data. In this work, we consider the *multi-dimensional HODMD* (Le Clainche & Vega, 2017b), an extension of the HODMD that substitutes the SVD by the higher-order SVD (HOSVD) (Tucker, 1966), where the spatial reduction is performed to data organized in tensor form. Finally, the second step of HODMD applies the DMD-d algorithm to the dimensionally reduced data from step one. To determine the number M of DMD modes retained in expansion (2), it is defined a second tolerance ε_2 over the amplitudes, so $\hat{a}_i = a_i/a_1 \geq \varepsilon_2$ for $i = 1, \dots, M$ (and $\hat{a}_{M+1} < \varepsilon_2$).

4 Results

This section introduces the results from the modal analysis performed to the database presented in Sect. 2. HODMD is carried out to study the turbulent canopy flow database to identify the main flow structures, which characterize the most relevant flow dynamics. Before applying the algorithm, it is necessary to calibrate the method to choose the correct set of parameters to ensure the robustness of the results (i.e., calculate the same DMD modes using different values of d and tolerances ε_1 and ε_2), where HODMD is applied recursively to the dataset (see more information in Le Clainche et al., 2020).

For the sake of brevity, we show the results corresponding with the optimal calibration. Figure 1 shows the frequencies and the amplitudes of the robust DMD modes for the turbulent canopy flow, where the optimal parameters are set to $d = 50$ and $\varepsilon_1 = \varepsilon_2 = 10^{-4}$. We identify six modes that can be classified as low-frequency ($St \leq 0.4$) and high-frequency ($St > 0.4$) modes, respectively. Within the low-frequency group, we distinguish the lowest frequency $St \cong 0.04$ and several harmonics, showing the periodic behavior of the flow. The three-dimensional representation of the DMD modes can be found in Fig. 2. We display the streamwise velocity component of each mode, organized from the lowest to the highest frequencies. Starting with $St \cong 0.04$, we identify large-scale

Fig. 1 Frequencies (non-dimensionalized with the Strouhal number, defined as $St = fH/U$, with f being the frequencies in Hz) vs. amplitudes of the robust DMD modes



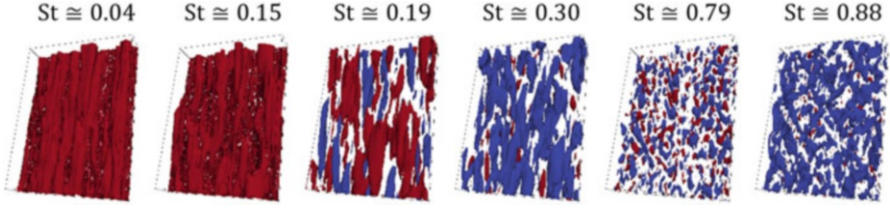


Fig. 2 Three-dimensional DMD modes. Modes are organized from low to high frequencies from left to right. Iso-surfaces of the streamwise velocity corresponding with the values -0.3 (dark blue) and $+0.3$ (dark red). In each subfigure, the flow enters the domain from the bottom side

streamwise-oriented flow structures in the outer region of the canopy. These streamwise-coherent structures extend throughout the computational domain, and their size is of the order of the height of the open channel H . However, they drastically reduce their size due to the presence of the stems in the inner region of the canopy. The canopy filters the flow structures from the outer region, like a porous wall, whose permeability depends on the density of the canopy (Monti et al., 2020). The flow structures represented in higher frequency modes are smaller than the former large streamwise structures found for $St \cong 0.04$, where the coherent structures become shorter as the frequency increases. This behavior illustrates the loss of the former coherence because of the instabilities arising in the flow.

Finally, within the canopy, the near-wall streamwise-coherent structures contained in the lowest frequency modes are well represented. Therefore, the filaments do not destroy the coherence, instead it is produced by the flow around biperiodic cylinders. These structures keep their coherence despite the drag introduced by the canopy bed and the stems, and their size is drastically reduced related with the same structures (i.e. with same frequency in (2)) in the outer region of the canopy. Furthermore, the streamwise-coherent structures look correlated in the inner region, although this correlation disappears in the outer region. This is in good agreement with the representation of the canopy as a permeable wall, where the flow structures in the outer region are different from the inner region of the canopy, respectively.

5 Conclusions

In this work, we present the modal analysis of the turbulent open-channel flow over a submerged and rigid filamentous canopy. We calculated the most relevant flow dynamics using the HODMD method, where we characterized the main coherent structures by representing the most fundamental temporal modes. First, large-scale streamwise-coherent structures appear along the open-channel domain in the streamwise direction, and they develop far from the canopy region. These large-size structures seem to lose their coherence in the higher frequency modes, suggesting the presence of flow instability mechanisms. The breakdown increases

the complexity of the flow, followed by the growth of the turbulence in both the inner and the outer regions of the canopy. On the other hand, we found the presence of the streamwise-coherent structures within the canopy region. Their size is significantly smaller, restricted by the inter-filament spacing. Additionally, the canopy filters the flow structures that can penetrate in the inner region, which are significantly smaller than those from the outer flow. Furthermore, the structures found within the canopy seem to be correlated. However, this correlation is apparently lost for the same structures in the outer region, so the surface of the canopy is perceived as a rough wall for the outer flow.

Acknowledgments This work was partially supported by the grant PID2020-114173RB-I00 funded by MCIN/AEI/10.13039/501100011033. C.A. acknowledges the financial support from the Ministry of Education and Vocational Training of Spain (Ministerio de Educación y Formación Profesional). M.E.R. and A.M. acknowledge the computational time provided by HPCI on the Oakbridge-CX cluster in the Information Technology Center, the University of Tokyo, under the grant no. hp210025 and the computer time provided by the Scientific Computing section of Research Support Division at OIST.

References

- Amor, C., Pérez, J. M., Schlatter, P., Vinuesa, R., & Le Clainche, S. (2022). Modelling the turbulent wake behind a wall-mounted square cylinder. *Logic Journal of the IGPL*, 30, 263–276.
- Favier, J., Dauptain, A., Basso, D., & Bottaro, A. (2009). Passive separation control using a self-adaptive hairy coating. *Journal of Fluid Mechanics*, 627, 451–483.
- Le Clainche, S., & Vega, J. M. (2017a). Higher order dynamic mode decomposition. *SIAM Journal on Applied Dynamical Systems*, 16, 882–925.
- Le Clainche, S., & Vega, J. M. (2017b). Higher order dynamic mode decomposition of noisy and experimental data: The flow structure of a zero-net-mass-flux jet. *Experimental Thermal and Fluid Science*, 88, 336–353.
- Le Clainche, S., Izvassarov, D., Rosti, M. E., Brandt, L., & Tammisola, O. (2020). Coherent structures in the turbulent flow of an elastoviscoplastic fluid. *Journal of Fluid Mechanics*, 888, A5.
- Monti, A., Omidyeganeh, M., & Pinelli, A. (2019). Large-eddy simulation of an open-channel flow bounded by a semi-dense rigid filamentous canopy: Scaling and flow structure. *Physics of Fluids*, 31, 065108.
- Monti, A., Omidyeganeh, M., Eckhard, B., & Pinelli, A. (2020). On the genesis of different regimes in canopy flows: A numerical investigation. *Journal of Fluid Mechanics*, 891, A9.
- Nepf, H. (2012). Flow and transport in regions with aquatic vegetation. *Annual Review of Fluid Mechanics*, 44, 123–142.
- Pinelli, A., Naqavi, I., Piomelli, U., & Favier, J. (2010). Immersed-boundary methods for general finite-difference and finite-volume Navier-Stokes solvers. *Journal of Computational Physics*, 229, 9073–9091.
- Schmid, P. (2010). Dynamic mode decomposition of numerical and experimental data. *Journal of Fluid Mechanics*, 656, 5–28.
- Tucker, L. R. (1966). Some mathematical notes on three-mode factor analysis. *Psychometrika*, 16, 279–311.
- Venkataraman, D., & Bottaro, A. (2012). Numerical modelling of flow control on a symmetric aerofoil via a porous, compliant coating. *Physics of Fluids*, 24, 9.

PD Controller with Particle Swarm Optimization for Satellite Attitude Control



Mehmet Fatih Erturk and Chingiz Hajiyev

Nomenclature

ITSE	Integral of time multiplied square error
PD	Proportional-derivative
PSO	Particle swarm optimization

1 Introduction

Magnetic actuators are getting popular, while the number of small satellites is increasing, due to their low power requirements, high robustness, and high effectiveness. This paper searches for optimized gain of a PD controller for magnetic control of a satellite with a deterministic approach. Achieving an optimal gain may increase the attitude accuracy and decrease price of it in terms of power and time.

The use of PD controllers as the main controller of magnetically controlled satellites has been studied since early times of space era. As a primary paper, Martel et al. (1998) used a PD controller with magnetorquer to achieve active attitude control. After proving the possibility of usage of PD controllers for attitude control with only magnetic actuators on satellites, performance of the PD controller is also tried to be increased with different approaches such as (Lovera & Astolfi, 2001).

PD controller is chosen as controller of solely magnetic actuated satellite. Main properties of the satellite and reference gains are taken from Makovec (2001). With

M. F. Erturk (✉) · C. Hajiyev
Istanbul Technical University, Istanbul, Türkiye
e-mail: mfatiherturk@outlook.com; cingiz@itu.edu.tr

using nonlinear attitude dynamics, gains of the controller tried to optimized with PSO. During the study, exact results of propagation are used.

1.1 Attitude Dynamics and Kinematics

Orientation of a spacecraft can be represented by quaternions. Quaternions have a vector and a scalar number. Equation 1 is the preferred representation of quaternions on the orbital frame for this study:

$$\mathbf{q} = \begin{bmatrix} \vec{q} & q_4 \end{bmatrix} = [q_1 \quad q_2 \quad q_3 \quad q_4] \quad (1)$$

Angular velocity of a satellite's body can be shown with \mathbf{w}_B . Rotational dynamics of a rigid satellite can be seen in (2):

$$\dot{\mathbf{w}}_B^{BI} = -\mathbf{I}^{-1} \mathbf{w}_B^{BI \times} \mathbf{I} \mathbf{w}_B^{BI} + \mathbf{I}^{-1} \boldsymbol{\tau}_{gg} + \mathbf{I}^{-1} \boldsymbol{\tau}_m \quad (2)$$

In Eq. (2), \mathbf{I} is satellite inertia, \mathbf{w}_B^{BI} is angular velocity vector of body with respect to inertia frame as represented in body, $\dot{\mathbf{w}}_B^{BI}$ is rate of it, $\boldsymbol{\tau}_{gg}$ is gravity gradient torque, and $\boldsymbol{\tau}_m$ is magnetic torque. As can be seen from Eq. (2), gravity gradient torque and magnetic torque are only considered torques.

On the other hand, propagation of a quaternion can be done by following Eq. (3) (Markley & Crassidis, 2014):

$$\dot{\mathbf{q}} = \frac{1}{2} \boldsymbol{\Omega}(\mathbf{w}_B^{BO}) \mathbf{q} = \frac{1}{2} \begin{bmatrix} q_2 w_{BO3} - q_3 w_{BO2} + q_4 w_{BO1} \\ q_3 w_{BO1} - q_1 w_{BO3} + q_4 w_{BO2} \\ q_1 w_{BO2} - q_2 w_{BO1} + q_4 w_{BO3} \\ -q_1 w_{BO1} - q_2 w_{BO2} - q_3 w_{BO3} \end{bmatrix} \quad (3)$$

In Eq. (3), $\boldsymbol{\Omega}(\mathbf{w})$ can be defined as Eq. (4), while \mathbf{w}^\times is cross-product matrix:

$$\boldsymbol{\Omega}(\mathbf{w}) = \begin{bmatrix} -\mathbf{w}^\times & \mathbf{w} \\ -\mathbf{w}^T & 0 \end{bmatrix} = \begin{bmatrix} 0 & w_3 & -w_2 & w_1 \\ -w_3 & 0 & w_1 & w_2 \\ w_2 & -w_1 & 0 & w_3 \\ -w_1 & -w_2 & -w_3 & 0 \end{bmatrix} \quad (4)$$

$$\mathbf{w}_B^{BO} = \mathbf{w}_B^{BI} - \frac{|\mathbf{r} \times \mathbf{v}|}{|\mathbf{r}|^2} \mathbf{A} \mathbf{q}_{BO} \quad (5)$$

Gravity gradient torque depends on quaternion, inertia, and mean motion of the satellite where r is distance between satellite and center of Earth and μ is gravitational parameter of Earth:

$$\boldsymbol{\tau}_{gg} = 3 \frac{\mu}{|\mathbf{r}|^3} \mathbf{o}_3 \times \mathbf{I} \mathbf{o}_3 \quad (6)$$

$$\mathbf{o}_3 = \mathbf{A} \mathbf{q}_{\text{BO}} [0 \quad 0 \quad 1]^T \quad (7)$$

Lastly, magnetic torque can be calculated by cross product of created magnetic moment and magnetic field of Earth on body frame. In this study, dipole magnetic field model is used. \mathbf{u} is the required magnetic moment. However, as natural fact of magnetic field, desired torque cannot be applied directly, so that projection of desired torque with respect to magnetic field is taken in Eq. (9) (Martel et al., 1998):

$$\boldsymbol{\tau}_m = \mathbf{B} \times \mathbf{M} \quad (8)$$

$$\mathbf{M} = \frac{\mathbf{u} \times \mathbf{B}}{|\mathbf{B}|} \quad (9)$$

1.2 PD Controller

PD controller is one of the most common and easy-to-apply control methods. There are various kinds of it. In this presented study, (Markley & Crassidis, 2014) approach is used as in Eq. (11):

$$\mathbf{u} = -K_p \text{sign}(q_{\text{err}4}) \mathbf{q}_{\text{err}1:3} - K_d \mathbf{w}_{\text{err}} \quad (10)$$

Here, target quaternion is defined as $\mathbf{q}_{\text{tgt}} = [0 \quad 0 \quad 0 \quad 1]$ or nadir pointing. Similarly, target angular velocity per axis is 0, so that \mathbf{q}_{err} and \mathbf{w}_{err} equal to Eqs. (11) and (12):

$$\mathbf{q}_{\text{err}} = \begin{bmatrix} q_4 \mathbf{I}_{(3 \times 3)} - \mathbf{q}^\times & \mathbf{q}_{1:3}^T \\ -\mathbf{q}_{1:3} & q_4 \end{bmatrix} \mathbf{q}_{\text{target}}^* = \begin{bmatrix} -q_4 q_1 - q_3 q_2 + q_2 q_3 - q_1 q_4 \\ q_3 q_1 - q_4 q_2 - q_1 q_3 - q_2 q_4 \\ q_2 q_1 + q_1 q_2 - q_4 q_3 - q_3 q_4 \\ q_1 q_1 + q_2 q_2 + q_3 q_3 - q_4 q_4 \end{bmatrix} \quad (11)$$

$$\mathbf{w}_{\text{err}} = \mathbf{w} - \mathbf{w}_{\text{target}} \quad (12)$$

1.3 Particle Swarm Optimization for PD Gain Tuning

Sharing knowledge of information within swarm during search for food is an important advantage for each member on the swarm. PSO roots on this principle to improve global benefit of the swarm (Kennedy & Eberhart, 1995). A swarm on the

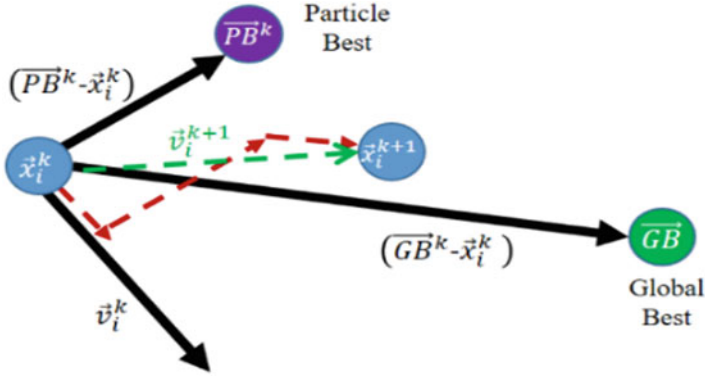


Fig. 1 Particle update in PSO

PSO consists of individual particles. Each particle has a position (\vec{x}) and a velocity (\vec{v}). Also, each (\vec{x}) has a cost, which is calculated from a fitness or cost function. The aim of the PSO is minimizing fitness function within given boundaries. During optimization process, each particle updates its (\vec{x}) with (\vec{v}). This update is not a direct summation of two vectors. The best particle in swarm (\vec{P}_B), the global best particle (\vec{G}_B), an inertia weight (w), acceleration constants (c_1) (c_2), and some random numbers (\vec{r}_1) (\vec{r}_2) between 0 and 1 have an effect on this update as it can be seen in 13. Figure 1 provides a better understanding about the update policy:

$$\vec{v}_{i+1}^k = w\vec{v}_i^k + c_1\vec{r}_1\left(\vec{P}_B^k - \vec{x}_i^k\right) + c_2\vec{r}_2\left(\vec{G}_B^k - \vec{x}_i^k\right) \quad (13)$$

$$\vec{x}_{i+1}^k = \vec{x}_i^k + \vec{v}_{i+1}^k \quad (14)$$

For this study, ready-to-use MATLAB “particle swarm” function is used. The maximum number of stall iteration is set to 10, and tolerance of function is set to 0.0001. Other parameters are set as default. The ITSE approach is a source of inspiration for the cost function. Error is taken as angle between current and target quaternions with small-angle assumptions. Also, time is considered in terms of period.

$$\text{ITSE cost} = \int_0^\infty te^2(t)dt, \quad \text{cost} = \sum_{t=0}^{5 \text{ period}} \frac{\cos^{-1}(\mathbf{q}_{BO} \cdot \mathbf{q}_{\text{target}})^2}{P} t \quad (15)$$

Table 1 Satellite orbit, inertia, and simulation time

Parameter	Value	Unit
Semi-major axis	6764.44	km
Eccentricity	0.0009877	–
Inclination	51.6	deg
Right ascension of ascending node	356.9	deg
Argument of perigee	143.5	deg
True anomaly	216.6	deg
Satellite inertia	$\begin{bmatrix} 1 & 0 & 0 \\ 0 & 1.4 & 0 \\ 0 & 0 & 0.6 \end{bmatrix}$	kg.m ²
Magnetic saturation	0.57	A.m ²
Simulation time	5	orbit
Date	27.07.1999T02 : 51 : 34.000Z	

Table 2 Gains, cost, and results of optimized gains

Parameter	Value	Parameter	Value [deg]
Kp	$I_{(3 \times 3)} * 7.02e - 6$	Mean yaw err	0.8224
Kd	$I_{(3 \times 3)} * 0.0014668$	Mean pitch err	1.0362
Cost	6.0510	Mean roll err	0.5223

2 Results and Discussion

2.1 Initialization

Table 1 is followed to initialize satellite. Initial quaternions are $[0.04963 \ 0.11436 \ 0.00138 \ 0.99220]$, while angular velocity of body equals to $[3.154 \ 6.9167 \ 1.2041] * 10^{-3}$ rad/sec (Makovec, 2001). Lastly, Psiaki (2000) is used to consider magnetorquer saturation.

2.2 PD Control with Optimized Gain via PSO

Discussed PSO algorithm is run with given cost function for this case. Obtained gains and its performance are given in Table 2, while the plots are given in Figs. 2 and 3.

Initial error was around 15° in total. It starts to oscillate approximately 1° per axes for non-optimized case. On the other hand, optimized case achieves this accuracy within an orbit and starts to oscillate around 0.5° per axes. Similarly, angular velocity decreases rapidly with respect to non-optimized case. To sum up, optimized PD gain decreased mean error of yaw-pitch-roll axes around 0.5°.

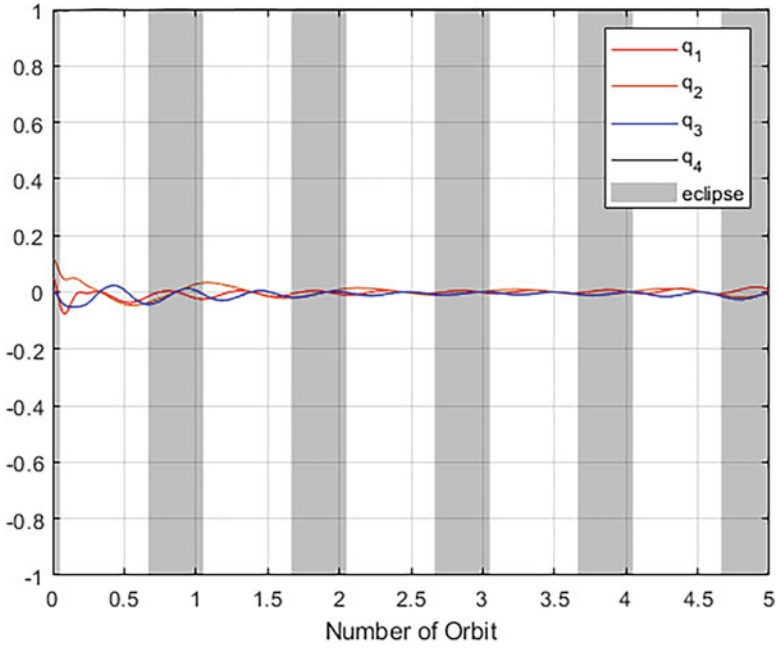


Fig. 2 Change of quaternions in body frame for non-optimized case

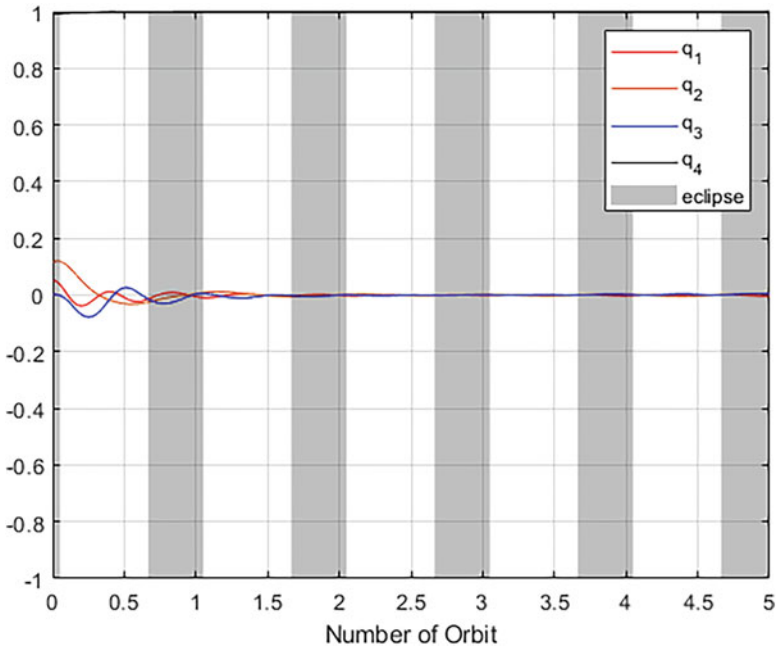


Fig. 3 Change of quaternions in body frame for optimized case

3 Conclusion


Usage of PSO for tuning the gains of PD controller is applied in this study. Considering this deterministic study, an important increase of the performance of controller is achieved, so that easily applicable and successful PSO can be used as PD gain tuner.

References

- Kennedy, J., & Eberhart, R. (1995). *Particle swarm optimization*. In Proceedings of ICNN'95 – International conference on neural networks 4:1942–1948. <https://doi.org/10.1109/ICNN.1995.488968>.
- Lovera, M., & Astolfi, A. (2001). *Global attitude regulation using magnetic control*. In Processing of the 40th IEEE conference on decision and control.
- Makovec, K. L. (2001). *A nonlinear magnetic controller for three-axis stability of nanosatellite* (MSc. thesis). Virginia Tech.
- Markley, F. L., & Crassidis, J. L. (2014). *Fundamentals of spacecraft attitude determination and control*. Springer.
- Martel, F., Pal, P., & Psiaki, M. (1998). *Active magnetic control system for gravity gradient stabilized spacecraft*. 2nd Annual AIAA/USU conference on small satellites.
- Psiaki, M. L. (2000). Magnetic torquer attitude control via asymptotic periodic linear quadratic regulation. *Journal of Guidance Control and Dynamics*, 24, 386–394.

A Predictive Physics-Aware Machine Learning Model for Reacting Flows



Adrián Corrochano, Rodolfo S. M. Freitas, Alessandro Parente,
and Soledad Le Clainche 

1 Introduction

Combustion is an extremely defiant research field in the aeronautical industry due to the difficultness of creating trustful models. These models, either experimental or numerical, are necessary for reducing the pollutants produced in the combustion process, improving the efficiency of combustion systems, or exploring fuel alternatives, as hydrogen or synthetic fuels.

On the one hand, carrying out experimental measurements can be challenging as it is necessary using sophisticated and expensive infrastructures, which are able to trace the small timescales found when the combustion process occurs, and the complex chemical reactions take place. In order to cope with these challenges, computational models can provide adequate tools for understanding the flow physics of reacting flows. However, with the large number of species involved in combustion processes, the wide variety of spatial and timescales and the nonlinear turbulence-chemistry interactions impose the use of large computer facilities (Cant, 2002). In this way, several attempts have been made to create reduced order models (ROMs) that contain as much information as possible with little computational cost.

ROMs have become popular within the field of reacting flows due to their success in being a proxy for high-fidelity models. Principal component analysis (PCA) (Parente & Sutherland, 2013) has been widely used in combustion to create steady ROMs, while higher order dynamic mode decomposition (HODMD) (Le Clainche

A. Corrochano (✉) · S. Le Clainche
School of Aerospace Engineering, Universidad Politécnica de Madrid, Madrid, Spain
e-mail: adrian.corrochanoc@upm.es; soledad.leclainche@upm.es

R. S. M. Freitas · A. Parente
École polytechnique de Bruxelles, Aero-Thermo-Mechanics Laboratory, Université Libre de Bruxelles, Bruxelles, Belgium
e-mail: rodolfo.da.silva.machado.de.freit@ulb.be; Alessandro.Parente@ulb.be

& Vega, 2017) has been able to reconstruct unsteady data in reacting flow databases. In this study, a new predictive ROM, combining proper orthogonal decomposition (POD) with deep learning architectures, has been applied to a reactive flow, attempting to predict the evolution in time of the thermodynamic states of a combustion process.

The paper is organized as follows. Section 2 briefly explains the hybrid algorithm used. The main results are explained in Sect. 3 and the conclusions in Sect. 4.

2 Method

This section briefly introduces the algorithm used to construct the predictive ROM presented in this article. The algorithm first applies POD to the database to retain the large scales, and after that, the deep learning model is used to predict the temporal coefficients of these POD modes, named as temporal modes.

Before applying the algorithm, it is essential to preprocess the database by centering and scaling the variables. Centering is the subtraction of the expected value of the variable to convert observations to fluctuations. Scaling the variables allows to compare the variables on similar terms but can also be used to highlight specific patterns. The centered and scaled variables can be defined as

$$\tilde{x}_j = \frac{x_j - \bar{x}_j}{c_j}, \quad (1)$$

where \bar{x}_j represents the temporal mean of the variable x_j and c_j is the scaling factor. Four scaling methods are considered for the analysis:

- Range scaling: Uses the difference between the maximum and minimum value of each variable as the scaling factor.
- Auto-scaling: Uses the standard deviation of each variable, σ_j , as the scaling factor.
- Pareto scaling: Uses the square root of the standard deviation of each variable, $\sqrt{\sigma_j}$, as the scaling factor.
- Variable stability (VAST) scaling: Uses the product of the standard deviation σ_j and the so-called coefficient of variation σ_j/\bar{x}_j as the scaling factor.

Each scaling method enhances the role of some species among others (Parente & Sutherland, 2013; Corrochano et al., 2022).

Once preprocessed, the data is organized into a snapshot matrix \mathbf{X} of dimensions $J \times K$, where K is the number of snapshots and $J = N_v \times N_x \times N_y$, with N_v being the number of variables analyzed and N_x and N_y the number of grid points along the two dimensions of the domain. Once organized, singular value decomposition (SVD) (Sirovich, 1987), an algorithm used to perform POD, is applied to the snapshot matrix as

$$X = U\Sigma T^T, \quad (2)$$

where U contains the POD modes, Σ the singular values, ordered in decreasing order, and T the temporal coefficients. A new temporal matrix $\hat{T} = \Sigma T^T$ is defined, and the first N modes will contain the larger structures of the flow. The deep learning architecture, which is hereafter presented, deals with this matrix \hat{T} , trying to predict the next time steps.

The deep learning structure is a multilayer neural network formed by long short-term memory (LSTM) layers and fully connected layers. More details of the neural network used can be found in Abadía-Heredia et al. (2021), as the main goal of the article is to extend its applicability to reacting flow data.

3 Results and Discussion

The proposed algorithm is going to be applied to a reacting flow database extracted from the numerical simulation explained in detailed in Corrochano et al. (2022). The database consists of ten variables with greater presence on the simulation (the temperature and nine chemical species), a mesh grid of 150×150 points, and $K = 999$ snapshots. For the prediction, the database is divided into training, validation, and test sets. The training set has a length of 60% of K (599 snapshots), the validation set of 15% of K (150 snapshots), and the test set of 25% of K (250 snapshots).

The database is centered and scaled and SVD is applied. For the neural network, only the first ten modes are going to be considered as this work is mainly focused on the suitability of the use of neural networks to predict the large scales of reacting flows. These modes contain the information of the periodic movement and the transient behavior. After that, the model is trained and validated with their correspondent sets and makes the temporal prediction on the test set.

Figure 1 depicts the relative root-mean-square error (RRMSE) calculated for the predictions of the thermodynamic states for the test set. The four scaling methods are considered, as well as a first case with no scaling to compare the improvement. As expected, the worst case is the one without scaling. This case presents a prediction error greater for all the variables studied. The main species and the temperature are better approximated than the minor species studied. This is expected as the minor species are more difficult to model (Corrochano et al., 2022). For the different scaling methods used, some tend to predict some thermodynamic states better than others and vice versa. That might be partially explained by the multiscale nature of the reacting flows, which raises difficulties in the scaling step. Also, beyond all the scaling methods, auto-scaling gives the best predictions for all the variables studied. This scaling method gives all the physical states the same importance (Parente & Sutherland, 2013), so a better approximation of the temporal modes gives a more homogeneous prediction among all the variables considered.

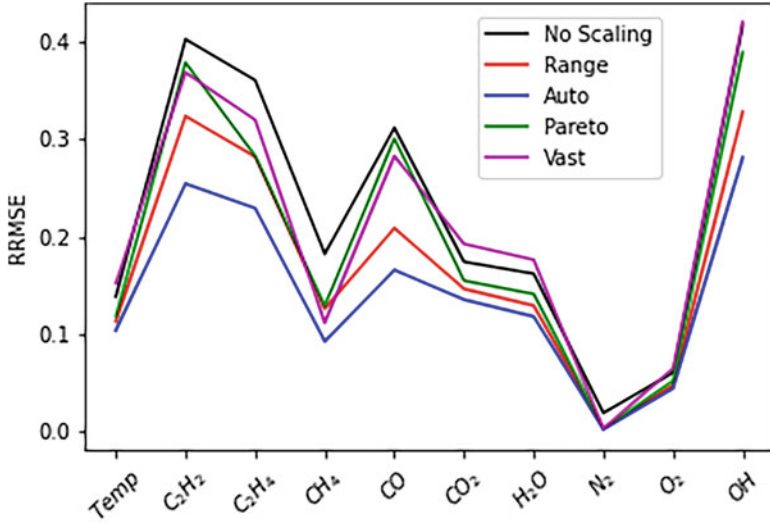


Fig. 1 Error made in the predictions using a LSTM neural network and different scaling methods

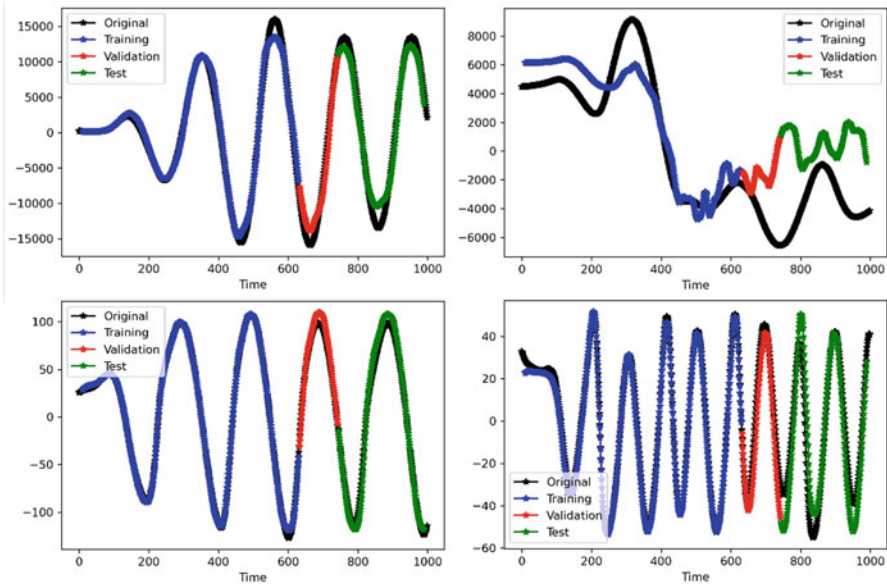


Fig. 2 Temporal predictions of the second (left) and fourth (right) temporal modes. Top: no scaling. Bottom: auto-scaling. The three sets (training, validation, and test) appear in three different colors (see legend)

A comparison between the predictions of the worst case (no scaling) and the best scaling method (auto) is shown in Fig. 2. More specifically, the second and the fourth modes are studied. It is worth remarking that the second temporal mode has the information related to the periodic behavior of the numerical simulation, which is the main dynamic of the simulation, so it is easier to predict. The fourth temporal mode has information about the transient behavior of the simulation, which is more challenging to predict. The second temporal mode is correctly predicted for both cases, while the greater differences appear in the fourth mode, specifically in the case with no scaling where large discrepancies appear between the predictions and the true value. However, for auto-scaling, the fourth temporal mode has a periodic-like behavior, so it is properly predicted by the algorithm.

4 Conclusion

This work studies the suitability of deep neural networks as a predictive ROM for reacting flows. An existing recurrent neural network formed by LSTM layers, which is robust in the prediction of single-phase flows in other fluid dynamics applications, is used combined with the preprocessing techniques mainly used in combustion. All the scaling methods used improve the time prediction of all the thermodynamic states. Auto-scaling gives the best predictions for all the variables studied. Considering the complexity of the problem studied, the results presented suggest that this kind of neural networks can be suitable for the development of predictive ROMs in reactive flows.

Acknowledgments AC and SLC acknowledge the grant PID2020-114173RB-I00 funded by MCIN/AEI/10.13039/501100011033.

References

- Abadía-Heredia, R., López-Martín, M., Carro, B., Arribas, J. I., Pérez, J. M., & Le Clainche, S. (2021). A predictive hybrid reduced order model based on proper orthogonal decomposition combined with deep learning architectures. *Expert Systems with Applications*, 187(32), 115910.
- Cant, S. (2002). High-performance computing in computational fluid dynamics: Progress and challenges. *Philosophical Transactions of the Royal Society of London. Series A: Mathematical, Physical and Engineering Sciences*, 360(1795), 1211–1225.
- Corrochano, A., D’Alessio, G., Parente, A., & Le Clainche, S. (2022). Higher order dynamic mode decomposition to model reacting flows. *International Journal of Mechanical Sciences*, 249, 108219.
- Le Clainche, S., & Vega, J. M. (2017). Higher order dynamic mode decomposition. *SIAM Journal on Applied Dynamical Systems*, 16, 882–925.
- Parente, A., & Sutherland, J. C. (2013). Principal component analysis of turbulent combustion data: Data pre-processing and manifold sensitivity. *Combustion and Flame*, 160(2), 340–350.
- Sirovich, L. (1987). Turbulence and the dynamics of coherent structures. Parts I III. *Quarterly of Applied Mathematics*, 45(3), 561–571.

Rendezvous and Docking for Space Vehicles



Mert Sever and Tuncay Yunus Erkeç

Nomenclature

CW	Clohessy-Wiltshire
EKF	Extended Kalman filter
GNSS	Global navigation satellite system

1 Introduction

Today, with the increase in interest and curiosity in space, studies have accelerated compared to previous years. In this context, the work of more complex tasks stands out compared to the previous tasks. The prominence of comprehensive studies such as interplanetary missions, asteroid missions, and multiple spacecraft missions has created multi-body problems and brought the need to calculate the relative state of objects with respect to each other. Different movements of objects in space have revealed the importance of rendezvous and docking problems, and studies in this field have gained importance.

Since interlocking is a present problem today, there are many studies on this subject. In the literature, studies on docking and rendezvous problems and solutions for both spacecraft and spacecraft and object are frequently included.

In the study titled “Compound control for autonomous docking to a three-axis tumbling target” by Dong Ye et al. (2019), the combined position and orientation control problem of a spacecraft serving in orbit that docks autonomously to a three-axis freely rotating target in space is discussed (Ye et al. 2019). A unified control

M. Sever (✉) · T. Y. Erkeç
National Defense University, Hezârfen Aeronautics and Space Technologies Institute,
Istanbul, Türkiye

approach is presented to ensure that the docking port of the shuttle spacecraft is always directed to the docking port of the rolling target. The proposed method is implemented with a combination of relative position tracking and relative state control.

In another study called “Automatic Spacecraft Docking Using Computer Vision-Based Guidance and Control Techniques” by Chi-Chang and McClamroch, an innovative approach to autonomous spacecraft docking was introduced by developing a computer vision-based control approach compared to previous methods (Chi-Chang and McClamroch, 1993). In the study, which suggests that precise control of the relative spacecraft velocity is required for a soft docking, it is suggested to use computer vision method as a position and direction sensor to obtain feedback information. In this context, a fixed camera was used in the study, and discrete-time position and rotation estimates of the spacecraft were obtained by solving the finite nonlinear least squares problem.

In another study named “Model Predictive Control for Spacecraft Rendezvous and Docking: Strategies for Handling Constraints and Case Studies” by Weiss et al., spacecraft relative motion guidance based on the application of linear quadratic model predictive control (MPC) with dynamically reconfigurable constraints and strategies for its control is presented (Weiss et al. 2015). The MPC controller is expressed using a simulation used for a nonlinear spacecraft orbital motion. Estimates of spacecraft states obtained from relative angle and distance measurements are used with the application, and the estimates used are shown to be resistant to dynamics and measurement noises.

Another study is “Relative position and attitude estimation and control schemes for the final phase of an autonomous docking mission of spacecraft” by Philip and Ananthasayanam. In this study, established relative position and orientation schemes for the final stage of an autonomous space rendezvous and docking system are shown. Within the scope of the study, it has been shown that fixed-gain observers are sufficient for users’ position and orientation estimations and how the parameters change with sensitivity changes (Philip and Ananthasayanam, 2003).

2 Global Navigation Satellite System

Unlike inertial and radio navigation systems, satellites positioned around the world are used instead of fixed stations and sensors on the user as transmitters. The main advantage of this system over the radio navigation system is the width of the coverage area. Transmitters positioned in the ground plane may face the disadvantages of landforms. It is possible to obtain position, velocity, and time information in the common reference plane, thanks to the signals received from the navigation satellites using the GNSS receiver without time and weather restrictions. However, sending GNSS satellites into orbit and controlling them in orbit is a costly work. When a GNSS receiver works, it must receive the signals of at least four GNSS

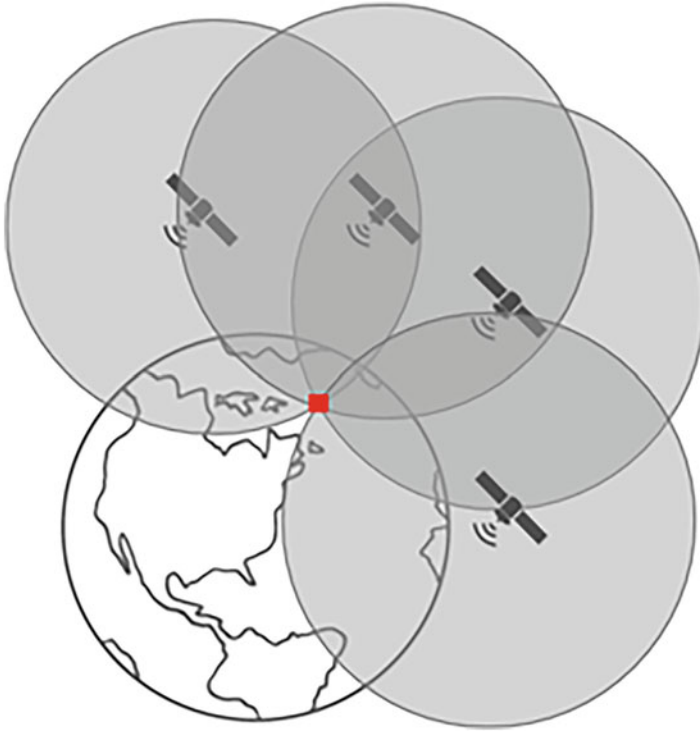


Fig. 1 Sphere intersection of navigation satellites

satellites in the coverage area. In this direction, the GNSS system has been created in such a way that it can always cover a point on the Earth with at least four satellites.

Precise atomic clocks in GNSS satellites work simultaneously with the clocks on the Earth and other satellites in Earth orbit, and these satellites continuously send their positions and time information from these precision atomic clocks to the Earth.

By calculating how much the clock information transmitted by these signals deviates from the absolute time, the distance between each satellite from which data is received and the GNSS receiver is determined. In this way, the position of the activated GNSS receiver on the world can be determined. As shown in Fig. 1, creating spheres in such a way that the distance between the navigation satellites and the user is determined as a radius constitutes the logic of the GNSS-based position determination method.

The point where the spheres around the navigation satellites intersect on the user whose position will be determined provides the user position determination. As shown in Eq. (1), user position (x, y, z) and time in three axes can be estimated by creating four different sphere equations for four GNSS satellites and solving these equations together:

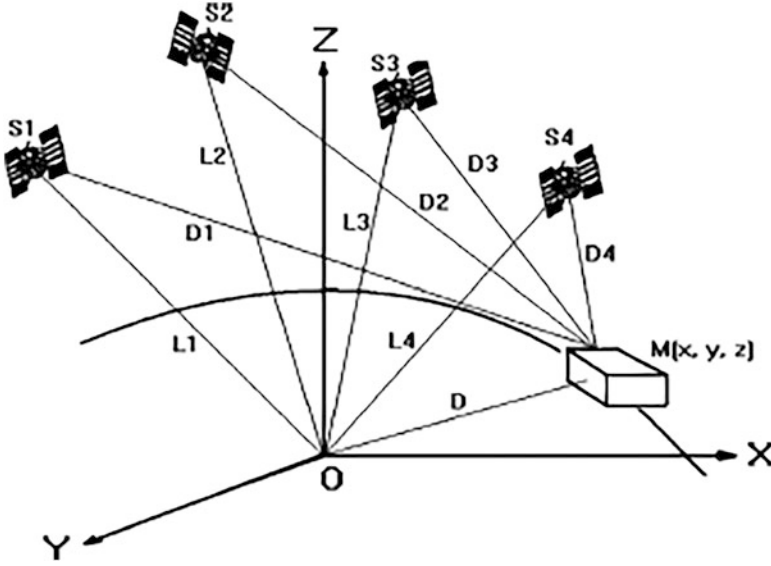


Fig. 2 Object localization scheme via distance measurement method

$$D_i = \sqrt{(x_i - x)^2 + (y_i - y)^2 + (z_i - z)^2} \quad (1)$$

Here, the value of i represents the navigation satellite. The terms x , y , and z , which are not specified with a subscript, indicate the location of the user. With this calculation, the distance between the satellite and the user is calculated as a resultant vector. This distance measurement method created is a nonlinear method.

In this study, four different navigation satellites created by simulation were determined, and the positions of the follower and target satellites were measured based on the distance method. The distance method is obtained by determining the distances between the user and the navigation satellite on each axis, taking the sum of their squares, and then taking the square root of the obtained value. With the help of the distances obtained, the state vectors of the user are estimated.

As shown in Fig. 2, M users are navigation satellites S1, S2, S3, and S4. The distances expressed with D are the distance between each navigation satellite and the user, while the distances indicated with L are the distance between the origin point of the reference plane and the navigation satellite.

3 Extended Kalman Filter

The Kalman filter, which is applied by linearizing nonlinear models by considering the Taylor approach for the previous state estimation of the system function and the estimated position of the observation function in the present time, is called the extended Kalman filter (SPF). The state and observation variables of the model, whose initial conditions are given, are linearized with the Taylor series (Kalman & Bucy, 1961):

$$\widehat{X}(k_0) = \mu_{x_0}, \quad P_x(k_0) = P_{x_0} \quad (2)$$

In this case, the estimation equation for the model whose initial conditions are shown in Eq. (1) is as shown in Eq. (2):

$$\widehat{X}(k+1) = \widehat{X}(k+1/k) + K(k+1) \left\{ Z(k+1) - h \left[\widehat{X}(k+1/k), k+1 \right] \right\} \quad (3)$$

The one-stage estimation algorithm is as shown in Eq. (3):

$$\widehat{X}(k+1/k) = \phi \left[\widehat{X}(k), k \right] \quad (4)$$

The gain matrix of the filter is shown in Eq. (4):

$$K(k+1) = P_X^-(k+1) \frac{\partial h^T \left[\widehat{X}(k+1/k), k+1 \right]}{\partial \widehat{X}(k+1/k)} \quad (5)$$

The extrapolation error algorithm of the filter is shown in Eq. (5):

$$\begin{aligned} P_X^-(k+1/k) &= \frac{\partial \phi \left(\widehat{X}(k), k \right)}{\partial \widehat{X}(k)} P_X^-(k) \frac{\partial \phi^T \left(\widehat{X}(k), k \right)}{\partial \widehat{X}(k)} \\ &+ G \left[\widehat{X}(k), k \right] Q(k) G^T \left[\widehat{X}(k), k \right] \end{aligned} \quad (6)$$

The estimation error is given in Eq. (6):

$$\begin{aligned}
& P_X^-(k+1) \\
& P_X^-(k+1/k) - P_X^-(k+1/k) \frac{\partial h^T [\widehat{X}(k+1/k)k+1]}{\partial \widehat{X}(k+1/k)} \\
& = + \left(\frac{\partial h [\widehat{X}(k+1/k)k+1]}{\partial \widehat{X}(k+1/k)} P_X^-(k+1/k) \frac{\partial h^T [\widehat{X}(k+1/k)k+1]}{\partial \widehat{X}(k+1/k)} \right) \quad (7) \\
& + R(k+1)^{-1} \frac{\partial h^T [\widehat{X}(k+1/k)k+1]}{\partial \widehat{X}(k+1/k)} P_X^-(k+1/k)
\end{aligned}$$

For the extended Kalman filter, calculations are made in accordance with the formulas given in the range of Eqs. (2–6). In contrast to the linear filter, the gain matrix (K) and covariance matrices are recalculated for each prediction. Giving the initial conditions of the filter too far from the true values will lead to instability of the filter. For this reason, the initial values given should be adjusted very well (Hacıyev, 2011).

4 Two-Impulse Rendezvous Maneuver

Considering the initial state of the spacecraft whose positions are determined by GNSS, their positions in three axes are calculated relatively. The resulting relative state vector is tried to reach zero in three axes. This process, known as the docking or rendezvous maneuver, is provided by the method called the two-fire rendezvous maneuver within the scope of this study. With the method application, the required thrust is calculated. In the system created with the help of Clohessy-Wiltshire (CW) matrices, the orbits of the spacecraft are determined first. The Clohessy-Wiltshire matrices are calculated by determining the angular velocities and the docking time in the determined orbit:

$$\Phi_{rr} = \begin{bmatrix} 4 - 3 \cos nt & 0 & 0 \\ 6(\sin nt - nt) & 1 & 0 \\ 0 & 0 & \cos nt \end{bmatrix} \quad (8)$$

$$\Phi_{rv} = \begin{bmatrix} \frac{1}{n}(\sin nt) & \frac{2}{n}(1 - \cos nt) & 0 \\ \frac{2}{n}(\cos nt - 1) & \frac{1}{n}(4\sin nt - 3nt) & 0 \\ 0 & 0 & \frac{1}{n} \sin nt \end{bmatrix} \quad (9)$$

$$\Phi_{vr} = [3n \sin nt \quad 0 \quad 0 \quad 6n(\cos nt - 1) \quad 0 \quad 0 \quad 0 \quad -n \sin nt] \quad (10)$$

$$\Phi_{VV} = [\cos nt \sin nt - 2 \sin nt \cos nt - 3000 \cos nt] \quad (11)$$

After obtaining the CW matrices, the relative positions for the initial and final state are determined. Since the last state will be the docking state, the relative state on each axis is treated as zero:

$$\delta r_0 = \begin{bmatrix} x_{\text{Target}} - x_{\text{Chaser}} \\ y_{\text{Target}} - y_{\text{Chaser}} \\ z_{\text{Target}} - z_{\text{Chaser}} \end{bmatrix} \quad (12)$$

$$\delta r_f = \begin{bmatrix} 0 \\ 0 \\ 0 \end{bmatrix} \quad (13)$$

If the obtained matrices are to be solved in the first CW equation,

$$\delta r_f = \Phi_{rr} \delta r_0 + \Phi_{rv} \delta v_0^+ \quad (14)$$

Here δv_0^+ is shown as Eq. (8):

$$\delta v_0^+ = (-\Phi_{rv})^{-1} \Phi_{rr} \delta r_0 \quad (15)$$

Then the second CW equation is solved:

$$\delta v_f^- = \Phi_{vr} \delta r_0 + \Phi_{vv} \delta v_0^+ \quad (16)$$

Using the obtained two CW equations, the total ΔV_0 value is calculated with the help of Eq. (10):

$$\Delta V_0 = \Delta V_0^+ + \Delta V_0^- \quad (17)$$

Similarly, if the total ΔV_f value is calculated:

$$\Delta V_f = \Delta V_f^+ + \Delta V_f^- \quad (18)$$

The total thrust required for the maneuver is calculated by summing the ΔV values obtained:

$$\Delta V_{\text{Total}} = \Delta V_0 + \Delta V_f \quad (19)$$

5 Results and Discussion

Within the scope of the study, position determination was carried out for two different spacecraft using the extended Kalman filter, and the position change of two different spacecraft with respect to each other was simulated at an interval of 100 s, and their graphs were drawn.

It was assumed that the orientations of the two spacecraft remained constant while the calculations were made, and no orientation problems were included in the study. Based on the initial states shown, the orbital behavior graphs of the spacecraft were created with the Kepler equations. It was assumed that the spacecraft were not exposed to any disturbance effects while the simulation was being created.

In this context, the graphs obtained by creating simulations are as shown below. The behavior and relative behavior of the spacecraft in each axis for each second is plotted as obtained by the extended Kalman filter. The orbital motions and relative motions of the two satellites are shared in three axes for the location in the case of no docking maneuver in Figs. 3, 4, 5. The value expressed with the red line is the actual value, and the value expressed with the blue line is the estimated values with DPF based on the measurements.

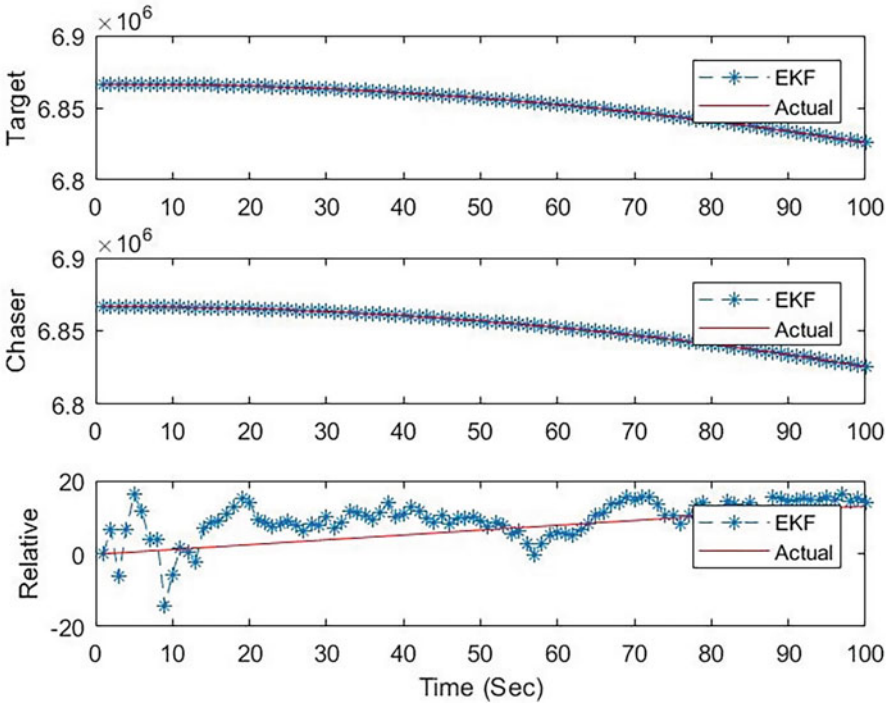


Fig. 3 X axis estimation by using GNSS

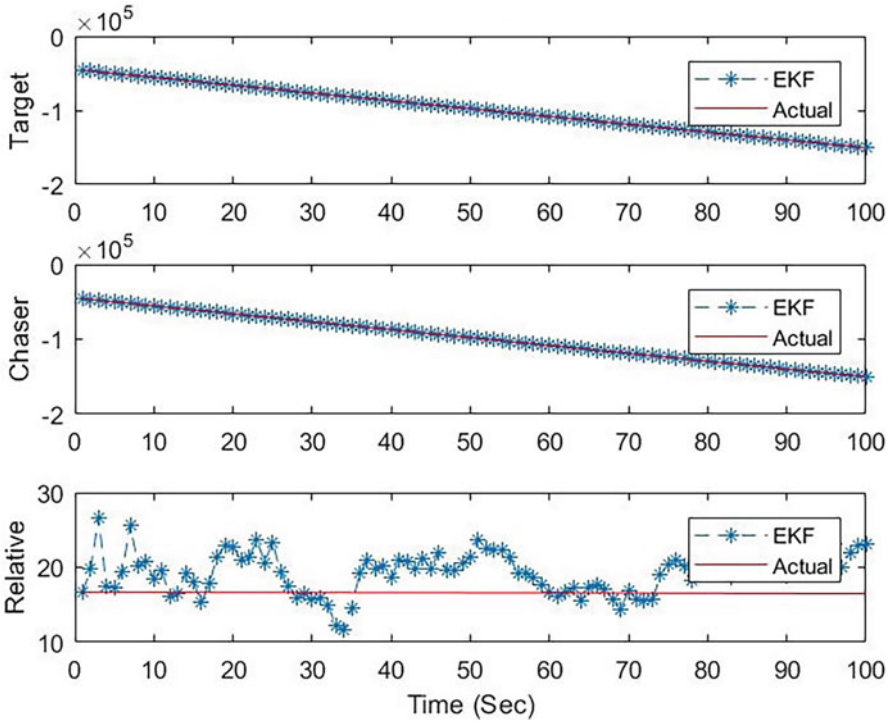


Fig. 4 Y axis estimation by using GNSS

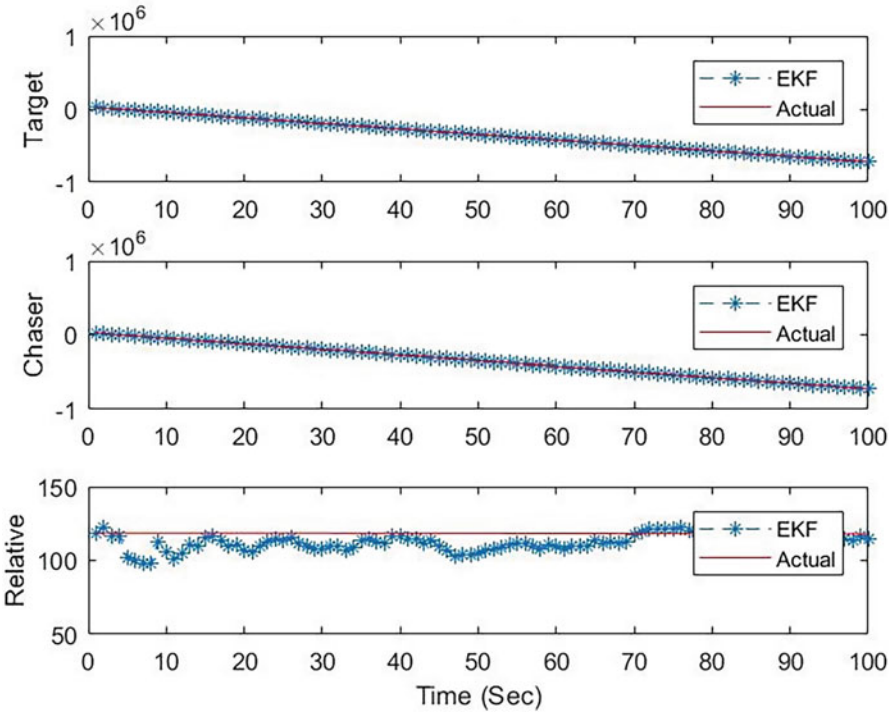


Fig. 5 Z axis estimation by using GNSS

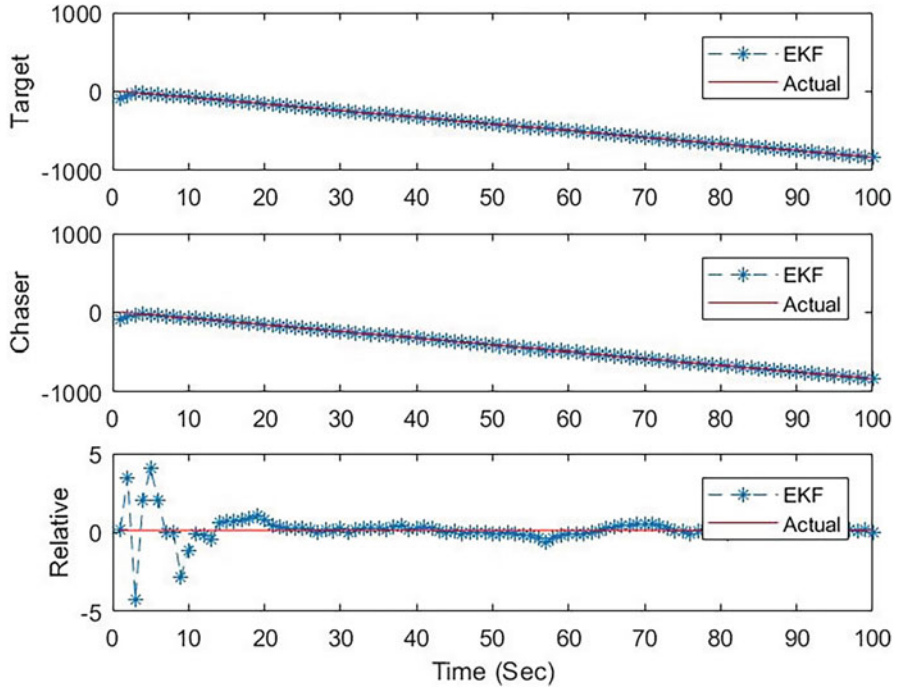


Fig. 6 Vx axis estimation by Using GNSS

The graphs shown in Figs. 6, 7, 8, on the other hand, are shared on three axes for velocity in the orbital motions and relative motions of the two satellites in the absence of docking maneuvers. The value expressed with the red line is the actual value, and the value expressed with the blue line is the estimated values with DPF based on the measurements.

In Table 1, the deltaV amounts required for the docking of two satellites calculated with the help of MATLAB are shown by calculating for different docking times. The amount of deltaV calculated in accordance with the formulas shared in the two-fire rendezvous maneuver part was obtained according to the relative position of the two satellites in the first second.

6 Conclusion

Within the scope of the study, the free motion of two spacecraft, which are in the same orbit and assumed to be approximately 120 m apart in the initial state, was observed for the specified simulation period. GNSS measurement and actual (theory) value graphs of spacecraft movements are shown. With the help of GKF, the measurement values converged to the real values, and a convergence graph was

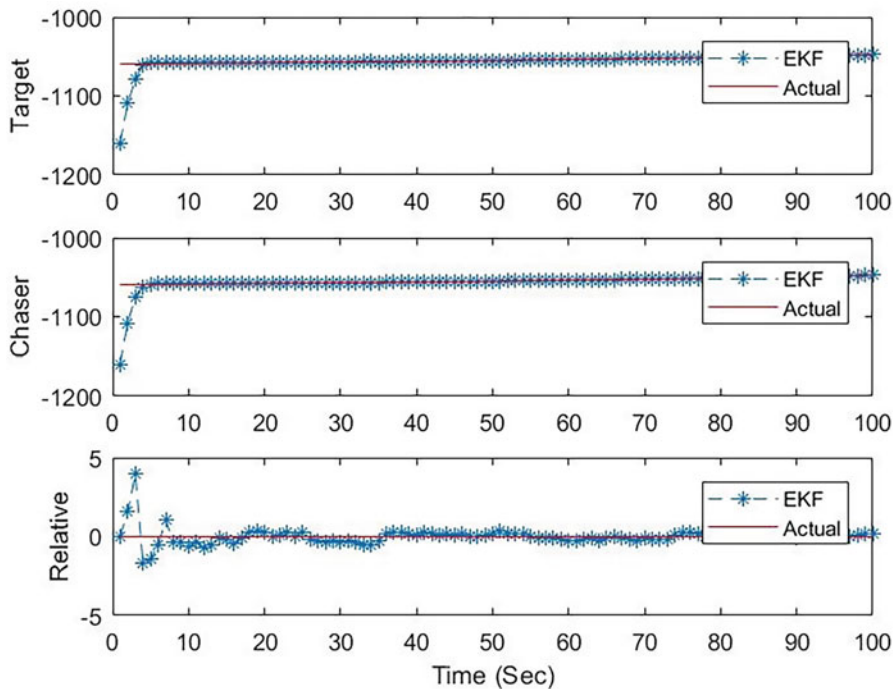


Fig. 7 V_y axis estimation by using GNSS

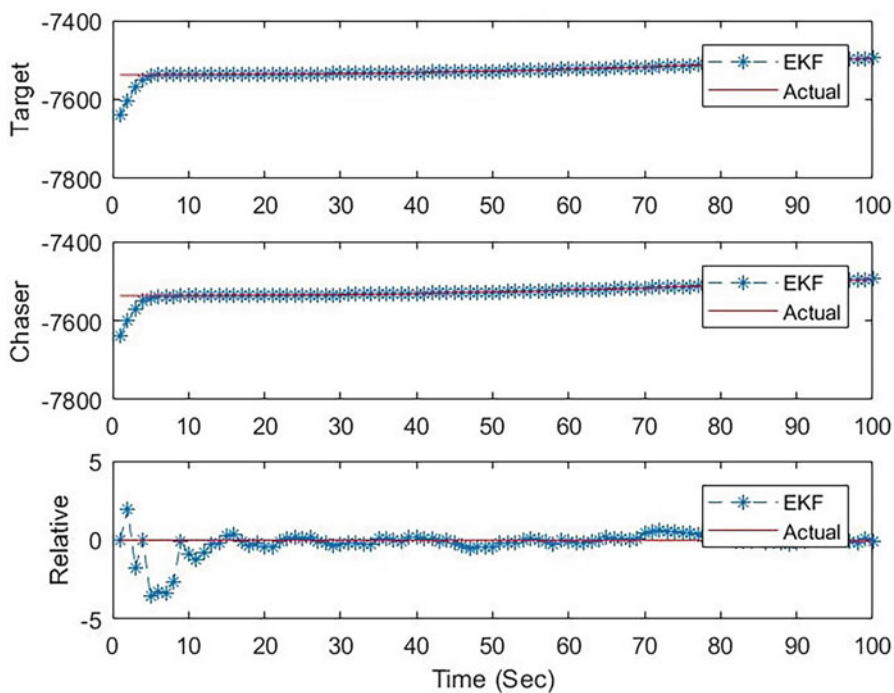


Fig. 8 V_z axis estimation by using GNSS

Table 1 Required ΔV obtained from CW equations

Required time for docking	Required ΔV (m/s)
10 s	2.396874e-02
50 s	4.792634e-03
100 s	2.394575e-03
1000 s	2.160157e-04

drawn. In the study, the model for determining the position of the spacecraft with GNSS is shown, and it is explained how to create a model for the GKF application. By considering the initial state values of the spacecraft positions obtained, the amount of deltaV required for docking was calculated using the two-fired rendezvous maneuver method, with the help of the CW equations shown.

With this study, an introduction to the subject of relative spacecraft has been made, and a preliminary study has been obtained about the rendezvous maneuver, which is explained at the basic level.

With future studies, it is planned to expand the study by including the effects of orientation and orbital disturbances to the problem and to obtain a study that will gain importance in the literature close to a more comprehensive real model.

References

- Hajiyev, C. (2011). GNSS signal processing via linear and extended Kalman filters. *Asian Journal of Control*, 13(2), 1–10.
- Ho, Chi-Chang J. & Mcclamroch, N. H. (1993). Automatic spacecraft docking using computer vision-based guidance and control techniques. *Journal of Guidance, Control, and Dynamics*, 16(2), 281–288.
- Kalman, R. E. & Bucy, R. S. (1961) New Results in Linear Filtering and Prediction Theory. *Journal of Basic Engineering*, 83(1), 95–108. <https://doi.org/10.1115/1.3658902>
- Philip, N. K., & Ananthasayanam, M. R. (2003). Relative position and attitude estimation and control schemes for the final phase of an autonomous docking mission of spacecraft. *Acta Astronautica*, 52(7), 511–522. [https://doi.org/10.1016/S0094-5765\(02\)00125-X](https://doi.org/10.1016/S0094-5765(02)00125-X)
- Weiss, Avishai, Baldwin, Morgan & Erwin, Richard & Kolmanovsky, Ilya. (2015). Model Predictive Control for Spacecraft Rendezvous and Docking: Strategies for Handling Constraints and Case Studies. *IEEE Transactions on Control Systems Technology*, 23, 1–1. <https://doi.org/10.1109/TCST.2014.2379639>
- Ye, D., Lu, W., & Mu, Z. (2019). Compound control for autonomous docking to a three-axis tumbling target. *Transactions of the Institute of Measurement and Control*, 41(4), 911–924. <https://doi.org/10.1177/0142331218758889>

Effect of the Grid Span on a Biomimetic UAV



Rafael Bardera, Ángel Rodríguez-Sevillano, Estela Barroso,
and Juan Carlos Matías

Nomenclature

CFD	Computational fluid dynamics
INTA	Instituto Nacional de Técnica Aeroespacial
UAV	Unmanned aerial vehicle
UPM	Universidad Politécnica de Madrid
b	Grid span
C_L	Lift coefficient
C_D	Drag coefficient
AoA, α	Angle of attack

1 Introduction

Presently, the development of unmanned aerial vehicles (UAVs) plays an important role in the international aerospace field. Over the last few years, bio-inspired aircraft that simulate the flying of animals have become one of the most attractive aviation technologies (Han et al., 2020). In particular, these developments applied to UAVs are a key part of the relentless quest to improve the performance of these vehicles, increasing its aerodynamic efficiency and reducing its weight and emissions. The National Institute for Aerospace Technology (INTA) and Technical University of

R. Bardera (✉) · E. Barroso · J. C. Matías
Instituto Nacional de Técnica Aeroespacial, Madrid, Spain
e-mail: barderar@inta.es; barrosobe@inta.es; matiasgjc@inta.es

Á. Rodríguez-Sevillano
Universidad Politécnica de Madrid (UPM), Madrid, Spain
e-mail: angel.rodriguez.sevillano@upm.es

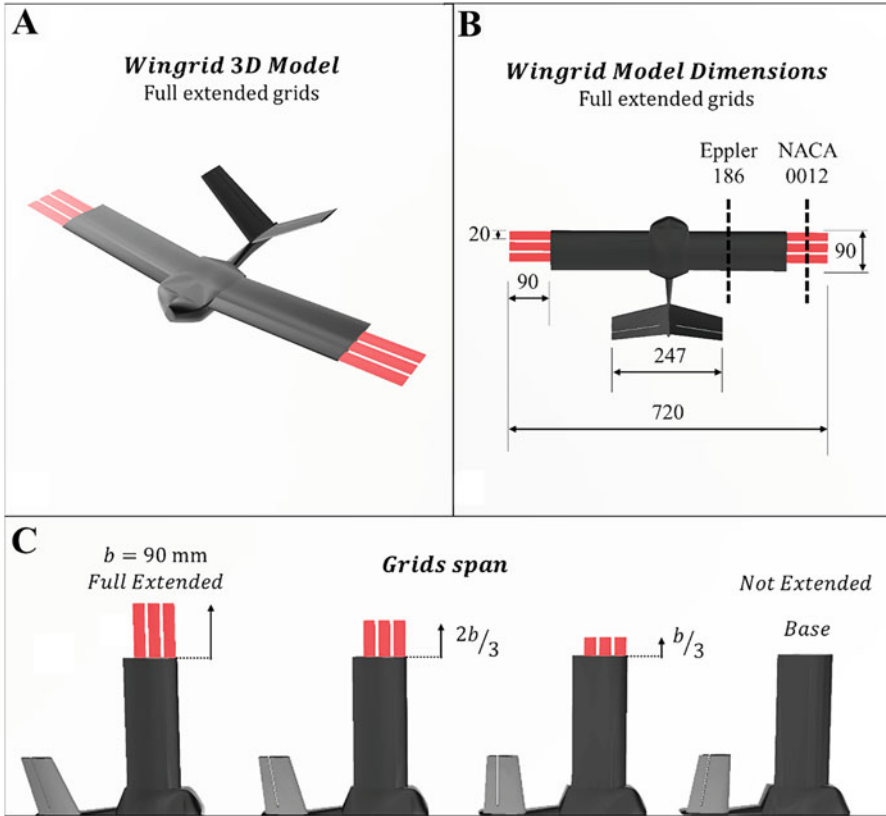


Fig. 1 Biomimetic UAV wingrid with different grid spans (base, $b/3$, $2b/3$, and b) and specific dimensions of the fully extended grid configurations

Madrid (UPM) have developed a biomimetic UAV inspired on the primary feathers of an eagle (Tucker, 1993; Rodríguez-Sevillano et al., 2019), Fig. 1a. It has rectangular wing with three semi-wings (grids) which increase the wingspan during the flights and help in reducing induced drag to improve the aerodynamic efficiency. The wingspan of the UAV configuration with the grids retracted is 540 mm and up to 720 mm when the grids are fully extended (Fig. 1b).

The aim of this paper is to use computational fluid dynamics (CFD) to determine the effect of the grid span on the UAV performance. It means to compare the lift, drag, and aerodynamic efficiency of the non-extended (base) and extended grids configurations ($b/3$, $2b/3$, fully extended) under different wind angles of attack, Fig. 1c.

2 Numerical Setup

The computational analysis has been performed using ANSYS-Fluent software. Only half of the model is calculated because the freestream velocity is along the chordwise direction and the effect of the propeller has not been considered which results in a shorter processing time to find the convergence solution and at the same time less memory, storage, and processing capability requirements. As can be seen in Fig. 2, an unstructured mesh with approximately 5 million of elements is used. Boundary conditions selected were a freestream velocity of 16 m/s which results in a Reynolds number of $9.2 \cdot 10^4$, a normal operating regime of this type of vehicles.

3 Results and Discussion

3.1 Lift and Drag Coefficients

The lift coefficient for the four UAV configurations simulated through CFD (from retracted to fully extended grids) is presented in Fig. 3a. The results clearly show two different regimes, above and below the value of zero degrees of angle of attack. For positive angles of attack, the lift coefficient increases linearly, and the higher its value, the larger the span of the grids. Opposite trend is presented for negative angles of attack. In numbers, the differences in C_L between the four configurations at 0° are almost null. At 5° they account for 20% and for higher angles up to 26%.

Figure 3b shows the drag coefficient for the same four UAV configurations. The minimum drag coefficient is obtained with zero angle of attack for retracted grids ($C_D = 0.051$) and for fully extended grids ($C_D = 0.060$). The drag increases with positive and negative values of angle of attack. This increase is slow during cruise flight conditions at low angles of attack ($-5^\circ \leq \alpha \leq 5^\circ$) in both configurations;



Fig. 2 Details of the unstructured mesh

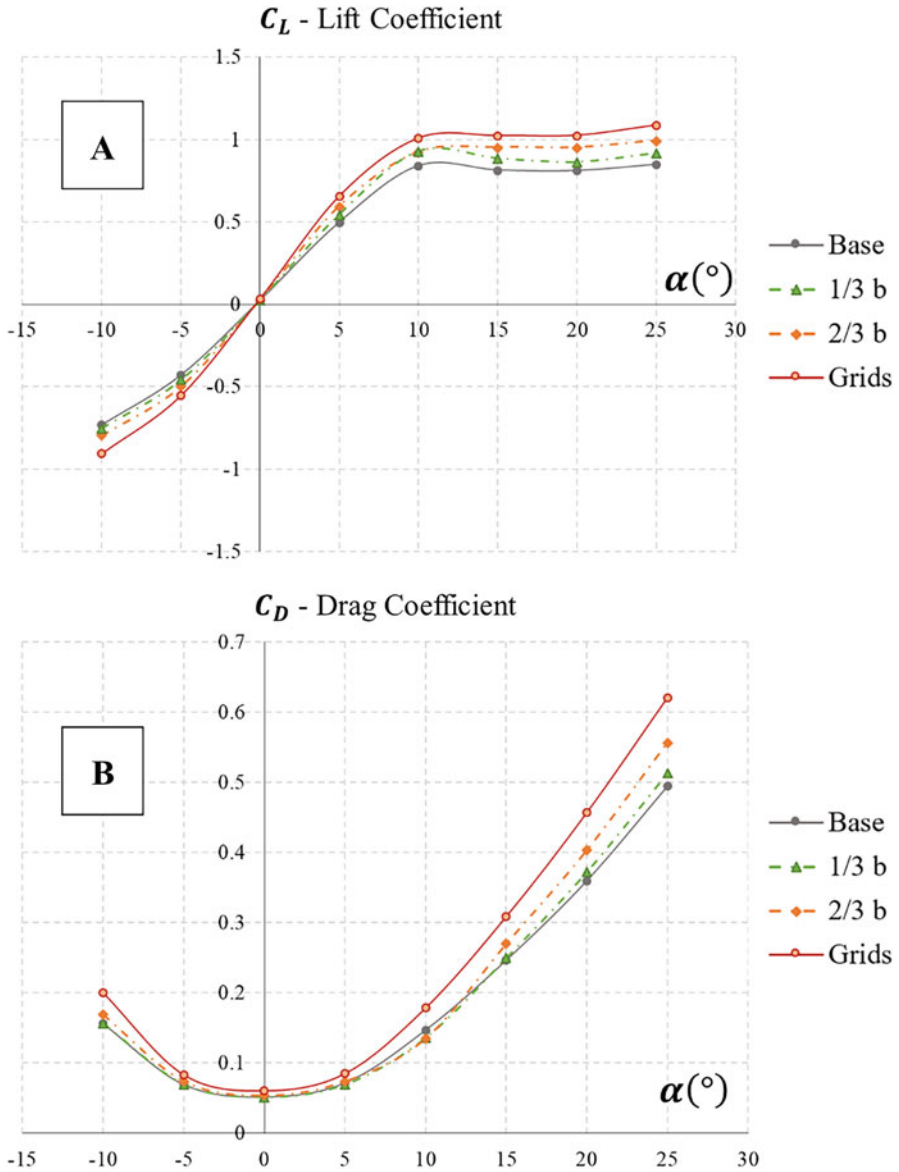


Fig. 3 (a) Lift and (b) drag coefficients for base, 1/3, 2/3, and fully extended grids

however, it gradually becomes more pronounced with higher and lower angles of attack. In addition, as the grid span increases, the drag coefficient becomes higher.

3.2 Aerodynamic Efficiency

Figure 4 shows the aerodynamic efficiency calculated as the relation between lift coefficient C_L and drag coefficient C_D under different angles of attack. It is obvious that the goal of a proper UAV design is to generate as much lift with as little drag as possible. For the angles of attack in ranges $-10^\circ \leq \alpha \leq 0^\circ$ and $\geq 15^\circ$, efficiency is practically not affected by the grids, so the UAV could operate with the grids retracted. The maximum efficiency is obtained for $\alpha = 6^\circ$. During this flight condition, which may correspond to cruise flight, the best results are obtained when grids are extended (1/3, 2/3, and full configurations). Note that for the 10° angle, the efficiency is higher when the grids are not fully extended. In summary, grids should not be used at negative or very high angles and must be fully extended in cruise phase and moderately ($b/3$ or $2b/3$) at 10° of AoA.

4 Conclusions

This paper presents a numerical study of a biomimetic UAV inspired on the primary feathers of an eagle. The configuration of the UAV has three grids at the wingtip. The effect of their span on the UAV performance has been analyzed. The results have shown that for cruise condition ($\alpha \sim 5^\circ$) the grids should be extended to improve aerodynamic efficiency up to 23%. During ascent flights with $\alpha = 10^\circ$, the grids can

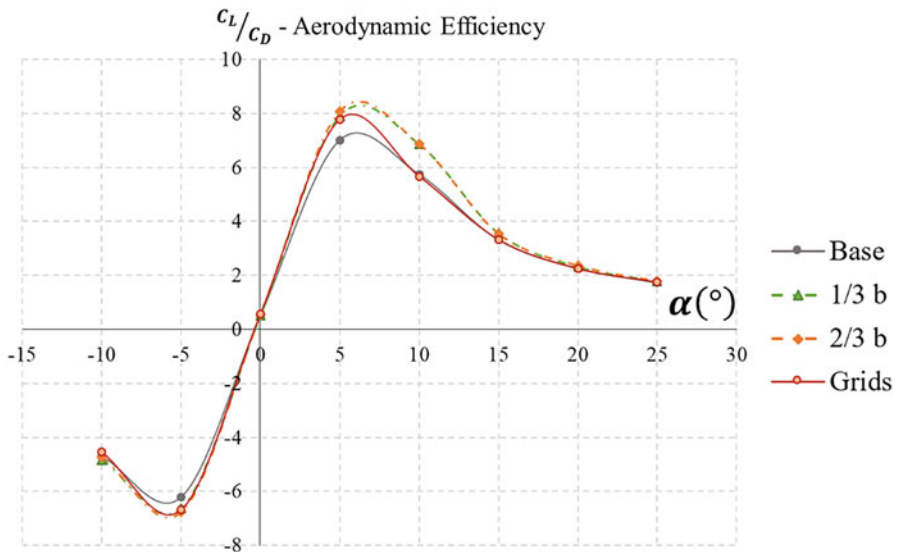


Fig. 4 Aerodynamic efficiency of the UAV with base, 1/3, 2/3, and fully extended grids

be extended in an intermediate configuration. In all other flight conditions, the grids may not be deployed because no substantial improvement in aerodynamics is seen.

References

- Han, J., Hui, Z., Tian, F., & Chen, G. (2020). Review on bio-inspired flight systems and bionic aerodynamics. *Chinese Journal of Aeronautics*, 34. <https://doi.org/10.1016/j.cja.2020.03.036>
- Rodríguez-Sevillano, A. A., Bardera-Mora, R., Barcala-Montejano, M. A., Barroso-Barderas, E., & Díez Arancibia, I. (2019). *Design of multiple winglets for enhancing aerodynamics in a micro air vehicle*. In: 8th European Conference for Aeronautics and Space Sciences (EUCASS).
- Tucker, V. (1993). Gliding birds: Reduction of induced drag by wing tip slots between the primary feathers. *Journal of Experimental Biology*, 180(1), 285–310.

Shallow Neural Networks and Turbulent Flows



Rodrigo Abadia-Heredia, Marco Crialesi-Esposito, Luca Brandt, and Soledad Le Clainche 

Nomenclature

ANN	Artificial neural network
DMD	Dynamic mode decomposition
LSTM	Long short-term memory
MAE	Mean absolute error
POD	Proper orthogonal decomposition
ROM	Reduced order model
SVD	Singular-value decomposition

R. Abadia-Heredia

E.T.S.I. Aeronáutica y del Espacio, Universidad Politécnica de Madrid, Madrid, Spain
e-mail: sr.abadia@upm.es

M. Crialesi-Esposito (✉)

FLOW Centre and SeRC, Department of Engineering Mechanics, KTH Royal Institute of Technology, Stockholm, Sweden

INFN, Sezione di Torino, Torino, Italy

e-mail: crialesi@to.infn.it

L. Brandt

Department of Energy and Process Engineering, NTNU, Trondheim, Norway

e-mail: luca@mech.kth.se

S. Le Clainche

School of Aerospace Engineering, Universidad Politécnica de Madrid, Madrid, Spain

e-mail: soledad.leclainche@upm.es

1 Introduction

In recent years, deep learning has become one of the most outstanding areas of machine learning. One reason for this is probably its impressive performance in classification problems like image classification. Consequently, the interest to apply this field to physical problems has recently grown. Indeed, it has been observed that given a data set consisting of observations from a dynamical system, deep learning architectures are able to find an approximation to this system with a high accuracy.

Deep learning is based, among others, on algorithms known as artificial neural networks (ANNs). In this research, we combine ANN architectures with dimensionality reduction techniques to design a ROM, which will be trained with data taken from simulations of air atomization (Crales-Esposito et al., 2021). This is a turbulent flow which is highly complex to analysis and simulations. The complexity of this flow motivates resorting to dimensionality reduction techniques in order to get the most meaningful dynamics of the flow and thus simplifying the training of the ANN.

2 Method

2.1 Dimensionality Reduction

ANNs are very sensitive to the data dimensionality. If the dimension is too high, bad performance on training, e.g., overfitting, low decreasing rate in gradient descent, or inability to extrapolate learning to unsampled data, may occur.

To avoid these problems, we propose to apply a dimensionality reduction while keeping the main dynamics which define the flow. In this spirit, we decided to use proper orthogonal decomposition (POD) (Sirovich, 1987), as in our recent study (Abadia-Heredia et al., 2021), to reduce the dimension of the data.

The air-atomized problem is a three-dimensional time-varying flow. Therefore, the data can be organized as a four-dimensional tensor \mathbf{T} as follows:

$$\mathbf{T} = [\mathbf{u}_1, \mathbf{u}_2, \dots, \mathbf{u}_K] \quad (1)$$

Here K is the total number of snapshots, and \mathbf{u}_i is a three-dimensional tensor containing the spatial information N_x , N_y , and N_z , respectively. To apply POD (also called singular-value decomposition, SVD), we convert the tensor \mathbf{T} into a matrix \mathbf{M} of dimension $(N_x * N_y * N_z, K)$.

SVD decomposes the matrix \mathbf{M} into three matrices: \mathbf{U} , \mathbf{S} , and \mathbf{V} , where \mathbf{U} is composed by POD modes (orthogonal in space), \mathbf{S} is a diagonal matrix formed by singular values (representing the amount of energy of each mode and its contribution to the flow field), and \mathbf{V} represents the temporal coefficients. Selecting N modes, the matrix \mathbf{M} can be reconstructed as follows:

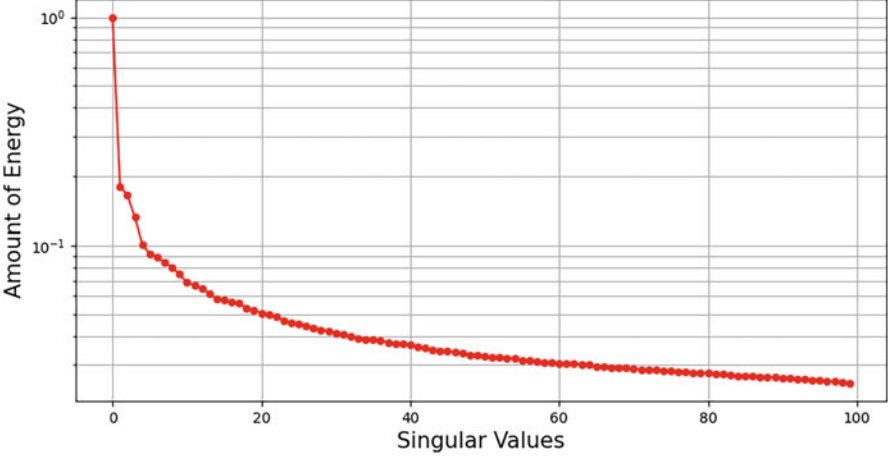


Fig. 1 Distribution of the first 100 singular values in logarithmic scale. Note that since the flow is highly turbulent, the decay of the singular values is slow

$$\widehat{\mathbf{M}} = \mathbf{U}[:, \mathbf{1} : N] \mathbf{S}[\mathbf{1} : N, \mathbf{1} : N] \mathbf{V}[:, \mathbf{1} : N]^t \quad (2)$$

with t the transpose operator. The number of retained modes, N , is chosen based on the singular values, which are sorted in a decreasing order, i.e., the first singular value is the highest and the last is the lowest. This means that the first singular values contain more information about the flow field (typically the mean flow and the large-scale structures) than the last ones, which can be small scales or noise. Figure 1 shows the first 100-singular-value decay for the air-atomized problem considered here.

In this work, we choose the first $N = 10$ modes to compute $\widehat{\mathbf{M}}$. In this context, the original data set \mathbf{T} will not be used to train the ANN; a matrix $\widehat{\mathbf{T}}$, defined as follows, will be used instead:

$$\widehat{\mathbf{T}} = \mathbf{S}[\mathbf{1} : N, \mathbf{1} : N] \mathbf{V}[:, \mathbf{1} : N]^t \quad (3)$$

Note that $\widehat{\mathbf{T}}$ has dimension $(N \times K)$. This matrix represents the temporal information (\mathbf{S}) weighted with the amount of energy of the singular values (\mathbf{V}). By using this matrix $\widehat{\mathbf{T}}$, to train the ANN, instead of \mathbf{T} we realize a huge dimensionality reduction.

2.2 Artificial Neural Network

The deep learning architecture used in this research is different than the one proposed by Abadia-Heredia et al. (2021). In this work, we train a shallow neural network, i.e., an ANN with two hidden layers: a long short-term memory layer

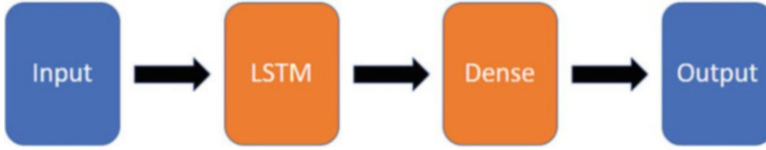


Fig. 2. Architecture of the ANN. The hidden layers are represented in orange

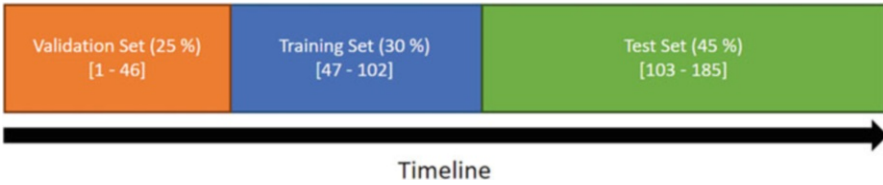


Fig. 3 Training, validation, and test set distribution. Each set shows the percentage and the number of snapshots it contains

(LSTM) (Hochreiter & Schmidhuber, 1997) and a fully connected layer (dense). Both hidden layers have 50 units/neurons. Figure 2 shows the architecture of this ANN.

This architecture is designed to use one snapshot from past to predict the next one, i.e., the ANN uses the snapshot t_n to predict the snapshot t_{n+1} . To train the ANN, the data set available from the numerical simulations needs to be split in three sets: training, validation, and test. The distribution of these sets depends on the problem. In this research, we decided to use the distribution shown in Fig. 3, where the training, validation, and test sets are composed by the 30%, 25%, and 45% of the whole data set.

3 Results and Discussion

A data set obtained from Ciralessi-Esposito et al. (2021) is used to test the hybrid model. This data set has a total number of snapshots $K = 185$. To measure the error between the original data set and the prediction from the hybrid model, we use the relative root-mean-square error (RRMSE). This measure is defined as follows:

$$\text{RRMSE} = \frac{\|M - M_{\text{ANN}}\|}{\|M\|} \quad (4)$$

Here M is the matrix obtained after reshaping the original tensor T , and the matrix M_{ANN} is the prediction obtained from the hybrid model. In this data set, choosing $N = 10$ modes, we obtained an $\text{RRMSE} = 38.64459\%$. A comparison of the

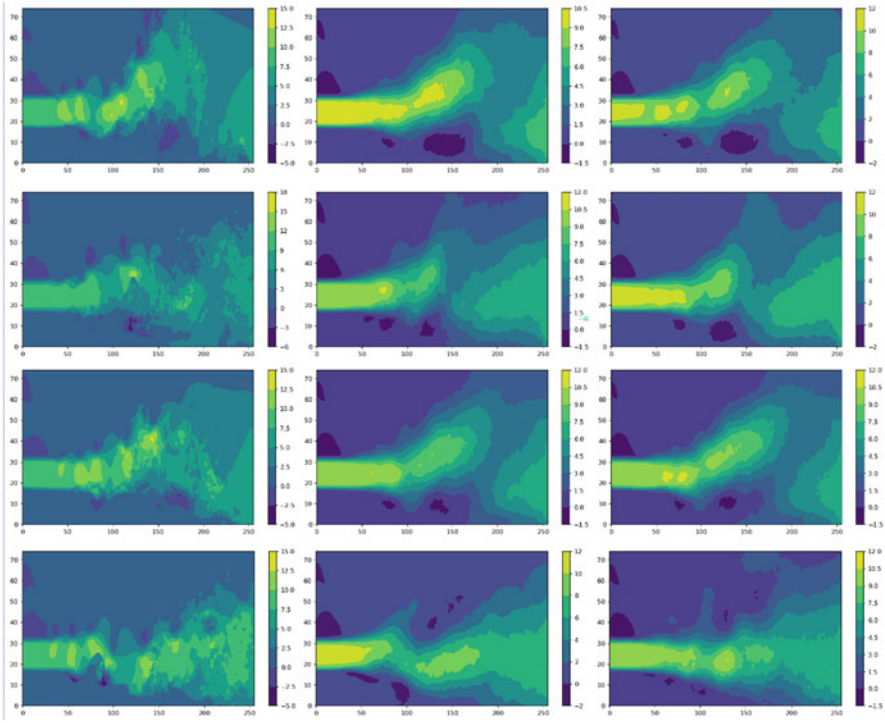


Fig. 4 From top to bottom, streamwise velocity component at timesteps: 120, 150, 170, and 183. From left to right: original data set, reconstruction performed by SVD, and prediction performed by the hybrid model

streamwise velocity component between the original data set, the SVD reconstruction selecting the first ten modes, and the prediction from the hybrid model is found in Fig. 4.

4 Conclusion

As shown in Fig. 4, the hybrid model is capable to predict the mean flow, which is the information contained in the first ten modes. However, it has problems to predict the smaller scales of the flow. As future work, we propose to select a greater number of SVD modes to compute \hat{T} (matrix used to train the ANN). This will allow the ANN to learn more about the smaller scales, which define the turbulence. In addition, different ANN architectures will be tested as another way to improve learning at smaller scales.

Acknowledgments RAH and SLC acknowledge the grant PID2020-114173RB-I00 funded by MCIN/AEI/10.13039/501100011033.

References

- Abadia-Heredia, R., Lopez-Martin, M., Carro, B., Arribas, J. I., Pérez, J. M., & Le Clainche, S. (2021). A predictive hybrid reduced order model based on proper orthogonal decomposition combined with deep learning architectures. *Expert Systems with Applications*, 187(32), 115910.
- Crialesi-Esposito, M., Pal, S., Zaleski, S., & Brandt, L. (2021). Statistical dispersion of flapping events in air-assisted atomization. *ICLASS*, 1(1). <https://doi.org/10.2218/iclass.2021.6155>
- Hochreiter, S., & Schmidhuber, J. (1997). Long short-term memory. *Neural Computation*, 9(8), 1735–1780. <https://doi.org/10.1162/neco.1997.9.8.1735>
- Sirovich, L. (1987). Turbulence and the dynamics of coherent structures. Parts I III. *Quarterly of Applied Mathematics*, 45(3), 561–571.

Data-Driven Methods Beyond Aerospace Field



Nourelhouda Groun, Beka Begiashvili, Eusebio Valero,
Jesús Garicano-Mena, and Soledad Le Clainche 

1 Introduction

There is no doubt that fluid dynamics plays a key role in plentiful scientific and industrial applications (aircrafts, wind energy, civil engineering, etc.). The ability of understanding and controlling fluid flows can significantly enhance the performance of these systems. But the very nature of fluid flow makes it very difficult to handle, since they are typically high dimensional, multiscale, and nonlinear. These difficulties have called for the intervention of data science and its various methods to offer an easier path to fluid flow understanding, modeling, and manipulation. Approaches such as deep learning (Liu et al., 2020; Yan et al., 2019), interpolation techniques (Frakes et al., 2008; Estruch et al., 2013), and data-driven methods, such as principal component analysis (PCA), are each time more used in fluid dynamics (Parente et al., 2009; Scherl et al., 2020).

N. Groun (✉)

ETSI Aeronáutica y del Espacio – Universidad Politécnica de Madrid, Madrid, Spain

ETSI Telecomunicación – Universidad Politécnica de Madrid, Madrid, Spain

e-mail: gr.nourelhouda@alumnos.upm.es

B. Begiashvili

ETSI Aeronáutica y del Espacio – Universidad Politécnica de Madrid, Madrid, Spain

e-mail: beka.begiashvili@alumnos.upm.es

E. Valero · J. Garicano-Mena

ETSI Aeronáutica y del Espacio – Universidad Politécnica de Madrid, Madrid, Spain

Center for Computational Simulation (CCS), Madrid, Spain

e-mail: eusebio.valero@upm.es; jesus.garicano.mena@upm.es

S. Le Clainche

School of Aerospace Engineering, Universidad Politécnica de Madrid, Madrid, Spain

e-mail: soledad.leclainche@upm.es

In this work, we are focusing on another fully data-driven method, the higher order dynamic mode decomposition (HODMD) (Le Clainche & Vega, 2017). This technique is an extension of the famous fluid dynamic tool, dynamic mode decomposition (DMD), which also has numerous applications in the aerospace engineering field (Schmid, 2010; Garicano-Mena et al., 2019). The HODMD method, which is solidly grounded on mathematics and computer science principles, identifies complex dynamics with outstanding denoising properties, due to the fact that HODMD uses the SVD as a primary step to filter noise and remove spatial redundancies. Furthermore, HODMD generalizes standard DMD by considering time-lagged snapshots, which allows to exploit not only the spatial redundancies but also the temporal redundancies providing higher robustness and accuracy. The HODMD algorithm has proved its efficiency on several occasions (Le Clainche et al., 2017, 2019). These achievements have motivated us to test the applicability of this technique on more complex and novel problems: (i) a compressible, turbulent jet flow and (ii) medical imaging problems. By addressing these problems and multidisciplinary character, we show that this technique is highly efficient and versatile, so it can be easily adapted to solve any kind of problems, not to mention another employment area of these data-driven methods with a lot of potential for applicability, which is unmanned aerial vehicles (UAVs). There are numerous promising applications, which have been carried out so far, such as aerodynamic wing optimization (Poole et al., 2015), modeling stall lift robustness design (Wang et al., 2018) even studying the effect of propeller position on the pressure and friction coefficients over the wing of an UAV (Serrano et al., 2022). Furthermore, in these systems, it is of vital importance to analyze flight stability and control (Chelaru & Pana, 2010), and the HODMD algorithm is capable of reducing computational complexity in real-time control and stability analysis for UAV systems.

The rest of the paper will be organized as follows: in Sect. 2, the HODMD methodology will be introduced. Section 3 will present the datasets used and the different results obtained, and Sect. 4 will hold the conclusions.

2 Method

In this section, we introduce the HODMD (Le Clainche & Vega, 2017) technique, which is a more robust extension of DMD (Schmid, 2010), mainly used to analyze noisy experimental data, nonlinear dynamical systems, and complex flows. The data collected are organized in a matrix form as follows:

$$\mathbf{V}_1^K = [\mathbf{v}_1, \mathbf{v}_2, \dots, \mathbf{v}_k, \dots, \mathbf{v}_K] \quad (1)$$

where \mathbf{v}_k is a snapshot collected at time t_k , with $k = [1, \dots, K]$. Similarly to DMD, HODMD decomposes the signal into an expansion of M modes \mathbf{u}_m , and each mode has his own amplitude a_m , frequency ω_m , and growth rate δ_m as follows:

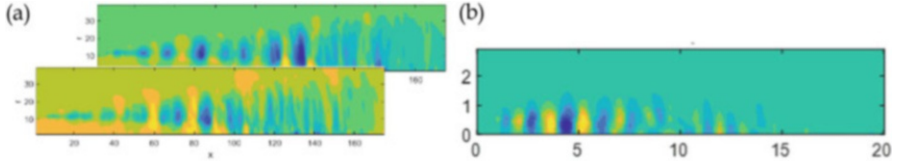


Fig. 1 Dominant spatiotemporal structures obtained by HODMD on a pressure field of a turbulent jet flow; (a) Flow field instantaneous two consecutive snapshots, (b) HODMD mode at $St = 0.44$

$$\mathbf{v}(t) \simeq \sum_{m=1}^M \mathbf{a}_m \mathbf{u}_m e^{(\delta_m + i\omega_m)(t - t_1)} \text{ for } t_1 \leq t \leq t_1 + T. \quad (2)$$

The HODMD algorithm follows two main steps to construct the expansion defined in Eq. (2), which are explained in detail in Le Clainche and Vega (2017).

3 Material and Results

3.1 Jet Data

This database is formed by an axisymmetric pressure field of a turbulent jet at Reynolds number¹ $Re_D = 10^6$ and Mach number² $Ma = 0.4$, with a time step of $\Delta t = 0.2s$ between snapshots. This dataset was generated and used in Towne et al. (2018), and it contains 5000 snapshots with 39×175 grid points.

Here, HODMD is used to identify dominant spatiotemporal features from the turbulent flow and to detect the dominant Strouhal number of the flow.

In this case, the dataset comes from a turbulent flow, where HODMD is able to detect dominant spatiotemporal features, since HODMD has good performance with datasets from complex and noisy flows. Figure 1a shows the flow instantaneous snapshots, whereas Fig. 1b shows the spatial structure, or HODMD mode. It is important to mention that HODMD also extracts the damping rate for each mode, which gets more importance when transient phenomenon takes place in the flow.

¹Reynolds number is the ratio between inertial and viscous forces in a fluid flow:

$$Re = \frac{uD}{\nu}$$

where u is the flow speed, D is a characteristic dimension, and ν is the kinematic viscosity of the fluid.

²Mach number is the ratio between flow velocity and local speed of sound:

$$M = \frac{u}{c}$$

where u is the flow speed and c is the speed of sound in the given fluid.

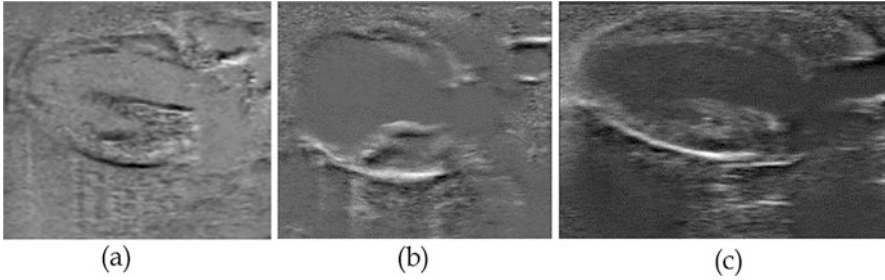


Fig. 2 DMD modes provided by the HODMD algorithm, representing the main patterns of hearts in different health conditions: (a) healthy, (b) myocardial infarction, and (c) TAC hypertrophy

3.2 Medical data

The database is composed of six echocardiography datasets: one representing a healthy heart and five more corresponding to different cardiac diseases. Each dataset consists of up to 300 snapshots with a resolution of $896 \times 1208 \times 3$ and a temporal distance $\Delta t = 4 \times 10^{-3}s$.

HODMD was used as a feature extraction technique to analyze a maximum number of 200 snapshots of each dataset. As shown in Fig. 2, despite the limited number of snapshots, the HODMD algorithm was able to identify and extract the main patterns and features related to different cardiac diseases and represent them in sets of DMD modes. These modes show the shape of a healthy heart as well as its shape in certain unhealthy conditions, such as the myocardial wall deformation in the myocardial infarction dataset (Fig. 2b) and the circular shape of the heart in the hypertrophic hearts (Fig. 2c). Detailed explanation about the data and more results can be found in our recently published paper (Groun et al., 2022).

4 Conclusion

In this work, we describe the application of the HODMD technique on two distinct datasets to showcase the efficiency and robustness of this technique in fields besides aerospace field. The HODMD was first used on a turbulent jet flow in order to extract the most important spatiotemporal structures, where other methodologies might have more difficulties because of the given turbulent multiscale characteristics of the flow. The proposed technique is also tested on a completely new field, which is the medical field. The HODMD algorithm was used to analyze echocardiography datasets, where it was able to extract the dominant patterns related to different cardiac diseases in a set of DMD modes. This will be used to classify the different cardiac diseases using convolutional neural networks (CNNs). The different results obtained from applying HODMD on both datasets have shown once again the ability of the proposed technique in functioning very well in different fields and handling

diverse datasets. HODMD applications expand to many areas, such as UAVs, due to the possibility it offers to detect spatiotemporal patterns of complex and turbulent flows, in real time. In UAV systems, flight stability and control take on great importance, where HODMD can take center stage.

Acknowledgments The authors would like to recognize doctors María Villalba-Orero and Enrique Lara-Pezzi from the Centro Nacional de Investigaciones Cardiovasculares (CNIC), for providing the medical data used in this work. SLC acknowledges the grant PID2020-114173RB-I00 funded by MCIN/AEI/10.13039/501100011033. This publication is part of the project TED2021-129774B-C21, funded by MCIN/AEI/10.13039/501100011033 and by the European Union “NextGenerationEU”/PRTR.

References

- Chelaru, T. V., & Pană, V. (2010). Stability and control of the UAV formations flight. *WSEAS Transactions on Systems and Control*, 5(1), 26–36.
- Estruch, O., Lehmkuhl, O., Borrell, R., Segarra, C. P., & Oliva, A. (2013). A parallel radial basis function interpolation method for unstructured dynamic meshes. *Computers & Fluids*, 80, 44–54.
- Frakes, D. H., et al. (2008). Modified control grid interpolation for the volumetric reconstruction of fluid flows. *Experiments in Fluids*, 45(6), 987–997.
- Garicano-Mena, J., Li, B., Ferrer, E., & Valero, E. (2019). A composite dynamic mode decomposition analysis of turbulent channel flows. *Physics of Fluids*, 31(11), 115102.
- Groun, N., et al. (2022). Higher order dynamic mode decomposition: From fluid dynamics to heart disease analysis. *Computers in Biology and Medicine*, 144, 105384.
- Le Clainche, S., & Vega, J. M. (2017). Higher order dynamic mode decomposition. *SIAM Journal on Applied Dynamical Systems*, 16(2), 882–925.
- Le Clainche, S., Vega, J. M., & Soria, J. (2017). Higher order dynamic mode decomposition of noisy experimental data: The flow structure of a zero-net-mass-flux jet. *Experimental Thermal and Fluid Science*, 88, 336–353.
- Le Clainche, S., Han, Z. H., & Ferrer, E. (2019). An alternative method to study cross-flow instabilities based on high order dynamic mode decomposition. *Physics of Fluids*, 31(9), 094101.
- Liu, B., Tang, J., Huang, H., & Lu, X. Y. (2020). Deep learning methods for super-resolution reconstruction of turbulent flows. *Physics of Fluids*, 32(2), 025105.
- Parente, A., Sutherland, J. C., Tognotti, L., & Smith, P. J. (2009). Identification of low-dimensional manifolds in turbulent flames. *Proceedings of the Combustion Institute*, 32(1), 1579–1586.
- Poole, D. J., Allen, C. B., & Rendall, T. (2015). Free-form aerodynamic wing optimization using mathematically-derived design variables. In 16th AIAA/ISSMO multidisciplinary analysis and optimization conference (p. 2491).
- Scherl, I., et al. (2020). Robust principal component analysis for modal decomposition of corrupt fluid flows. *Physical Review Fluids*, 5(5), 054401.
- Schmid, P. J. (2010). Dynamic mode decomposition of numerical and experimental data. *Journal of Fluid Mechanics*, 656, 5–28.
- Serrano, J. R., García-Cuevas, L. M., Bares, P., & Varela, P. (2022). Propeller position effects over the pressure and friction coefficients over the Wing of an UAV with distributed electric propulsion: A proper orthogonal decomposition analysis. *Drones*, 6(2), 38.

- Towne, A., Schmidt, O. T., & Colonius, T. (2018). Spectral proper orthogonal decomposition and its relationship to dynamic mode decomposition and resolvent analysis. *Journal of Fluid Mechanics*, *847*, 821–867.
- Wang, X., Wang, S., Tao, J., Sun, G., & Mao, J. (2018). A PCA–ANN-based inverse design model of stall lift robustness for high-lift device. *Aerospace Science and Technology*, *81*, 272–283.
- Yan, X., Zhu, J., Kuang, M., & Wang, X. (2019). Aerodynamic shape optimization using a novel optimizer based on machine learning techniques. *Aerospace Science and Technology*, *86*, 826–835.

Modeling and Simulation of Double-Acting Hydropneumatic Suspension System for 6×6 Terrain Vehicle with Different Performance Parameters



Kaan Berke Ulusoy, Bensu Değirmenci, Derin Türedi, Erkin Filiz, Mustafa Karaman, and Erhan İlhan Konukseven

Nomenclature

m_{us}	Unsprung mass, 400 [kg]
m_s	Sprung mass, 1200 [kg]
A_{v1}, A_{v2}	Orifice area, 0.3×10^{-4} [m ²]
A_{pis}	Piston area, 0.007 [m ²]
V_{30}, V_{40}	Accumulator gas volume, 0.0045 [m ³], 0.0010 [m ³]
A_r	Rod area, 0.0042 [m ²]
A_{pr}	Area between the rod and piston, 0.0028 [m ²]
l_{arm}	Suspension connection arm length, 0.8 [m]
l_{susp}	Suspension arm length, 0.316 [m]
l_{cons}	Distance between the connection of piston and arm rod with sprung mass, 0.917 [m]
$k_{t\text{spring}}$	Tire stiffness, 800,000 $\frac{N}{m}$
β	Angle between l_{cons} and lateral axis
z_s	Sprung mass displacement
z_{us}	Unsprung mass displacement

K. B. Ulusoy (✉) · B. Değirmenci · E. Filiz
Middle East Technical University, Ankara, Türkiye

Hidroan Ankara Hidrolik, Ankara, Türkiye
e-mail: kaan.ulusoy@metu.edu.tr; bensu.degirmenci@metu.edu.tr; erkin.filiz@metu.edu.tr

D. Türedi · E. İ. Konukseven
Middle East Technical University, Ankara, Türkiye
e-mail: derin.turedi@metu.edu.tr; konuk@metu.edu.tr

M. Karaman
Hidroan Ankara Hidrolik, Ankara, Türkiye
e-mail: mkaraman@hidroan.com.tr

θ_{arm}	Angle between suspension arm and longitudinal axis
h_0	Distance from highest point of the arm to the ground
D_{susp}	Suspension displacement

1 Introduction

Suspension systems are used to connect the vehicle chassis to the wheel hub. Their two main functions are to provide ride comfort for passengers and ensure contact between the tire and the road. The two most important performance metrics are ride comfort and traction conflict stability. While passive suspension systems are simple and cost-effective, designing them presents a remarkable challenge for engineers as they have to choose between two metrics. This problem becomes more apparent for vehicles with very different loading conditions, such as trucks or military vehicles. Hydropneumatic suspensions are developed to resolve this issue while keeping the simplicity of passive suspensions. Even though costs are higher than passive systems, they are commonly used in heavy vehicles where their advantages meet their costs (Sağlam & Ünlüsoy, 2014). Pressurized gas is used in hydropneumatic suspension systems instead of a mechanical spring to temporarily store energy. The energy dissipation function is realized by feeding pressurized oil into an orifice. Compression of gases is inherently nonlinear, so under increasing loading conditions, the spring becomes stiffer, thus stabilizing the suspension system (Bauer, 2011).

A single-acting suspension system for the vehicle shown in Fig. 1a is studied (Kocakulak et al., 2019). Although single-acting systems are simpler, double-acting systems have superior performance. In this study, a double-acting hydropneumatic suspension system is modeled. The suspension system shown in Fig. 1b is placed between the suspension arm and the sprung mass. With this configuration, forces acting on the structure increase, but mobility also increases significantly as the piston's stroke decreases.

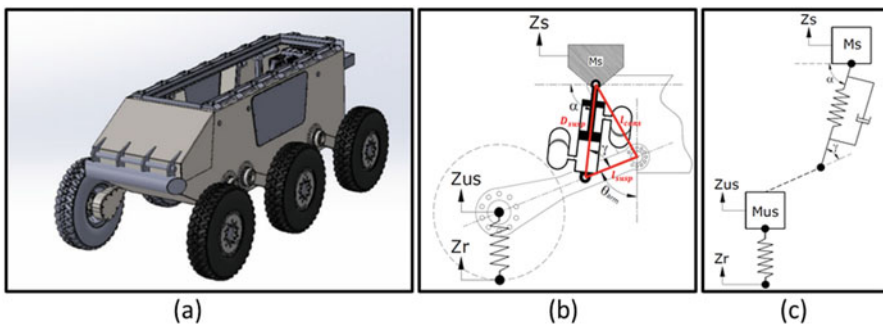


Fig. 1 (a) 6×6 rough terrain vehicle, (b) kinematic relation of hydropneumatic suspension, and (c) simplified kinematic relationship of suspension system

Since wheels planned to be used for the vehicle (14.00R20) are significantly larger than passenger vehicles', the effects of tire kinematics are much more evident. Therefore, in addition to hydropneumatic suspension, tire stiffness is also included in the model.

2 Double-Acting Hydropneumatic Suspension System Model

The model is designed to study system behavior and develop control algorithms. Previous work on quarter car models in the literature models the suspension as directly connected to the vehicle chassis and wheel and does not include the kinematic effects of suspension structures. The vehicle shown in Fig. 1a has a different suspension configuration than conventional ones. A hydropneumatic cylinder is attached to an arm connecting the vehicle chassis and wheel. Independent motion of all six wheels is possible, and the stroke of the piston is decreased to increase overall mobility.

To keep the model simple, the dynamic effects of connection elements are neglected. The model has two degrees of freedom: position of unsprung and sprung mass. Road profile (displacement of the bottom point of the tire) is used as an input for the dynamic model.

2.1 Kinematic Relationships

The suspension system is attached to the arm, as shown in Fig. 1a, c. Therefore, the compression, that suspension undergoes, is affected by both displacements of sprung (z_s) and unsprung (z_{us}) masses. Compression of suspension can be calculated using θ_{arm} which is related to both z_s and z_{us} . The relation is described in Eq. (1):

$$\cos \theta_{\text{arm}} = \frac{z_s - z_{us} + h_0}{l_{\text{arm}}} \quad (1)$$

After angle θ_{arm} is calculated, it is possible to determine the suspension's compression with the cosine theorem Eq. (2) that is applied to the connection points of the hydropneumatic cylinder, arm, and chassis as shown in Fig. 1b. Also, by differentiating the displacements, velocities of sprung and unsprung masses are obtained:

$$D_{\text{susp}}^2 = l_{\text{susp}}^2 + l_{\text{cons}}^2 - 2l_{\text{susp}}l_{\text{cons}} \cos(\beta + 90 - \theta_{\text{arm}}) \quad (2)$$

As demonstrated in Fig. 1c, suspension forces act with different angles on sprung and unsprung masses. These angles are calculated using θ_{arm} (3, 4):

$$\sin \gamma = \frac{l_{\text{cons}} \sin(\beta + 90 - \theta_{\text{arm}})}{D_{\text{susp}}} \quad (3)$$

$$\alpha = 90 - \theta_{\text{arm}} + \gamma \quad (4)$$

2.2 Equation of Motion and Free Body Diagrams of the Unsprung and Sprung Masses

Equation of motion of the unsprung mass (Fig. 2):

$$\begin{aligned} + \uparrow \sum F_z = m_{\text{us}} \ddot{z}_{\text{us}} &\Rightarrow F_{\text{tspring}} - m_{\text{us}} g - F_{\text{susp}} \sin \gamma = m_{\text{us}} \ddot{z}_{\text{us}} \\ &\Rightarrow k_{\text{tspring}} (z_r - z_{\text{us}}) - m_{\text{us}} g - F_{\text{susp}} \sin \gamma = m_{\text{us}} \ddot{z}_{\text{us}} \end{aligned} \quad (5)$$

Suspension force F_{susp} consists of F_{spring} and F_{damper} . Force F_{tspring} is the force exerted by the tire (1400R20). Spring characteristic is obtained from similar work presented in the literature (Luty & Simiński, 2008). The center of gravity of unsprung mass is assumed to be at the center. Equation of motion of the sprung mass is:

$$+ \uparrow \sum F_z = m_s \ddot{z}_s \Rightarrow F_{\text{spring}} \sin(\alpha) + F_{\text{damper}} \sin(\alpha) - m_s g = m_s \ddot{z}_s \quad (6)$$

Relation between pre-charge pressures P_{30} and P_{40} is established in Eq. (7). Pressure P_{40} is calculated considering vehicle mass with the parameters presented at (Sağlam, 2016):

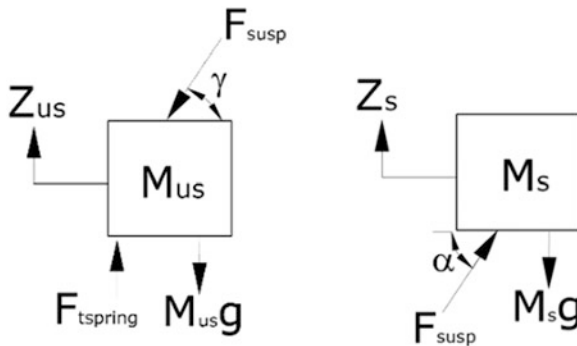


Fig. 2 Free body diagram of the unsprung and sprung masses

$$P_{30} = \left(\frac{m_s g}{\sin(\alpha)} + \left(\frac{(P_{40} + P_{\text{atm}})A_{\text{fp}} - M_{\text{fp}}g}{A_{\text{fp}}} \right) A_{\text{pr}} \right) \frac{A_{\text{fp}}}{A_{\text{pis}}} - M_{\text{fp}}g \Big) A_{\text{fp}} + P_{\text{atm}} \quad (7)$$

The stiffness of the spring is dependent on the pre-charge pressures of accumulators (P_{30} , P_{40}), initial gas volumes V_{30} , V_{40} , and the area between the piston and rod A_{pr} . Stiffness can be obtained as:

$$k_{\text{spring}} = \frac{A_{\text{pis}}^2 P_{30} V_{30}^k k}{(V_{30} + A_{\text{pis}}(z_s - z_{\text{us}}))^{k+1}} + \frac{A_{\text{pr}}^2 P_{40} V_{40}^k k}{V_{40} - A_{\text{pr}}(z_s - z_{\text{us}})^{k+1}} \quad (8)$$

The spring force can be obtained using spring stiffness (Joo, 1991). The static compression amount is also added to the dynamic response equation. Damping force F_{damper} results from the velocity difference between sprung and unsprung masses. Damping force can be altered by changing the diameters of two orifices. The relation between damping force and orifice diameters is established in Eq. 9 (Reddy et al., 2014):

$$F_{\text{damper}} = A_{\text{pis}} \left(\frac{A_{\text{pis}}(\dot{z}_s - \dot{z}_{\text{us}})}{C_d A v_2} \right)^2 \frac{\rho}{2} \times \text{sign}(\dot{z}_p - \dot{z}_{\text{us}}) + A_{\text{pr}} \times \left(\frac{A_{\text{pr}}(\dot{z}_s - \dot{z}_{\text{us}})}{C_d A v_1} \right)^2 \frac{\rho}{2} \text{sign}(\dot{z}_p - \dot{z}_{\text{us}}) \quad (9)$$

3 Simulation Results

The dynamic model of double-acting suspension is simulated for different pre-charge pressures and orifice areas in order to study the effects of these parameters on sprung mass motion. As inputs, a road profile with a single bump of 10 cm height is supplied to the system while cruising at 20 km/h speed (Hassaan, 2014).

As a measure of performance, the position RMS values were calculated by considering the difference between the reference road profile and the position of the sprung mass. On the other hand, while calculating the acceleration RMS values, the reference is taken as zero in order to evaluate ride comfort, and the RMS values are shown in Table 1. The deviation of position decreases as the pre-charge pressure increases, while the deviation of acceleration has a positive correlation with the pre-charge pressure. The reduction in orifice opening increases the damping of the system and results in a less oscillatory behavior. Table 1 supports this argument as the position RMS value gets relatively smaller when orifice area decreases, and as it can be seen in Fig. 3b, the sprung mass can follow the road profile more closely. ISO-2631-1 (International Organization for Standardization, 1997) indicates that

Table 1 RMS values of suspension displacement and acceleration with respect to different pre-charge pressures and different orifice openings

Orifice opening [m ²]	RMS value	Pre-charge pressure [bar]			
		12	25	35	40
$A_{v1}, A_{v2} = 1.26 \times 10^{-5}$	Position [m]	0.0052	0.0048	0.0045	0.0044
	Acceleration [m/s ²]	0.8238	0.8349	0.8450	0.8502
$A_{v1}, A_{v2} = 1.96 \times 10^{-5}$	Position [m]	0.0080	0.0072	0.0067	0.0065
	Acceleration [m/s ²]	0.6724	0.6945	0.7118	0.7192
$A_{v1}, A_{v2} = 3 \times 10^{-5}$	Position [m]	0.0103	0.0093	0.0086	0.0083
	Acceleration [m/s ²]	0.5534	0.5890	0.6135	0.6234
$A_{v1}, A_{v2} = 3.85 \times 10^{-5}$	Position [m]	0.0120	0.0110	0.0103	0.0100
	Acceleration [m/s ²]	0.4915	0.5394	0.5731	0.5875

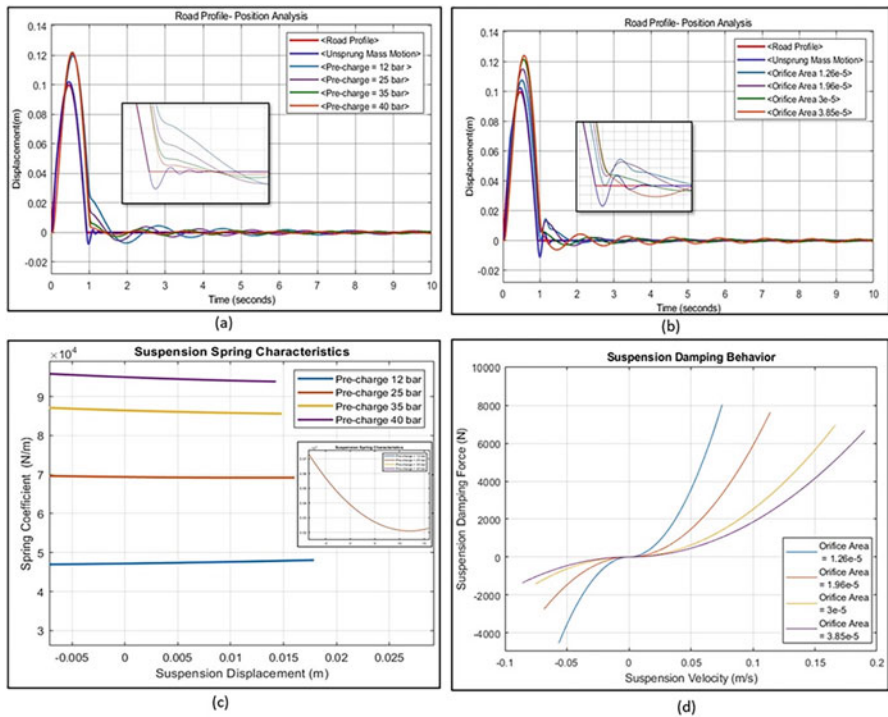


Fig. 3 Behavior of hydropneumatic suspension system for 6 × 6 vehicle

RMS values of acceleration greater than 1.25 m/s² are very uncomfortable. As it can be seen from Table 1, the RMS acceleration values obtained in this study are below that threshold.

Spring stiffness reaches the minimum point (Fig. 3c) for a specific amount of suspension compression which depends on the pre-charge pressures and initial gas volumes. After that, spring stiffness increases whether suspension is compressed

further or decompressed. This behavior is the most distinct and apparent superiority of double-acting systems over single-acting ones. Damping force with respect to the system's velocity is presented in Fig. 3d (Oscarsson, 2015).

4 Conclusion

Double-acting hydropneumatic suspension system with two DOFs is modeled using MATLAB/Simulink software. The dynamic response of the model is studied for a set of different parameter values. Effects of spring and damping forces are examined. The RMS values for both position and acceleration under different system specifications are obtained. The ride comfort, traction stability, and overall ride performance of 6×6 vehicles can be improved using this system. Parameter optimization can be performed in the future, and it is also possible to develop controllers for more advanced features such as rollover prevention using this model.

References

- Bauer, W. (2011). *Hydropneumatic suspension systems* (pp. 19–66). Springer.
- Hassaan, G. A. (2014). Car dynamics using quarter model and passive suspension, part I: Effect of suspension damping and car speed. *International Journal of Computer Techniques*, 1(2), 1–9.
- International Organization for Standardization [ISO] (Geneva). (1997). Mechanical vibration and shock-evaluation of human exposure to whole-body vibration-Part 1: General requirements (2631–1).
- Joo, F. R. (1991). Dynamic analysis of a hydropneumatic suspension system (Doctoral dissertation). Concordia University.
- Kocakulak, T., Çokgünlü, S. A., & Konukseven, E. İ. (2019, September). 6×6 Taktik Tekerlekli Askeri Kara Platformu Üzerinde Kullanılacak Hidropnömatik Süspansiyon Sisteminin Modellenmesi ve Sistem Elemanlarının Sönümlemeye Etkisinin İncelenmesi. In International symposium on automotive science and technology (pp. 99–110).
- Luty, W., & Simiński, P. (2008). Analiza sprężystości promieniowej ogumienia 14.00 R20 z wkładką typu RUN-FLAT. *Czasopismo Techniczne. Mechanika*, 105(6-M), 131–138.
- Oscarsson, M. (2015). *A hydropneumatic suspension parameter study on heavy multi-axle vehicle handling*. Royal Institute of Technology.
- Reddy, C. V., Shankapal, S. R., & Gowda, M. H. (2014). Modelling and simulation of hydropneumatic suspension for a car. *SASTech-Technical Journal of RUAS*, 13(1), 24–30.
- Sağlam, F. (2016). *Optimization of ride comfort for vehicles equipped with passive and active hydropneumatic suspensions*. Middle East Technical University.
- Sağlam, F., & Ünlüsoy, Y. S. (2014). Hidro-Pnömatik Süspansiyonlu Araçlar İçin Tümleşik Sürüş Konforu ve Yükseklik Kontrolü. *OTEKON*, 14(7), 26–27.

Inspection of Welding Joints Using Topological Derivative Methods



Sergio Muñoz and María-Luisa Rapún

1 Introduction

Inspection of welding joints is an unavoidable process to guarantee safety in steel structures in many manufacturing processes in the automotive and aeronautical industries. These inspection processes should be very robust because small defects in welding joints might result in cracking or breaking the joint during its use over time.

The present work is framed within the field of mathematical engineering for the defence industry. Our main goal is to develop new mathematical tools for the treatment of data obtained in ultrasonic tests, aiming to improve the manufacturing and inspection processes presently used in the defence industry.

2 Inspection of Welding Joints in Defence Vehicles

Every defence vehicle has a main structure called hull, which is assembled by a lower structure (lower hull) and an upper structure (upper hull); see Fig. 1. All welding joints in the hull are considered critical welding joints, so it is necessary to guarantee that they are free of defects.

In this work, we will focus on the welding joint that joins the roof plate (yellow plate in Fig. 2) with the upper side plate (orange plate).

Standard acquisition systems presently used in the industry consist of locating 60 sensors (which can act as both emitters and receivers) in the opposite side of the

S. Muñoz · M.-L. Rapún (✉)
Universidad Politécnica de Madrid, Madrid, Spain
e-mail: marialuisa.rapun@upm.es

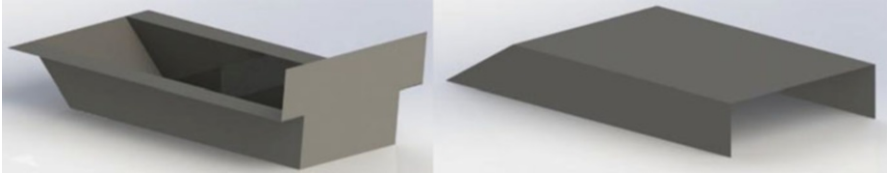


Fig. 1 Parts of the hull. Left: lower hull. Right: upper hull

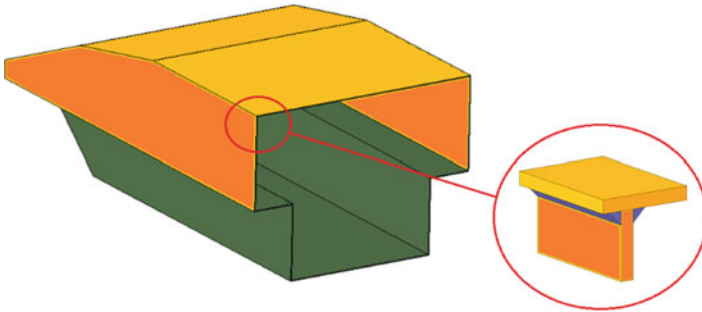


Fig. 2 Example of a welding joint

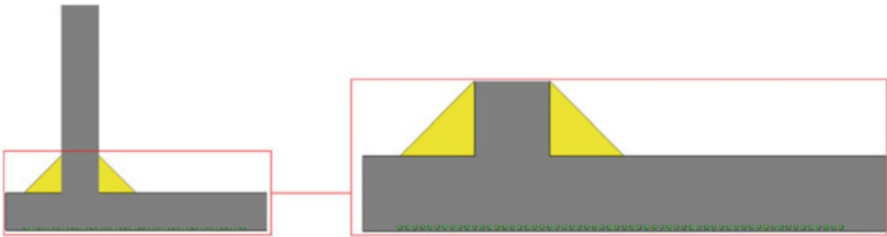


Fig. 3 Location of the sensors for the inspection of the welding joints

welding joint to be inspected, as sketched in Fig. 3, where the welding joints are the yellow regions and green points indicate the location of the sensors.

There are three regions to be considered in the welding process of two plates: the original plates made of the base material (grey colour in Fig. 4), the region with the filler material (yellow region in Fig. 4, left) and the contact region between the former two ones, consisting of base material and filler material (red region). Figure 4, right, shows the welding joint dimensions (in millimetres) for the joint which will be considered for the numerical experiments in Sect. 3.

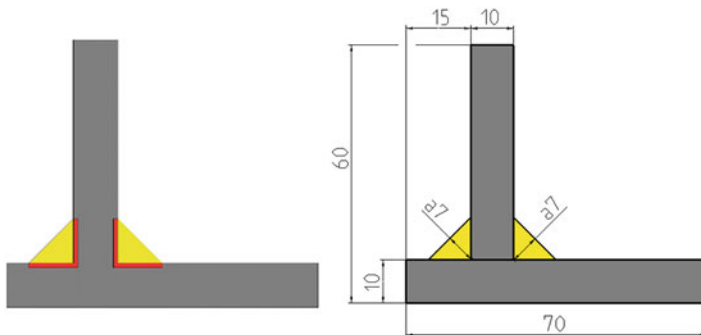


Fig. 4 Left: welding joint regions. Right: welding joint dimensions

3 Mathematical Formulation and Inversion Algorithm

Our aim is to find the number n and location of the defects $D = \bigcup_{i=1}^n D_i$ for which the received signal at the receivers located at the positions $\mathbf{x}_1, \dots, \mathbf{x}_{N_{\text{rec}}}$ is the same as the measured data at the same positions. If we denote by $p_{\mathbf{x}_s, \omega}^{\text{meas}, r}$ the measured acoustic pressure at the r th receiver when the medium is excited from an emitter located at \mathbf{x}_s at a given frequency ω and $p_{\mathbf{x}_s, \omega}^D(\mathbf{x}_r)$ is the acoustic pressure that would be measured at the receiver located at \mathbf{x}_r when the defects are D , then we aim to find the defects D for which the following identities hold:

$$p_{\mathbf{x}_s, \omega}^D(\mathbf{x}_r) = p_{\mathbf{x}_s, \omega}^{\text{meas}, r}, \quad r = 1, \dots, N_{\text{rec}} \text{ with } r \neq s, \quad (1)$$

where $p_{\mathbf{x}_s, \omega}^D$ is the solution to the forward problem

$$\Delta p_{\mathbf{x}_s, \omega}^D + \frac{\omega^2}{c^2} p_{\mathbf{x}_s, \omega}^D = \delta_{\mathbf{x}_s} \text{ in } \Omega \setminus \bar{D}; \quad \mathbf{n} \cdot \nabla p_{\mathbf{x}_s, \omega}^D = 0 \text{ on } \partial\Omega \cup \partial D, \quad (2)$$

where c is a piecewise constant wave speed that could take three different values in the regions of the welding joint Ω and where $\delta_{\mathbf{x}_s}$ is the Dirac delta distribution.

Since the formulation (1) is too restrictive and the problem is severely ill-posed, we reformulate it in a weaker form: find the defects D that minimize the cost functional:

$$J_{\mathbf{x}_s, \omega}(\Omega \setminus \bar{D}) := \frac{1}{2} \sum_{r=1; r \neq s}^{N_{\text{rec}}} |p_{\mathbf{x}_s, \omega}^D(\mathbf{x}_r) - p_{\mathbf{x}_s, \omega}^{\text{meas}, r}|^2 \quad (3)$$

where $p_{\mathbf{x}_s, \omega}^D$ is the solution to the forward problem (2). When each sensor can act as an emitter and as a receiver and in addition tests corresponding to different frequencies $\omega_1, \dots, \omega_{N_{\text{rec}}}$ are performed, then we will consider the cost function:

$$J(\Omega \setminus \bar{D}) := \sum_{m=1}^{N_{\text{rec}}} \alpha_m J_{\omega_m}(\Omega \setminus \bar{D}) \quad \text{with } J_{\omega} := \sum_{s:=1}^{N_{\text{rec}}} J_{x_s, \omega} \quad (4)$$

where the weights α_m are selected as in Funes et al. (2016).

To solve this constrained optimization problem, we propose to use the topological derivative concept (first introduced in Sokolowski and Zochowski (1999) as a measure of the sensitivity to infinitesimal perturbations) to design an indicator function able to classify each point of the joint as belonging to the filler region or to a defect. Our proposal is to evaluate the topological derivative D_T in a region R where the defects are searched (in our case, R is union of the regions represented in yellow and red colours in Fig. 4, left) and to identify the region where the largest negative values are attained. Then, our approximated damaged region is defined as:

$$D_c := \{\mathbf{x} \in R \text{ such that } D_T(\mathbf{x}) < (1 - C) \min_{\mathbf{y} \in R} D_T(\mathbf{y})\} \quad (5)$$

where $0 < C < 1$ is a constant to be calibrated. In our examples, we select $C = 0.1$.

A closed-form expression of the topological derivative D_T^{ω} of the cost function J_{ω} defined in (4) is derived in Muñoz and Rapún (2023):

$$D_T^{\omega}(\mathbf{x}) := \text{Re} \left[\frac{\omega^2}{c(\mathbf{x})^2} p_{x_s, \omega}^{\otimes}(\mathbf{x}) p_{x_s, \omega}^{\text{adj}}(\mathbf{x}) - 2 \nabla p_{x_s, \omega}^{\otimes}(\mathbf{x}) \cdot \nabla p_{x_s, \omega}^{\text{adj}}(\mathbf{x}) \right] \quad (6)$$

where $p_{x_s, \omega}^{\otimes}$ is the solution to the problem:

$$\Delta p_{x_s, \omega}^{\otimes} + \frac{\omega^2}{c^2} p_{x_s, \omega}^{\otimes} = \delta_{x_s} \quad \text{in } \Omega; \quad \mathbf{n} \cdot \nabla p_{x_s, \omega}^{\otimes} = 0 \quad \text{on } \partial \Omega, \quad (7)$$

while $p_{x_s, \omega}^{\text{adj}}$ is the solution to the adjoint problem:

$$\Delta p_{x_s, \omega}^{\text{adj}} + \frac{\omega^2}{c^2} p_{x_s, \omega}^{\text{adj}} = \sum_{r=1, r \neq s}^{N_{\text{rec}}} (p_{x_s, \omega}^{\text{meas}, r} - p_{x_s, \omega}^{\otimes}) \delta_{x_r} \quad \text{in } \Omega; \quad \mathbf{n} \cdot \nabla p_{x_s, \omega}^{\text{adj}} = 0 \quad \text{on } \partial \Omega. \quad (8)$$

4 Results

We have tested several challenging situations where different defects were placed either at the left or the right welding joints sketched in Fig. 4. We observed that due to the location of the sensors, the left joint is the most demanding one, and for brevity, defects will be placed inside this joint. In all the forthcoming figures, the first plot shows the geometrical configuration, where the region in red is the damaged one. The value $C = 0.1$ has been chosen for the approximated domain D_c defined in (5), which is the white region in the plots.

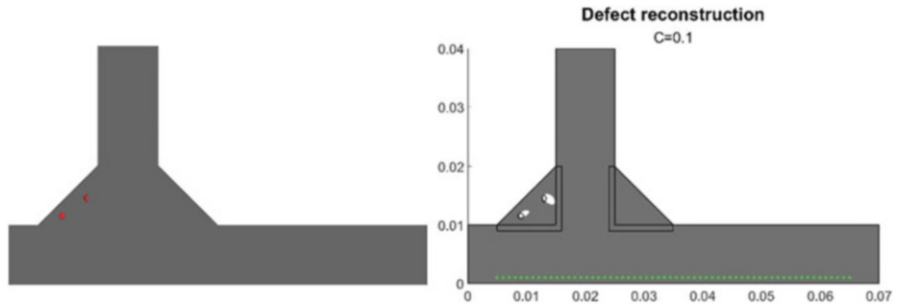


Fig. 5 Reconstruction of two defects inside the left welding joint

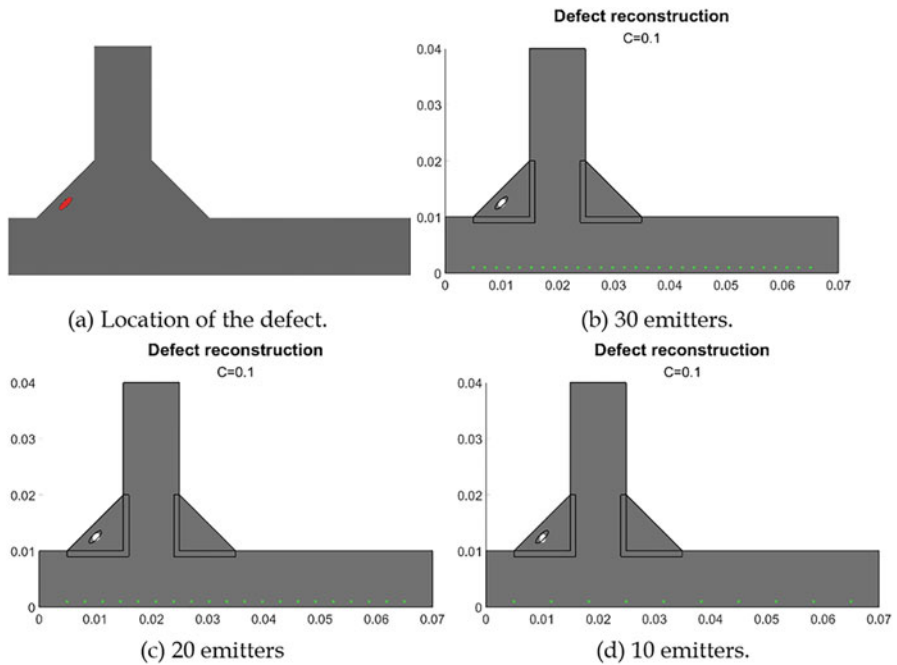


Fig. 6 Results for different sensor configurations (green dots in the plots)

In Fig. 5, we observe that in case of having two different damages inside the same joint, and even when their size is very small, the method is able to properly locate both, although their size is overestimated when selecting $C = 0.1$.

Figure 6 shows the results when considering 30, 20 and 10 emitters instead of the standard 60 emitters used in present acquisition systems. We observe impressive accuracy.

5 Conclusions

The topological derivative seems to be a very powerful tool for defect detection in welding joints. It could also be very useful for designing optimal sensor configurations for non-destructive testing.

Dealing with more realistic three-dimensional models and processing actual experimental data obtained in laboratory tests is the aim of our present work.

Acknowledgements This research is funded by MCIN/AIE/doi 10.13039/501100011033, Grant PID2020-114173RB-I00.

References

- Funes, J. F., Perales, J. M., Rapún, M. L., & Vega, J. M. (2016). Defect detection from multi-frequency limited data via topological sensitivity. *Journal of Mathematical Imaging and Vision*, 55, 19–35.
- Muñoz, S., & Rapún, M. L. (2023). Non-destructive testing of welding joints via multi-frequency topological derivative methods. Submitted.
- Sokolowski, J., & Zochowski, A. (1999). On the topological derivative in shape optimization. *SIAM Journal on Control and Optimization*, 37, 1251–1272.

Machine Learning to Reconstruct Aeronautical Databases with Deep Neural Networks



Paula Díaz, Adrián Corrochano, Manuel López-Martín,
and Soledad Le Clainche 

1 Introduction

The aeronautical industry is closely linked to computational fluid dynamics due to the need to perform virtual models that simulate the behavior of the aircraft (Rizzi et al., 2010). One of the most challenging areas of any design is the prediction of the aerodynamic coefficients present in, during, and after stall of the aircraft (Ciliberti et al., 2017). To obtain such coefficients, multiple wind tunnel (Hall et al., 2004) and flight (Heinz, 2020) tests are necessary, which are not always feasible due to the increased cost and the requirement of sophisticated infrastructures.

Another example where obtaining data through experimental tests is complicated is in acoustic tests, motivated by reducing the noise produced by aircraft on takeoff and landing. In this type of test, hundreds of microphones to measure noise and thousands of meters of cables are needed (Veggeberg, 2009).

Due to the above, there is a growing interest in mathematical methods that allow the most realistic possible representation of the aircraft's behavior by performing as few tests as possible. In this way, experimental data would be combined with predicted data to correct the design prior to the flight test program.

One of the solutions proposed so far is the combination of interpolation methods with deep neural networks (Abadía-Heredia et al., 2022), which allows the reconstruction of databases from a few points (Güemes et al., 2022). In this article, a novel application of interpolations and neural networks combined with methods of pattern

P. Díaz (✉) · A. Corrochano · S. Le Clainche
School of Aerospace Engineering, Universidad Politécnica de Madrid, Madrid, Spain
e-mail: adrian.corrochanoc@upm.es; soledad.leclainche@upm.es

M. López-Martín
School of Aerospace Engineering, Universidad Politécnica de Madrid, Madrid, Spain
Universidad de Valladolid, Valladolid, Spain
e-mail: mlopezm@ieee.org

detection (Le Clainche, 2019) is introduced for atmospheric boundary layer sensor database with low computational cost and high accuracy. This methodology, fully data-driven, could be easily extended to other aeronautic applications (i.e., unmanned aerial vehicles).

The paper is organized as follows. In Sect. 2, the two interpolation methods are explained. The main results are shown and discussed in Sect. 3. Finally, the main conclusions are presented in Sect. 4.

2 Method

The objective is to reconstruct complete fields with the minimum possible error by applying different techniques used in image reconstruction.

The database selected for this development corresponds to data from the atmospheric boundary layer. These measurements are collected by means of sensors distributed in space and which collect streamwise speed, pressure, and temperature data (Hargreaves & Wright, 2007). It should be noted that the variables of the ABL layer are stationary.

The database provided is in the form of a three-dimensional tensor of dimensions $3 \times 501 \times 2001$, which means that there are three matrices of dimensions 501×2001 , one matrix for each physical variable measured (streamwise speed, pressure, and temperature). Since the objective is to reconstruct the field, these real matrices will be reduced by choosing one point every 50 points, leaving dimensions of 11×41 . These reduced matrices will be the ones to be introduced in the models, aiming to reach the original dimensions. The great reduction of the points will also allow to test the limitations of the methods explained below.

In this work, two field reconstruction techniques will be developed in order to compare the results. In both methods, the previous step is the application of singular value decomposition (SVD) to the three reduced matrices. Subsequently, a linear interpolation or a neural network will be implemented depending on the method (López-Martín et al., 2021).

The SVD method (Sirovich, 1987) is applied to each reduced matrix. This method consists of a modal decomposition of a matrix \mathbf{D} into three matrices: the matrix of modes \mathbf{U} , the matrix with the spatial coefficients \mathbf{V} , and the singular values in \mathbf{S} as

$$\mathbf{D} = \mathbf{U}\mathbf{S}\mathbf{V}^T \quad (1)$$

where \mathbf{V}^T is the matrix transpose of \mathbf{V} . The modes are organized in decreasing order by their singular value; hence, a few numbers of modes can represent the main dynamics of the whole snapshot matrix.

Once SVD has been applied, two different methodologies are applied: the first consists of performing a simple linear interpolation, and the second consists of replacing the interpolation with a neural network (NN) formed by dense layers.

The error made in the calculations can be calculated measuring the relative root-mean-square error (RRMSE) comparing the original field with the reconstruction, as follows:

$$RRMSE = \sqrt{\frac{|D - \hat{D}|^2}{|D|^2}} \tag{2}$$

3 Results and Discussion

The original snapshots analyzed can be seen in Fig. 1. The most challenging snapshot is the one representing the streamwise velocity because the velocity profile is highly nonlinear.

When applying the first method (Fig. 2), the variables that show linear evolution in space (pressure and temperature) are correctly reconstructed, while the streamwise speed is badly reconstructed, especially at low altitudes.

The reconstruction is improved when using the second method (Fig. 3), the one interpolating using neural networks. The improvement is highlighted at low altitudes, where the snapshots present more nonlinearities.

For a better comparison, the RRMSE has been calculated for each interpolation method. These results are presented in Table 1. As expected, the RRMSE of the

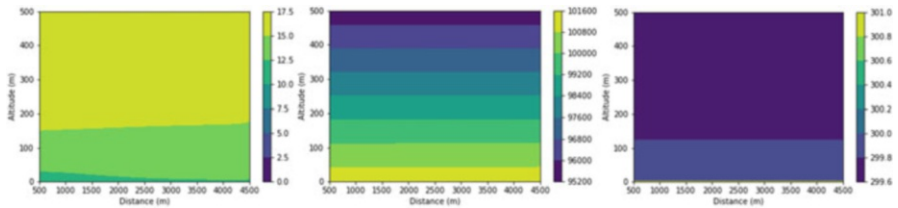


Fig. 1 Original snapshots of the streamwise velocity (*left*), pressure (*center*), and temperature (*right*) fields

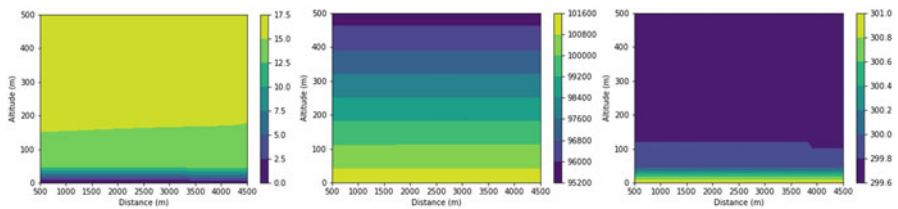


Fig. 2 Reconstructed snapshots using the combination of SVD and linear interpolation of the streamwise velocity (*left*), pressure (*center*), and temperature (*right*) fields

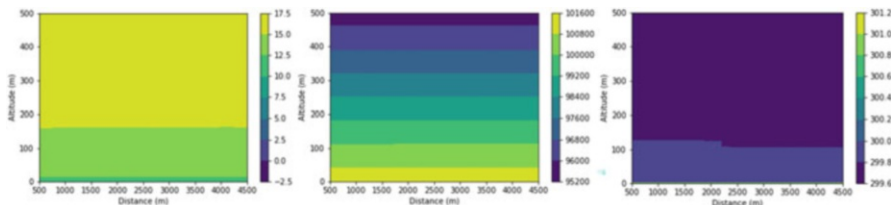


Fig. 3 Same as Fig. 2 but applying SVD and neural networks

Table 1 Relative root-mean-square error (RRMSE) calculated for each variable in each different method. Also, a total RRMSE has been included to summarize

Method	Streamwise speed	Pressure	Temperature	Total
SVD + linear interpolation	0.14	$1.1 \cdot 10^{-4}$	$6.5 \cdot 10^{-4}$	$1.1 \cdot 10^{-4}$
SVD + NN	$7.3 \cdot 10^{-3}$	$2 \cdot 10^{-6}$	$8 \cdot 10^{-6}$	$3 \cdot 10^{-6}$

neural network is two orders of magnitude lower than the error made with simple interpolation. This reveals that the neural network method significantly improves the results. Furthermore, when reconstructing the streamwise speed field with linear interpolation, the RRMSE increases up to 14% due to its nonlinearity. Nevertheless, with the neural network, the error is improved to acceptable levels, below 1%.

4 Conclusion

In short, the use of methods with interpolations with neural networks, having previously reduced the modes using the SVD method, makes it possible to reconstruct fields from a few points obtaining accurate results (Fig. 3).

In terms of computational cost, the method with linear interpolation allows obtaining results in less time than with neural networks. However, the accuracy of the neural network method is much better.

Finally, it is worth noting the potential of these methods. By not using the Navier-Stokes equations (since they are fully data-driven), these methods can be applied to any database, a very beneficial result in cases where experimental tests require large facilities to obtain a significant amount of data.

As future work, it remains to test with different databases, including industrial aeronautic problems, as well as to improve the network and make comparisons with nonlinear interpolation methods combined with SVD.

Acknowledgments AC and SLC acknowledge the grant PID2020-114173RB-I00 funded by MCIN/AEI/10.13039/501100011033.

References

- Abadía-Heredia, R., López-Martín, M., Carro, B., Arribas, J. I., Pérez, J. M., & Le Clainche, S. (2022). A predictive hybrid reduced order model based on proper orthogonal decomposition combined with deep learning architectures. *Expert Systems with Applications*, 187, 115910.
- Ciliberti, D., Della Vecchia, P., Nicolosi, F., & De Marco, A. (2017). Aircraft directional stability and vertical tail design: A review of semi-empirical methods. *Progress in Aerospace Sciences*, 95, 140–172.
- Güemes, A., Vila, C. S., & Discetti, S. (2022). Super-resolution GANs of randomly-seeded fields. arXiv preprint arXiv:2202.11701.
- Hall, R. M., Woodson, S. H., & Chambers, J. R. (2004). Overview of the abrupt wing stall program. *Progress in Aerospace Sciences*, 40(7), 417–452.
- Hargreaves, D. M., & Wright, N. G. (2007). On the use of the $k-\epsilon$ model in commercial CFD software to model the neutral atmospheric boundary layer. *Journal of Wind Engineering and Industrial Aerodynamics*, 95(5), 355–369.
- Heinz, S. (2020). A review of hybrid RANS-LES methods for turbulent flows: Concepts and applications. *Progress in Aerospace Sciences*, 114, 100597.
- Le Clainche, S. (2019). Prediction of the optimal vortex in synthetic jets. *Energies*, 12(9), 1635.
- Lopez-Martin, M., Le Clainche, S., & Carro, B. (2021). Model-free short-term fluid dynamics estimator with a deep 3D-convolutional neural network. *Expert Systems with Applications*, 177, 114924.
- Rizzi, A., Eliasson, P., McFarlane, C., Goetzendorf-Grabowski, T., & Vos, J. (2010, August). Virtual aircraft design and control of transcruiser-A canard configuration. In AIAA atmospheric flight mechanics conference (p. 8245).
- Sirovich, L. (1987). Turbulence and the dynamics of coherent structures, parts I, II and III. *Quarterly of Applied Mathematics*, 45, 561–590.
- Veggeberg, K. (2009). High channel-count aircraft noise mapping applications. *Sound and Vibration*, 43(5), 14.

Reduced-Order Models Using Clustering-Based Methods in Synthetic Jets



Eva Muñoz, Himanshu Dave, Giuseppe D'Alessio, Alessandro Parente, and Soledad Le Clainche 

Nomenclature

a_m Amplitude of the mode m
D Orifice diameter
St Strouhal number
 u_m m DMD mode
 x Coordinate in the streamwise direction
 y Coordinate in the spanwise direction

Greek Letters

δ_m Growth rate of the mode

E. Muñoz (✉)

E.T.S.I. Aeronáutica y del Espacio, Universidad Politécnica de Madrid, Madrid, Spain

École polytechnique de Bruxelles, Université Libre de Bruxelles, Brussels, Belgium

H. Dave · A. Parente

École polytechnique de Bruxelles, Université Libre de Bruxelles, Brussels, Belgium

e-mail: himanshu.dave@ulb.be; alessandro.parente@ulb.be

G. D'Alessio

Princeton University, Princeton, NJ, USA

e-mail: gd6644@princeton.edu

S. Le Clainche

School of Aerospace Engineering, Universidad Politécnica de Madrid, Madrid, Spain

e-mail: soledad.leclainche@upm.es

Subscripts

- i* Index for the discretization in the coordinate x
- j* Index for the discretization in the coordinate y
- k* Index for the discretization in time
- m* Index for the number of mode

Superscripts

- l* Magnitude which is described in the mode

1 Introduction

The research on alternative propulsion systems is increasing. Not only have synthetic jets become interesting in maritime industry, as a marine propulsion system (Buren et al., 2018), but also in the aerospace industry, because of their potential to improve aircraft efficiency as an active flow control mechanism (Leschziner & Lardeau, 2011).

In this vein, Muñoz and Le Clainche studied the physical mechanism of these devices in different regimens, one and two jets synchronized and asynchronized, at different Reynolds numbers (Muñoz & Le Clainche, 2022). The principal conclusion they obtained is that synchronized jets produce approximately double of the thrust of one jet. They also found that the thrust when jets move synchronized in time is much higher than when their movement is asynchronized with phase shifts $\pi/2$ and π , respectively. Furthermore, a symmetry breaking was identified for different Reynolds numbers in each regimen, and it is pointed out to be a subharmonic of the forcing frequency.

This work presents three different approaches to study synthetic jets and to obtain more information about the mechanism of symmetry breaking with locally linear and nonlinear approaches to use these devices to control the flow and produce thrust while maximizing the system efficiency.

2 Method

Three data analysis techniques (higher order dynamic mode decomposition, autoencoders, and vector quantization principal component analysis) are going to be applied. Each technique is briefly explained in the following subsections.

2.1 Higher Order Dynamic Mode Decomposition (HODMD)

In this section, we have presented the iterative multidimensional higher order dynamic mode decomposition algorithm (HODMD) (Le Clainche et al., 2017). It is a data-driven method introduced as an extension of the standard dynamic mode decomposition (DMD) (Schmid, 2010) which is suitable to analyze the flow physics in noisy data and complex flows (Le Clainche & Vega, 2017).

A tensor form is used to organize spatiotemporal data, $v^l(x_i, y_j, t_k)$, where $l = 1, 2, 3$ denotes the variable measured, streamwise and spanwise velocity components, and pressure, respectively. The data are equidistant in space and time, being the grid points $x_i = (i - 1)\Delta x$, $y_j = (j - 1)\Delta y$ and $t_k = (k - 1)\Delta t$, where Δx , Δy , and Δt are the distance between two consecutive grid points and the time step of the snapshots selected. HODMD decomposed the tensor as an expansion of M DMD modes, $u_m^l(x_i, y_j)$, as follows:

$$v^l(x_i, y_j, t_k) \cong \sum_{m=1}^M a_m u_m^l(x_i, y_j) e^{(\delta_m + i\omega_m)t_k},$$

where M , the spectral complexity, is the number of terms of the expansion, $a_m \geq 0$ are the amplitude of the modes, and δ_m and ω_m are the temporal growth rates and frequencies, respectively.

2.2 Vector Quantization Principal Component Analysis (VQPCA)

VQPCA is a locally linear approach to achieve dimensionality reduction presented by Kambhatla and Leen (1997). This unsupervised algorithm partitions the data in different clusters in which the variables share common features. The peculiarity of this approach is that the partition step and the PCA analysis are performed simultaneously as the clustering is based on the minimization of the reconstructed error on a low dimensional PCA projection (Parente et al., 2011).

PCA reduces p , the number of correlated variables, to q , a smaller number of uncorrelated variables, while retaining as much variance of the original data variance as possible. The dataset is structured in a matrix \mathbf{X} , with dimensions $n \times p$, where n is the number of observations and p is the number of original variables. The covariance matrix is computed as: $\mathbf{S} = \frac{1}{n-1} \mathbf{X}^T \mathbf{X}$, and then its eigenvectors and eigenvalues are extracted: $\mathbf{S} = \mathbf{A} \mathbf{L} \mathbf{A}^T$. The eigenvectors, the columns of the matrix \mathbf{A} , are known as principal components (PCs), and the eigenvalues, the diagonal terms of the matrix \mathbf{L} , represent the portion of variance of each PC. The dimensionality reduction is realized considering $q < p$ PCs, a number which depends on the global variance desired (D'Alessio et al., 2019).

2.3 Autoencoders

An autoencoder is a deep neural network (DNN) with a particular architecture which provides unsupervised feature extraction (Hinton & Salakhutdinov, 2006). The network can be divided in two main parts: an encoder that reduces the data dimension to a latent space $x \rightarrow r$ and a decoder which projects it back to the reference space $r \rightarrow \tilde{x}$. By this way, it is possible to obtain a reduced-order model without previous specifications and which can obtain nonlinear features.

3 Results and Discussion

This section discussed the similarities and differences between the three methods presented in Sect. 2. With such aim, they are applied on the same dataset that models two synthetic jets moving synchronously at Reynolds number 100 (Muñoz & Le Clainche, 2022). Figure 1 shows the main patterns on this flow.

Figure 2 shows the streamwise component of the velocity of the mode with the highest amplitude of the HODMD, which is $St = 0.03$, the forcing frequency driving the piston oscillations (Muñoz & Le Clainche, 2022). To facilitate the interpretation

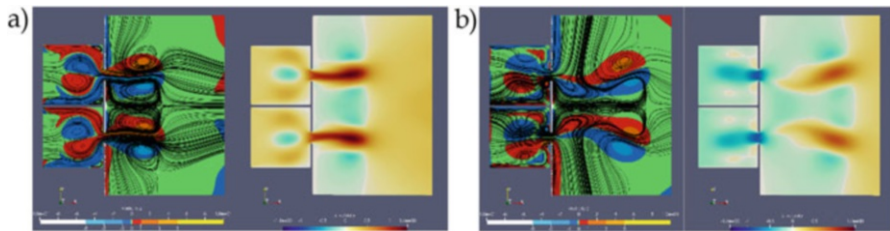


Fig. 1 Vorticity and streamlines (left) and streamwise component of the velocity (right) of the dataset during the injection (a) and suction (b) phases

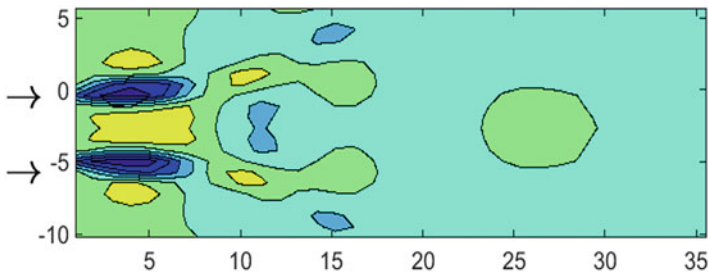


Fig. 2 Real part of the streamwise velocity component of the first DMD mode obtained with HODMD. Arrows represent the jet input

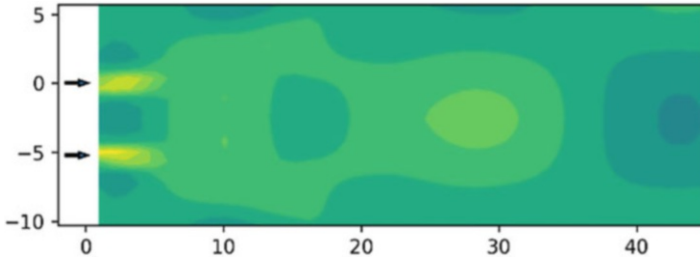
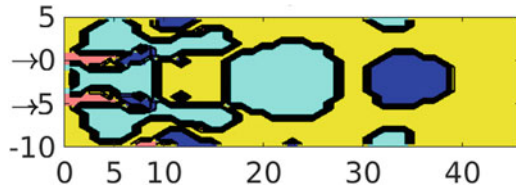


Fig. 3 Streamwise velocity component of the first mode obtained using autoencoders

Fig. 4 Clustering of the streamwise component of the velocity using VQPCA and four clusters



of the results, the axes of each jet are represented with arrows, in $y=0$ and $y= -5.2D$, with $D = 1$ being the diameter of the jet nozzles.

In Fig. 3, the streamwise component of the velocity of the first autoencoder mode is shown, when applying the dimensionality reduction in time. That is, it is obtained a temporal pattern of the flow with this nonlinear approximation based on machine learning algorithms. Comparing Figs. 1 and 2, we clearly see a similarity in the patterns near jet exit, while differences are mostly observed in the middle region ($10 \leq x \leq 20$).

In Fig. 4, a division of the streamwise velocity on the domain in four clusters is shown applying the VQPCA algorithm to analyze also temporal patterns. With this approximation, the jet streams are perfectly identifiable (pink cluster), a region with slow movement (yellow cluster), and both blue clusters can be associated with the structures identified with the DMD and autoencoders modes.

4 Conclusion

Different data analysis methods are applied on the same dataset, which present high complex flow structures, to identify new information about synthetic jets and to use them for future applications of flow control. As shown, the three methods identify similar structures in their different ways, with the clustering being highly similar to the dominant modes when applying both DMD and autoencoder reductions. More results will be presented at the time of the conference.

All in all, each different approach gives different and meaningful information about the temporal patterns of complex flows, which complement each other to provide wide perspective of them.

References

- Buren, T., Floryan, D., & Smits, A. (2018). Bio-inspired underwater propulsors. arXiv:1801.09714v2.
- D'Alessio, G., Parente, A., Stagni, A., & Cuoci, A. (2019). Adaptive chemistry via pre-partitioning of composition space and mechanism reduction. *Combustion and Flame.*, 211, 68–82. <https://doi.org/10.1016/j.combustflame.2019.09.010>
- Hinton, G. E., & Salakhutdinov, R. R. (2006). Reducing the dimensionality of data with neural networks. *Science*, 313, 504–507.
- Kambhatla, N., & Leen, T. (1997). Dimension reduction by local principal component analysis. *Neural Computation.*, 9, 1493–1516. <https://doi.org/10.1162/neco.1997.9.7.1493>
- Le Clainche, S., & Vega, J. M. (2017). Higher order dynamic mode decomposition. *SIAM Journal on Applied Dynamical Systems*, 16(2), 882–925.
- Le Clainche, S., Vega, J. M., & Soria, J. (2017). Higher order dynamic mode decomposition for noisy experimental data: Flow structures on a zero-net-mass-flux jet. *Experimental Thermal and Fluid Science*, 88, 336–353.
- Leschziner, M. A., & Lardeau, S. (2011). Simulation of slot and round synthetic jets in the context of boundary-layer separation control. *Philosophical Transactions of the Royal Society A*, 369, 1495–1512.
- Muñoz, E., & Le Clainche, S. (2022). On the topology patterns and symmetry breaking in two planar synthetic jets. *Physics of Fluids*, 34(024103), 10.1063/5.0080834.
- Parente, A., Sutherland, J. C., Dally, B. B., Tognotti, L., & Smith, P. J. (2011). Investigation of the MILD combustion regime via principal component analysis. *Proceedings of the Combustion Institute.*, 33(2), 3333–3341. <https://doi.org/10.1016/j.proci.2010.05.108>
- Schmid, P. J. (2010). Dynamic mode decomposition of numerical and experimental data. *Journal of Fluid Mechanics*, 656, 5–28.

Ethics and Autonomous Systems: An Ethical Landscape of Autonomous Weapons



Aysegul Ozerdem

Nomenclature

AI Artificial intelligence
HRW Human Rights Watch
UN United Nations

1 Introduction

In the technological developments leading to Industrial Revolution 5.0, a rapid technological transformation toward fully autonomous systems is taking place. These transformative effects can also be observed in the military sector. The most striking change in the military domain is being achieved by artificial intelligence-assisted autonomous/semiautonomous weapons. Although these are not yet fully autonomous systems, semiautonomous weapons are seen as a revolutionary innovation that will lead to a reconceptualization of the concept of war. These systems have the potential to become the “third revolution in warfare” after the invention of gunpowder and the atomic bomb (Open Letter From AI& Robotics Researchers, IJCAI, 2015). Today, there is a serious debate about whether autonomous weapons can be programmed with ethical values. Soldiers, scientists, journalists, nongovernmental organizations, and politicians are calling for the ethical use of autonomous weapons.

A. Ozerdem (✉)
Independent Researcher, Ankara, Türkiye

1.1 Ethics and Just War Theory

Ethics refers to the theory of morality. Ethics is the formulation of principles that define the right or wrong of societies and behavior that affects other living or nonliving beings (Bartneck et al., 2021; Dalziel, 2014). It defines the consensus on what is socially acceptable behavior.

Finding the “right law” for ethical dilemmas regarding the use of autonomous weapons is complex, if not impossible. This is so because the difference between theoretical normative ethics and applied ethics is not as clear as it may seem at first glance. Normative ethics is highly contextual, and it is possible to derive general principles (Lang, 2002), such as “killing is wrong.” Normative ethics is concerned with when an action is right or wrong and the issues that arise when the action is performed. Normative ethics can also be used to constrain the behavior of perpetrators (Aditya et al., 2020).

Normative ethics can create moral codes that directly affect people’s actions and lives. Moral codes should also be created for actions of people that can result in the ending of human life. Since the nineteenth century, attempts have been made to create laws of war based on ethical values, particularly just war theory as it relates to warfare. The generally accepted code is the just war theory.

Just war theory consists of two concepts that govern the ethical use of war (*jus ad bellum*) and conduct in war (*jus in bello*). Both have historical origins and were created as normative responses to different values and goals. According to this theory, war is just and ethical only if it has a just cause and is in direct proportion to the harm done to a state. The war must have a reasonable prospect of success, it must be authorized by a legitimate authority, and the state that declared the war must be waging it with the right intentions. In this regard, war should be considered a last resort, and if it is unavoidable, it should be publicly declared as such. In summary, *jus ad bellum* states that the use of force in war must be just and proportionate and should be the last resort to resort to war. *Jus in bello* is the set of codes that govern the way in which warfare is conducted. *Jus in bello*, or just warfare, refers to the distinction between combatants and noncombatants and justifies harm to noncombatants only if it is indirect and unintended (Ozerdem, 2021). Just war theory holds that a state’s actions (*jus in bello*) in war can be just, even if the war itself is unjust. Thus, if the conditions of *jus in bello* are met, the use of a weapon may be ethical regardless of whether the war itself is just. The use of autonomous weapons in wars and military operations is relevant to *jus in bello*. Thus, given the military necessity, what constitutes the ethical use of these systems during a conflict is important.

Since the beginning of the just war tradition, there have been uncertainties, but today this situation has increased its impact. The laws of just war, which serve to determine the ethical limits of war, are beginning to crack under the pressure of new technological developments. The classical logic of just war has difficulty making judgments in the face of the uncertainties created by new weapons and technologies. This is because autonomous weapons and artificial intelligence are in the blind spot of just war theory. Yet this tradition, which refuses to normalize violence, continues

to seek healing. Answers to some questions are important to revisionist theorists. To identify the ethical problems associated with the use of autonomous weapons in the context of just war norms, one should ask what actions these weapons perform under the conditions when they are used, what the characteristics of the operators and creators of autonomous or semiautonomous weapons are, and with what intent they are used. This is because ethical use is also context-dependent.

1.2 Ethical Imperatives for Autonomous Weapons

In the use of weapons, an evaluation should be made in the context of the ethics of a weapon's actions in a particular situation and not from the perspective of virtue ethics. In other words, in determining the ethical problems associated with the use of autonomous or semiautonomous weapons, it should be questioned what actions are taken under what conditions and what the intentions of the users are. However, ethical evaluation of activities involving autonomous weapons also involves interactions beyond the intentions of the users. Even if there is just cause and goodwill for the use of weapons, ultimately the answers to the questions of what and how the actions are affected will determine the definition of ethical action. In summary, this is a preliminary ethical analysis that provides standard normative ethical principles about how a person or people are influenced in the use of autonomous weapons. This influence in military operations is related to the "principle of respect." The principle of respect underlies the adjudication of war crimes. This fundamental moral duty to respect a human being simply because he is a human being is based on Kantian ethics. This principle extends to the categorical imperative, which states that human beings should not act merely as means to an end but must recognize their own worth and humanity. This principle, already challenging for humans in practice, is even more problematic for autonomous systems. For an autonomous system in which the principle of respect is encoded runs the risk of behaving unethically if it does the "right thing" given what it knows. Its perception is limited by the parameters of its design, and flexibility, judgment, and common sense are problematic. Even if an autonomous system is taught an ethical value or principle, it is ultimately only as good as its knowledge. In other words, even if the user of an autonomous weapon wants to act ethically, he may not be able to do so because of the situation created by the use of the autonomous technology.

Another misleading factor in data sets is the software factor. Machines are not inherently immoral; their unethical use is the work of the software developer and user. The bias of the machine learning developer ultimately encompasses his or her worldview and, in particular, his or her mistakes.

However, whether the actions of autonomous weapons are ethical, regardless of whether they are data- or software-driven, also depends on whether they make appropriate distinctions between civilians in accordance with the principle of respect and *jus in bello*. Regardless of the number of civilian deaths, the methods violate the

principle of just war and principle of respect for life, and unethical acts are presumed to have been committed.

So who is responsible when an autonomous weapon kills civilians or destroys homes, schools, and settlements? The commander? The programmer who designs the algorithms? The hardware or software developers?

The possibility that a human-controlled weapon is unethical always exists, but it is clearer who is responsible for the consequences of that possibility. However, the problem of accountability for the unethical actions of an autonomous weapon is not only related to the definition of autonomy and ethical behavior but also to the ethical behavioral limits of the weapon and is not clear. This is an ethical and legal problem associated with the use of lethal weapons supported by artificial intelligence, and this gap in accountability facilitates unethical uses.

The assertion that the problematic decision-making mechanisms of artificial intelligence systems can not only harm innocent people but also have undesirable political and social consequences is another point of discussion. The blowback effect of civilian deaths is one of the undesirable consequences. It is argued that blowback can undermine the confidence needed to successfully use autonomous weapons, leading to further radicalization and the “creation of accidental guerrillas.”

Another possible outcome is that unethical operations lead to political and diplomatic pressure that weakens public support for military operations. While this rejectionist attitude prevents the use of autonomous weapons, it will have a negative impact on the long-term strategic interests of democratic states. However, semiautonomous weapons are useful weapons for democratic states for procedural and normative reasons. Namely, they prevent the loss of soldiers. More importantly, they are consistent with the ethical principles that have traditionally governed warfare. Semiautonomous weapons are likely to be used by governments and terrorist organizations with a geopolitical erosion, and artificial intelligence-assisted weapons are an indispensable military technology for forces seeking to combat this. For this reason, there is a need for restrictions and rules against possible public reactions due to unethical abuse. The present laws of war are not prepared for autonomous systems. However, it is possible to enact laws and regulations guided by agreed-upon and accepted laws of war and rules of engagement to limit the unethical and abusive use of autonomous weapons. Analysts believe that the rules of international law, conventions, norms, and basic human values should be the primary sources for establishing an ethical framework (Arkin, 2009).

In establishing principles for ethical engagement, it should be considered that the way a military operation is conducted (*jus in bello*) may affect the likelihood of strategic success (*jus ad bellum*) to the extent that moral assessments of force are relevant. For this reason, just war principles should be the defining ethical criteria for the use of autonomous weapons outside of war. The use of autonomous weapons for self-defense only with the full knowledge and consent of the elected representatives of the people according to the just war principle should be another fundamental criterion of ethical evaluation. As long as autonomous weapons are used to protect one's own forces, the principles of distinction and proportionality must be observed.

Transparency and traceability in the use of autonomous technologies is another important issue as a sign of responsibility and respect to hostile states and the international community. Providing truthful and accurate information on autonomous weapon use is critical to transparent policy. Laws and rules are needed for reporting protocols.

2 Methods and Materials

The study examined discussions of autonomous weapons. Moral and ethical limits of thought and action of autonomous weapons and how to overcome them were evaluated in the context of normative ethics and within the framework of just war theory. Just war theory, chosen as the research method, consists of two concepts governing the ethically justifiable call to war (*jus ad bellum*) and conduct in war (*jus in bello*). Both have historical origins and were created as normative responses to different values and goals. According to this theory, war is just and ethical only if it has a just cause and is in direct proportion to the harm done to a state. The war must have a reasonable chance of success, it must be authorized by a legitimate authority, and the state that declared the war must be waging it with the right intentions. In this regard, war should be considered a last resort, and if it is unavoidable, it should be publicly declared.

3 Results and Discussion

Autonomous or semiautonomous weapons should be used within an ethical and legal framework. Normative ethical values should be revised for autonomous weapons. Revising ethical and legal values is difficult but not impossible. The ethical evaluation of the use of autonomous weapons should take into account the context. It should be questioned what actions are performed under what conditions and what are the intentions of the users of autonomous weapons. Even if there is just cause and goodwill compatible with just war theory in the use of autonomous weapons, it should be considered that the answers to the questions of what and how the actions are affected determine the definition of ethical action. The perceptions of autonomous systems are limited by the parameters of their design, and flexibility, judgment, and common sense are problematic. Even if an autonomous system is taught an ethical value or principle, it is ultimately only as good as its knowledge. For this reason, autonomous weapons should be deployed under human control in a manner that respects normative ethical values and the rules of just war.

4 Conclusion

Today, it is a major challenge to develop fully autonomous weapons that meet ethical values by overcoming the ethical double standard inherent in war. Another compelling factor is the lack of data to empirically assess the ethical benefits of these new technologies. However, it is possible and necessary to demonstrate new ethical values in light of the rules and theories of war, even if it is not speculative or entirely accurate. This is because the lack of control and ethical evaluation in the use of autonomous weapons not only violates human dignity but can also threaten the right to life. Establishing an ethical and legal framework, enforcing meaningful human control, and closing the accountability gap will help protect human rights and dignity in war.

From the moral point of view, the power to use weapons should be given to man. The ability of humans to make precautionary judgments depends on more than data and numerical analysis, and present technology is not yet capable of making precautionary human decisions. It is possible that autonomous systems will have such a capability, but until that happens, autonomous weapons should be deployed under human control, ethical values, and legal rules. Research should be conducted on how basic knowledge of the ethics of war, especially just war principles, can prevent unethical lethal behavior. The solution is not to ban such weapons but to revisit the parameters of modern warfare and ethical criteria and develop coherent universal rules.

References

- Aditya, H., Vibhav, A., & Shrisha, R. (2020). Ethics, prosperity, and society: Moral evaluation using virtue ethics and utilitarianism In: 29th International Joint Conference on Artificial Intelligence and the 17th Pacific Rim International Conference on Artificial Intelligence (IJCAI-PRICAI 2020), pp. 167–174. <https://doi.org/10.24963/ijcai.2020/24>.
- Arkin, R. (2009). *Governing lethal behavior in autonomous robots*. CRC Press.
- Bartneck, C., Lütge, C., Wagner, A., & Welsh, S. (2021). What is ethics? In *An introduction to ethics in robotics and AI*. Springer Briefs in Ethics.
- Dalziel, N. (2014). Drone strikes: Ethics and strategy. *New Zealand International Review*, 39(3), 2–6.
- Future of Life Institute. (2015, July 28) *Autonomous weapons: An open letter from AI & robotics researchers*. IJCAI conference. <https://futureoflife.org/open-letter-autonomous-weapons/?cn-reloaded=1>
- Lang, C. S. (2002). Promise or Peril? Reflecting on computer technology: Educational, psychological, and ethical implications. In *Ethics for artificial intelligences*. Wisconsin State Wide Technology Symposium.
- Ozerdem, A. (2021). SIHA'ların Kullanımında Etik Boyut. *Liberal Düşünce Dergisi.*, 26(104), 145–162. <https://doi.org/10.36484/liberal.1018568>

The Analysis of Collision Avoidance in Honeybee Flights



Shreyansh Singh, Rishabh Desai, Mandyam Veerambudi Srinivasan,
and Sridhar Ravi

Nomenclature

REV Retinal expansion velocity
RREV Relative retinal expansion velocity

1 Introduction

The challenges of navigation and obstacle avoidance have been of interest in the field of robotics for a very long time. For flying robots, the problem of obstacle detection and collision avoidance is exacerbated by the introduction of height control and yaw/roll-based manoeuvres. On the other hand, insects and birds tackle such problems all the time while navigating through complex natural environments or avoiding predators. Understanding this robust behaviour and possible applications in robotics is therefore a major avenue for research.

While navigating through the natural environment, insects such as honeybees must be able to avoid collisions with a multitude of obstacles in their path. The behavioural patterns of honeybees in relation to their spatial and situational awareness have been a heavily investigated area of research since the 1980s. Honeybees have been shown to be able to estimate the distance to a foraging source (visual odometry) by using the motion of the image across the retina, known as optic flow

S. Singh (✉) · R. Desai
University of New South Wales, Sydney, NSW, Australia
e-mail: shreyansh.singh@adfa.edu.au; r.desai@adfa.edu.au

M. V. Srinivasan · S. Ravi
University of Queensland, Brisbane, Australia
e-mail: m.srinivasan@uq.edu.au; sridhar.ravi@adfa.edu.au

(Lehrer, 1988). This ability to perceive range using optic flow results in a centring response in bees free flying in narrow tunnels, as they try to stay equidistant from the walls, thereby balancing the optic flow on both sides (Srinivasan et al., 1991). It has been shown that bees may use a number of optic flow strategies for visual flight control and collision avoidance in a cluttered environment (Lecoeur et al., 2019). A more detailed review of the perception of the world in three dimensions by honeybees and its subsequent implementation in obstacle avoidance, control of flight speed and landings can be found in Srinivasan (2011).

Some studies have also probed the effects of a bee's individual characteristics, such as body size, on the performance of navigation through cluttered environments (Crall et al., 2015). However, there is limited literature examining a bee's response to immediate smaller obstacles in the frontal view field, with recent research suggesting that bumblebees rely on a minimum viewing angle to assess and respond to changes in their environment (Linander et al., 2018). Some bio-inspired and biomimetic models have relied on visual cues such as looming to assist in the navigation controls of robots (Bertrand et al., 2015; Serres & Ruffier, 2017). Another recent study (Ravi et al., 2022) suggested a combination of sensory and motor control strategies in bumblebees for flight control along with the potential use of relative retinal expansion velocity (RREV) by the bees to modulate steering. In this study, we probed obstacle avoidance behaviour of honeybees by training them to fly in an empty tunnel and then presenting them with a single vertical cylindrical obstacle, which they must tackle to reach the feeder. Analysis of the flight trajectories was performed to uncover the cues responsible for the evasive manoeuvres.

2 Materials and Methods

Experiments were conducted using honeybees from an *Apis mellifera* colony that was kept on the premises at UNSW, Canberra. Bees were trained to enter and fly through a tunnel, $0.3 \times 0.3 \times 2.0$ m, made of plywood, to feed at a gravity feeder containing 10% sucrose solution placed in a chamber at the far end. They entered the tunnel through a 6.5 cm diameter hole at the front end and exited through another 6.5 cm diameter hole at the far end, to reach the feeder chamber. Satiated bees were released from the feeder chamber by briefly opening a transparent lid at the top of the chamber.

The walls and floor of the tunnel were lined with a 50% contrast black and white cloud pattern to provide the bees with a visual reference to the boundaries of the tunnel and to generate optic flow. The ceiling of the tunnel consisted of a single $5 \times 300 \times 20,000$ mm transparent UV blocking acrylic sheet. The honeybees were initially trained to fly through the empty tunnel and then filmed while flying past a vertically oriented cylindrical obstacle (65 mm or 160 mm diameter, covered with a 4×4 cm checkerboard pattern) placed in the middle of the tunnel. Bees were not marked individually in these experiments. However, due to the large number of foragers observed near the feeder combined with the large number of trajectories

recorded from a large number of foragers ensured that the naive response of bees to the presented obstacle has been captured. To analyse the collision avoidance manoeuvres, only flights in which the bees flew directly to the feeder were considered.

A GoPro camera was placed on top of the tunnel at a height of 1.5 m. This provided a two-dimensional view of the bee’s trajectory along the tunnel. The trajectories were recorded at 240 fps. Post-processing was performed using a custom MATLAB code, and spatial calibration was performed using the known width of the tunnel to relate pixels to distance. For each video frame, an ellipse was fitted to the body of the bee. The centroid of the ellipse was taken as the position of the bee, while the orientation of the ellipse in the x - y plane was used to indicate the bee’s yaw orientation. Pitch and roll could not be measured as only one camera was used. Digitisation errors were attenuated by passing the flight trajectory data through a fourth-order low-pass Butterworth filter with normalised cutoff frequency of 0.03 Hz. Flight velocity and acceleration in the longitudinal and lateral directions were estimated by differentiation and double differentiation, respectively, of the flight trajectory data. The acceleration data was passed once again through the same filter in order to minimise noise introduced by double differentiation, and a total of 176 flights were recorded.

To uncover possible cues that might be used by the bees for detecting obstacles and avoiding collisions, three classically considered visual parameters, including retinal size (visual angle subtended by the obstacle) (γ ; see Eq. 1), rate of change of retinal size (REV) ($\dot{\gamma}$; see Eq. 1) and relative retinal expansion velocity (RREV) (see Eq. 1), were evaluated for each instant of the flight trajectory:

$$\gamma = 2 * \frac{(r(t))}{d(t)}; \dot{\gamma} = \frac{d\gamma}{dt}; \text{RREV} = \frac{\text{REV}}{\text{Retinal angle}} = \frac{\dot{\gamma}}{\gamma} \tag{1}$$

where r is the radius of the obstacle and d is the distance from the centre of the obstacle. To uncover the significance of various potential cues in initiating the bees’ avoidance manoeuvre, we defined our point of interest to be the point of longitudinal deceleration before the obstacle. At this point, we looked at the coefficient of variation of various visual cues, to identify the cues that were most salient. The coefficient of variation is the measure of the dispersion of the data around the mean and is given by the first part of Eq. 2:

$$\text{COV}(X) = \frac{\sigma(X)}{\mu(X)}; \text{COV}(X) = \frac{\text{MAD}}{\text{Median}} = \frac{\text{med}(|x_i - m|)}{m} \tag{2}$$

where σ is the standard deviation and μ is the mean of the data. For enhancing robustness to outliers, we use the median absolute deviation-based version of the coefficient of variation (Arachchige, 2022) as given by the second part of Eq. 2.

3 Results

3.1 Flight Trajectory

The digitised trajectories of all flights, after interpolation to x values from -800 mm to 800 mm, and the average trajectory are shown in Fig. 1. The average trajectory is obtained by taking absolute values in the lateral direction so that all flights are flipped in the positive y -direction and then taking an average at each point in x . In the obstacle-free regions of the tunnel, the bees maintained a position close to the centreline of the tunnel, which agrees with the well-known centring behaviour.

3.2 Flight Speed and Acceleration

Figure 2 shows the profiles of the total speed and its components in the lateral (X) and longitudinal (Y) directions throughout the tunnel across all flights along with the standard deviation at each point. Across all 175 flights, the average longitudinal velocity through the tunnel was observed to be 0.78 ± 0.136 m/s (Fig. 2). Approximately 0.2 m into the tunnel, when flight recording began, the honeybees displayed an average longitudinal flight speed of 0.64 ± 0.36 m/s. The average longitudinal velocity during the bee's flight through the tunnel varied more than the average lateral velocity, which had a mean value close to zero and exhibited smaller fluctuations: 0.03 ± 0.09 m/s, except within the obstacle avoidance region. It is interesting to note the reduction in average velocity (deceleration) before the obstacle is encountered and that this reduction occurs earlier and is larger in magnitude for the 160 mm obstacle, as compared to the 65 mm obstacle. The average acceleration

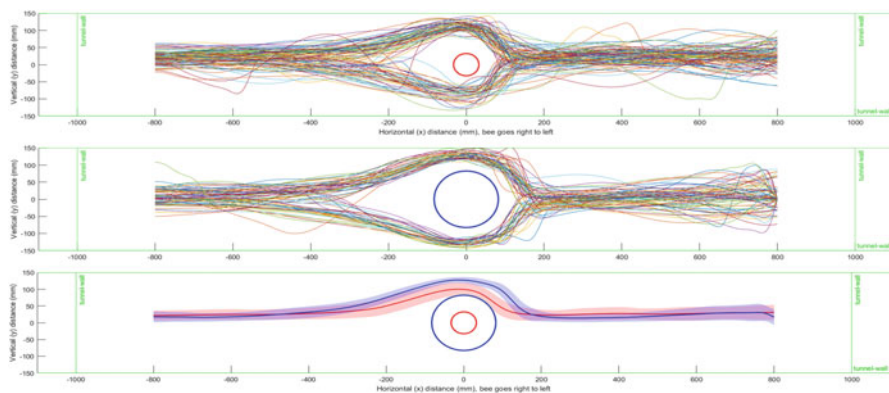


Fig. 1 All 175 flight trajectories of the honeybees and the corresponding average flights shown at the top. The 65 mm cylinder is shown in red and the 160 mm cylinder in blue

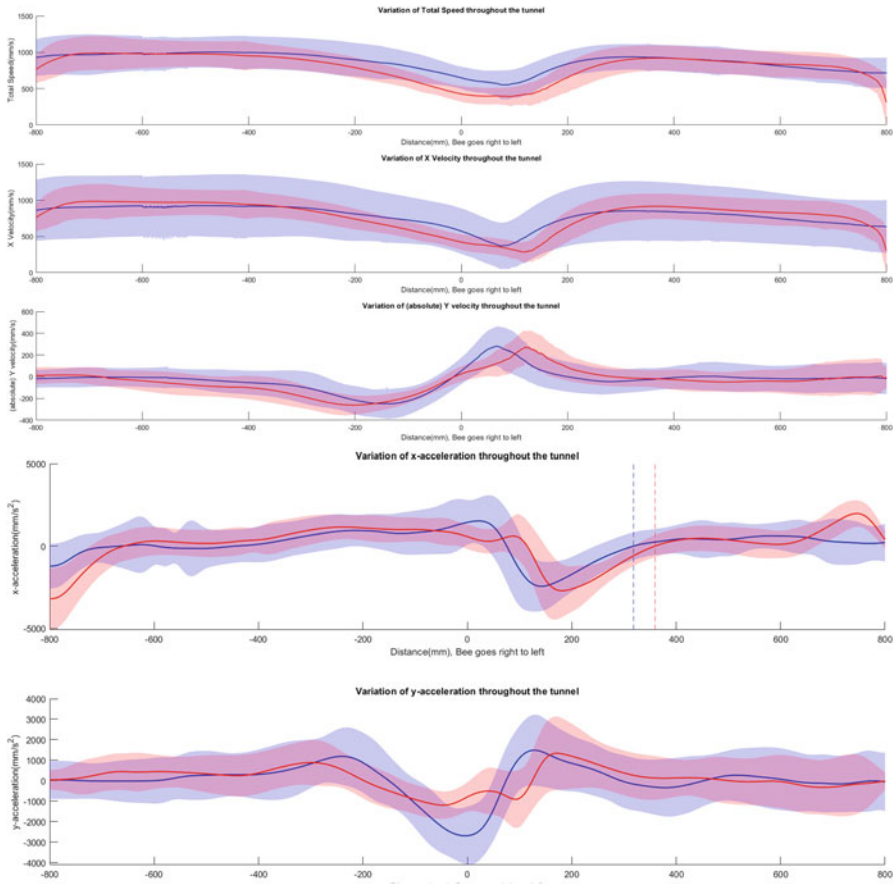


Fig. 2 The total speed, x -velocity and y -velocity of the bee in the tunnel (left) and the longitudinal and lateral acceleration (right). Motion from right to left is assumed positive. The dashed vertical lines in the acceleration profile represent the points of onset of the deceleration

of the bees in the horizontal (x) and vertical (y) directions is shown in Fig. 2. On average, the bees initially accelerated at the start of their flight and started decelerating before they reached obstacle. The point before the obstacle at which the bees started to decelerate (i.e. the acceleration changed from positive to negative values) was chosen as our point of interest and was treated as the point where bees first reacted to the obstacle. This point is marked by the vertical dotted lines in Fig. 2. Using this criterion, we determined that on average the avoidance manoeuver is initiated at a (X) distance of 323 mm from the cylinder surface for the 65 mm obstacle and 361 mm for the 160 mm obstacle (on average). The deceleration in the x -direction was followed by an increase in y -acceleration. The y -acceleration was negligible in the areas other than the vicinity of the obstacle.

3.3 Visual Cues: Retinal Angle, REV and RREV

The changes in retinal angle, REV and RREV throughout the flight are shown in Fig. 3. As expected, the retinal angle increases as the bee approaches the obstacle, reaches a maximum and then decreases after the bee has moved past the obstacle. The REV and RREV also change correspondingly, as shown.

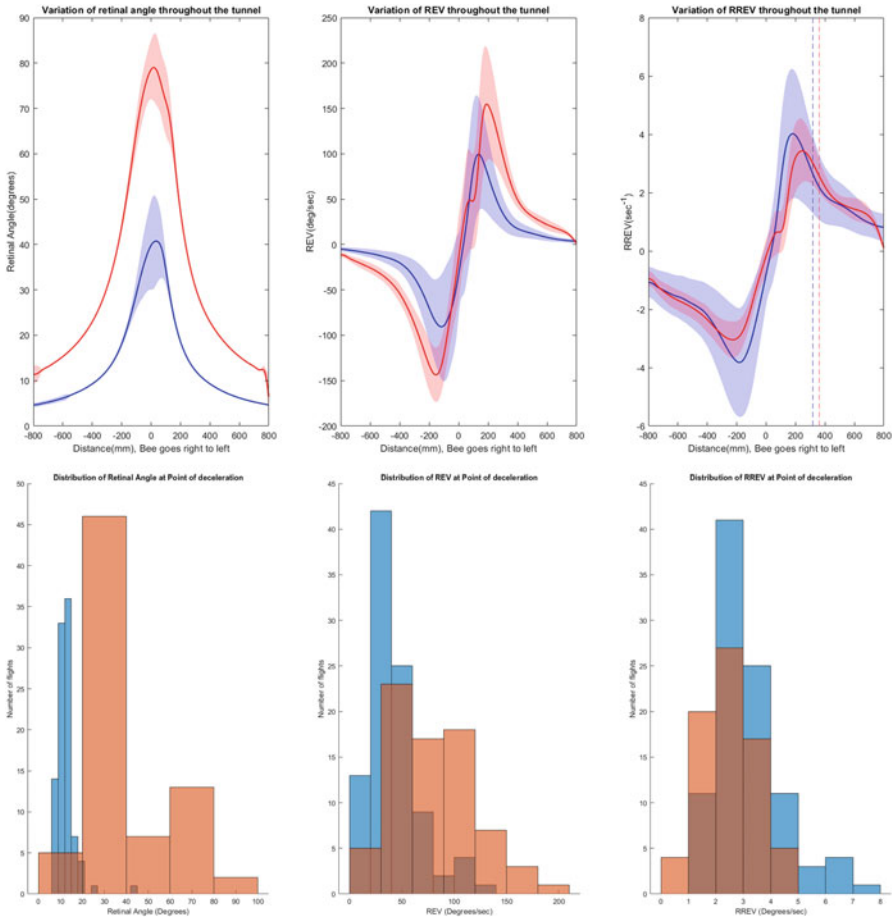


Fig. 3 Left to right: Average retinal angle, REV and RREV with shaded standard deviations for all trajectories. The dashed vertical lines in the RREV profile show the point of onset of deceleration. Plots in blue are for the 65 mm obstacle, and the ones in red are for the 160 mm obstacle. Histogram on the right shows the distribution of these values at the point of deceleration for all flights

3.4 Coefficient of Variation

As defined in Sect. 2, the coefficient of variation is a measure of the magnitude of dispersion of data relative to the magnitude of the mean, which in our case is replaced by the median for robustness. We examined the coefficients of variation of the various potential visual cues at the point of deceleration, to glean information about the cues that might initiate the collision avoidance manoeuvre. The distributions of retinal angle, REV and RREV at the point of deceleration are shown in Fig. 3. The values of their coefficients of variation are shown in Table 1. If we only consider the 65 mm obstacle, the coefficients of variation for both the retinal angle and RREV are low: 18.04% for the retinal angle and 23.58% for RREV. However, with additional data from the 160 mm obstacle, it is evident that RREV clearly displays the lowest coefficient of variation suggesting that it be a cue that plays a significant role in triggering obstacle avoidance. We find that, at the point of initiation of the avoidance response, the RREV has reached a threshold value of 3 s^{-1} (averaged across the two obstacle sizes; see third panel, Fig. 3). Since the RREV is the reciprocal of the extrapolated time to collide with the obstacle, this implies that the collision avoidance manoeuvre is triggered when the estimated time-to-contact falls below 0.33 s.

4 Conclusion

In this study, we analysed the flights of honeybees avoiding a single obstacle in the form of a vertical cylinder. By looking at the point of initiation of deceleration and treating it as the point of reaction to the obstacle, we found that the coefficients of variation for both retinal angle and RREV were low when we considered just a single obstacle. However, when results from the flights for both obstacles were combined, it became apparent that the RREV (and thus the estimated time-to-contact) is likely to play a major role in initiating the obstacle avoidance. Our findings suggest that, in honeybees, avoidance of an imminent head-on collision with an obstacle is triggered when the estimated time-to-contact drops to a value of about a third of a second. This window of time is evidently necessary to orchestrate a collision-free trajectory past the cylinder. In summary, this study elucidates how biological systems use vision to initiate obstacle avoidance tasks, as well as suggest strategies for obstacle avoidance that can be implemented in unmanned aerial vehicles.

Table 1 Coefficients of variation of potential visual cues at the point of deceleration

Obstacle size	Retinal angle (%)	REV (%)	RREV (%)
65 mm	18.04	38.86	23.58
160 mm	19.92	34.15	30.77
Combined	40.01	44.54	25.89

References

- Arachchige, C. N. (2022). Robust analogs to the coefficient of variation. *Journal of Applied Statistics*, *49*(2), 268–290.
- Bertrand, O. J., Lindemann, J. P., & Egelhaaf, M. (2015). A bio-inspired collision avoidance model based on spatial information derived from motion detectors leads to common routes. *PLoS Computational Biology*, *11*, e1004339.
- Crall, J. D., Ravi, S., Mountcastle, A. M., & Combes, S. A. (2015). Bumblebee flight performance in cluttered environments: Effects of obstacle orientation, body size and acceleration. *The Journal of Experimental Biology*, *218*, 2728–2737.
- Lecoeur, J., Dacke, M., Floreano, D., & Baird, E. (2019). The role of optic flow pooling in insect flight control in cluttered environments. *Scientific Reports*, *9*, 7707. <https://doi.org/10.1038/s41598-019-44187-2>
- Lehrer, M. A.-W. (1988). Motion cues provide the bee's visual world with a third dimension. *Nature*, *332*, 356–357.
- Linander, N., Dacke, M., Baird, E., & Hempel de Ibarra, N. (2018). The role of spatial texture in visual control of bumblebee learning flights. *Journal of Comparative Physiology A*, *204*, 737–745.
- Ravi, S., Siesenop, T., Bertrand, O. J., Li, L., Doussot, C., Fisher, A., et al. (2022). Bumblebees display characteristics of active vision during robust obstacle avoidance flight. *Journal of Experimental Biology*, *225*, jeb243021.
- Seres, J. R., & Ruffier, F. (2017). Optic flow-based collision-free strategies: From insects to robots. *Arthropod Structure & Development*, *46*, 703–717.
- Srinivasan, M. V. (2011). Honeybees as a model for the study of visually guided flight, navigation, and biologically inspired robotics. *Physiological Reviews*, *91*, 413–460.
- Srinivasan, M. V., Lehrer, M., Kirchner, W. H., & Zhang, S. W. (1991). Range perception through apparent image speed in freely flying honeybees. *Visual Neuroscience*, *6*, 519–535.

Numerical Investigation of a Uniform Viscous Transonic Flow Past a Rotating Circular Cylinder



Inés Arauzo and José Miguel Pérez

1 Introduction

Since the inauguration of the International Space Station (ISS) in 1998, human presence in space has slowly become a common event. Nonetheless, the relaunch of the space race, with private companies such as SpaceX, Blue Origin, or Virgin Galactic as its protagonists, has recently implied a radical change when it comes to planning space missions. Furthermore, the promise of affordable space tourism in the relatively near future exposes the urgent necessity to improve the present technology and designs, being necessary for optimizing alternatives that are more convenient for the long run, in other words, reusable space vehicles. In this context, the pioneer company was SpaceX, which had put its efforts into developing reusable launchers in the last few years, reaching ten successful launches with the same booster (B1051) in 2021. However, recovering the launcher is just a fraction of the technological development needed to retrieve the full vehicle, firstly, because this stage does not leave the close atmosphere at any moment of its flight and, secondly, because this stage has enough fuel to make a controlled comeback. With this information in mind, it is quite evident that the most technologically challenging phase will be the last one, the reentry. In this phase, the ship (also called debris when it is uncontrolled) starts to decay due to the combination of gravity forces and the atmospheric-induced drag. When the vehicle reaches altitudes below 120 km over the Earth's surface, the air density becomes significant enough for the aerodynamic drag to make the ship slow down to speeds below the necessary one to orbit at that altitude (the orbital velocity). This is the starting point of the reentry trajectory.

During the reentry phase, the ship quickly falls into a much denser atmosphere, increasing the aerodynamic drag, the dynamic pressure, and the ship's surface

I. Arauzo · J. M. Pérez (✉)

Universidad Politécnica de Madrid, Madrid, Spain

e-mail: ines.arauzo.andres@alumnos.upm.es; josemiguel.perez@upm.es

temperature. These almost instantaneous changes in the flight conditions make the ship reach a huge range of speeds, going from hypersonic to subsonic, depending on the geometry and the initial conditions. For that, thermal protection systems (TPS) are needed; see Wu et al. (2007) and Abdi et al. (2018) in the case of a circular cylinder. These systems can be ablative, refractory insulation, and passive and active cooling systems. Another possibility is reducing the reentry velocity in the upper layers of the atmosphere, highlighting the retro-propulsion systems, as used by B105.

One option that could be added to the second category of techniques, but without fuel consumption, would be to increase lift at the beginning of reentry. This would reduce speed without excessive friction and heat transfer (due to the low density at high altitudes). However, since reentry vehicles are usually blunt (reentry capsules), they do not usually generate high lift. One way to achieve such lift would be through the Magnus effect, which can be achieved by rotating the reentry vehicle fuselage. In the present paper, we intend to analyze with CFD, using a simplified problem, the changes in the aerodynamics that the Magnus effect would introduce in a rotating ship. This ship is replaced in this work by a rotating circular cylinder, with a constant angular velocity defined in a two-dimensional and uniform subsonic/transonic flow. This problem has been studied in the literature primarily in the incompressible (Tokumaru & Dimotakis, 1993; Sengupta et al., 2003) or low subsonic flow regime (Teymourash & Salimipour, 2017) but without the presence of shock waves and regions with the supersonic flow. More recent works have investigated this problem in the hypersonic regime; see John et al. (2016).

Three dimensionless parameters characterize the problem: the Reynolds number based on the diameter of the circular cylinder and the properties of the free flow $Re = \frac{\rho V_\infty D}{\mu}$, the ratio between tangential velocity on the cylinder surface and that of the freestream velocity $\alpha = \frac{\omega D}{2V_\infty}$, and the Mach number of the free flow $M_\infty = \frac{V_\infty}{\sqrt{\gamma RT_\infty}}$. Other parameters such as the Prandtl number or the ratio between specific heats will remain constant and equal to their standard values for air. The rotation implies that in some places of the cylinder's surface, the freestream velocity is in the same direction as the flow driven by the rotation. In contrast, these velocities will be opposite on the opposite side. In our case, the cylinder will rotate clockwise, so the part with the highest velocity will be the upper part of the cylinder and the part with the lowest velocity will be the lower part. This changes the pressure distribution over the cylinder surface and can generate a normal shock wave at the top (suction side).

Although the objective is to study supersonic and hypersonic flows, in this work, we are going to focus on high subsonic flows in such a way that adding the effect of rotation generates a shock wave on the suction side of the body.

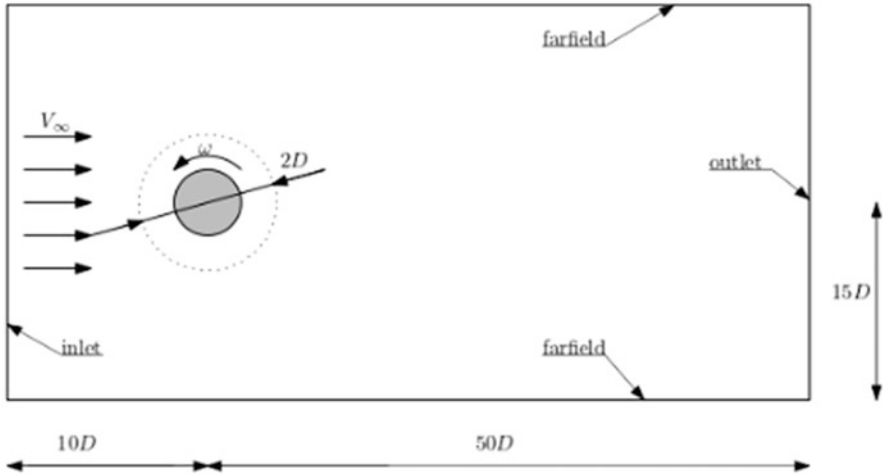


Fig. 1 Domain and boundary conditions

2 Problem Definition

Figure 1 shows a sketch of the problem. This is defined by a rotating cylinder whose diameter is $D = 2R$, and its angular velocity is ω . The cylinder is immersed in a flow with a freestream velocity U_∞ . The ratio between these two velocities is the coefficient described above, $\alpha = \frac{\omega D}{2U_\infty}$. The simulations have been performed for negative values of α (clockwise rotation). In order to study the dependence of the aerodynamic coefficients with the Mach number of the freestream and the nondimensional rotating speed α , three cases will be analyzed: case A, $Re = 10,000$, $M_\infty = 0.5$, and $\alpha = 1$; case B, $Re = 10,000$, $M_\infty = 0.1$, and $\alpha = 1$; and case C, $Re = 10,000$, $M_\infty = 0.5$, and $\alpha = 0.1$. The circular cylinder is located at the origin of the coordinate system (see Fig. 1 for details). Concerning the boundary conditions, the value of the velocity and the values of the total pressure and temperature have been imposed in the inflow, while the static pressure has been considered in the outflow. Finally, an adiabatic no-slip boundary condition on the cylinder's surface has been used.

3 Numerical Simulation

For the numerical resolution of the system, the domain must be discretized with a mesh. In this case, the mesh is a structured mixture of a C-mesh in the area close to the cylinder and an H-mesh for the rest of the domain. Furthermore, stretching was implemented in the whole domain in order to capture the desired information with a

good resolution while easing the computational cost. The governing equations for the simulation are the 2D Navier-Stokes equations:

$$\frac{\partial}{\partial t} \int_{\Omega} \vec{W} d\Omega + \oint_{\partial\Omega} (\vec{F}_c - \vec{F}_v) dS = 0 \quad (1)$$

$$\vec{W} = \begin{bmatrix} \rho \\ \rho u \\ \rho v \\ \rho E \end{bmatrix}; \quad \vec{F}_c = \begin{bmatrix} \rho V \\ \rho u V + n_x p \\ \rho v V + n_y p \\ \rho H V \end{bmatrix}; \quad \vec{F}_v = \begin{bmatrix} 0 \\ n_x \tau_{xx} + n_y \tau_{xy} \\ n_x \tau_{xy} + n_y \tau_{yy} \\ n_x \Theta_x + n_y \Theta_y \end{bmatrix} \quad (2)$$

where Ω is the volume of the domain, $\partial\Omega$ is its contour, $V \equiv \vec{v} \cdot \vec{n} = n_x u + n_y v$ is the normal direction on the boundaries, E is the total energy per mass unit, τ_{ij} are the components of the stress tensor, and Θ_x and Θ_y are given by $\Theta_x = u\tau_{xx} + v\tau_{xy}$ and $\Theta_y = u\tau_{xy} + v\tau_{yy}$. The method used for the temporal integration is an implicit second-order scheme accelerated with a dual time step.

4 Results and Discussion

As aforementioned, the aim is to study the dependence of the aerodynamic coefficients on the Mach number and α . These results are shown in Figs. 2, 3, and 4 which show the gradient of the pressure field colored with the Mach number and the instantaneous streamlines defined by the momentum density ($\rho u, \rho v$).

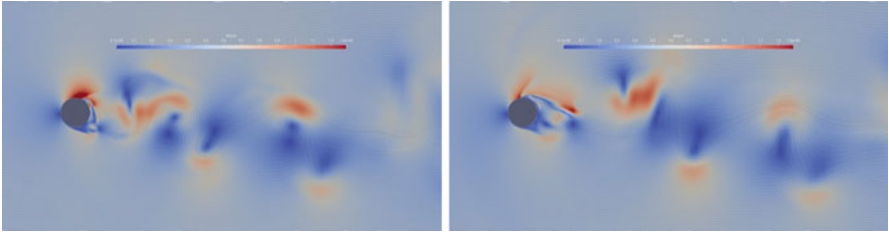


Fig. 2 Case A: Flow past a cylinder at $M_\infty = 0.5$ and $\alpha = 1$. Maximum mach number = 1.3

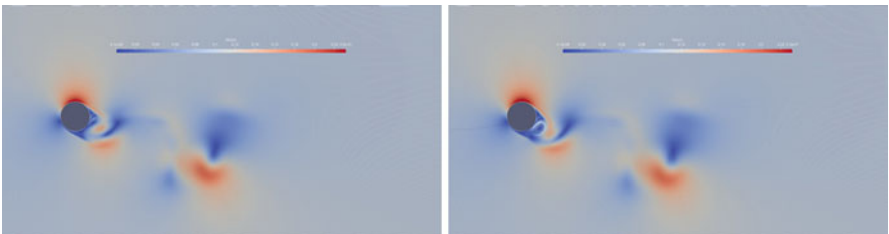


Fig. 3 Case B: Flow past a cylinder at $M_\infty = 0.1$ and $\alpha = 1$. Maximum mach number = 0.23

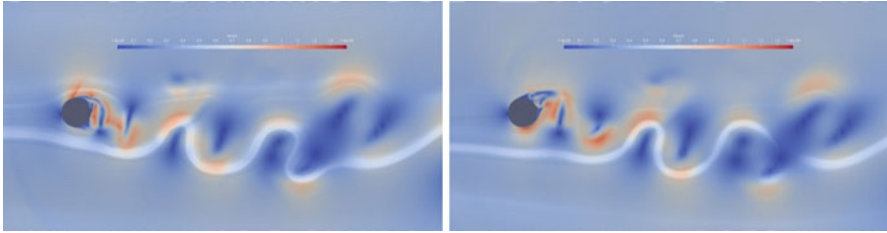


Fig. 4 Case C: Flow past a cylinder at $M_\infty = 0.5$ and $\alpha = 0.1$. Maximum mach number = 1.4

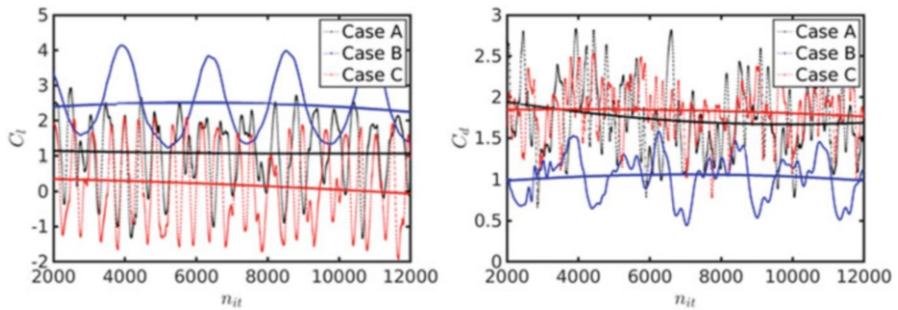


Fig. 5 Average values of lift and drag coefficients for the three test cases as a function of the number of temporal iterations. Case A (black line), case B (blue line), and case C (red line)

Case A ($Re = 10,000$, $M_\infty=0.5$, and $\alpha = 1$): Figure 2 shows two consecutive snapshots in which a shock wave can be seen on the suction side of the cylinder surface (left fig.) and how this is expelled upstream by the effect of the wake movement behind the cylinder (right fig.). The generation of this shock wave is due to the extra acceleration experienced by the fluid on the upper side induced by the cylinder rotation.

Case B($Re=10,000$, $M_\infty=0.1$, and $\alpha = 1$): Unlike the previous case, the Mach number is lower in this case (Fig. 3). This implies that the extra acceleration due to rotation is insufficient to accelerate the flow to the supersonic regime. As in the previous case, the rotation of the cylinder induces a downward deflection of the wake.

Case C ($Re=10,000$, $M_\infty=0.5$, and $\alpha = 0.1$): This case differs from case A in the value of α . A priori, it could be thought that the value of alpha so small is not enough to obtain a supersonic flow. However, as shown in Fig. 4, the flow is supersonic again.

Figure 5 shows the instantaneous (dot lines) and average (continuous lines) aerodynamic coefficients; $C_l = F_l / \left(\frac{1}{2\rho V_\infty^2 D} \right)$, and $C_d = F_d / \left(\frac{1}{2\rho V_\infty^2 D} \right)$ as functions on time. As seen in the first figure, C_L increases when Mach decreases. This effect had already been seen previously in the literature for small Mach numbers.

Regarding the dependence with α , C_L decreases when α decreases. Note also that the difference between these two curves is of an order of magnitude, which agrees with the predictions made with the potential theory in which C_L is proportional to the value of α . As for the coefficient C_D , as can be seen, it hardly depends on the value of α (compare red and black curves) and decreases as the Mach number decreases.

5 Conclusion

This work studied the transonic flow defined on a rotating circular cylinder immersed in a transonic flow. Different simulations have been carried out, which have allowed characterizing qualitatively the behavior of the aerodynamic forces (drag and lift) as a function of the problem's parameters. We have also obtained information on the dynamics of the problem, such as the effect of the vortex shedding (wake) on the shock wave. We are presently performing different modal decomposition analyses: POD and DMD. These analyses will be completed shortly. In the case of the POD analysis, the objective is to obtain a reduced-order model that allows us to retain most of the energy of the system with the smallest possible number of modes.

References

- Abdi, R., Rezazadeh, N., & Abdi, M. (2019). Investigation of passive oscillations of flexible splitter plates attached to a circular cylinder. *Journal of Fluids and Structures*, *84*, 302–317.
- John, B., Gu, X., Barber, R. W., & Emerson, D. R. (2016). High-speed rarefied flow past a rotating cylinder: The inverse Magnus effect. *AIAA Journal*, *54*, 16070–11680.
- Sengupta, T. K., et al. (2003). Temporal flow instability for Magnus-robins effect at high rotation rates. *Journal of Fluids and Structures*, *17*, 941–953.
- Teymourash, A. R., & Salimipour, S. E. (2017). Compressibility effects on the flow past a rotating cylinder. *Physics of Fluids*, *29*, 016101.
- Tokumaru, P. T., & Dimotakis, P. E. (1993). The lift of a cylinder executing rotary motions in a uniform flow. *Journal of Fluid Mechanics*, *255*, 1–10.
- Wu, C., Wang, L., & Wu, J. (2007). Suppression of the von Kármán vortex street behind a circular cylinder by a travelling wave generated by a flexible surface. *Journal of Fluid Mechanics*, *574*, 365–391.

Design and Analysis of Rocket Launch Vehicle for CubeSats



Alper Şanlı, Tuncay Yunus Erkeç, Melih Beceren,
and Mehmet Furkan Kemalli

1 Introduction

Mankind has sought ways to reach space from past to present. With the development of technology, the vehicles produced have differed. Today, it has become easier to reach the Kalman line, which is the space border, with modern launch vehicles. The stratosphere layer is used for training CubeSats. The number of artificial satellites sent into space increases every year. With the advancement of CubeSat technology, CubeSat has started to replace big satellites. The purpose of the launch systems is to raise the payload on which it is placed, to the desired stratosphere layer altitude healthy. According to altitude, low-altitude, medium-altitude, and high-altitude launch systems are available. Launch systems generally consist of three subsystems. They are payload, structural subsystem, and the propulsion subsystem. Launch vehicles can be used for military, scientific, and research purposes. In this study, the design and analysis of the launch vehicle that will carry the CubeSats to the stratosphere layer has been carried out. In the next stages, vehicle studies will be carried out to carry the CubeSats to the Kalman line. Before the Kalman line, a launch vehicle that would carry CubeSats for educational purposes to the stratosphere layer was studied.

A. Şanlı (✉) · T. Y. Erkeç · M. Beceren · M. F. Kemalli
National Defense University, Hezârfen Aeronautics and Space Technologies Institute,
Istanbul, Türkiye

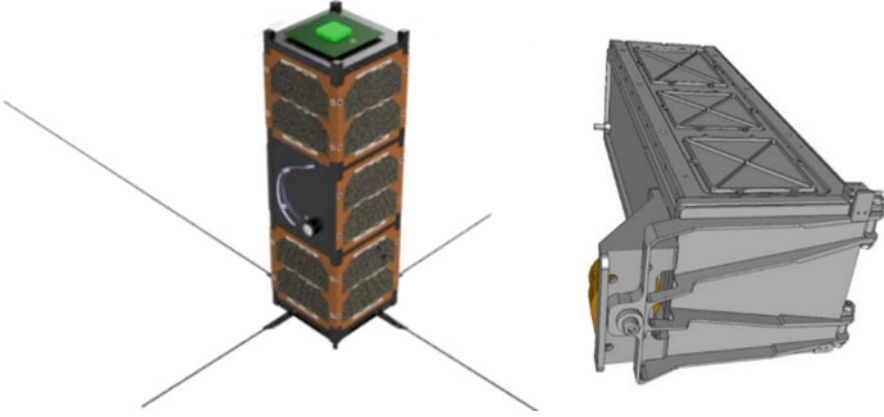


Fig. 1 AstinSat-1 CubeSat example that can be placed on the launch vehicle (Şanlı & Aslan, 2021) and POD example that CubeSat can be placed (Johnstone, 2020)

2 Rocket Launch Vehicle for CubeSats

In this study, a launch system is designed to carry a CubeSat designed for educational use to the stratosphere layer. The launch system consists of two stages. There is one rocket engine in the second stage and three rocket engines in the first stage. The area where the CubeSat will be placed is in the second level. POD where 3U CubeSat can be placed is placed. The CubeSat will be released from the launch vehicle with the help of POD at apogee altitude (Fig. 1).

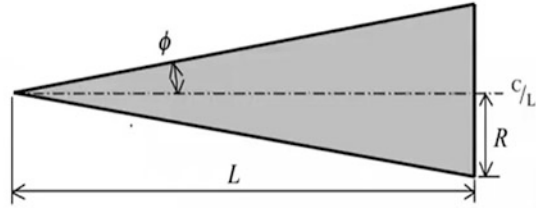
2.1 Design of Launch Vehicle

The launch vehicle has a total length of 419 cm and a total weight of approximately 106,602 g with payload. The nose cone material is fiberglass, and the construction material of the stages and fins is carbon fiber. The length of the POD section where the CubeSat will be placed is 30 cm, and its diameter is 17 cm. Conical, biconical, power series, ogive series, elliptical, parabolic, and Haack series nose cones can be used in launch systems. The design of the nose cones directly affects the coefficient of friction. Conical-type nose cone is used in CubeSat launch vehicle (Fig. 2).

$$y = \frac{xR}{L}; \quad \varphi = \tan^{-1}(R/L) \quad (1)$$

The nose cone geometry was created using the parameters in Eq. 1. The weight of the nose cone used is 585 g. The total drag coefficient of the conical nose cone was calculated as 0.02. The fin type used directly affects the center of pressure of the

Fig. 2 Launch vehicle nose cone geometry



launch vehicle (Bossert et al., 2003). The launch vehicle does not have active control systems, and stability is provided by fins. In order for the launch vehicle to perform a stable flight, the center of gravity is located behind the center of pressure. Six blades were used, three in the first stage and three in the second stage. The total drag coefficient of the ailerons used in the second stage is 0.02, and the drag coefficient of the blades used in the first stage is 0.05. The drag force formula is given in Eq. 2. F_D is the drag force, ρ is the density of the atmosphere, V is the speed, and A is the surface area (Taylor, 2017):

$$F_D = C_d \rho V^2 A / 2 \tag{2}$$

The launch vehicle has two stages connected in series, and its design is as shown in Fig. 3.

In the second stage, there is a rocket engine with a refillable diameter of 161 mm and a length of 597 mm with a total impulse value of 41,125 s. In the first stage, there are three Cesaroni rocket engines with a total impulse value of 21,041 s, a radius of 98 mm, and a length of 1239 mm. Eq. 3 includes I_s the total impulse eq. F is force, t is time, g is gravitational acceleration, m is total fuel mass burn rate, and c is effective exhaust velocity equations (Sutton & Biblarz, 2016):

$$I_s = \left(\int_0^t F dt \right) / \left(g_0 \int_0^t \dot{m} dt \right); \quad c = I_s g_0 = F / \dot{m} \tag{3}$$

Rocket engines are fixed to stage structures with engine blocks and gripping elements. The launch vehicle has an apogee of 32,676 m, a maximum speed of 3.61 Mach, and a maximum acceleration of 170 m/s^2 . The distance of the launch vehicle pressure center from the reference plane is 321 cm, and the distance of the center of gravity from the reference plane is 269 cm. Equation 4 is the center of gravity and center of pressure equations. c_g is the distance from the center of gravity to the reference plane, W is the total weight, d_n is the distance from the reference plane of the subsystems, and w_n is the weight of the subsystems. c_p is the distance of the center of gravity from the reference plane, and a_n is the surface area of the subsystems.

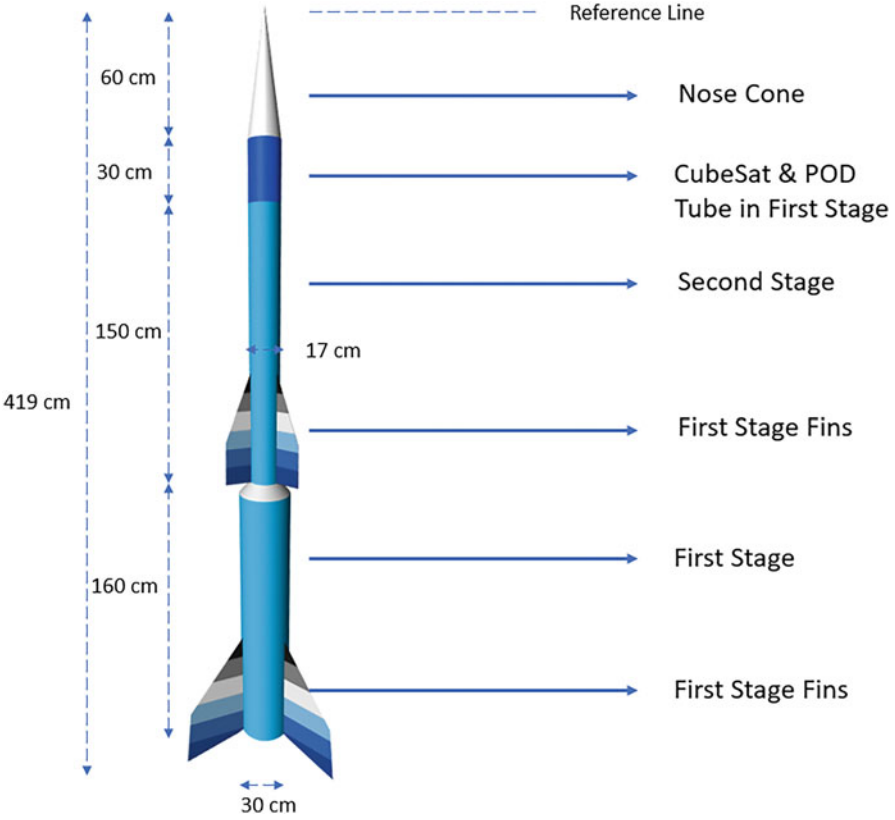


Fig. 3 Rocket launch vehicle design and subsystems

$$c_g W = \sum d_n w_n; \quad c_p A = \sum d_n a_n \tag{4}$$

2.2 Analysis Results of Launch Vehicle

The launch vehicle’s center of gravity and the location of the center of pressure directly affect the stability of the launch vehicle. This stability allows it to gain vertical altitude. In Fig. 4, the total altitude values of the launch vehicle are given. Total flight time is 725 s.

Figure 5 shows the changes in the center of gravity and center of pressure during the total flight time of the launch vehicle. During the flight, the center of pressure did not come in front of the center of gravity and exhibited a stable flight. The stability value was always found to be positive.

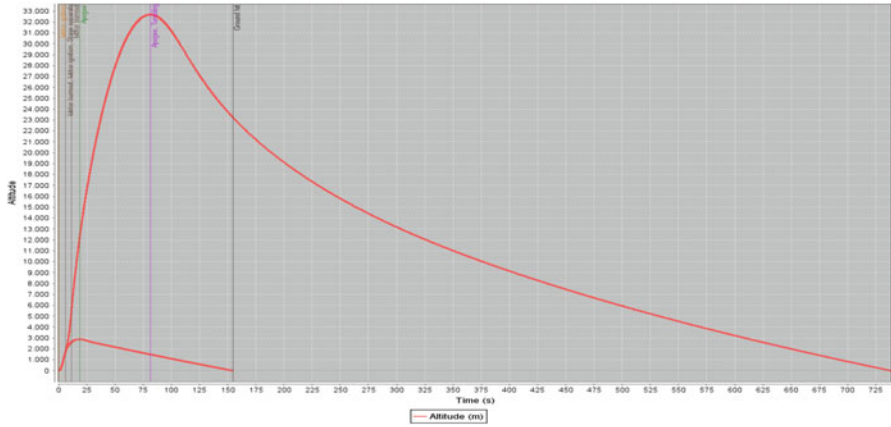


Fig. 4 Launch vehicle total altitude graph

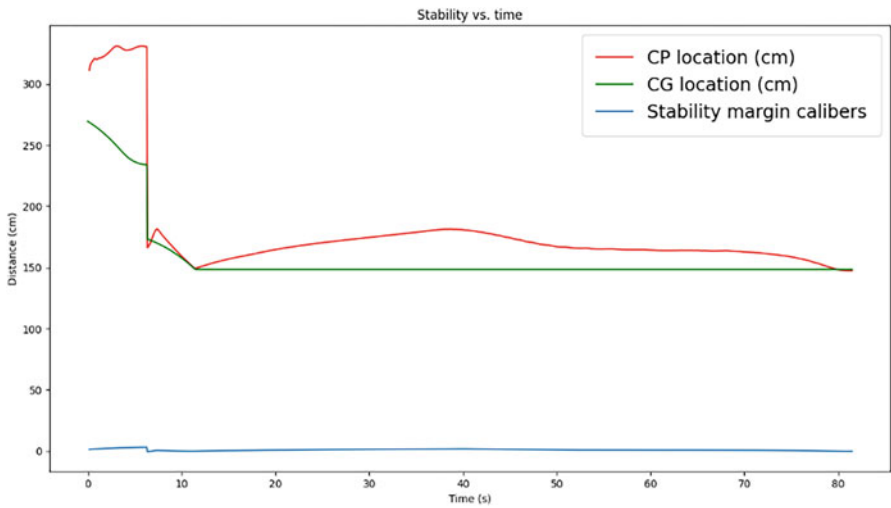


Fig. 5 Launch vehicle stability and time graph

The launch vehicle is exposed to drag force throughout the flight time, and this affects its altitude and stability. Figure 6 shows drag coefficient, friction drag coefficient, base drag coefficient, and pressure drag coefficient values according to the Mach number value.

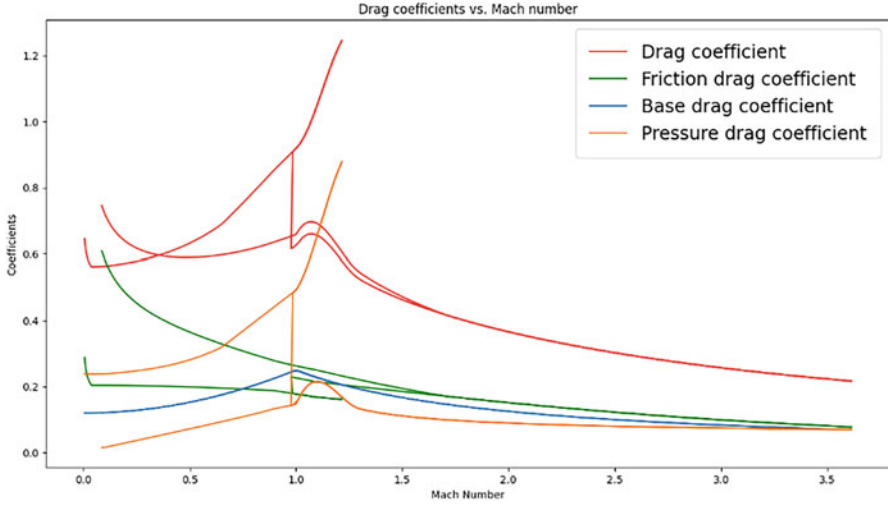


Fig. 6 Vehicle drag coefficients and Mach number graph

3 Conclusion

In this study, the detailed design and flight analyses of the launch vehicle were carried out. The first version of the launch vehicle, it was aimed to the training CubeSat to the stratosphere layer. In the next versions, the CubeSats will be dropped above the Kalman line. In this study, the design of the launch vehicle was made by increasing the 10 kg payload to 32,676 m altitude. The total length of the two-stage launch vehicle is 419 cm, and its weight is 106,602 g. The drag coefficients are investigated throughout the flight, and the stability value is always positive. The launch vehicle displayed a stable flight throughout the flight.

References

- Bossert, D. E., Morris, S. L., Hallgren, W. F., & Yechout, T. R. (2003). *Introduction to aircraft flight mechanics: Performance, static stability, dynamic stability, and classical feedback control*. American Institute of Aeronautics and Astronautics.
- Johnstone, A. (2020). *Cubesat design specification (1U-12U) Rev 14 CP-CDS-R14*. The Cubesat Program, Cal Poly SLO, July.
- Şanlı, A., & Aslan, A. R. (2021). *Design of ASTINSAT-1 and structural analysis, use of generative design*. International Congress on Engineering And Technology Management.
- Sutton, G. P., & Biblarz, O. (2016). *Rocket propulsion elements*. Wiley.
- Taylor, T. S. (2017). *Introduction to rocket science and engineering*. CRC Press.

Aeroelastic Flutter Detection by Higher Order Dynamic Mode Decomposition (HODMD)-Based Techniques and Convolutional Neural Networks (CNN)



Joseba López, Rubén Moreno-Ramos, and Soledad Le Clainche 

Nomenclature

U_∞/V	Velocity
ω	Frequency
g/δ	Damping rate
M	Spectral complexity (number of modes)
N	Spatial complexity (rank of the matrix of the spatial modes)
K	Number of snapshots
a	Amplitude
\vec{U}	Spatial modes
R	Koopman operator (linear)
d	Number of snapshot windows

1 Introduction

Flutter is an aeroelastic phenomenon that causes a self-excitation in a structure, because of being coupled to a fluid. The mentioned coupling joint modifies the inertia, stiffness, and damping of the structure, leading to an aerodynamic inertia, stiffness, and damping. When the amount of energy communicated by the fluid is greater than the one that the structure can dissipate (positive aerodynamic damping),

J. López (✉) · R. Moreno-Ramos
Capgemini Engineering, Madrid, Spain
e-mail: joseba.lopez-bruno@capgemini.com; ruben.morenoramos@capgemini.com

S. Le Clainche
School of Aerospace Engineering, Universidad Politécnica de Madrid, Madrid, Spain
e-mail: soledad.leclainche@upm.es

divergent oscillations appear, which can cause a catastrophic structural failure (García-Fogeda and Arévalo, 2014). The velocity that sets the border between stable and unstable oscillations is called flutter velocity, and flying at that velocity induces harmonic oscillations as a consequence of zero damping.

Due to the dangerousness of flutter, it is important to know at which velocity it appears. Nowadays, many flying tests are made in order to have this information, placing accelerometers in different parts of the plane, so that the type of the produced oscillations can be identified. The main advantages that reliable algorithms would have with regard to real tests are that the need to push the aircraft to its limit could disappear, the results would be obtained more quickly and safely, and economic costs would be reduced.

In this work, starting from the matrix of a space-state model obtained from Nastran (the complete database consists of the matrixes related to 200 different velocities, which go from 1 m/s to 996 m/s with increments of 5 m/s), the resulting dynamic system will be integrated in order to generate some artificial signals linked to an aeroelastic response (aerodynamics is potential). This database could be used to model real accelerometer readings (in the real life, readings normally have an associated noise so this case will also be considered). First, using HODMD the evolution of the damping of the modes as velocity increases will be analyzed, and the results given by the algorithm will be compared with the real ones (it is very easy to do this comparison, since the damping of the real modes is given by the real part of the eigenvalues of the space-state model matrix, with the imaginary part being its associated frequency). On the other hand, to demonstrate the usefulness of convolutional neural networks, a classifier of signals into stable (without flutter) or unstable (with flutter) will be generated.

2 Method

2.1 Higher Order Dynamic Mode Decomposition (HODMD)

The objective of DMD is to represent the snapshot \vec{x}_k , collected at time t_k , as:

$$\vec{x}_k \approx \sum_{m=1}^M a_m \vec{u}_m e^{(\delta_m + i\omega_m)(k-1)\Delta t} \quad k = 1, \dots, K$$

which is the product of amplitudes, spatial modes, and temporal modes. To do so, it is necessary to solve the following system:

$$\vec{x}_{k+1} \approx \mathbf{R}\vec{x}_k$$

The conventional DMD fails in those cases when the spectral complexity is greater than the spatial complexity, which is something that normally happens in very noisy problems, in problems of high turbulence fluid flow, or in studying flutter.

This is the reason why in this paper, giving continuity to what was done in a previous dissertation (Méndez, 2020), HODMD will be used, which is a higher order DMD. The system to solve now is (Le Clainche & Vega, 2017):

$$\overrightarrow{x_{k+1}} \approx \mathbf{R}_1 \overrightarrow{x_k} + \mathbf{R}_2 \overrightarrow{x_{k+1}} + \dots + \mathbf{R}_d \overrightarrow{x_{k+d-1}} \quad k = 1, \dots, K - d + 1$$

Due to the fact of considering some groups of snapshots delayed in time, temporal dynamics are identified much better than in DMD.

2.2 Convolutional Neural Networks (CNN)

A CNN will be tested when classifying signals into stable or unstable. The generated network is built with the following layers (Table 1):

The dense layer is the one that makes the classification, giving each one of its two neurons the probability for a signal to be stable and unstable. Convolutional layers are activated by a ReLU activation function, whereas in the dense layer a softmax function is used, which is typical in classification problems (5) (Torres i Viñals, 2020).

3 Results and Discussion

3.1 Higher Order Dynamic Mode Decomposition (HODMD)

The damping rates vary the following way as velocity increases (Fig. 1):

The previous plots show the comparison between the results obtained for HODMD (no flutter in blue and flutter in red) and calculating the eigenvalues of the matrix of the model (no flutter in black and flutter in green). It can be clearly seen that the HODMD correctly detects the flutter modes, so it is a method that can be useful to predict the speed at which this phenomenon appears. The real flutter speed is approximately 323.75 m/s, so in order to see the effectiveness of the algorithm

Table 1 Created convolutional neural network

Layer number	Type	Number of filters/(neurons)	Dimension of filters
1	Input	–	–
2	Convolution	32	3 × 3
3	Pooling	32	2 × 2
4	Convolution	64	5 × 5
5	Pooling	64	2 × 2
6	Flatten	(205,504)	–
7	Dense	(2)	–

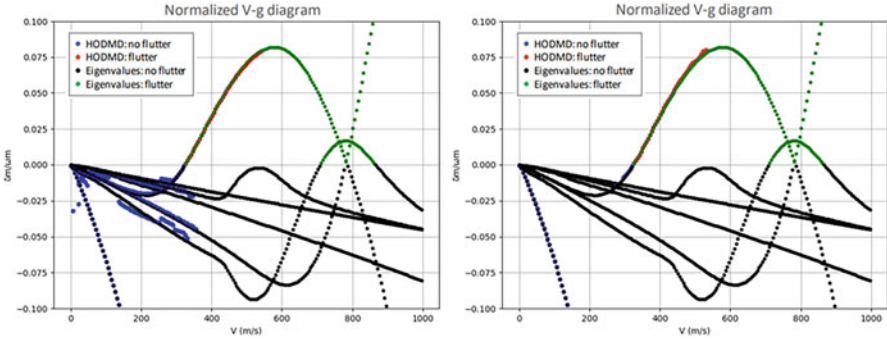


Fig. 1 Evolution of normalized damping (δ_m/ω_m) as velocity (V) varies without noise (left) and with 10% noise (right)

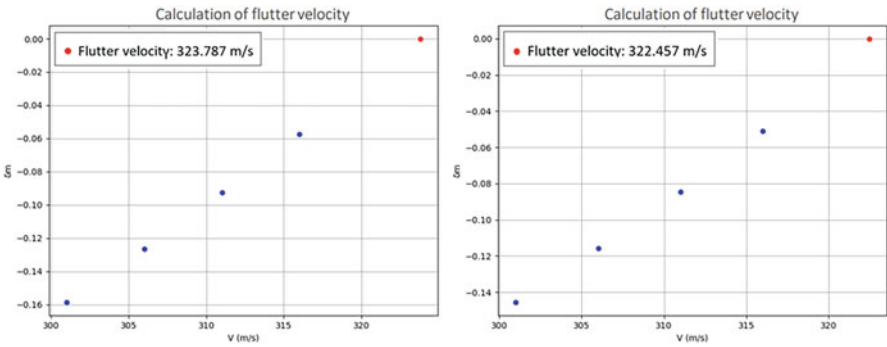


Fig. 2 Flutter velocity without noise (left) and with 10% noise (right)

Table 2 Relative error for predicted flutter velocity

Case	Flutter velocity (m/s)	Relative error (%)
Without noise	323.787	0.011
With noise	322.457	0.399

when calculating it, the previous graph will be interpolated to see at what speed zero damping would be obtained (Fig. 2):

The relative error in both cases is (Table 2):

3.2 Convolutional Neural Networks (CNN)

The analysis has been carried out considering cases with and without noise, and critical cases have also been considered in which different numbers of sensors fail (there are 63 sensors in total). The number of correct predictions obtained for 50 training epochs is (Table 3):

Table 3 Results for the CNN

Failing sensors	Noise (%)	Test dataset	Validation dataset
–	–	40/40	10/10
–	30	40/40	10/10
2	–	40/40	8/10
2	30	40/40	8/10
10	–	40/40	6/10
10	30	40/40	9/10
15	–	40/40	9/10
15	30	40/40	10/10

The results shown prove the effectiveness of the convolutional neural network generated when making classifications, even considering cases with a lot of noise or critical cases in which many sensors fail.

4 Conclusion

First of all, the power that HODMD can have when predicting a destructive phenomenon such as aeroelastic flutter has been demonstrated, since it has been possible to generate a program that gives the chance to see the evolution of the damping of the modes with an increasing speed. There are some modes that decay as velocity increases, but others are amplified, so using HODMD it has been possible to predict from which speed on unstable modes would appear, that is, those modes that contain positive damping. The speed at which the first mode with zero damping appears is known as flutter speed, and it is the speed that needs to be known, since if it is surpassed, the structure can suffer a catastrophic damage. The model generated with this algorithm has turned out to be very robust, working correctly even when there is noise in the data, which is close to what happens in reality.

On the other hand, using the branch of machine learning known as deep learning, a convolutional neural network (CNN) model has been generated, which is capable of classifying signals into stable and unstable after receiving correct training. The training consists of giving a label to the signals, and after selecting the correct training hyperparameters, the network classifies them with a very high precision in general.

Therefore, it has been shown that the algorithms that are being developed today can be very useful for tackling very complex problems, such as the prediction of flutter phenomenon.

Acknowledgements SLC acknowledges the grant PID2020-114173RB-I00 funded by MCIN/AEI/10.13039/501100011033.

References

- García-Fogeda, P., & Arévalo, F. (2014). *Introducción a la aeroelasticidad*. Garceta, Grupo Editorial, Madrid.
- Le Clainche, S., & Vega, J. M. (2017). *High order dynamic mode decomposition*. Elsevier, London.
- Méndez, C. (2020). *Detección de modos de flameo en ensayos en vuelo, utilizando métodos basados en HODMD*. PhD Thesis, Universidad Politecnica de Madrid.
- Torres i Viñals, J. (2020). *Python Deep Learning: Introducción práctica con Keras y TensorFlow*. Marcombo, Online.

An Invariant Feature Space for Flow Region Identification Using Machine Learning



Kheir-eddine Otmani, Esteban Ferrer, and Gerasimos Ntoukas

Nomenclature

ML Machine learning
CFD Computational fluid dynamics

1 Introduction

Machine learning (ML) and data-driven approaches can help computational fluid dynamics (CFD) simulations to enhance numerical performance. For example, ML models are used in the CFD community to reduce the computational cost of numerical simulations (Kochkov et al., 2021; Manrique de Lara & Ferrer, 2022), building alternative closure turbulence models (Ling et al., 2016; McConkey et al., 2022) or using deep learning to recover missing CFD data (Carlberg et al., 2019).

The analysis/detection of flow regions has been also investigated using classification and clustering ML models. For example, Li et al. (2020) and Wu et al. (2019) successfully used data-driven models to detect turbulent/nonturbulent regions in the flow. To automate the detection of boundary layer and wake regions in the flow field, Saetta and Tognaccini (2021) adopted the traditional viscous sensors to Gaussian mixture clustering model while, Callaham et al. (2021) applied clustering techniques to identify dominant physical processes in the flow field.

In our work, we aim to automate the flow region identification using clustering techniques. To this aim, we construct a feature space that can be used as an input to a

K. Otmani (✉) · E. Ferrer · G. Ntoukas
School of Aeronautics, Universidad Politécnica de Madrid, Madrid, Spain
e-mail: otmani.kheir-eddine@alumnos.upm.es; esteban.ferrer@upm.es;
gerasimos.ntoukas@upm.es

soft clustering approach to provide a satisfactory categorization of the flow field. We constrain this space to be independent of the coordinate frame used to generate the data, and a Gaussian mixture model is used to cluster the data. We apply the method to a LES simulation of a cylinder flow at $Re = 3900$ to distinguish boundary layer, wake, and outer flow regions. The resulting regions are compared to the regions obtained using classic sensors of viscous/inviscid regions. These sensors are highly dependent on the choice of a threshold, a choice that can be subjective and challenging in many scenarios (Lanzetta et al., 2015). ML clustering eludes the necessity of any threshold. The rest of the paper is organized as follows. In Sect. 2, we present the methodology. In Sect. 3, we briefly discuss the clustering results obtained for LES test case of a flow past cylinder at $Re = 3900$. Finally, conclusions are summarized in Sect. 4.

2 Methodology

In this work, we construct a flow feature space E that carries the necessary physical insights to discriminate boundary layer and wake region from the outer flow region. Our approach is based on the assumption that the boundary layer and wake region are characterized by non-negligible viscous dissipation and high rotations, while the outer flow region is close to inviscid and irrotational. The feature space E is constrained to maintain Galilean invariance; therefore, we propose to use the invariants of strain and rotational rate tensors as they carry relevant physical insights. The strain rate tensor has two principal invariants:

$$Q_s = \frac{1}{2} \left((\text{tr}(S))^2 - \text{tr}(S^2) \right); \quad R_s = -\frac{1}{3} \det(S) \quad (1)$$

where $S = \frac{J+J^T}{2}$ is the strain rate tensor, $J = \nabla U$ is the gradient of the velocity field $U = (u, v, w)$, and tr and \det are the trace and determinant operators, respectively. The rotational rate tensor $\Omega = \frac{J-J^T}{2}$ has one invariant defined as:

$$Q_\Omega = -\frac{1}{2} (\text{tr}(\Omega^2)) \quad (2)$$

Q_s is proportional to viscous dissipation of kinetic energy ϵ as $\epsilon = -4\mu Q_s$ where μ is fluid viscosity, whereas positive and negative values of R_s indicate strain production or strain destruction processes, respectively, Q_Ω is proportional to vorticity and enstrophy \mathcal{E} , and then Q_Ω is relevant in indicating rotational regions in the flow field (da Silva & Pereira, 2008). We also include the L_2 -norm of the lamb vector $L = U \times \omega$ as an additional physical insight to the feature space, where U and ω are velocity and vorticity fields, respectively, and the L_2 -norm of the lamb vector is strictly 0 in irrotational regions and strictly positive in rotational regions. The feature space proposed here is:

$$E = (Q_s, R_s, Q_\Omega, \|L\|_2) \quad (3)$$

2.1 Gaussian Mixture

Gaussian mixture (GM) model is a probabilistic clustering approach, which assumes that the data is generated from a combination of normal distributions called mixture components. The model tends to estimate the parameters (mean and variance) of each of these normal distributions; this process is done iteratively using the expectation-maximization method. For clustering purposes, each of the normal mixture components is considered as a cluster, and each sample in the data is then assigned to one of the clusters based on a membership probability (McLachlan et al., 2019). In this work, we implement the GM model using *scikit-learn* python library (Pedregosa et al., 2011); *scikit-learn* provides several classification, regression, and clustering ML models. GM model needs to be pre-supplied with the number of normal components N before initializing the training process; for our purposes, we choose $N = 2$ since we aim to detect two different flow regions: on the one hand, the boundary layer and wake region and, on the other hand, the outer flow region.

3 Results and Discussion

We simulate the flow past a cylinder at $Re = 3900$ using a high-order discontinuous Galerkin method (Manzanero et al., 2020) with polynomial order 4 and a Smagorinsky subgrid LES closure model. The clustering results obtained for a snapshot of the cylinder case are presented and compared with the regions detected with eddy viscosity sensor F_{μ_t} (Paparone & Tognaccini, 2003) defined as:

$$F_{\mu_t} = \frac{\mu + \mu_t}{\mu}, \quad (4)$$

where μ_t and μ are turbulent viscosity and fluid viscosity, respectively. F_{μ_t} is used to detect viscous regions in turbulent flows. Detecting flow regions based on F_{μ_t} sensor needs a careful choice of a threshold K which can be highly subjective and challenging (Lanzetta et al., 2015), while ML methods do not need any threshold value to perform the clustering. In Fig. 1, the detected regions obtained using GM model are shown and compared with regions obtained with F_{μ_t} ; notice that the selected threshold K in this case is chosen subjectively since no guidelines are available to accurately select this value.

As shown in Fig. 1, the detected regions using ML clustering are comparable to the regions detected using F_{μ_t} sensor (after tuning the sensor threshold).

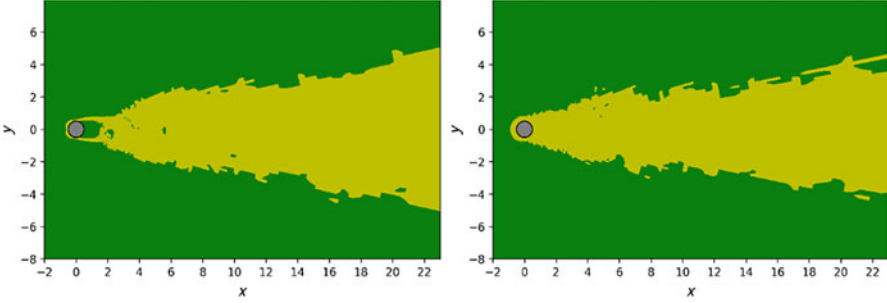


Fig. 1 Flow region identification using F_{μ_t} sensor (left) with $K=1.75$ and GM clustering with feature space E (right). Green, outer flow region; yellow, boundary layer and wake region

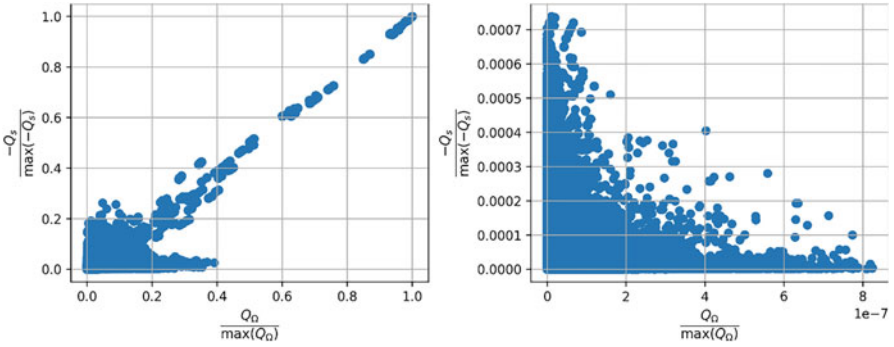


Fig. 2 Scatter plot of (Q_Ω, Q_s) in the detected boundary layer and wake region (left) and the detected outer flow region (right)

To elaborate further the detected regions with ML clustering, we show the scatter plot of (Q_Ω, Q_s) in the two detected regions, and we scale the plots with the maximum values of Q_Ω, Q_s . As shown in Fig. 2, the detected boundary layer and wake region is characterized by high viscous dissipation and high vorticity, while the outer flow region is almost inviscid and irrotational.

4 Conclusion

Our ML clustering methodology reveals satisfactory results for the clustering of flow regions and is free of subjective threshold. In the future, these regions will be used to define local mesh adaption, where the polynomial order is increased to enhance the numerical accuracy.

References

- Callaham, J. L., Koch, J. V., Brunton, B. W., Kutz, J. N., & Brunton, S. L. (2021). Learning dominant physical processes with data-driven balance models. *Nature Communications*, *12*, 1016. <https://doi.org/10.1038/s41467-021-21331-z>
- Carlberg, K. T., Jameson, A., Kochenderfer, M. J., Morton, J., Peng, L., & Witherden, F. D. (2019). Recovering missing CFD data for high-order discretizations using deep neural networks and dynamics learning. *Journal of Computational Physics*, *395*, 105–124. <https://doi.org/10.1016/j.jcp.2019.05.041>
- da Silva, C. B., & Pereira, J. C. F. (2008). Invariants of the velocity-gradient, rate-of-strain, and rate-of-rotation tensors across the turbulent/nonturbulent interface in jets. *Physics of Fluids*, *20*, 055101. <https://doi.org/10.1063/1.2912513>
- Kochkov, D., Smith, J. A., Alieva, A., Wang, Q., Brenner, M. P., & Hoyer, S. (2021). Machine learning accelerated computational fluid dynamics. *ArXiv210201010 Physics*, *118*(21), e2101784118.
- Lanzetta, M., Mele, B., & Tognaccini, R. (2015). Advances in aerodynamic drag extraction by far-field methods. *Journal of Aircraft*, *52*, 1873–1886. <https://doi.org/10.2514/1.C033095>
- Li, B., Yang, Z., Zhang, X., He, G., Deng, B.-Q., & Shen, L. (2020). Using machine learning to detect the turbulent region in flow past a circular cylinder. *Journal of Fluid Mechanics*, *905*, A10. <https://doi.org/10.1017/jfm.2020.725>
- Ling, J., Kurzwaski, A., & Templeton, J. (2016). Reynolds averaged turbulence modelling using deep neural networks with embedded invariance. *Journal of Fluid Mechanics*, *807*, 155–166. <https://doi.org/10.1017/jfm.2016.615>
- Manrique de Lara, F., & Ferrer, E. (2022). Accelerating high order discontinuous Galerkin solvers using neural networks: 1D Burgers' equation. *Computers & Fluids*, *235*, 105274. <https://doi.org/10.1016/j.compfluid.2021.105274>
- Manzanero, J., Ferrer, E., Rubio, G., & Valero E. (2020). Design of a smagorinsky spectral vanishing viscosity turbulence model for discontinuous galerkin methods. *Computers & Fluids*, *200*, 104440.
- McConkey, R., Yee, E., & Lien, F. S. (2022). Deep structured neural networks for turbulence closure modeling. *Physics of Fluids*, *34*, 035110. <https://doi.org/10.1063/5.0083074>
- McLachlan, G. J., Lee, S. X., & Rathnayake, S. I. (2019). Finite mixture models. *Annual Review of Statistics and Its Application*, *6*, 355–378. <https://doi.org/10.1146/annurev-statistics-031017-100325>
- Paparone, L., & Tognaccini, R. (2003). Computational fluid dynamics-based drag prediction and decomposition. *AIAA Journal*, *41*, 1647–1657. <https://doi.org/10.2514/2.7300>
- Pedregosa, F., Varoquaux, G., Gramfort, A., Michel, V., Thirion, B., Grisel, O., Blondel, M., Prettenhofer, P., Weiss, R., Dubourg, V., Vanderplas, J., Passos, A., Cournapeau, D., Brucher, M., Perrot, M., & Duchesnay, E. (2011). Scikit-learn: Machine learning in Python. *Journal of Machine Learning Research*, *12*, 2825–2830.
- Saetta, E., & Tognaccini, R. (2021). Identification of flow field regions by machine learning. In *AIAA SCITECH 2022 Forum*. <https://doi.org/10.2514/6.2022-0457>
- Wu, Z., Lee, J., Meneveau, C., & Zaki, T. (2019). Application of a self-organizing map to identify the turbulent-boundary-layer interface in a transitional flow. *Physical Review Fluids*, *4*, 023902. <https://doi.org/10.1103/PhysRevFluids.4.023902>

Smart Disaster Management Using Big Data Analytics



Ali Burak Can, İsmail Burak Parlak, and Tankut Acarman

1 Introduction

Emergencies are the events caused by natural factors or human factors, causing human losses, environmental damage, material losses, and psychological effects, threatening and disrupting people's lives and livelihoods. In disaster management, the social microblogging becomes a knowledge host where people search information resources in their community (Mangalathu & Burton 2019). The crisis is analyzed by emergency and rescue organizations. However, the complex behavior of the risk is not trivial to handle in massive disasters. It requires the hierarchical organization of locations and the description of the emergency through the feedbacks from the inhabitants. The feedback generated in Twitter about disaster situations contains excessive information for the emergency calls. Nevertheless, unexplained information is considered as noise, and true emergency calls might be ignored if the microblogs are not properly classified. Thus, this information can reduce the level of humanitarian response to an emergency that occurs. In text-based disaster analysis, an accurate model is required to tackle with real-time information in a stack of flooding information for emergency and nonemergency cases. Twitter has an important role in providing all kinds of information about disaster events such as damage, number of victims, and warnings in text, pictures, and videos. Therefore, microblogs can be used to conduct smart disaster management, especially regarding information about earthquake events. In this case, natural language processing becomes an extension of data extraction for textual data, where all activities are analyzed with earthquake-related terms. The lexical analysis arises the semantic gap between emergency/rescue and nonemergency/non-rescue classes. The significance of the microblogs might be ranked through their distance to epicenter of the disaster. The

A. B. Can · İ. B. Parlak (✉) · T. Acarman
Galatasaray University, Department of Computer Engineering, NLPLAB, Istanbul, Türkiye
e-mail: aliburak.can@ogr.gsu.edu.tr; bparlak@gsu.edu.tr; tacarman@gsu.edu.tr

priority of the disaster knowledge is associated to the relevance in social media and mobile applications. In a similar way, collaborative mapping and crowd sensing tools would be applied in data analysis during action planning and emergencies. Our study focuses on this problem by considering the classification routines as a potential premise in disaster analysis given by the community. The smart disaster management cycle encompasses four main steps: mitigation, preparedness, responses, and recovery. Our study considers a dataset for the 2020 Izmir earthquake in the post-disaster phase for the measurement of responses. In order to analyze the responses, two classes, rescue and non-rescue, have been created. Tweets become meaningful to identify the spatiotemporal severity of earthquake fluctuations and validate the rotation of emergency and rescue organizations in disaster zones. Our main contribution is the spatiotemporal analysis of rescue/non-rescue classes by creating manually annotated corpus and classifying rescue tweets. BERT transformer model has been trained to generate automatic labels. The performance of smart disaster classification has been measured through three different methods: linear support vector machines (SVM), multinomial naïve Bayes (NB), and DistilBERT-Turkish. The study is organized as follows. Section 2 encompasses the methodology and the main steps of classifiers, the dataset, and the evaluation process. Moreover, the classification results have been reviewed in Sect. 3 where the results have been presented through the statistical scores. Consequently, we have concluded our study by highlighting the key points and our future steps in Sect. 4.

2 Method

Our dataset has been created for the 2020 Izmir earthquake that took place on November 30, 2020. Turkish tweets have been retrieved using earthquake-related terms, street, neighborhood, and building names for a time interval of 1 year. 170,000 tweets have been obtained after the setup of data collection. At a glance, tweets, time, and location information have been collected with Twitter API. Microblog preprocessing is a crucial step to improve classification performance. In this step, mentions, links, emoticons, hashtags, and punctuations have been removed. The dataset has been normalized with diacritic and spelling correction. However, the preprocessing step differs in BERT modeling due to its own process. BERT-based models apply transformers where punctuations, numbers, whitespaces, stop words, and lemmatizing steps are not applied. The second step of this study is the binary classification of tweets. Our initial guess was to generate equally distributed rescue and non-rescue labels. For this purpose, we have manually labeled 2000 tweets (1000, rescue; 1000, non-rescue), and we have trained BERT transformer model to create automatic labels in a semi-supervised way. Three different methods have been used in this study: linear support vector machines, multinomial naïve Bayes, and DistilBERT-Turkish. A support vector machine (SVM) is a supervised algorithm that aims to create a machine learning model for prediction or classification. In the classification process, considering K -dimensional data, SVM finds

K-dimensional hyperplane. If there is a linearly separable dataset in the binary classification problem, there are infinitely many hyperplanes that can separate this dataset. Multinomial Naive Bayes models the distribution of words in a document as polynomial. The document is treated as a string of words, and it is assumed that the position of each word is formed independently of the other. BERT is a generalized language model with 24 transformer blocks, 1024 hidden layers, and 349M parameters. Pre-trained with large text data, BERT allows it to be transferred for other small language processing tasks as needed (fine-tuning). Thus, it has demonstrated state-of-the-art success for 11 natural language processing tasks. Unlike other previous learning models used in natural language processing, it can process multiple words simultaneously. This both supports parallel work and contributes to the capture of the context. DistilBERTurk is an open source distilled version of Turkish BERT model which is trained by using the cased version of BERTurk as teacher model.

3 Results and Discussion

Our Twitter dataset has been preprocessed in order to remove unrelated information such as hashtags and emoticons. The data visualization becomes a qualitative measurement to reveal the spatiotemporal effects in data dynamics. The non-rescue map has been prepared according to non-rescue tweets as shown in Fig. 1. Even if the earthquake center behaves as a hot zone, other metropolises provide non-rescue information. Therefore, Istanbul and Ankara would be much more predominant and relevant in non-rescue class in Fig. 1. The rescue information has been projected on Izmir map as shown in Fig. 2. The Izmir center provided a meaningful distribution of rescue class. The rescue and non-rescue classification

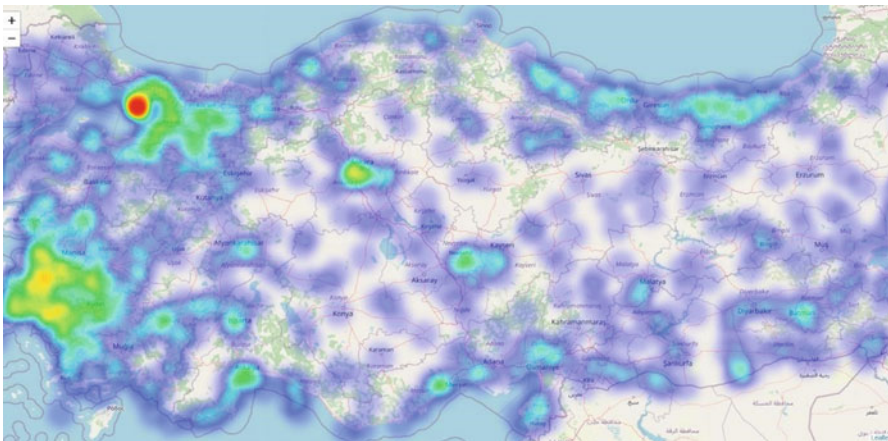


Fig. 1 Non-rescue heatmap for the 2020 Izmir earthquake

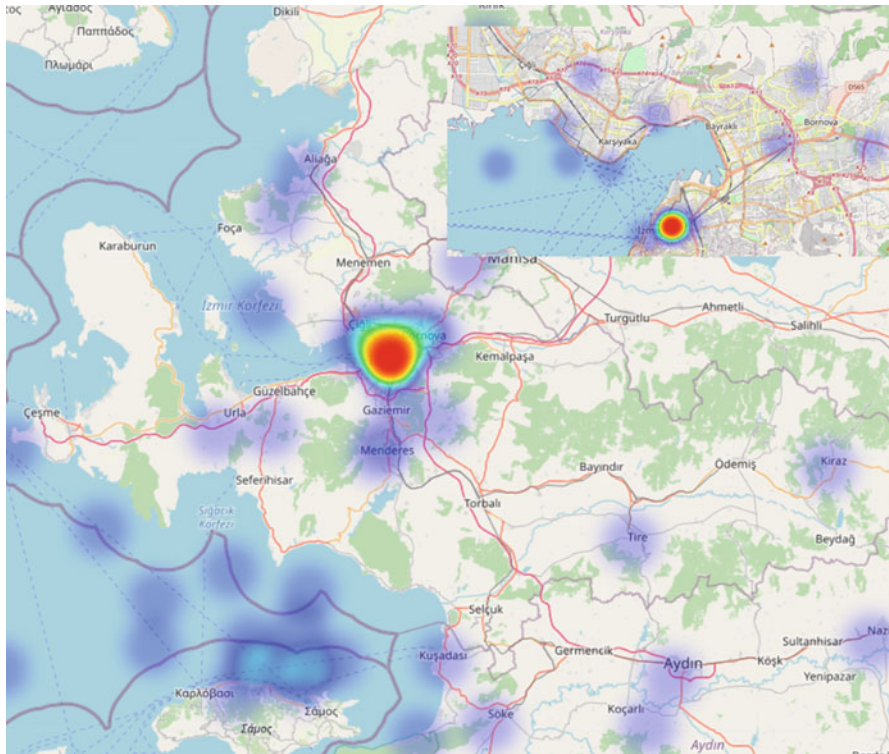


Fig. 2 Rescue heatmap for the 2020 Izmir earthquake

Table 1 Evaluation of non-rescue and rescue classes using DistilBert-Turkish, linear SVM, and multinomial naïve Bayes classification

Dataset	Evaluation	DistilBert-Turkish (%)	Support vector machines (%)	Naive Bayes (%)
Non-rescue	Precision	96	93	88
	Recall	94	94	89
	F1	95	93	88
Rescue	Precision	94	94	89
	Recall	97	92	88
	F1	95	93	88

results have been evaluated through precision, recall, and F1 metrics. DistilBERT-Turkish provided more accurate classification in terms of rescue class. The scores for linear SVM and multinomial NB were almost equal in both classes. Table 1 shows the statistical evaluation of classification techniques. We have observed that fine-tuned DistilBERT would tackle with the word disambiguation and the semantic complexity (Table 1).

4 Conclusion

The capability of disaster management becomes more efficient with the accurate and relevant information resources. The synthesis of disaster information channels is considered as the most challenging issues in smart city analysis. Even if multi-scale and multi-platform resources increase the capacity of information flood, they introduce irrelevant noise that reduces the planning of service quality. In this case, automatic analysis with big data analytics becomes crucial regarding the disaster-affected people. Our study focused on the 2020 Izmir earthquake in order to classify rescue and non-rescue events. The classification scores are presenting promising values in the planning phase of emergencies within the short time interval of post-earthquake phase. In the future steps, we are planning to develop our framework to create an interactive dashboard to perform a real-time analysis of disaster-related microblogs.

References

- Mangalathu, S., & Burton, H. V. (2019). Deep learning-based classification of earthquake-impacted buildings using textual damage descriptions. *International Journal of Disaster Risk Reduction*, 36, 101111.
- Monteil, C., Simmons, P., & Hicks, A. (2020). Post-disaster recovery and sociocultural change: Rethinking social capital development for the new social fabric. *International Journal of Disaster Risk Reduction*, 42, 101356.
- Sanh, V., Debut, L., Chaumond, J., & Wolf, T. (2019). DistilBERT, a distilled version of BERT: Smaller, faster, cheaper and lighter. *arXiv Preprint arXiv:1910.01108*.
- Saroj, A., & Pal, S. (2020). Use of social media in crisis management: A survey. *International Journal of Disaster Risk Reduction*, 48, 101584.
- Schweter, S. (2020). *Berturk-bert models for turkish*. Online: <https://doi.org/10.5281/zenodo.3770924>.

A Critical Review of Deployable Truss Masts and Proposal of a New Mast: HiDAM



Yunus Cebeci, Murat Demirel, and Gökhan Kiper

1 Introduction

Small cargo volumes of space crafts are a big limitation in space applications. This restriction is the main design parameter for structures requiring larger aperture diameters and longer focal lengths, because it inherently affects the functionality of these structures such as their resolutions and working spaces (Puig et al., 2010). Deployable structures are used when compactness is required during transportation and storage. Packing ratio of these structures is an important design parameter. Several studies address the compactness problem for space applications (Darooka & Jensen, 2001; Hanaor & Levy, 2001; Jensen & Pellegrino, 2001; Tibert, 2002; Kiper & Söylemez, 2009; Puig et al., 2010; Straubel, 2012).

This study is on deployable masts (DMs), which are commonly used in satellites and other space structures. DMs can be classified as coilable booms and articulated masts which are truss-like structures containing rigid components (Straubel, 2012). Generally, masts have larger cross section compared to booms (Ihle et al., 2016). In choosing a DM, the length of the mast and the quantity of payload necessary for the application are critical factors. While the coilable structures are preferred where low endpoint positioning accuracy (mm-cm level) and less load-bearing capacity are needed, articulated and telescopic masts are suitable for the applications requiring higher load-bearing capacity (up to 100 kg) and high endpoint accuracy (μm -mm level) (Puig et al., 2010). Telescopic masts have a higher folding rate compared to articulated masts, but articulated masts are more convenient for space applications that require higher bearing capacity, deployment reliability, and positioning accuracy. Deployable truss masts (DTMs) usually have similar parts such as longerons for longitudinal elements and battens for transverse elements (Fig. 1A).

Y. Cebeci · M. Demirel · G. Kiper (✉)

Izmir Institute of Technology, Izmir, Türkiye

e-mail: yunuscebeci@iyte.edu.tr; muratdemirel@iyte.edu.tr; gokhankiper@iyte.edu.tr

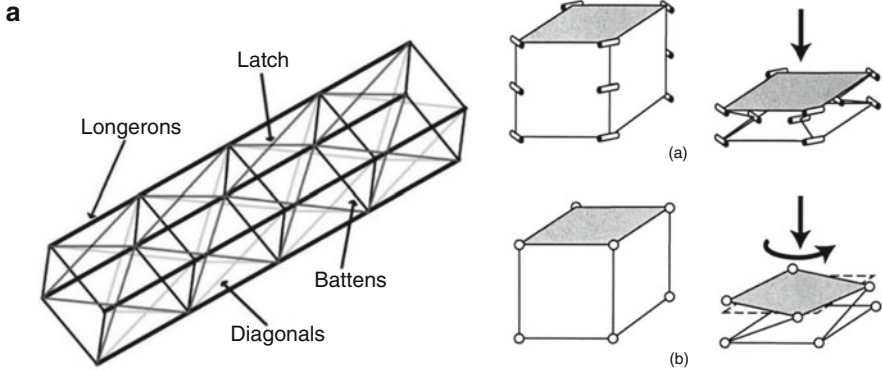


Fig. 1 (A) DTM terminology, (B) DM folding principles, (a) translational type, (b) screw type (Pellegrino, 2014)

The polygonal structures formed by battens can also be called as platforms. There may be hinges at the ends of the longerons and battens. Also, these structures may require diagonal cables and latch mechanisms to increase stiffness. Pellegrino (2014) describes two folding principles for deployable masts (Fig. 1B) which can be named as translational-type folding and screw-type folding. Obviously, these folding principles directly affect the motion of the DMs. For instance, a mast performs a synchronous deployment if its folding principle is based on the screw type, but if it is the translational type, it executes a sequential deployment.

In this paper, first, a critical review for DTMs is presented. Then a new design with higher packing ratio compared to existing structures is introduced.

2 Existing Deployable Truss Masts

Several types of articulated masts have been patented (Mauch, 1969; Benton & Robbins Jr, 1986; Hedgepeth & Adams, 1986; Kitamura et al., 1990). ATK/ABLE Engineering Company designed the Folding Articulated Square Truss (FAST) to support the solar arrays on the International Space Station (ISS) (Warden, 1987). Able Deployable Articulated Mast (ADAM) was designed as an improved version of the FAST, and it has been flight proven with many applications such as Shuttle Radar Topography Mission (Ramirez, 1998; Gross & Messner, 1999). Xue et al. (2018) studied the influence parameters of the ADAM in detail as well. Since these masts have longer focal lengths and higher payload capacity, they are mainly used in applications requiring baseline extension with a radar at the tip of the mast or high-resolution optical systems. Additionally, while FAST realizes translational type of folding principle, ADAM has screw-type folding principle.

Working on the parametric modeling of the open and closed states of DTMs, Deng et al. (2011) designed a tapered DM with low mass and increased stiffness, for

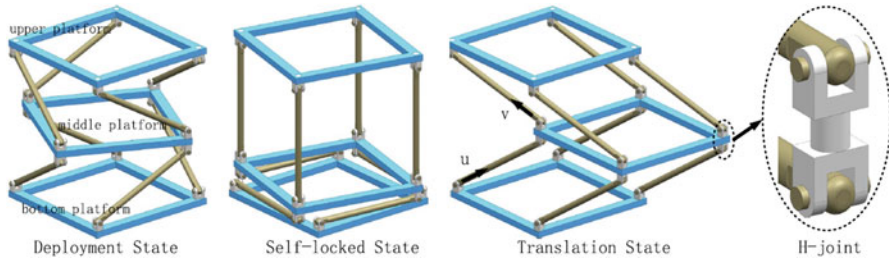


Fig. 2 Self-lockable deployable structure (SDS) presented by Zhao et al. (2018)

which the height of the DTM can be determined with the given geometrical analysis with no regard to its constructional design. In their study, it is shown that the mechanical properties of the tapered design are improved compared to DTMs with identical cross-sectional areas. Guo and You's (2012) DTM design with serially connected Bennett linkages has single degree of freedom (DoF), and its open and closed dimensions can be calculated parametrically. Another novel DTM is proposed by Lu et al. (2014) using the Hoecken linkage as a deploying unit, and they determined appropriate actuation systems according to static analysis and structural behavior.

In most space applications, a constant orientation of the tip of the mast is desired during the motion. For instance, deploying the solar panels of the ISS requires only translational motion, and most components to be located at a distance out of the satellite body such as cameras and sensors should not rotate during deployment. To achieve this, the Borel-Bricard motion was used (Bricard, 1896; Borel, 1905). It is a spatial motion in which all point paths are spherical curves. It is used in design of a DTM based on Wren platforms by Kiper and Söylemez (2011), where over-constrained single-DoF mechanisms with Borel-Bricard motion are issued. Lee and Hervé (2014) also studied mechanisms with the Borel-Bricard motion in detail.

Based on the work by Kiper and Söylemez, Zhao et al. (2018) proposed a DTM system, which has better stiffness characteristics than ADAM. They designed and made a prototype of the self-lockable deployable structure (SDS) which comprises reconfigurable extended joint (REJ). Later the design was patented (Wang et al., 2016). This unit also realizes Borel-Bricard motion. Once the mast is fully deployed, singularity occurs due to the self-motion of the longerons. As a result, it becomes self-locked against longitudinal forces. When the mast is fully deployed, only the first two units need to be folded to lock the entire structure completely.

Figure 2 shows the SDS and its configurations. Here, the hinges used to connect the longerons and battens at the corners are called H-joints which have 3-DoF with two parallel axes and an axis perpendicular to them. Another DTM based on Wren platforms is proposed by Wang et al. (2022) recently, in which the link lengths are optimized to maximize the packing ratio by replacing universal joints with a pair of skew revolute joints. In other words, the H-joint in SDS is altered by adding an offset. They also developed a mathematical model and proved that this DM has the largest packing ratio of all comparable structures in the literature (Fig. 3). By examining these DTMs, it is seen that the packing ratio can be increased by

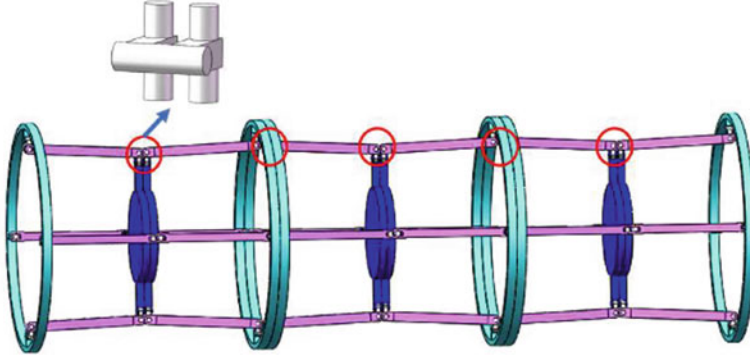


Fig. 3 DTM by Wang et al. (2022)

modifying constructional details. In the next section, a new DTM called highly deployable articulated mast (HiDAM) is introduced and compared with the other DTMs in the literature.

3 Design of Highly Deployable Articulated Mast

To be able to compare any two DTMs in terms of their packing ratios, their footprint should be equal. Since the canisters used to store these structures are mostly cylindrical (Galvez et al., 2011), the base area covered by the structure is a circle. The polygonal platforms composed of battens and the longerons connecting these platforms at their corners must be circumscribed by this circle.

In Wang et al.'s (2022) study, the joint axis perpendicular to the parallel axes to which the longerons are attached is designed with an offset. With the help of this modification, it is possible to design the platforms to act as the perimeter boundary to avoid overlaps within the allowable volume. Although this design makes it easier to position the parts, it also causes a loss of usable circumference due to the platform wall thickness, so it causes using shorter longerons which adversely affect the packing ratio. Since the goal is to increase packing ratio in the proposed design, we used three-sided star-shaped platforms, which allows us to locate longer longerons inside the circumscribing circle. As a result, a deployable unit realizing Borel-Bricard motion is constructed.

4 Conclusion and Future Works

The final optimization computations will be carried out for HiDAM after the constructional design is finalized according to the aforementioned design constraints. However, initial results showed that packing ratios larger than 17 can be

easily obtained with the proposed model. This is about 12% better than 15.17 which is reported by Wang et al. (2022). The DTMs have the same circumradius of 45 mm. For larger circumradius values, larger packing ratios can be obtained.

Due to the limitations, the link lengths of a DTM mechanism cannot be determined considering geometrical restrictions only. Therefore, the mechanism design should be performed along with the constructional design. Once the CAD design is finalized along with structural and modal analyses, a prototype of HiDAM will be produced, and functional and performance tests will be carried out to check the packing ratio, stiffness, and positioning accuracy.

Acknowledgments This study was financially supported by the Scientific and Technological Research Council of Turkey (TUBITAK) under 1005 – National New Ideas and Products Research Support Program with the project number 120 M812.

References

- Benton, M. D., & Robbins Jr, W. M. (1986). *Extendible structures*. Patent US4599832A.
- Borel, É. M. (1905). *Mémoire sur les Déplacements à Trajectoires Sphériques*. Imprimerie Nationale.
- Bricard, R. (1896). Géométrie cinématique—sur un déplacement remarquable. *Comptes-Rendus de l'Académie des Sciences, Paris*, 123(22), 939–940.
- Darooka, D., & Jensen, D. (2001). *Advanced space structure concepts and their development*. In 19th AIAA applied aerodynamics conference (p. 1257).
- Deng, Q., et al. (2011). Design and analysis of a tapered deployable mast. In *Key engineering materials* (pp. 31–34). Trans Tech Publishing.
- Galvez, R., et al. (2011). The space shuttle and its operations, in wings. In *Orbit scientific and engineering legacies of the space shuttle* (3409th ed., pp. 53–73). Government Printing Office.
- Gross, D., & Messner, D. (1999). *The ABLE deployable articulated mast—enabling technology for the Shuttle Radar Topography Mission*. In 33rd Aerospace mechanisms symposium.
- Guo, H., & You, Z. (2012). Deployable masts based on the Bennett linkage. In *Advances in reconfigurable mechanisms and robots I* (pp. 739–747). Springer.
- Hanaor, A., & Levy, R. (2001). Evaluation of deployable structures for space enclosures. *International Journal of Space Structures*, 16(4), 211–229.
- Hedgepeth, J. M., & Adams, L. R. (1986). *Rigid diagonal deployable lattice column*. Patent US4569176A.
- Ihle, A., et al. (2016). *Deployable structures activities at the European space agency's structures section*. In 14th European conference on spacecraft structures, materials and environmental testing (pp. 1–14).
- Jensen, F., & Pellegrino, S. (2001). *Arm development review of existing technologies*. Cambridge University.
- Kiper, G., & Söylemez, E. (2009). *Deployable space structures*. In 4th International conference on recent advances in space technologies (pp. 131–138). İstanbul.
- Kiper, G., & Söylemez, E. (2011). *Modified Wren platforms*. In 13th IFToMM world congress (Vol. 1, pp. 1183–1187). Guanojuato, Mexico.
- Kitamura, T., et al. (1990). *Development of a high stiffness extendible and retractable mast 'Himat' for space applications*. In 31st structures, structural dynamics and materials conference (p. 1054).

- Lee, C.-C., & Hervé, J. M. (2014). Bricard one-dof motion and its mechanical generation. *Mechanism and Machine Theory*, 77, 35–49.
- Lu, S., et al. (2014). A new family of deployable mechanisms based on the Hoekens linkage. *Mechanism and Machine Theory*, 73, 130–153.
- Mauch, H. R. (1969) *Deployable lattice column*. Patent US3486279A.
- Pellegrino, S. (2014). *Deployable structures*. Springer.
- Puig, L., Barton, A., & Rando, N. (2010). A review on large deployable structures for astrophysics missions. *Acta Astronautica*, 67(1–2), 12–26.
- Ramirez, E. (1998). *Shuttle Radar Topography Mission*. Available at: https://www2.jpl.nasa.gov/srtm/mast_photos.html. Accessed 11 Sept 2019.
- Straubel, M. (2012). *Design and sizing method for deployable space antenna*. Deutsches Zentrum für Luft-und Raumfahrt eV.
- Tibert, G. (2002). *Deployable tensegrity structures for space applications*. KTH.
- Wang, H., et al. (2016). *Reconfigurable extended joint*. Patent CN104608117B.
- Wang, J., Kong, X., & Yu, J. (2022). Design of deployable mechanisms based on Wren parallel mechanism units. *Journal of Mechanical Design*, 144(6), 63302.
- Warden, R. M. (1987). *Folding, articulated, square truss*. In 21st Aerospace mechanisms symposium, LB Johnson Space Center, Houston, Texas.
- Xue, N., et al. (2018). *The influence parameters of 60m ABLE deployable articulated mast mode*. In Proceedings of the international symposium big data and artificial intelligence (pp. 299–305).
- Zhao, L., et al. (2018). Sequentially assembled reconfigurable extended joints: Self-lockable deployable structure. *Journal of Aerospace Engineering*, 31(6), 4018103.

Implementation of Trajectory Propagator for Artillery Projectiles Based on Artificial Neural Networks



Alejandro Céniz Bragado, Alberto Solera-Rico, and M. A. Gómez

Nomenclature

GNC	Guidance, navigation, and control
CEP	Circular error probability
CCF	Course correction fuses
GPS	Global positioning system
MPMM	Modified punctual mass model
DOF	Degree of freedom

1 Introduction

This work focuses on external ballistics, studying the trajectory and atmospheric flight of the projectile from the moment it is launched, until the impact on the target occurs. In non-guided conventional weapons, accuracy worsens with range, enlarging the CEP. The CEP can be defined as the radius of the circle where there is a probability of 50% of projectiles hitting inside. To solve the precision problem, course correction fuses (CCF) were developed. These fuses normally form part of actualization programs of non-guided projectiles, where the older fuses are replaced by CCF. CCF electronics calculates the trajectory in mid-flight by the previously mentioned propagators, comparing the calculated impact point with the GPS target (Fresconi & Plostins, 2008). Then, aerodynamic actuators present in the CCF modify the trajectory, so the calculated impact point and the target signal coincide (Fresconi

A. C. Bragado (✉) · A. Solera-Rico · M. A. Gómez
Universidad Politécnica de Madrid, Madrid, Spain

Instituto Nacional de Técnica Aeroespacial, San Martín de la Vega, Spain
e-mail: a.ceniz@alumnos.upm.es; asolric@inta.es; gomezlma@inta.es

et al., 2011). Normally, the performance and precision of these propagators improve with the quality of electronics, thus increasing the price of the system.

2 Method

2.1 Propagator

2.1.1 Models

A simulator is developed within MATLAB and Simulink for creating the dataset to train the neural network (NN). For this, two different ballistic trajectory models have been implemented: MPMM and the five-degree-of-freedom (DOF) model. MPMM stands for modified punctual mass model (McCoy, 2012), which consists of a four-degree-of-liberty model where all the mass is concentrated in the center of gravity. The first three degrees correspond to the three degrees of translation of the punctual mass. The fourth degree corresponds to what it could be considered a degree of freedom of the projectile as a solid rigid, which is the equilibrium yaw angle. For this model, the only forces considered are the lift force, drag force, and Magnus force. However, to calculate the equilibrium pitch angle, there have been implemented coefficients of other forces such as the spin damping force, overturning moment, and Magnus moment.

On the other hand, the five-degree-of-freedom model is a simplification of the six-degree-of-freedom model (Lieske & Reiter, 1966). In this model, the degree of freedom of the spin of the projectile is taken out. This is because the time step needed to represent accurately the projectile spin is much lower than the one normally used to integrate the trajectory, so there is a considerable increase in the time taken by the computer to perform the calculations (Fresconi et al., 2011). In this work, it will be studied how this difference affects the training. In the two models, a rounded-flattened Earth model has been used.

Additionally, atmospheric and perturbation models were implemented. In the first model, pressure, density, and temperature change with height, while in the second model a different module and direction wind gust are simulated at each “shot”. Each shot is defined by its initial conditions: gun elevation, azimuth, latitude, and initial projectile velocity. All shots share the same projectile, of which its data has been provided by the National Institute of Aerospace Technology (INTA). This data consists of projectile weight, aerodynamic nonlinear coefficients, mass inertia moments, and the cannon bore. The cannon bore defines the initial spin velocity of the projectile that is crucial in the calculation of the equilibrium yaw angle (Theodoulis & Wernert, 2017).

2.1.2 Dataset Creation

These initial variables are defined in MATLAB that are sent to Simulink which performs the simulation. Then the desired variables are extracted from Simulink into MATLAB, where a postprocess classifies these variables, namely: position and velocity in launch axis, wind module and wind direction and the initial conditions previously described, into variables that affect the location of the impact point, and variables that affect the flight duration of the projectile.

These simulated shots create the datasets. Datasets are set up by discretizing the initial variable space, making all the possible shot combinations of initial variables. Since the number of variations of the initial variables affects directly to the size of the datasets, a heuristic approach based on the duration of the projectile flight is used for selecting the combinations used for each shot, with the aim to minimize the training time, without losing propagator performances.

2.2 Neural Network

The neural network (NN) is fed with the datasets. The input data are all the variables stated previously, and the NN predictions of the point of impact are compared with the target data, used as the “correct solution.”

The created NN architecture consists of seven hidden layers with 256 neurons in each layer. The model of neural network is a densely connected neural network, where each neuron of a layer is connected to every neuron of the adjacent layers. The neural network has been trained for 500 epochs. The results can be observed below (Fig. 1).

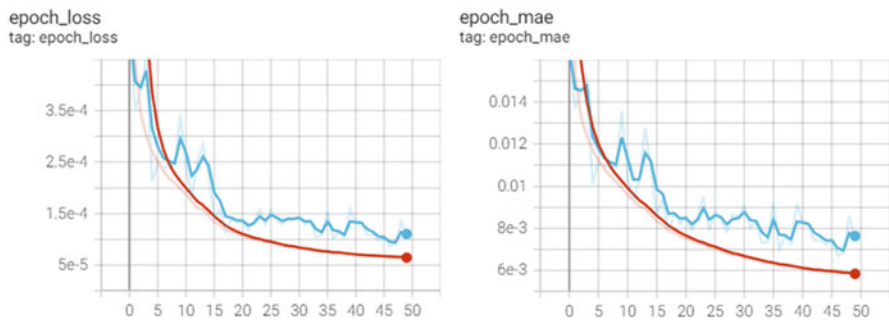


Fig. 1 Training error (red) and validation error (blue) in the training process at 500 epochs. Mean squared error (left) and mean absolute error (right)

2.3 Calculation

As it was previously stated, the MPMM principal idea is to analyze the equilibrium angle of attack during the whole trajectory. In this model, the oscillation around this angle of equilibrium is disregarded in contrast to the complete model. This equilibrium angle can be calculated by the following expression as stated in McCoy (2012), where a more complete model can be found:

$$\bar{\alpha}_{eq} = - \frac{8I_x p (\bar{v} \times \dot{\bar{u}})}{\pi \rho d^3 (C_{M\alpha} + C_{M\alpha^3} \alpha_{eq}^2) v^4} \quad (1)$$

It was previously stated that the five-DOF model is a simplification over the six DOF where the roll angle is taken out of the equations due to the hypothesis of geometric and mass symmetry around the projectile longitudinal axis. The model is now calculated in function of the angular momentum of the projectile with the following expression. The details of the assumptions and limitations of this simplification can be found in Lieske and Reiter (1966):

$$\bar{H} = I_x p \bar{x} + I_y (\bar{x} \times \dot{\bar{x}}) \quad (2)$$

3 Results and Discussion

Once the neural network is trained, it would be ready to be deployed in the electronic fuse of the artillery shell.

Its performance is evaluated using a test dataset that would represent the real shots in the field performed. Should be mentioned that, in this test dataset, the initial conditions are not necessary among the ones used for the training process. This is important in terms of NN trajectory generalization. This dataset consists of the data of three shots: high gun, with elevation around 60°, a maximum range shot around 45°, and a tense shot around 20°.

The accuracy of the predictions was calculated just in the launch moment, where the error is larger. As the projectile advances along the trajectory, the data updates by the navigation subsystem highly accurately as can be seen in Ohlmeyer et al. (1997) or Fresconi et al. (2011), making the possible impact points become closer between them. As expected, the error in the prediction of the impact point and resting time to impact of the neural network gets lower along the trajectory. The results are shown below (Tables 1 and 2).

Table 1 Comparison between the neural network prediction and the MPMM model in the impact point and time to impact at launch moment

Shot	Variable	MPMM	Prediction	Difference	Precision (%)
Height elevation shot	Impact position in x-axis (IPx)	18,878 m	18,916 m	38 m	99.8
	IPy	-921 m	-927 m	6 m	99.35
	Impact time (IT)	104.1 s	104,1 s	0 s	100
Maximum range shot	IPx	22,245 m	22,194 m	51 m	99.77
	IPy	-437 m	-435 m	2 m	99.54
	IT	77.6 s	77.8 s	0.2 s	99.74
Tense shot	IPx	21,714 m	21,695 m	19 m	99.91
	IPy	-329 m	-323 m	6 m	98.18
	IT	77.4 s	77.7 s	0.3 s	99.61

Table 2 Comparison between the neural network prediction and the five-DOF model in the impact point and time to impact at launch moment

Shot	Variable	Five DOF	Prediction	Difference	Precision (%)
Height elevation shot	IPx	7307 m	7329 m	22 m	99.69
	IPy	64 m	54 m	10 m	84.37
	IT	24.5 s	24.5 s	0 s	100
Maximum range shot	IPx	10,556 m	10,545 m	11 m	99.90
	IPy	273 m	305 m	32 m	88.27
	IT	49 s	49.11 s	0.11 s	99.77
Tense shot	IPx	9159 m	9082 m	77 m	99.15
	IPy	452 m	479 m	27 m	94
	IT	60.5 s	60.69 s	0.19 s	99.69

4 Conclusion

The previous table shows that the results of the predictions of the point of impact and the time remaining to impact are satisfactory. This can be affirmed because the accuracy obtained in the predictions with respect to the simulator results is high. Also, the predictions of these trajectories are evaluated in a very short time, being one a simplified model, which is the MPMM, and one more complex model, which is the five-DOF model that only needs to assume axial symmetry.

This solution offers an alternative to propagators which need a quality software to make precise calculations. The neural networks offer the advantage of that, once trained, they don't need to understand, analyze, or calculate the physics of the movement such as the aerodynamics. As the model gets more complex, it is harder for the neural network to represent the underlying physics, because of the increased number of factors that take part in that movement compared to the simpler model.

References

- Fresconi, F., & Plostins, P. (2008). *Control mechanism strategies for spin-stabilized projectiles*. <https://doi.org/10.21236/ada494194>
- Fresconi, F., Cooper, G., & Costello, M. (2011). Practical assessment of real-time impact point estimators for smart weapons. *Journal of Aerospace Engineering*, 24(1), 1–11. [https://doi.org/10.1061/\(asce\)as.1943-5525.0000044](https://doi.org/10.1061/(asce)as.1943-5525.0000044)
- Lieske, R. F., & Reiter, M. L. (1966). *Equations of motion for a modified point mass trajectory*. <https://doi.org/10.21236/ad0485869>
- McCoy, R. L. (2012). *Modern exterior ballistics: The launch and flight dynamics of symmetric projectiles*. Schiffer Publishing.
- Ohlmeyer, E., et al. (1997). *GPS-aided navigation system requirements for smart munitions and guided missiles*. In Guidance, navigation, and control conference. <https://doi.org/10.2514/6.1997-3683>
- Theodoulis, S., & Wernert, P. (2017). Flight dynamics & control for smart munition: The ISL contribution. *IFAC-PapersOnLine*, 50(1), 15512–15517. <https://doi.org/10.1016/j.ifacol.2017.08.2127>

Manufacturing of a Hybrid VTOL UAV Using Rapid Prototyping Techniques



Sinan Alnıpak, Turan Konyalođlu, İbrahim Halil Şahin, and Erdinç Altuđ

Nomenclature

FDM	Fused deposition modeling
LW-PLA	Lightweight PLA
PLA	Polylactic acid
UAV	Unmanned aerial vehicle
VIP	Vacuum infusion process
VTOL	Vertical takeoff and land

1 Introduction

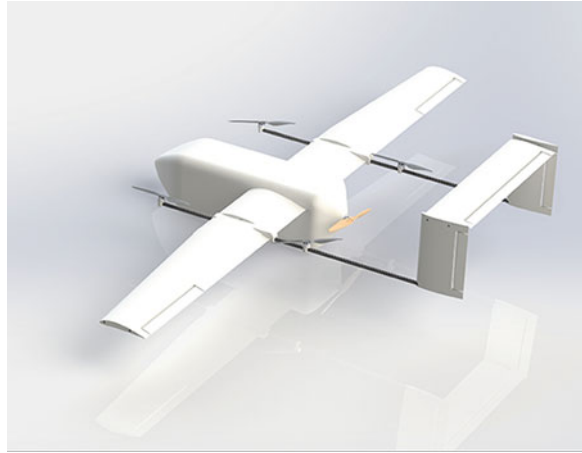
Unmanned aerial vehicle technologies have gained a serious momentum in recent years (Çetinsoy et al., 2012; Hissa & Mothe, 2018). Despite these developments, the production of a UAV still requires expensive equipment and detailed processes.

Rapid prototyping has gained popularity in engineering in recent years. 3D printers enabled custom production to come to our homes. Recently, there are some examples of manufacturing of small drones and UAV aircrafts using 3D printers (Banfield, 2013; McKinnon, 2016). Some of these aircraft can be easily manufactured with a small FDM printer or with custom printers.

Wings and control surfaces are the most important parts of an aircraft. They have to be strong to withstand various forces and moments, and they should also be lightweight as possible. Therefore, manufacturing of a wing requires costly processes and equipment. In order to reduce the cost of the aircraft, and to speed up the manufacturing process, a 3D printer and composite manufacturing processes can be

S. Alnıpak (✉) · T. Konyalođlu · İ. H. Şahin · E. Altuđ
Department of Mechanical Engineering, Istanbul Technical University, İstanbul, Türkiye

Fig. 1 Proposed hybrid vehicle's CAD drawing



used together. The vacuum infusion process (VIP) which is a technique that uses vacuum pressure to drive resin into a laminate was used to produce wings and other control surfaces (Baker, 2004; McIlhagger et al., 2020).

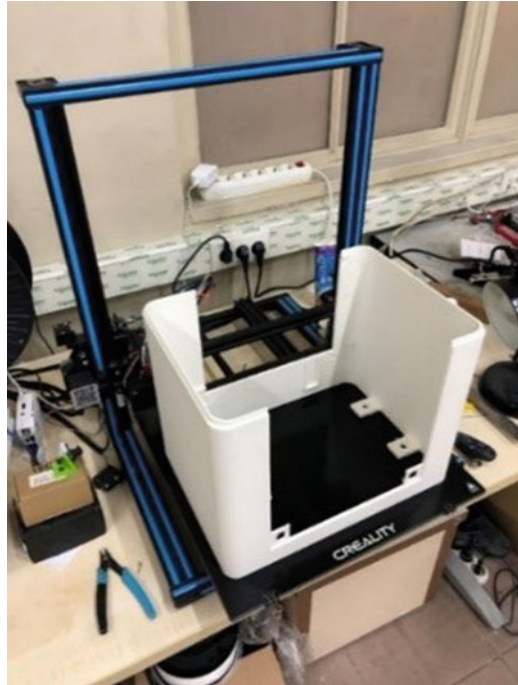
In this study, we investigate the possibility of using 3D printer technology for the manufacturing of a 3.8-m wingspan hybrid UAV (Konyalıođlu et al., 2021). Aircraft body, as well as molds to produce wings and control surfaces (with the vacuum infusion method), was manufactured with an FDM 3D printer. The CAD drawing of the VTOL hybrid UAV to be manufactured has been presented in Fig. 1. The length and height of the aircraft are about 2.5 m and 0.6 m, respectively.

2 Manufacturing of the UAV Body

Recent developments in 3D printing have caused this technique to be used in a widespread manner. The main advantage of this method is its capability to produce parts with complex geometric features. Also, according to needs, materials with different properties can be used. One of the application areas in which this technique is used is manufacturing unmanned air vehicle parts. This type of drones needs to be lightweight and sturdy at the same time. The additive manufacturing approach not only satisfies these properties but also replacing damaged parts is easy and simple.

Unlike the conventional manufacturing processes, in this method, the material is deposited. Three varieties of this method are mainly used today. These are fused deposition modeling, selective laser sintering, and stereolithography. Fused deposition modeling process is preferred over others for its inexpensiveness over others in this project. Firstly, the fuselage is designed using the Solidworks program (BIOVIA, 2022). The fuselage is then separated into six main parts so that it can be printed by the Creality CR-10 S4 printer in the laboratory (Fig. 2). It has $400 \times 400 \times 400 \text{ mm}^3$ printing volume. After converting the files to STL format,

Fig. 2 Aircraft body printing



gcode is generated using Cura software (Ultimaker Cura, 2022). The parameters in the Cura software are then optimized based on weight and durability criterion.

Since producing parts with 3D printers, especially with FDM method, is easy, some research groups are using this technique as well. Depending on the requirements, some parts of drones or entire drone body can be 3D printed. In 2009, the world's first 3D printed drone is demonstrated by Southampton University. Since producing parts in this manner is not expensive and relatively fast, even large companies in aviation industry such as Airbus and Boeing utilize this process. Most of these parts are made from plastic.

As material lightweight PLA, known as LW-PLA, is used. This material can form bubbles, also called foaming, when printing above a specific temperature. The amount of foaming can be changed by varying the nozzle temperature; therefore, the density of the part can be changed. With this material, in the same volume, the weight can be reduced up to 65% compared to its unfoamed state. This way the weight of the parts is greatly reduced compared to regular PLA. However, the strength of the material is decreased proportional to density. The more the density is lowered, the more fragile the parts become. Since LW-PLA is a new filament, there are several producers. To produce the UAV's body, ColorFabb brand LW-PLA is used. It has a density of $0.4\text{--}1.24\text{ g/cm}^3$ and a glass transition temperature of $55\text{--}60\text{ }^\circ\text{C}$. To optimize the three parameters mentioned above, the nozzle temperature is set to $235\text{ }^\circ\text{C}$ and the flow rate 45%. In this way, the same part, which weighs approximately 1 kilogram with regular PLA, weighs 0.33 kg.

3 Manufacturing of the Wings and Control Surfaces

Mostly used rapidly prototyping techniques to manufacture an aerodynamic surface for the low-weight fixed-wing aircraft are covering balsa structured wings with tissue, shaping foam into airfoil structure, 3D printing, and composite manufacturing techniques. Because composite materials provide a solution to weight, performance, and cost optimization, they fit the requirements for the aircraft on this scale.

Carbon fiber is selected as a reinforcement material over fiberglass considering its strength and weight properties. There exist many production techniques for carbon fiber-reinforced polymers (CFRP) such as prepreg/autoclave processes, vacuum infusion, vacuum bagging, or hand lay-up (McIlhagger et al., 2020). Whereas prepreg/autoclave processes are widely used techniques in the industry for UAV wing production, it is relatively expensive compared to other techniques. The hand lay-up technique is insufficient for the product to get all details from the mold, especially in the region where the leading and trailing edge is located. On the other hand, vacuum infusion has the advantage of vacuuming the excess resin out of the mold over the vacuum bagging process which reduces the weight of the product significantly. Therefore, the wings of the aircraft were produced with vacuum infusion, and control surfaces were produced with vacuum bagging due to the high cost of preparing small parts for the vacuum infusion process.

3.1 Mold Manufacturing

Molds were produced in two different ways in order to reduce the time and material cost. As it is seen in Fig. 3 left, relatively small molds were produced by using a 3D printer with PLA filament. Because most of the molds are larger in volume than that the printer has, they are segmented into pieces and reunited afterward. As it is seen in the figure, voids located in the joint edges are filled with polyester putty, and after it dries, the whole mold is sandpapered until the height difference between each layer



Fig. 3 3D printed mold (left). The MDF wood mold (right)

flattens. It is critical to fill the voids because epoxy gel coats are not thick enough to fill the voids which can later cause leakages during the vacuuming process.

On the other hand, relatively larger molds were produced by processing laminated MDF woods which is seen in Fig. 3 right. After processing MDF woods with a CNC milling cutter, the molds should be varnished as soon as possible to avoid swelling due to the moisture. Lastly, an epoxy-based gel coat is applied to both 3D printed and MDF wood molds.

3.2 Resin Infusion Process

A figure from the resin infusion process is shown in Fig. 4 left. After applying the release agent to the cavity, the reinforcement materials, peel ply, release film, and infusion mesh are placed. Then, the spiral tubes are located regarding the desired flow shape. It is critical to obtain a V-shaped flow to wet all the regions. Then, the setup is finished by sealing the vacuum bag. In order to avoid overstretching of the bag, an adequate number of pleats should be created. Another important part is checking the sealing tape and vacuum bag for any leakages. It should be performed by using a barometer which is located on the catch pot or a leakage detector. If there is no leakage in the setup, the resin is prepared and degassed, and then the infusion process is started by turning on the vacuum pump. The resin flows from the feed line to the vacuum line, and once it reaches the vacuum line with no dry region on the reinforcement material, clamps are used in both lines to compress the tube and maintain the vacuum after the process ends. The part is removed from the cavity when the resin is cured.



Fig. 4 Resin infusion process (left). Vacuum bagging process (right)

3.3 *Vacuum Bagging Process*

The vacuum bagging technique is an extension of the hand lay-up. After applying the release agent and preparing reinforcement materials, the epoxy resin is applied with a brush firstly to the cavity and then to the reinforcement materials ply by ply. The peel ply and breather are placed on the reinforcement material, and then the setup is sealed with a vacuum bag and sealant tape. The breather is used to spread the vacuum all over the cavity. Vacuum is provided by a pump, and it is awaited for approximately 24 h for the resin to completely cure. Then, the part is removed from the cavity (Fig. 4 right).

3.4 *Assembly*

After completing the production of composite parts, undesired sections of the parts are trimmed and ground by using a hand rotary tool as it is seen in Fig. 5. Balsa plywood and carbon tubes which are produced with the filament winding method are used as the main structure of the wings. Balsa ribs are cut by using CNC laser cutting machine and placed in the composite part. Then, the carbon tubes are placed, and in order to align all ribs, firstly tubes are attached to the ribs by using epoxy adhesive. The ribs are attached to the first composite shell, and then by putting one layer of reinforcement material to the joint edges as it will be inside of the wing, the second shell is attached to the ribs and the first composite shell. If it is necessary, the grinding process is performed for joint edges after the epoxy adhesive is completely cured.

Once the body parts, wings, and control surfaces are manufactured, assembly process has been started (Fig. 6).

Fig. 5 Assembly of the horizontal tail wing





Fig. 6 The hybrid UAV in the assembly phase

4 Conclusion

In this study, we investigate the possibility of using 3D printer technology for the manufacturing of a 3.8-m wingspan hybrid UAV. Aircraft body, as well as molds to produce wings and control surfaces (with vacuum infusion method), was manufactured with an FDM 3D printer. It has been observed that it is possible to manufacture bigger UAVs with this approach, which is promising in making the production of UAVs accessible to the general public.

Acknowledgments This paper has been funded by TÜBİTAK with project 120E182.


References

- Baker, A. A. (2004). *Composite materials for aircraft structures*. AIAA.
- Banfield, P. B. (2013). *Design and development of a 3D printed UAV, bachelor of science in aerospace engineering thesis study*. Oklahoma State University.
- BIOVIA. (2022). *Dassault systèmes, solidworks, version 2017*. Dassault Systèmes.
- Çetinsoy, E., Dikyar, S., Hançer, C., Oner, K. T., Sirimoglu, E., Unel, M., & Aksit, M. F. (2012). Design and construction of a novel quad tilt-wing UAV. *Mechatronics*, 22(6), 723–745.
- Hissa, L., & Mothé, J. E. M. (2018). *Development of an autonomous UAV*. <https://doi.org/10.26678/ABCM.CONEM2018.CON18-1600>
- Konyalıoğlu, T., Alnıpak, S., & Altuğ, E. (2021). *Model predictive control of a hybrid UAV for parcel delivery applications*. In 2021 Aerial robotic systems physically interacting with the

- environment (AIRPHARO) (pp. 1–8). <https://doi.org/10.1109/AIRPHARO52252.2021.9571035>.
- McIlhagger, A., Archer, E., & McIlhagger, R. (2020). Manufacturing processes for composite materials and components for aerospace applications. In *Polymer composites in the aerospace industry* (pp. 59–81). Woodhead Publishing.
- McKinnon, A. (2016). The possible impact of 3D printing and drones on last-mile logistics: An exploratory study. *Built Environment*, 42(4), 576–588.
- Ultimaker Cura. (2022). *Powerful, easy-to-use 3D printing software*. <https://ultimaker.com>. Retrieved November 14, 2022, from <https://ultimaker.com/software/ultimaker-cura>

Efficient Data-Driven Algorithms to Identify Patterns in Aeronautical Industrial Problems



Eneko Lazpita, Beka Begiashvili, Jesús Garicano, Soledad Le Clainche , and Eusebio Valero

1 Introduction

Multi-scale, noisy, transitional, or turbulent flows, has sparked significant interest due to its extensive application in various industrial problems (i.e., combustion systems, aircraft stability and control, etc.), and growing ecological concerns. For example, there is a drive to model urban flows to achieve more environmentally friendly cities (Lazpita et al., 2022).

To deal with large databases, which generally solve realistic or industrial problems, it is necessary to develop reduced order models (ROMs) using efficient data analysis techniques combined with parallelization strategies. These methods, fully data-driven, are very versatile and robust and can be used in various aeronautical industrial processes, for instance, to improve the design of airplanes and its different elements, consequently improving their efficiency.

2 Methodology

Into a snapshot matrix $\mathbf{M} \in \mathbb{R}^{J \times N_t}$, where $J \equiv N_u \times N_x \times N_y \times N_z$, N_u is the number of components of the velocity vector, N_x , N_y , and N_z are the spatial dimensions of the system (number of grid points in the streamwise, normal, and spanwise components, respectively), and N_t is the number of snapshots.

E. Lazpita (✉) · B. Begiashvili · J. Garicano · E. Valero
ETSI Aeronáutica y del Espacio, Universidad Politécnica de Madrid, Madrid, Spain
e-mail: e.lazpita@alumnos.upm.es; beka.begiashvili@alumnos.upm.es;
jesus.garicano.mena@upm.es; eusebio.valero@upm.es

S. Le Clainche
School of Aerospace Engineering, Universidad Politécnica de Madrid, Madrid, Spain
e-mail: soledad.leclainche@upm.es

2.1 Singular Value Decomposition and Proper Orthogonal Decomposition

Singular value decomposition (SVD) decomposes the previous snapshot matrix \mathbf{M} of rank $r < \min(J, N_t)$ into three different matrices as:

$$\mathbf{M} = \mathbf{U}\mathbf{\Sigma}\mathbf{V}^T, \quad (1)$$

where $(\cdot)^T$ is the matrix transpose, $\mathbf{\Sigma} = \text{diag}(\sigma_1, \dots, \sigma_r) \in \mathbb{R}^{r \times r}$ contains the singular values, $\mathbf{U} = [\mathbf{u}_1, \dots, \mathbf{u}_r] \in \mathbb{R}^{J \times r}$ are the left singular vectors associated with these singular values, and $\mathbf{V} = [\mathbf{v}_1, \dots, \mathbf{v}_r] \in \mathbb{R}^{N_t \times r}$ are the right singular vectors. In this work, we use SVD to reduce the data dimensionality (from J to r) and calculate the proper orthogonal decomposition (POD) modes (Lumley, 1967), which are suitable to identify coherent structures and flow patterns.

2.2 Parallel SVD

Parallelization algorithms are important when dealing with large databases, since the computational cost can be reduced several times depending on the case. Let \mathbf{M} be the snapshot matrix with $8n$ rows and n columns, which is partitioned across four map tasks, and each map task computes a local QR factorization:

$$\mathbf{M} = \begin{bmatrix} M_1 \\ M_2 \\ M_3 \\ M_4 \end{bmatrix} = \begin{bmatrix} Q_1 & & & \\ & Q_2 & & \\ & & Q_3 & \\ & & & Q_4 \end{bmatrix} \begin{bmatrix} R_1 \\ R_2 \\ R_3 \\ R_4 \end{bmatrix} \quad (2)$$

The indirect tall-and-skinny QR method ignores the intermediate \mathbf{Q} factors and simply outputs the $n \times n$ factors \mathbf{R}_i at the intermediate stage and $\tilde{\mathbf{R}}$ at the final stage (Benson et al., 2013). The performance of this parallel SVD algorithm is tested to identify the POD modes in the section presented below. Also, this algorithm is combined with the two algorithms presented in the next sections: dynamic mode decomposition and resolvent analysis.

2.3 Dynamic Mode Decomposition

Dynamic mode decomposition (Schmid, 2010) is another data analysis technique, suitable to identify the main patterns of the flow. This method is based on the idea of decomposing a signal as an expansion of modes, as:

$$M(t) \simeq \sum_{m=1}^M a_m \mathbf{u}_m e^{(\delta_m + i\omega_m)t} \text{ for } t_1 \leq t \leq t_1 + T, \quad (3)$$

where M is the snapshot matrix defined previously, \mathbf{u}_m are the normalized DMD modes, a_m are the mode amplitudes, and δ_m and ω_m are the associated growth rates and frequencies, respectively. The DMD algorithm is based on SVD so it can be combined with the parallel SVD algorithm previously introduced. This article uses also the exact DMD variant (Tu, 2013), which scales the adjoint DMD modes to form an orthogonal basis.

2.4 Resolvent Analysis

The resolvent analysis is another technique that studies how harmonic forcing inputs are amplified by the linear dynamics of a system and mapped onto harmonic response outputs. A forced linear dynamical system is considered:

$$\dot{\mathbf{x}} = \mathbf{A}\mathbf{x} + \mathbf{f} \quad (4)$$

where $\mathbf{x} \in \mathbb{C}^l$ is the state vector, $\mathbf{A} \in \mathbb{C}^{l \times l}$ is the linear dynamic matrix, and $\mathbf{f} \in \mathbb{C}^l$ is an external driving force. Calling ω to the angular driving frequency, the response is harmonic $\mathbf{x}(t) = \hat{\mathbf{x}}e^{-i\omega t} + c.c.$ when a harmonic forcing is applied. The problem is governed by the particular solution given by $\hat{\mathbf{x}} = \mathbf{H}(\omega)\hat{\mathbf{f}}$ where $\mathbf{H}(\omega) = (-i\omega \mathbf{I} - \mathbf{A})^{-1}$ is the resolvent operator. A data-driven method based on exact DMD that also uses SVD (Herrmann et al., 2021) is employed to obtain the forcing and response modes. The method can also be combined with the parallel SVD algorithm.

3 Results and Discussion

We analyze the two-dimensional wake past a circular cylinder at Reynolds number $Re = 50$, defined as $Re = UD/\mu$, where U is the free stream velocity, D is the cylinder diameter, and μ is the kinematic viscosity. The analyzed database is obtained from Corrochano et al. (2022). The temporal evolution of the velocity components in database analyzed is presented in Fig. 1 (left). The database also considers the transient region of the numerical simulation (to raise the complexity in the analysis carried out and to test the capabilities of the methods to clean noise). The database is formed by 1000 snapshots equidistant in time with time interval 1.

The two most relevant (highest energetic) POD modes are presented in Fig. 1 (middle). The shape of these modes is in good agreement with the results presented in the literature (Vega & Le Clainche, 2020). The performance of the parallel SVD algorithm is presented in Fig. 1 (right). The algorithm scales linearly when using up

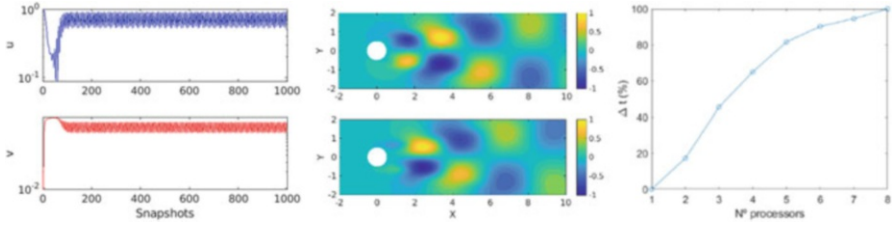


Fig. 1 (Left) Temporal evolution of the streamwise (top) and normal (bottom) velocity components. (Middle) Streamwise velocity contour of the first and second POD modes. (Right) Decreasing percentage of the computational time as function of the number of processors for the parallel SVD algorithm

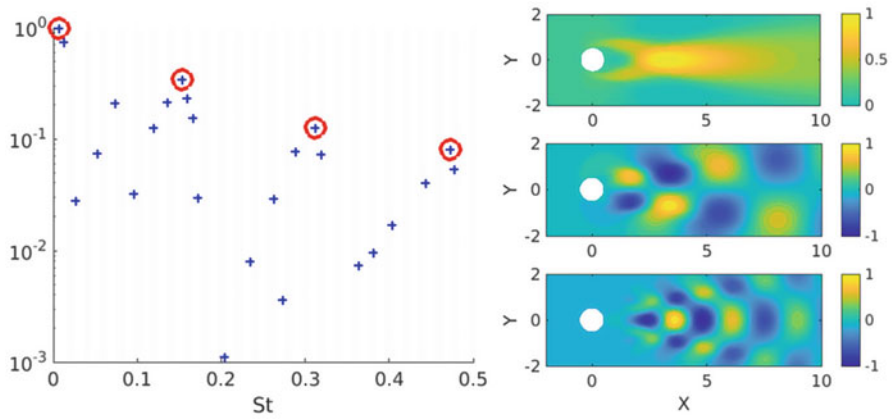


Fig. 2 (Left) DMD frequency spectrum. (Right) Streamwise velocity contours of the most representative DMD modes

to five processors, and then the scalability curve is slightly attenuated. This is because the method analyzes a case formed by 250,000 grid points; hence, using a larger number of processors working in parallel for such case is not worth it. Nevertheless, this test case shows the capabilities of the parallel algorithm to reduce the computational cost. Also, we expect better performance of the method, when the algorithm will be applied to larger databases, which remains as open topic for future work.

The dataset has also been analyzed with the DMD technique (both standard DMD and exact DMD algorithms have been tested, showing the same results) to obtain the main patterns leading the flow dynamics. Figure 2 shows the amplitude and contours of the most representative DMD modes: the steady mode (with nondimensional frequency Strouhal number $St = 0$, with $St = fD/U$, where f is the frequency), which represents the mean flow, the dominant mode ($St = 0.16$), and the its two harmonics. The solution is periodic, although, as seen in Fig. 2 (left), the method identifies more modes and frequencies, connected to the transient dynamics of the flow, which are

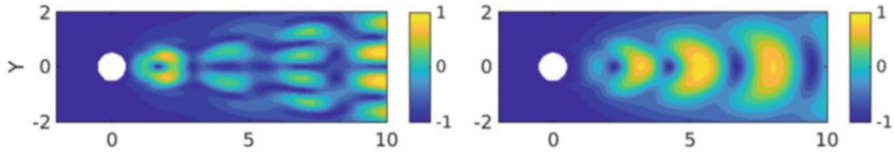


Fig. 3 Resolvent analysis. Contours of the norm of the dominant mode with $St = 0.16$ ($\|u\| = \sqrt{u_x^2 + u_y^2}$): (left) forcing mode and (right) response mode

spurious modes. Reducing the data dimensionality using SVD (retaining a smaller number of SVD modes in the DMD algorithm, for instance, 8 SVD modes instead of 21 as in the example presented in blue) reduces the spatial redundancies and filters out the noise from the database analyzed, and then the method only retains the highlighted modes from the figure. So, using DMD requires some calibration when it is applied to complex databases. Also, other variants of DMD, more robust, could be a good alternative to clean the database, as presented by Vega and Le Clainche (2020). Finally, if the database analyzed only considers the saturated regime ($time > 800$ in Fig. 1 left), the method will only identify the physical modes (since the transient and spurious modes are not presented in this regime).

Finally, Fig. 3 shows the result of applying the resolvent analysis to the two-dimensional cylinder database. The figure shows the forcing mechanism with $St = 0.16$ and the system response. As seen, the highest intensity of these modes is found in the cylinder wake. Future works should explore the possibility of using the results obtained for flow control applications.

4 Conclusion

This work shows several data-driven methods to identify patterns in complex flows: POD, DMD, and data-driven resolvent analysis. The performance of these methods has been tested in the two-dimensional wake of a circular cylinder.

All the data-driven methods used to identify the main flow patterns are based on the algorithm SVD. SVD has been parallelized, and also the good performance of this parallel tool reveals the possibility of extending these methods to the analysis of large and complex databases, which are able to solve realistic problems for the aerospace engineering industry.

Acknowledgments S.L.C. acknowledges the grant PID2020-114173RB-I00 funded by MCIN/AEI/10.13039/501100011033.

References

- Benson, A. R., Gleich, D. F., & Demmel, J. (2013, October). *Direct QR factorizations for tall-and-skinny matrices in MapReduce architectures*. In 2013 IEEE international conference on big data (pp. 264–272). IEEE.
- Corrochano, A., D’Alessio, G., Parente, A., & Le Clainche, S. (2023). Higher order dynamic mode decomposition to model reacting flows. *International Journal of Mechanical Sciences*, 249, 108219.
- Herrmann, B., Baddoo, P. J., Semaan, R., Brunton, S. L., & McKeon, B. J. (2021). Data-driven resolvent analysis. *Journal of Fluid Mechanics*, 918, A10.
- Lazpita, E., Martínez-Sánchez, Á., Corrochano, A., Hoyas, S., Le Clainche, S., & Vinuesa, R. (2022). On the generation and destruction mechanisms of arch vortices in urban fluid flows. *Physics of Fluids*, 34(5).
- Lumley, J. L. (1967). The structure of inhomogeneous turbulent flows. *Atmospheric turbulence and radio wave propagation*, 166–178.
- Schmid, P. J. (2010). Dynamic mode decomposition of numerical and experimental data. *Journal of Fluid Mechanics*, 656, 5–28.
- Tu, J. H. (2013). *Dynamic mode decomposition: Theory and applications* (Doctoral dissertation). Princeton University)
- Vega, J. M., & Le Clainche, S. (2020). *Higher order dynamic mode decomposition and its applications*. Academic.

The Use of Tethered Unmanned Aerial Vehicles in the Field of Defense and Current Developments



Alpaslan Durmus, Erol Duymaz, and Mehmet Baran

Nomenclature

FOB	Forward operating bases
TUAV	Tethered unmanned aerial systems
UAS	Unmanned aerial systems
UAV	Unmanned aerial vehicles
VLOS	Visual line of sight
MGTW	Maximum gross takeoff weight

1 Introduction

The use of UAV systems for military reconnaissance and surveillance activities is one of the most frequently used methods (Kabadayı & Uysal, 2019). However, problems related to flight time cause restrictions in the use of UAV systems (Balasubramanian et al., 2014). In the report called “Eyes of the Army” prepared by the USA, UAV systems were divided into five categories. The groups used by the USA for the classification of military UAV systems are shown in Table 1.

In the classification made by the USA, UAV systems in the “small” class are frequently used for reconnaissance and surveillance for security purposes. The biggest shortcoming of the systems in the small class and using BLDC motors is their very short flight times. Today, the use of wired UAV systems to extend flight times is rapidly becoming widespread (Qassim, 2022) (Fig. 1).

A. Durmus (✉) · E. Duymaz · M. Baran
Ostim Technical University, Ankara, Türkiye
e-mail: alpaslan.durmus@ostimteknik.edu.tr; erol.duymaz@ostimteknik.edu.tr

Table 1 UAV classification according to the US Department of Defense (DoD)

Category	Size	Maximum gross takeoff weight (MGTW) (lbs)	Normal operating altitude (ft)	Airspeed (knots)
Group 1	Small	0–20	<1200 AGL*	<100
Group 2	Medium	21–55	<3500	<250
Group 3	Large	<1320	<18,000 MSL**	<250
Group 4	Larger	>1320	<18,000 MSL	Any airspeed
Group 5	Largest	>1320	>18,000	Any airspeed

Eyes of the Army U.S. Army Roadmap for UAS 2010–2035 (2022)

*AGL Above ground level

**MSL Mean sea level



Fig. 1 Drone use of border security

Tethered drones are commonly used for border patrol, online image transmission, temporary base stations, wireless Internet service provision, and low-altitude surveillance (What are the Benefits of Tethered Drones?, 2022).

1.1 Tethered UAV Systems

Wired unmanned aerial vehicles started to be used in the field of defense in 2016. Today, it is stated by many defense industry experts that cabled UAV systems will be an integral part of bases and outposts.

Tethered UAV systems can be defined as unmanned aerial vehicles physically connected to the ground control station. The basic components of the wired UAV systems are the unmanned aerial vehicle, the ground control-power station, the cable and pulley system that includes the cable tension measurement system that provides the connection of the UAV system to the ground, and the energy need (What are the Benefits of Tethered Drones?, 2022).

1.1.1 Ground Control Station

Ground control stations used in wired UAV systems fulfill many tasks. UAV ground control stations can be located far from the flight location. The basic functions of UAV ground control systems are given below (Geospatial Applications of Unmanned Aerial Systems, 2022):

1. To provide the necessary power for the UAV system
2. To transfer the DC current by converting it to AC current
3. To provide communication between the UAV and the ground control station
4. To ensure that the UAV system maintains its position in hovering
5. Micro-tethered UAV Systems

UAV systems in the micro- or small group are among the systems that are frequently used in the defense industry for taking images from low altitudes. Wired UAV systems can fly as high as wireless UAV systems. This allows images to be taken from a very wide area. The cable system, which is used to provide the necessary energy to the UAV systems, can also be used to ensure that the UAV maintains its position. Wired UAV systems are primarily used for taking live video recordings. In addition, it can be used to collect data and receive telemetry data.

1.2 Advantages of Tethered UAV Systems

Wired UAV systems bring many advantages. The most advantages of wired systems are given below. These are:

1. Time of flight: The biggest limitation of UAV systems is related to flight time. UAV systems can fly for approximately 30 minutes. Landing, replacing the batteries, and flying the UAV during the mission may cause disruptions in the mission. With wired UAV systems, the flight time restriction is eliminated.
2. Safe flight: UAV systems are used to follow the masses in festivals, natural disasters or emergencies, and meetings or demonstrations. However, despite all the precautions taken, accidents and crashes can occur in UAV systems. On the other hand, since the flight area is fixed or limited in wired UAV systems, accidents and injuries caused by the fall of UAV systems can be prevented.

GPS systems are not required. Since wired UAV systems can fly in a limited area, the risk of collision with other aircraft is zero.

3. Ease of use: Wired UAV systems are much easier to fly and land than other UAV systems. Piloting skills are not required for the flying and landing of wired UAV systems.
4. Autonomy: Wired UAV systems allow operators to focus on their mission. Wired UAV systems help operators focus on their tasks, as they fly autonomously. Wired drones can reach heights of up to 300 feet.
5. Advantages in terms of legislation: Cable UAV systems are not classified as UAVs according to civil aviation regulations in many countries. At the same time, wireline UAV systems do not have to be registered with authorized aviation authorities. Wired UAV systems are independent of the regulations that other UAV systems must comply with. In other words, they can exceed an altitude of 120 m.
6. Secure data transfer: UAV systems may occasionally lose their data connections with the ground during flight. Wired UAV systems, on the other hand, benefit from an uninterrupted and secure communication line from the ground station. Thus, video or image transfer can be done without interruption.
7. Deterrence: Wired UAV systems can act as a deterrent for security threats.

2 Use of Tethered Unmanned Aerial Vehicle Use in Military Domain

The first pilotless vehicles were developed by Britain and the USA during the First World War. The first radio-controlled aircraft was tested by Britain in 1917. The first UAV system, known as the Kettering Bug, was used by the USA in 1918. Although the systems developed by England and the USA were not used in the First World War, they started the era of unmanned aerial vehicles in the field of aviation.

Wired and wireless UAV systems used in the military are developing rapidly. Wired UAV systems are especially important for reconnaissance and surveillance activities. Wired UAV systems are promising for border security and the protection of base areas. With wired UAV systems, reconnaissance and surveillance activities can be carried out for long hours.

Military reconnaissance aircraft can be examined under four headings. These can be classified as micro, short-range, medium-range, and long-range reconnaissance aircraft. Micro-class UAV systems, which can be used as wired among these systems, provide important advantages to military units and police stations. At the same time, micro-class wired UAV systems placed behind the vehicle are used for border security.

Micro-class UAV systems are widely used for reconnaissance and surveillance. However, the optical resolutions of the camera systems used by micro-class UAV systems are quite limited. However, micro-class wired UAV systems are very useful



Fig. 2 Drone use of defense domain

systems in terms of detecting any threat situation. The use of a micro-class wired UAV system for reconnaissance and surveillance provides significant advantages to military units.

Military reconnaissance aircraft can be examined under four headings. These can be classified as micro, short-range, medium-range and long-range reconnaissance aircraft. Micro-class UAV systems, which can be used as wired among these systems, provide important advantages to military units and police stations. At the same time, micro-class wired UAV systems placed behind the vehicle are used for border security.

Micro-class UAV systems are widely used for reconnaissance and surveillance. However, the optical resolutions of the camera systems used by micro-class UAV systems are quite limited. However, micro-class wired UAV systems are very useful systems in terms of detecting any threat situation. The use of a micro-class wired UAV system for reconnaissance and surveillance provides significant advantages to military units (Fig. 2).

2.1 Usage Examples of Wireless UAV Systems in the Field of Defense

2.1.1 Ensuring Border Security

The protection and security of border areas is an extremely difficult and complex process. The fact that the border regions are geographically wide and long, the terrain is naturally rough, and the borders contain rocky, rough areas makes it difficult to protect the borders. Ensuring general security, surveillance at check-points, and monitoring of entry/exit points constitute border security.

For example, border security is a major problem in rough terrain, including geographically rocky areas. In addition, irregular or uncontrolled immigration is one of the threats that endanger border security. With wired UAV systems, borders can be monitored for 24 h.

2.1.2 Advanced Bases of Operation Protection

Defending forward operating bases or outposts is a very difficult and complex process. Protecting bases and gaining superiority against enemy units in attacks require a large amount of military personnel and ammunition. In addition, it is difficult for military bases to maintain communication with outposts due to infrastructure problems. This is an important factor that complicates the protection of forward operational bases. Watchtowers and perimeter walls can be used to protect outpost or base areas. In many cases, however, enemy troops are quite close to outposts. In this case, wired UAV systems are a very suitable solution for detecting enemy units.

Cameras placed in towers are very useful in protecting outposts. However, the cameras on the towers cannot observe as far as the cameras on the UAV systems. Optically enhanced camera systems on wired UAV systems can ensure the security of outposts. Cameras with an optical zoom of 30 times or more can observe vehicles and other large objects at 10 km. The cameras on the wired UAV systems can easily detect the enemy units beyond the line of sight. Thus, when danger is detected, soldiers have more time to prepare for any attack.

Another advantage of wired UAV systems is their uninterrupted mission. Thus, they can perform 24-h surveillance duty regardless of the 8-h shifts seen in the guards.

3 Results and Discussion

UAVs or unmanned aerial vehicles are one of the biggest threats faced by fighters. They can fly manually, but these days many are flown by a remote operator or even autonomously by onboard computers. UAVs are the main part of unmanned aerial systems (UAS), which also includes an operator or computer and a communication system that allows the two parts to work together. The types of UAVs can be classified in different ways for better defense strategies (UAV Types & Detection, 2020).

Tethered UAV systems are used in the field of defense today as a serious alternative to eliminate the disadvantages such as flight time limitation and data security in existing UAV systems. Since the communication between the drone and the ground control station is carried out over the cable line, interception or mixing of data can be prevented. The pulley system in the ground control station is used to supply the necessary energy to the tethered UAV system and to receive image and video data from the tethered UAV system.

A Cable tension-controlled pulley system prevents data and energy cable lines from being damaged. Thus, by providing the necessary power to the UAV, the uninterrupted operation of the UAV system is ensured. The operator can instantly monitor the relevant sensor data and coordinate and/or image information from the camera for the mission performed through the ground control station. One of the most important problems of rotary wing UAV systems is that it is dangerous to fly in areas where GPS jamming is present. Using certain algorithms and sensors, the wired drone system can fly without being dependent on GPS data compared to other drone systems.

4 Conclusion

The aerial torpedo, radio-controlled vehicle, remotely piloted vehicle (RPV), remote-controlled vehicle, autonomously controlled vehicle, pilotless vehicle, unmanned aerial vehicle (UAV), unmanned aircraft system (UAS), and drone are names that may be used to describe a flying object or machine without a pilot on board (Geospatial Applications of Unmanned Aerial Systems, 2022).

The use of wired UAV systems in the field of defense is rapidly spreading. The advantages of cabled UAV systems make their use widespread. The fact that wired UAV systems are an alternative for limited flight times can be considered as the most important advantage. At the same time, thanks to the fact that wired UAV systems carry data and control signals over the cable, it is prevented that the transmitted data is confused or eavesdropped. Data security is extremely important in the defense field. For a wide range of different needs such as border security, reconnaissance and surveillance, communication, search and rescue, and critical facility security, the tethered UAV systems, which could stay in the air for a long time, become more

advantageous than a regular wireless rotary-wing or fixed-wing UAV (Küçükçelebi & Yıldız, 2020).

Although these systems seem to be a disadvantage because they are connected to a certain point on the ground, the useful load capacity they provide for application and the long stay in the air make cable UAV systems preferable (Yılmaz & Gencer, 2018). When the costs related to flight times of UAV systems are considered, cabled UAV systems become very useful due to both their cost-effectiveness and their ability to stay in the air for a long time. Thanks to their ability to carry a high payload, they can carry more than one payload in the same operation and provide the user with the opportunity to use them actively (Karaağaç, 2016).

References

- Balasubramanian, P., Sati, S. C., Pal, A., & Gautam, R. (2014). A novel method for improving aerostat endurance using microprocessor controlled feedtube. *International Journal of Advances in Science Engineering and Technology*, 2(3), 114–120.
- ElistAir. (2022). *What are the benefits of tethered drones?* Retrieved from <https://elistair.com/tethered-drones-benefits/>
- Kabadayı, A., & Uysal, M. (2019). İnsansız Hava Aracı ile Elde Edilen Verilerden Binaların Tespiti. *Türkiye İnsansız Hava Araçları Dergisi*, 1(1), 8–14.
- Karaağaç, C. (2016). *İHA Sistemleri Yol Haritası: Geleceğin Kartalları 2016-2050*. Savunma Teknolojileri Mühendislik ve Ticaret A.Ş.
- Küçükçelebi, A., & Yıldız, E. (2020). Kablolü İHA Sistemleri ve Uygulamaları. *Avrupa Bilim ve Teknoloji Dergisi*, (Özel Sayı), 154–159.
- Penn State College of Earth and Mineral Sciences. (2022). *Geospatial applications of unmanned aerial systems*. Retrieved from <https://www.e-education.psu.edu/geog892/node/643>
- Qassim, A. A. (2022). *Classification of the unmannned aerial systems*. Retrieved from <https://www.e-education.psu.edu/geog892/node/5>
- RADA Technologies. (2020). *UAV types & detection*. Retrieved from <https://radausa.com/blog/uav-types>
- U.S. Army. (2022). *Eyes of the Army U.S. Army Roadmap for UAS 2010-2035*. Retrieved from <https://irp.fas.org/program/collect/uas-army.pdf>
- Yılmaz, N., & Gencer, C. T. (2018). Where to locate tethered aerostats for an effective surveillance system: A case study on Southern Turkey. *Gazi University Journal of Sciences*, 31(1), 189–200.

Optimal Thermal Sensor Placement for Accurate Heat Transfer Measurements



Jorge Saavedra and Agustín Villa Ortiz

1 Introduction

The flight envelope and autonomy of UAVs are limited by the energy sources present in the airframe. The propulsion systems have the largest energy and power demand, followed by the power electronics required to control, manage, and exploit the airframe. However, as the mission requirements advance and the onboard electronics become more complex, the thermal gradients and hot spots in the microprocessors become a relevant thermal source. Additionally, the power supply systems installed onboard electric-powered UAVs are also a considerable heat source. As a result, to maintain and control the internal operating temperature of the airframe, it is vital to size and design an adequate cooling system (Renau et al., 2016). Additionally, in some applications, the UAVs must maintain stealth operability, which could be ballasted by thermal signals that could be spotted using IR thermography. For these reasons, a vast majority of UAVs require cooling solutions beyond maintaining a reasonable microchip or hardware operational temperature. However, the introduction of the cooling systems constitutes an additional power source demand, either derived from the electric power to drive active coolers or due to the induced drag produced by passive coolers. As presented by Tanda, there is a myriad of cooling solutions that could be integrated into the airframe, and selecting the optimal approach based on the airframe thermal response and power demand could limit the operability of the airframe (Tanda, 2020).

On the other hand, to decide what is the best cooling system or to control the use of the cooling system, it is critical to accurately assess the heat load and the heat transfer that the system is suffering (Sushchenko et al., 2021). As introduced by Barroso et al., the accurate calculation of the heat transfer magnitude is the key to the

J. Saavedra (✉) · A. V. Ortiz
Universidad Rey Juan Carlos, Fuenlabrada, Madrid, Spain
e-mail: Jorge.saavedra@urjc.es; agustin.villa@urjc.es

design of optimized cooling systems and their efficient usage (Barroso et al., 2015). In this line, among the multiple heat transfer measurement approaches available, the one based on dual-sided thermal measurements is the most extended. By monitoring the thermal evolution of both sides of the material and solving the heat conduction between them, it is possible to derive the heat flux. However, the use of this approach presents the challenge of accurately measuring the wall temperature on the inner and outer surface of the battery or power electronics casing. The outer surface temperature could be monitored through IR thermography, local thermocouples, thin film sensors, or resistive thermal detectors. On the outer surface, the thermal variation happens at a much lower temporal rate, and the installation of sensing devices is simpler. On the contrary, the inner surface may suffer faster temperature changes, and the installation of the sensing apparatus is much more limited, given the lower clearance and the inherent requirements of the power electronic systems that the casing is protecting. Additionally, depending on the type and, particularly, on the number of sensors required, the impact on the airframe budget could be relevant. This manuscript presents an optimization approach to determine the number of sensors and their location to allow an accurate heat transfer characterization of the casing of power electronic or battery systems.

2 Method

The heat flux can be extracted from the wall temperature evolution using the impulse response method proposed by Oldfield (2008) or computing the internal heat conduction as presented by Saavedra et al. (2017). The thermal load is derived from the 1D unsteady heat conduction equation:

$$\frac{1}{\alpha} \frac{\partial T}{\partial t} = \frac{\partial^2 T}{\partial x^2} \quad (1)$$

Applying the upper and lower boundary condition to the equation, the unsteady heat flux can be accurately computed. A Crank–Nicolson numerical discretization is employed to solve the 1D or 2D unsteady heat conduction equation (Crank & Nicolson, 1996). This formulation is spatially implicit, so it requires the solution of the whole system at once due to its nonlinear nature. Using its temporal evolution, the problem is written as an implicit Runge–Kutta evaluation. The discretization characteristic of such a scheme is presented in Fig. 1a. The method is verified for a convective heat flux problem against the analytical solution (Bergman et al., 2011), Fig. 1a.

A conjugate unsteady Reynolds averaged Navier–Stokes simulation is used to model the heat loading over a thin slab and proof the derivation of heat flux from the computation solution based on multiple thermal probing options, as presented in Fig. 2a. A local heat source is introduced in the center of the numerical domain to

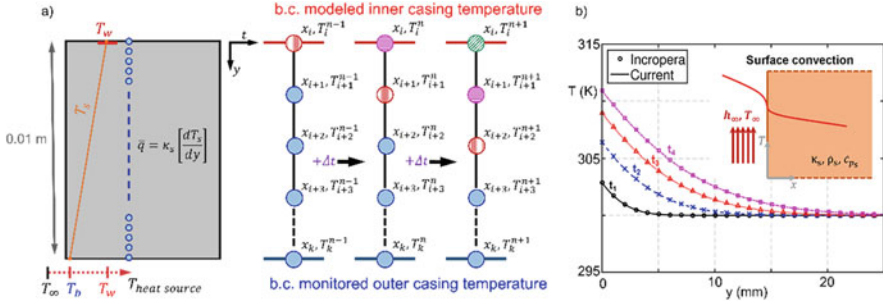


Fig. 1 (a) Numerical scheme and domain to solve the heat flux. (b) Validation of numerical scheme

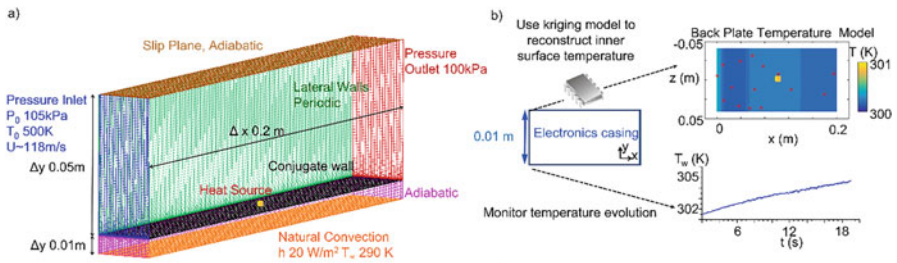


Fig. 2 (a) Conjugate URANS numerical domain. (b) Processing approach to derive the heat flux

replicate the impact of a hot spot in the processors. The bottom wall temperature is directly extracted from the simulation and used as the lower boundary condition for the heat flux derivation. On the other hand, to model the presence of discrete thermal sensors, the temperature at various upper surface positions can be extracted to reconstruct the upper boundary condition for the thermal solver, as depicted in Fig. 2b.

The local measurements on the upper surface are introduced into a Kriging interpolation method that derives the overall surface temperature distribution, as presented by Cuadrado et al. (2018). For a given distribution of sensors, the surface temperature reconstruction from the Kriging model is compared against the actual wall temperature. A larger wall temperature deviation promotes lower heat transfer accuracy. To find the optimal location of the probes, the sensor coordinates, surface temperature reconstruction based on Kriging interpolation, and comparison against the actual temperature are coupled to a simulated annealing optimizer that attempts to minimize the error of the heat flux prediction.

3 Results and Discussion

The optimization derives the location where the readings from the sensors reproduce the most accurate surface temperature distribution and hence the most accurate heat transfer derivation. The optimization loop requires two variables for each sensor being used, spanwise and streamwise location of the sensor. Figure 3a represents an example with 15 sensing locations and 30 variables for the optimizer. Using the Kriging interpolation and the optimizer, we can derive the optimal number of sensors and their location to accurately predict the heat flux across the surface. Figure 3b summarizes the error on the heat flux prediction for the different numbers of sensors being used to monitor the upper surface temperature. In this case, modeling a plate of $0.2 \times 0.1 \times 0.01$, the heat flux prediction reaches its optimal accuracy beyond the use of 14 sensors. When using six sensors, the derived heat flux presents an error of approximately 54%. As the number of sensors used is augmented, the error is logarithmically reduced. Interestingly, the heat flux error is practically insensitive to the number of sensors being used once more than 15 sensors are installed. The error in the heat flux derivation for 15 sensors and beyond stays between 2.4% and 2.6%.

4 Conclusion

This manuscript presents a procedure to identify the optimal location and number of sensors required to monitor heat flux and thermal load on the casing of power electronic systems installed in UAVs. The proposed methodology combines simulated annealing optimization with a Kriging interpolation. The Kriging interpolation is used to recreate the surface temperature distribution from a series of discrete thermal sensors. The interpolated surface temperature is then fed to heat conduction solver to derive the heat flux across the casing. Comparing the computed heat flux against the expected value, the optimization routing identifies the locations where

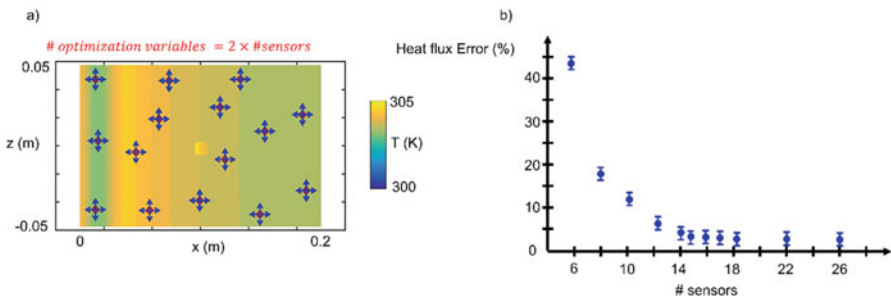


Fig. 3 (a) Example of sensor distribution and optimization variables. (b) Error on heat flux measurement by different numbers of sensors placed in their optimal location

the sensors should be installed to maximize the accuracy of the heat flux measurements. Defining the number and distribution of sensors to monitor the heat flux over the casing of vital UAV components is essential toward maintaining stealth capabilities and reducing the power consumption of cooling systems.

References

- Barroso, J., Renau, J., Lozano, A., Miralles, J., Martín, J., Sánchez, F., & Barreras, F. (2015). Experimental determination of the heat transfer coefficient for the optimal design of the cooling system of a PEM fuel cell placed inside the fuselage of an UAV. *Applied Thermal Engineering*, 89, 1–10.
- Bergman, T. L., Incropera, F. P., DeWitt, D. P., & Lavine, A. S. (2011). *Fundamentals of heat and mass transfer*. Wiley.
- Crank, J., & Nicolson, P. (1996). A practical method for numerical evaluation of solutions of partial differential equations of the heat-conduction type. *Advances in Computational Mathematics*, 6(1), 207–226.
- Cuadrado, D. G., Marconnet, A., & Paniagua, G. (2018). Inverse conduction heat transfer and kriging interpolation applied to temperature sensor location in microchips. *Journal of Electronic Packaging*, 140(1), 010905.
- Oldfield, M. (2008). Impulse response processing of transient heat transfer gauge signals. *Journal of Turbomachinery*, 130(2), 31–40.
- Renau, J., Barroso, J., Lozano, A., Nueno, A., Sánchez, F., Martín, J., & Barreras, F. (2016). Design and manufacture of a high-temperature PEMFC and its cooling system to power a lightweight UAV for a high altitude mission. *International Journal of Hydrogen Energy*, 41(43), 19702–19712.
- Saavedra, J., Paniagua, G., & Saracoglu, B. (2017). Experimental characterization of the vane heat flux under pulsating trailing-edge blowing. *Journal of Turbomachinery*, 139(6), 061004.
- Sushchenko, O., Bezkorovainyi, Y., Chernetskyi, Y., & Golitsyn, V. (2021). *Thermoregulation of UAV equipment*. In 2021 IEEE 6th international conference on actual problems of unmanned aerial vehicles development (APUAVD): IEEE (pp. 15–156).
- Tanda, G. (2020). Cooling solutions for an electronic equipment box operating on UAV systems under transient conditions. *International Journal of Thermal Sciences*, 152, 106286.

Time-Varying Consensus Formation Control of a Group of Quadrotor System with Collision Avoidance



Kaan Can and Abdullah Başçi

Nomenclature

UAV Unmanned aerial vehicle
CFC Consensus formation control
L-F Leader-follower

1 Introduction

Nowadays, many formation control algorithms have been proposed by researchers and academicians to realize a predefined formation shape based on a simple or complex formation control algorithms. The main idea in designing a formation controller is that more than one quadrotor in a swarm performs flight with communicating each other by maintaining a certain geometric shape depending on a control theory. While realizing formation flight, every quadrotor uses its neighbor's relative distance or velocity information to keep its position on desired point.

Many different formation control algorithms have been designed and derived such as L-F, decentralized or consensus, etc. The most commonly known and easy to apply of these is the L-F-based formation control algorithm (Can & Başçi, 2021; Zhao & Wang, 2018). The L-F-based formation control presents a concept based on one leader and one follower at least. The follower follows the leader, thanks to the predefined distance information, and thus the follower follows the leader by checking the distance information instantly. On the other hand, this fundamental formation algorithm has some disadvantages such as weakness experienced at the

K. Can · A. Başçi (✉)
Ataturk University, Erzurum, Türkiye
e-mail: kaan.can@atauni.edu.tr; abasci@atauni.edu.tr

time of leader loss, being guided by a single leader, and lack of information exchange between the followers. For these reasons, other methods are presented in the literature to ensure that each quadrotor is aware of its neighbor's position or velocity information during the formation flight. As an example, decentralized formation control has been proposed and applied to quadrotors to validate desired formations. In this method, the control algorithm is derived by determining the neighborhoods of the quadrotors in the swarm and the distance between the neighbors, taking into account any predetermined formation shape (Roque et al., 2020). However, due to some considerations such as collision or obstacles, this kind of control algorithms is not able to realize formation flight alone. Therefore, obstacle and collision avoidance control algorithms are added to the main controller that is designed to perform formation flight smoothly (Toksöz et al., 2019). In addition to all the aforementioned control algorithms, the consensus-based formation control is widely used especially by the academic circles due to its suitable characteristics to apply linear system theory, Lyapunov stability, and so on. Moreover, while designing the main control algorithm, only the linearized system dynamics is generally considered. Therefore, in real-time flights, each quadrotor may collide with each other and crash while executing the consensus protocol. Thus, while designing a consensus-based formation controller, various auxiliary controller can be combined with the main control algorithm to prevent collisions (Muslimov & Munasypov, 2021; Zhang et al., 2018).

In this paper, a consensus-based formation control algorithm is studied for five quadrotors to perform a cooperative formation control. In order to realize the formation throughout a time-varying trajectory and avoid any collision between quadrotors, a trajectory tracking control and collision avoidance algorithms are both combined to the main proposed CFC. The simulation results show the performance and the effectiveness of the proposed control algorithm.

2 Preliminaries

2.1 Quadrotor with Double-Integrator Dynamics

The dynamics of i th quadrotor can be described as given below (Dong et al., 2015):

$$\begin{cases} \dot{x}_i(t) = v_i(t) \\ \dot{v}_i(t) = u_i(t) \end{cases} \quad (1)$$

where $i = 1, 2, \dots, N$ represents the number of quadrotor; $x_i(t) \in R^m$ and $v_i(t) \in R^m$ are position and velocity of the i th quadrotor, respectively; and $u_i(t)$ is the control input of the system.

2.2 Consensus Formation Control

Before designing CFC algorithm, some mathematical expressions must be defined. First, we used graph $G = (V, E)$ so as to realize information among the N quadrotors. Here, $V = \{v_1, v_2, \dots, v_N\}$ represents the set of nodes, and $E = \{\epsilon_1, \epsilon_2, \dots, \epsilon_N\}$ represents the edges of the G (Namerikawa et al., 2018). The edge (v_j, v_i) in the edge set of the defined G denotes that there is a network-based information flow between quadrotor i and quadrotor j . Therefore, quadrotor i can use the position or velocity information of the quadrotor j to satisfy an evident geometric formation. The adjacency matrix can be defined by (Kuriki & Namerikawa, 2014):

$$A_{ij} = \begin{cases} 1, & \text{for } (v_j, v_i) \in E \\ 0, & \text{otherwise} \end{cases} \quad (2)$$

Here, A_{ij} is set to one if the quadrotor i is able to obtain position or velocity information from the quadrotor j , if not $A_{ij} = 0$ (Kuriki & Namerikawa, 2014). Moreover, the Laplacian matrix $L = D - A$ is obtained in which D represents the degree matrix of the whole formation system.

The consensus algorithm can be expressed for this study by (Ren & Atkins, 2007):

$$u_c = - \sum_{j \in N_i} A_{ij} [(x_i(t) - x_j(t)) + (\dot{x}_i(t) - \dot{x}_j(t))] \quad (3)$$

which satisfies $(x_i(t) - x_j(t)) = 0$ and $v_i(t) = 0$. Also, trajectory tracking control input can be given as:

$$u_i = (\ddot{\delta}_{ij} + \ddot{h}_i(t)) - \gamma(x_i(t) - (h_i(t) + \delta_{ij})) - \beta(\dot{x}_i(t) - (\dot{h}_i(t) + \dot{\delta}_{ij})) \quad (4)$$

where $\gamma, \beta > 0$ are both position control gains, δ_{ij} is the desired formation vector, $h_{ij}(t)$ is the position vector, and $x_{ij}(t)$ is the actual position of the i th quadrotor. Moreover, a collision avoidance strategy was proposed for a safe cooperative formation flight as given below (Toksöz et al., 2019):

$$u_r = \begin{cases} a \left(e^{-\mu|r_{ij}|} - e^{-\mu r_s} \right), & \text{for } |r_{ij}| \leq r_s \\ 0, & \text{otherwise} \end{cases} \quad (5)$$

where $a > 0$ and r_s represents safety distance between quadrotor i and j and $|r_{ij}| = \sqrt{(x_i - x_j)^2 + (y_i - y_j)^2}$ is the measured relative distance in the x - y plane. The total hybrid CFC algorithm's aim is to drive whole system to a final agreement state for all quadrotors throughout time-varying trajectory without any collision (Falconi et al., 2015). Therefore, besides the consensus-based algorithm, the main control input can be expressed by:

$$u_{\text{total}} = u_t + u_c + u_r \quad (6)$$

Instead of just a consensus control algorithm, a hybrid controller was proposed that will allow the system to agree on a formation, maintain the formation along the time-varying trajectory, and avoid collisions.

3 Results and Discussion

In this section, the simulation results are presented. The initial positions of the quadrotors are given as $[x_{i0}, y_{i0}]^T = [0, -2, -3, -2, 2; 2, 0, 0, -1, 2](i = 1, 2, \dots, 5)$. The eight-shaped trajectory is applied for i th quadrotor as given below:

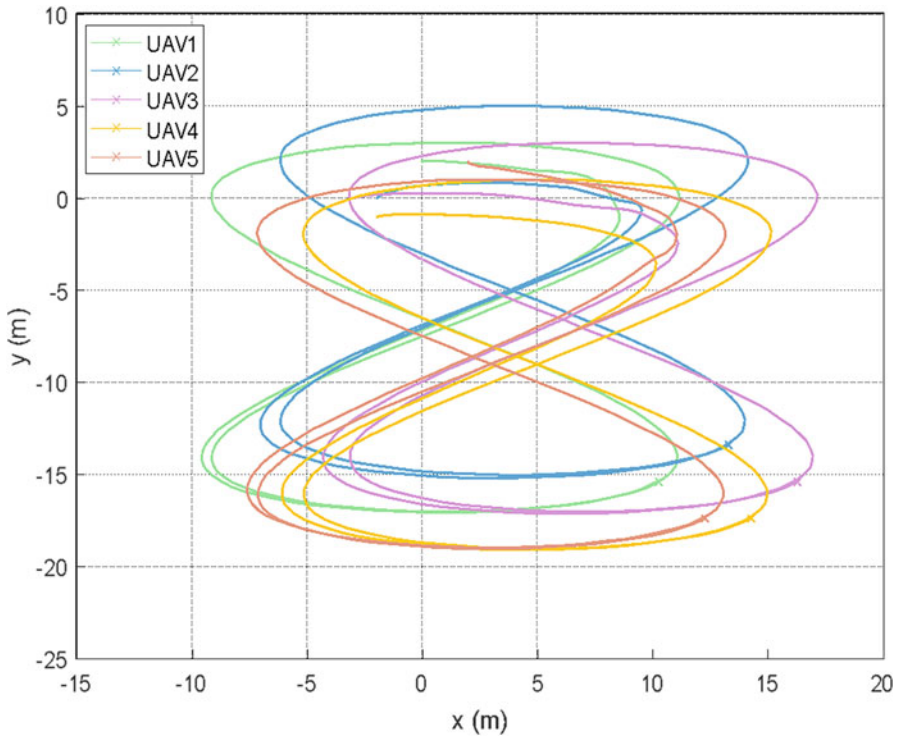


Fig. 1 Eight-shaped based time-varying pentagon formation flight of five quadrotors

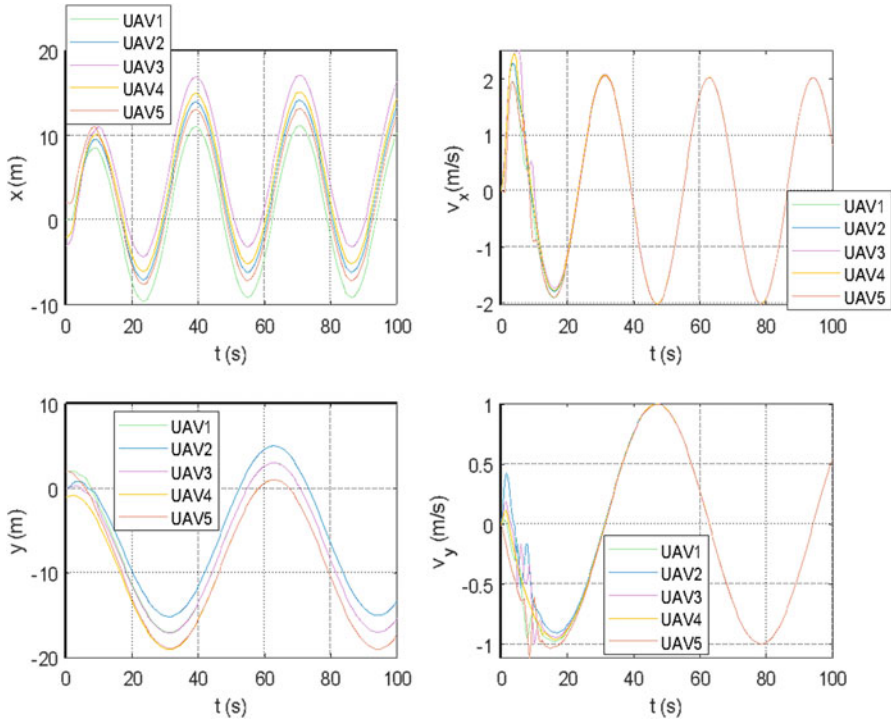


Fig. 2 Position and velocity information of each quadrotors

$$\begin{aligned}
 &h_i(t) \\
 &= [r \sin(2\omega t + (i - 1)\pi/2) 2\omega r \cos(2\omega t + ((i - 1)\pi/2)) r \cos(\omega t + (i - 1)\pi/2) \\
 &\quad - \omega r \sin(\omega t + (i - 1)\pi/2)] (i = 1, 2, 3, 4, 5)
 \end{aligned}
 \tag{7}$$

where $r = 1\text{ m}$ and $\omega = 0.1\text{ rad/s}$. In Fig. 1, trajectory tracking results of the quadrotors are given. One can see that all quadrotors followed the trajectory after establishing the pentagon formation order from their initial positions quickly.

In Fig. 2, the position and velocity information of i th quadrotor are presented. From the figure, after nearly 5 s, it is observed that all quadrotors in the formation maintain the pentagonal formation throughout the trajectory stably and follow the reference trajectory very well. It is also seen that the linear velocities of the all quadrotors in the formation are the same magnitude in order to maintain the formation. Also, in Fig. 3, the formation steps have been presented between 0 and 100 seconds for pentagonal formation through the eight-shaped trajectory.

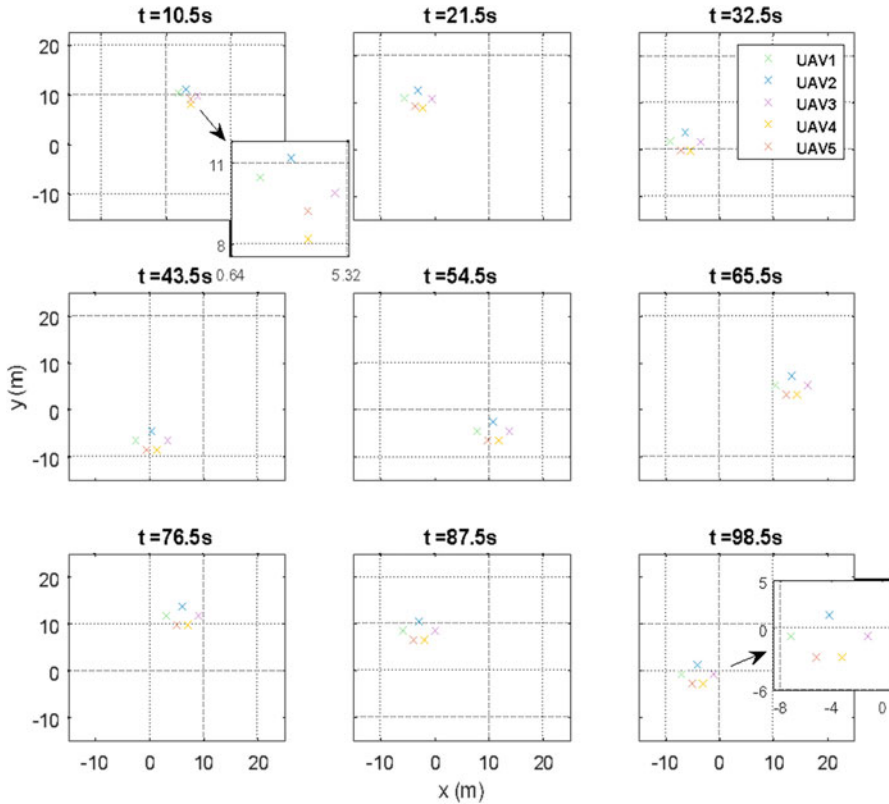


Fig. 3 Pentagonal formation steps of the quadrotors

4 Conclusion

In this paper, we proposed a consensus-based formation control algorithm to achieve a cooperative formation of five quadrotors. First, we expressed the second-order system model of the quadrotor briefly, and then the graph theory-based CFC algorithm was proposed based on the relative position and velocity information. Moreover, we were added collision avoidance and trajectory tracking algorithms to the main formation controller so as to realize a time-varying formation and to avoid any crash among the quadrotors. The simulation results showed that the proposed CFC is able to keep the quadrotors in pentagonal formation shape cooperatively in two-dimensional space.

References

- Can, K., & Başı, A. (2021). A leader-follower formation control of quadrotor: A virtual leader approach. In *2nd international symposium on applied science and engineering, 07–09 April*, Erzurum, Turkey.
- Dong, X., Zhou, Y., Ren, Z., & Zhong, Y. (2015). Time-varying formation control for unmanned aerial vehicles with switching interaction topologies. *Control Engineering Practise*, 46(2016), 26–36.
- Falconi, R., Sabattini, L., Secchi, C., Fantuzzi, C., & Melchiorri, C. (2015). Edge-weighted consensus-based formation control strategy with collision avoidance. *Robotica*, 33(2), 332–347. <https://doi.org/10.1017/S0263574714000368>
- Kuriki, Y. and Namerikawa, T., 2014. Consensus-based cooperative formation control with collision avoidance for a multi-UAV system. In *American Control Conference (ACC), June 4–6*, Oregon, USA.
- Muslimov, T. Z., & Munasyrov, R. A. (2021). Consensus-based cooperative control of parallel fixed-wing UAV formations via adaptive backstepping. *Aerospace Science and Technology*, 109, 1–22.
- Namerikawa, T., Kuriki, Y., & Khalifa, A. (2018). Consensus-based cooperative formation control for multi-quadcopter system with unidirectional network connections. *Journal of Dynamic Systems Measurement and Control*, 140, 044502-1-8.
- Roque, P., Heshmati-Alamdari, S., Nikou, A., & Dimarogonas, D. V. (2020). Decentralized formation control for multiple quadrotors under unidirectional communication constraints. *IFAC Papers Online*, 53-2, 3156–3161.
- Ren, W., & Atkins, E. (2007). Distributed multi-vehicle coordinated control via local information exchange. *International Journal of Robust and Nonlinear Control*, 17, 1002–1033.
- Toksöz, M.A., Oğuz, S., & Gazi, V. (2019). Decentralized formation control of a swarm of quadrotor helicopters. In *IEEE 15th International Conference on Control and Automation (ICCA), Edinburg, Scotland, 16–19 July*, pp. 1006–1013.
- Zhang, H., Li, Y., & Xu, G. (2018). Consensus-based control for unmanned aerial vehicle formation with speed adaptability. In *Chinese Control and Decision Conference (CCDC), 2018*, pp. 6106–6111.
- Zhao, Z., & Wang, J. (2018). Leader-follower formation control of multiple quadrotors. In *IEEE CSAA Guidance, Navigation and Control Conference (CGNCC)*, pp. 1–6.

Aerodynamic Effects of Airfoil Shape on Tandem Airfoil Configuration in Low-Reynolds-Number Transonic Flows



Nitin Vinodh, Ashwin Sridhar, Pavan Asha Sreekanth, Nivetha Srinivasan, Sanjiv Krishna Vetrivel, Balajee Ramakrishnananda, and T. Rajesh Senthil Kumar

1 Introduction

A tandem wing aircraft presents two independent lift generating aerodynamic surfaces (Minardo, 2014). Both wings have comparable aspect ratios and are typically set on two different planes separated both vertically and horizontally. In a low-Reynolds-number range, the boundary-layer characteristics on a static airfoil surface can be divided into four regimes, laminar, subcritical, transitional, and supercritical, which are dependent on the Reynolds number (Re) and the angle of attack. This detail implies that boundary-layer events are dramatically sensitive to Reynolds number. Understanding this would allow design engineers to make efficient choices while choosing the airfoil for an application in the low- Re transonic flow regime. Hence, starting the investigation with transonic airfoils and low-Reynolds-number airfoils for their performance in the combined low-Reynolds-number transonic regime would be more sensible. The transonic airfoil chosen was RAE 2822, and the low-Reynolds-number airfoil chosen was Wortmann FX 63-137. Supercritical effects are typically observed over the RAE 2822 airfoil when it is subjected to a transonic flow. The selection of Wortmann FX 63-137 was done on the basis of the extent of laminar flow expected over the airfoil and the results obtained from previous studies (Winslow et al., 2018). Significantly smaller drag bucket with an increase in minimum drag values was observed in this work. A reduction in peak lift coefficient when Re decreased from 10^6 to 10^5 , along with a nonlinear lift curve

N. Vinodh · A. Sridhar · P. A. Sreekanth · N. Srinivasan · S. K. Vetrivel

B. Ramakrishnananda (✉) · T. R. S. Kumar

Amrita Vishwa Vidyapeetham, Coimbatore, India

e-mail: cb.en.u4aee18026@cb.students.amrita.edu; cb.en.u4aee18008@cb.students.amrita.edu;

cb.en.u4aee18028@cb.students.amrita.edu; cb.en.u4aee18027@cb.students.amrita.edu;

cb.en.u4aee18037@cb.students.amrita.edu; r_balajee@cb.amrita.edu; t_rajesh@cb.amrita.edu

slope were observed in (Winslow et al., 2018). All the tandem analysis simulations were carried out at an angle of attack of 5° on the fore airfoil.

1.1 Applications

Ultrahigh-altitude micro-aerial vehicles (UHAMAV) envisaged to be used by military travel at low Reynolds number but high Mach number. Analysis of a single lift-producing surface in a low-Reynolds-number transonic flow shows scope for such applications theoretically till an altitude of 35 km (Drela, 1992). Primarily, with high altitude and long-range capabilities, military and defense application can be taken into consideration and may be utilized. The flow regime investigated in this work can also contribute to designing UAVs, atmospheric science research, and flying Martian rovers. Aircrafts like ER-2 AFRC and WB-57-JSC, with a maximum altitude of 21 km and 18 km, respectively, due to their structural and propulsive limitations may not be able to observe the phenomenon to its entirety. With UHAMAV platforms complementing advanced composite technology and energy-specific propulsion system, the predicted altitude of 35 km can be achieved.

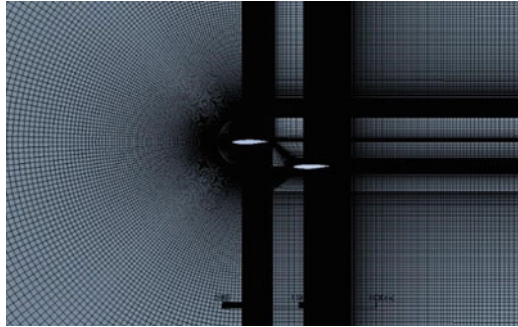
2 Methodology

2.1 Validation

A C-mesh was generated for performing the simulations as it was observed that it gave better results while providing ease of clustering (Abbey et al., 2020). Experimental results (Fanjoy & Dorney, 1997) were referred to for transonic regime validation of tandem setup. Two NACA 0012 airfoils of 1 m chord length were chosen for the setup. The simulations were conducted at operating conditions of Mach 0.7, angle of attack of 1.5° with the free stream, and a flow Reynolds number of 9×10^6 . Gap was set as 0 with a stagger of 3 s/c. The ANSYS Fluent setup was carried out using K- ω -SST model. It was observed that the solution matches closely with that of the experimental values.

Replicating the process for the low-Reynolds-number regime validation, experimental results obtained by (Scharpf & Mueller, 1992) were used. A tandem setup of two Wortmann FX 63-137 airfoils was chosen. The gap value was set at 0 g/c and stagger at 1.5 s/c. The angles of attack for aft and fore airfoils were set at 0° . Flow Reynolds number was 8.5×10^4 . The four-equation transition SST model was employed to model turbulence for validating the main tandem airfoil configurations.

Fig. 1 RAE 2822
TAC mesh



2.2 Simulation Setup and Method

ANSYS Fluent software was used for the simulations. The four-equation transition SST $K-\omega$ model was used for modelling turbulence. Density-based solver was deployed. Since varying all the parameters for the investigation would be a humongous task, stagger was fixed as 1.5 s/c , gap as 0.6 c , decalage as zero, and angle of attack as 5° , and chord length was chosen to be 0.8 m for both fore and aft airfoils.

Two setups were made to carry out the study:

RAE 2822 (both fore and aft airfoils)

Wortmann fx63137 setup (both fore and aft airfoils)

Grid independence studies were carried out, and the grid for RAE 2822 TAC setup is shown in Fig. 1. The grid for Wortmann fx63137 setup is similar.

3 Results and Discussion

The total lift coefficient of the aft and fore airfoils decreased, and drag coefficient increased in both setups with increase in the Mach number while keeping the Reynolds number constant. To evaluate the relative benefits of the various cases, the change in aerodynamic efficiency (L/D) of the tandem setups when compared to that of the corresponding individual airfoil setups was determined, and a trend was plotted.

The trend showed that Wortmann FX 63-137 which is optimized for low-Reynolds-number flows showcased an increase in aerodynamic performance at low transonic Mach numbers which then decreased and flatlined toward Mach 0.85 as seen in Fig. 2.

The trend showed that RAE 2822, which is optimized for handling supercritical effects over the airfoil, showed an initial decrement in aerodynamic efficiency at low transonic Mach numbers which then increased all the way to 48% at 0.85 Mach at Reynolds number $2.26E+5$ as seen in Fig. 3.

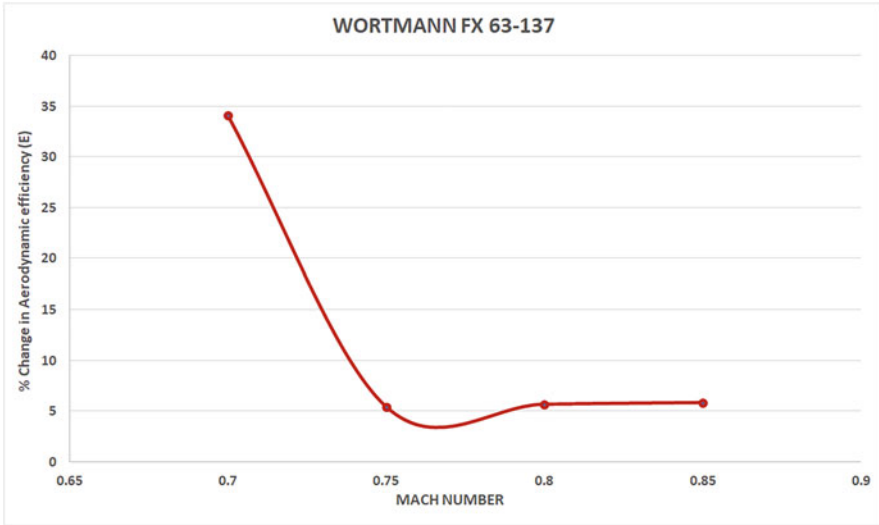


Fig. 2 Percentage change in aerodynamic efficiency vs Mach number for Wortmann FX 63-137 at 5° AoA

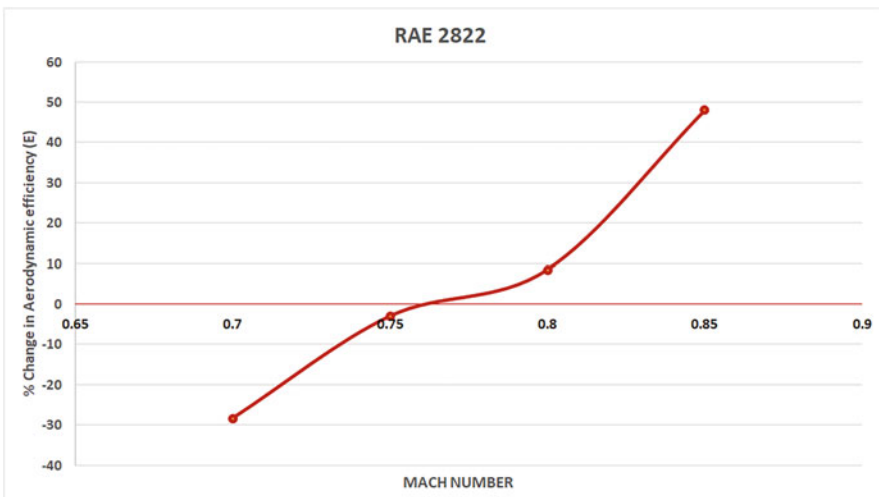


Fig. 3 Percentage change in aerodynamic efficiency vs Mach number for RAE 2822 at 5° AoA

λ -shocks were observed over the airfoil in all the cases proving that the flow over the airfoil is supercritical (Drela, 1992). From the Mach contours, it was observed that the shock interaction in the aft airfoil was weaker in the RAE 2822 setup in comparison to the Wortmann FX 63-137 setup. It was also observed that the shock-induced flow separation was delayed in the aft airfoil of the RAE 2822 setup, with the $M = 0.75$ and 0.7 , $Re = 2.26 \times 10^5$ case having negligible separation.

4 Conclusion

From the observations made, it could be said that at low transonic Mach numbers (Mach 0.7 to 0.8), the low-Reynolds-number airfoil (Wortmann FX 63-137) showed better aerodynamic efficiencies, while the converse is true for the supercritical airfoil tested (RAE 2822). However, it was observed that as we move toward sonic speeds (Mach > 0.8), the transonic influence of the flow overshadows the low Reynolds effects, giving RAE 2822 which is optimized for supercritical flow an edge over Wortmann FX 63-137. Flow separation is delayed in the supercritical airfoil compared to low-Reynolds-number airfoil for the specified regime at low transonic Mach numbers. Stronger shock interactions are seen in the fore and aft airfoils of the Wortmann FX 63-137 when compared to RAE 2822 as the Mach number was increased (within the transonic regime). The change in the aerodynamic efficiency trend from $M = 0.75$ to 0.8 at $Re = 2.26E+05$ that is seen in both RAE 2822 and Wortmann FX 63-137 can be attributed to the aerodynamics of the aft airfoil in both the setups as we observed a nonlinear variation in C_l values for them between those two cases.

Acknowledgments This work is part of a final year B.Tech dissertation project of the first five authors. The authors would like to thank all the faculty of Department of Aerospace Engineering Department, Amrita Vishwa Vidyapeetham, Ettimadai, for their constructive suggestions and fruitful discussions at various stages of this work.

References

- Abbey, S., Dankhara, K., & Senthilkumar, S. (2020). Aerodynamic characteristics of flow over two unsymmetrical tandemly arranged airfoils—numerical simulation. In *IOP conference series: Materials science and engineering* (Vol. 912.4, p. 042033). IOP Publishing.
- Drela, M. (1992). Transonic low-Reynolds number airfoils. *Journal of Aircraft*, 29(6), 1106–1113.
- Fanjoy, D., & Dorney, D. (1997). A study of tandem-airfoil interaction in different flight regimes. In *35th aerospace sciences meeting and exhibit*, p. 515.
- Minardo, A. (2014). *The tandem wing: Theory, experiments and practical realisations*. Masters thesis, Polytechnico di Milano.
- Scharpf, D. F., & Mueller, T. J. (1992). Experimental study of a low Reynolds number tandem airfoil configuration. *Journal of Aircraft*, 29(2), 231–236.
- Winslow, J., Otsuka, H., Govindarajan, B., & Chopra, I. (2018, May). Basic understanding of airfoil characteristics at low Reynolds numbers (104–105). *Journal of Aircraft*, 55(3), 1050–1061.

Neural Networks to Speed Up Multiphase Flow Numerical Simulations



León Mata, Rodrigo Abadía-Heredia, José Miguel Pérez,
and Soledad Le Clainche 

Nomenclature

Re Reynolds number
We Weber number
St Strouhal number

1 Introduction

This article considers the interaction of two liquid concentric jets, which is similar to the problem of fuel injection in a jet engine (Lefebvre & McDonell, 2017). For a nonviscous case, the difference in tangential velocities along the interface triggers the nonviscous Kelvin-Helmholtz instability (Hoyt & Taylor, 1977). In this case, other types of similar instabilities are responsible for the interaction and mixing of both phases.

An industrial application to this method can be the speedup of numerical simulations in a parametric study at a fuel injector. For instance, given the geometry in Fig. 1 (right), it could be possible to use this method to carry out an optimization process of the obstacle shape at the end of the inlet upper tube, also known as a bluff body. This bluff body is generally responsible for improving the mixture degree

L. Mata (✉) · R. Abadía-Heredia · J. M. Pérez
E.T.S.I. Aeronáutica y del Espacio, Universidad Politécnica de Madrid, Madrid, Spain
e-mail: leon.mata.cervera@alumnos.upm.es; sr.abadia@alumnos.upm.es;
josemiguel.perez@upm.es

S. Le Clainche
School of Aerospace Engineering, Universidad Politécnica de Madrid, Madrid, Spain
e-mail: soledad.leclainche@upm.es

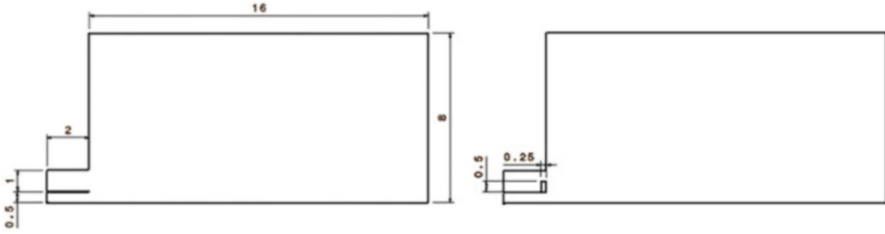


Fig. 1 Two geometries are considered in the problem of concentric jets. Notice the one in the right includes a bluff body. Dimensions are specified as multiples of a characteristic length $l = 1$ m

between both phases. The optimization process requires simulating a huge number of different configurations, and therefore computational costs will be high. By using this new method, simulations can be sped up using artificial intelligence, therefore saving an important amount of time.

First of all, a large amount of data is generated by conducting numerical simulations of both the single-phase flow and the multiphase flow problem using OpenFOAM® (Weller et al., 1998). Two different geometries are studied, one of them having a bluff body just before both jet streams get in contact, which is used to promote mixing. Another aspect considered is the effect of surface tension, which affects the mixing process. The next step consists of analyzing the data via HODMD to understand the physical mechanisms involved in both the single-phase and the multiphase flow cases in order to justify that it is possible to predict one case from the other. HODMD drastically reduces the dimensionality of the problem and allows to clean the noise. Finally, the multiphase flow results are predicted from single-phase flow data using a neural network.

2 Method

2.1 Equations

In this section, the equations corresponding to the volume of fluid model introduced by Hirt and Nichols (1981) are presented. The main idea underlying this model is to treat both phases as if they were a single effective phase by defining an indicator function α , also known as volume fraction, which tells which phase is present in a certain point in space. Both fluids are considered to be incompressible, immiscible, and isothermal. The following equations describe continuity, transport equation for volume fraction, and momentum equation:

$$\nabla \cdot \mathbf{v} = 0, \quad (1)$$

$$\frac{\partial \alpha}{\partial t} + \nabla \cdot (\alpha \mathbf{v}) = 0, \quad (2)$$

$$\frac{\partial(\rho\mathbf{v})}{\partial t} + \nabla \cdot (\rho\mathbf{v}\mathbf{v}) = -\nabla p + \nabla \cdot \overline{\boldsymbol{\tau}} + \mathbf{f}_\sigma, \quad (3)$$

where \mathbf{v} is velocity, ρ is density, p represents pressure, $\overline{\boldsymbol{\tau}}$ is the viscous stress tensor, and \mathbf{f}_σ corresponds to surface tension. Physical properties are not those of any real fluids but are chosen so that dimensionless numbers take the following values:

$$\text{Re}_1 = \frac{\rho_1 v_1 l}{\mu_1} = 600 \quad \text{Re}_2 = \frac{\rho_2 v_2 l}{\mu_2} = 30 \quad \text{We} = \frac{\rho v^2 l}{\sigma} = 80, \quad (4)$$

where σ and μ represent surface tension and viscosity. Notice there are two different Reynolds numbers since two phases are present.

2.2 Numerical Simulation

In order to simplify the original problem of two coaxial streams, a simpler geometry is used. Instead of solving the 3D problem, an axisymmetric version is considered so that the simulations are performed in a wedge-type geometry. At the left, two inlet tubes are separated by a thin plate through which both flow phases are injected into a main chamber, where interaction occurs. The boundary conditions at the top and right of the domain are set as outflow. The geometry shape and domain dimensions are adapted from Ling et al. (2019).

Six different numerical simulations have been carried out, four of which correspond to multiphase flow and the rest of them are single-phase flow simulations. Two different geometries are studied in order to understand the consequences of the presence of a bluff body as well as including or not the effect of surface tension.

2.3 HODMD

The data are analyzed using the higher order dynamic mode decomposition (HODMD) algorithm (Le Clainche & Vega, 2017). It performs a dimension reduction via SVD which allows to reduce the noise level and extract the SVD spatial and temporal modes. Then, the DMD-d method is applied, which uses d windows of snapshots to increase the dimension of the reduced snapshot matrix and forces the dynamics to be the same along all windows, which is useful to reduce noise and eliminate chaotic dynamics related to small-size flow scales, see Le Clainche et al. (2017).

A tensor of the form $v^l(x_i, y_j, t_k)$ contains the different variables over a structured grid in a certain number of equidistant snapshots. HODMD expresses the tensor as an expansion of M DMD modes, $u_m^l(x_i, y_j)$, each of them having its own frequency ω_m , growth rate δ_m , and amplitude a_m :

$$v^l(x_i, y_j, t_k) \cong \sum_{m=1}^M a_m u_m^l(x_i, y_j) e^{(\delta_m + i\omega_m)t_k} \quad (5)$$

2.4 Neural Network

A long short-term memory neural network has been used to run the predictions. Its structure is simple, consisting of an input layer with 20,000 neurons (corresponding to the total number of grid points in the computational domain), a dense layer with 100 neurons, and an output layer with 20,000 neurons. The LSTM layer also contains 100 neurons. See details in Abadía-Heredía et al. (2022).

2.5 Algorithm

The algorithm to obtain the multiphase predictions is as follows. First, numerical simulations of both the single-phase and multiphase are performed over a time interval $[t_0, t_1]$. Then, modal decomposition and a reduced order model are created for both cases. The following step is to train a neural network to predict the multiphase results from single-phase data. Single-phase simulations are carried out over an interval $[t_1, t_2]$. Finally, the previous neural network is used to predict the multiphase case over $[t_1, t_2]$.

3 Results and Discussion

After an initial stage in which both fluids advance through the computational domain, a permanent state is reached, in which one can identify patterns which evolve over time. Figure 2 exhibits the different amount of interaction between both jets when a bluff body is included as part of the geometry. Figure 3 shows one of the HODMD modes representing the flow physics, showing the similarities and differences in multiphase and single-phase flows. The neural network is trained to predict a multiphase flow case from the single-phase flow database, and the results are



Fig. 2 Comparison between the mixing degrees when including a bluff body in two concentric jets. Volume fraction is plotted, and the two colors represent each one of the flow phases

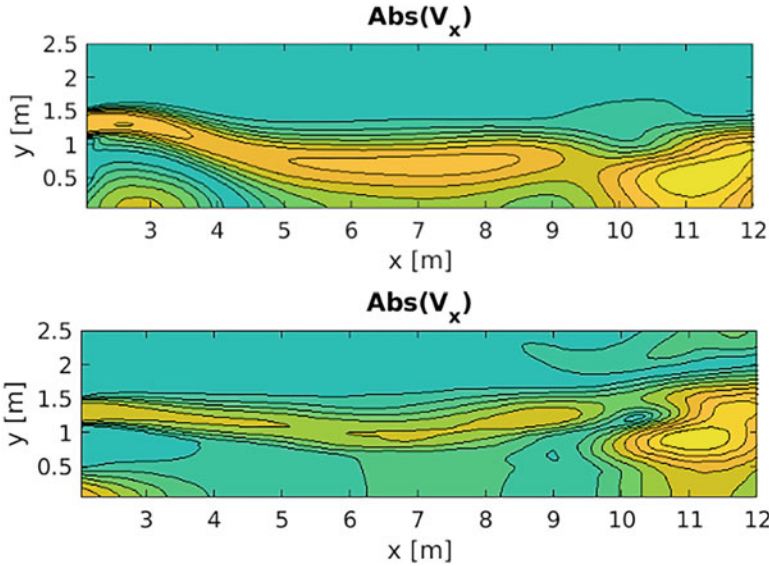


Fig. 3 Dominant DMD mode. Module of the streamwise velocity component corresponding to the single-phase flow case (top) and multiphase flow case without surface tension (bottom)

Table 1 Relative root-mean-square error (RRMSE) in the temporal predictions of multiphase flows using single-phase flow databases: Prediction 1 is done from simulation data and Prediction 2 uses the reduced order model. The computation time for the numerical simulations is also shown

Surface tension	Prediction 1 RRMSE	Prediction 2 RRMSE	Simulation time (h)
Single phase	–	–	1.66
Not included	0.182	0.108	5.24
Included	0.154	0.065	4.38

shown in Table 1. Two test cases are performed. In the first case, the neural network is trained using the raw data from the simulations. In the second case, HODMD is used to reconstruct the solution, only using the main modes modeling the flow physics. This is known as the *reduced order model*. The prediction relative root-mean-square error (RRMSE) shows that the best results are obtained when the reduced order model is used, which is due to the low amount of noise and the simpler dynamics since only a few modes are used. Computation times are also compared, and overall the single phase requires half to one third of the time compared to the multiphase case.

4 Conclusion

We present a model using recurrent neural networks that is able to predict the temporal evolution of multiphase flows from single-phase flow databases. The model is able to reduce the computational time of the simulations by a factor of 2–3, and the error of these predictions varies between 15% and 18% when considering noisy databases. Removing the noise, this error is reduced to 5–10%.

Acknowledgments The authors acknowledge the grant PID2020-114173RB-I00 funded by MCIN/AEI/10.13039/501100011033.

References

- Abadía-Heredia, R., López-Martín, M., Carro, B., Arribas, J. I., Pérez, J. M., & Le Clainche, S. (2022). A predictive hybrid reduced order model based on proper orthogonal decomposition combined with deep learning architectures. *Expert Systems With Applications*, 187, 115910.
- Hirt, C. W., & Nichols, B. D. (1981). Volume of fluid (VOF) method for the dynamics of free boundaries. *Journal of computational physics*, 39(1), 201–225.
- Hoyt, J. W., & Taylor, J. J. (1977). Waves on water jets. *Journal of Fluid Mechanics*, 83(1), 119–127.
- Le Clainche, S., & Vega, J. M. (2017). Higher Order Dynamic Mode Decomposition. *SIAM Journal on Applied Dynamical Systems*, 16(2), 882–925.
- Le Clainche, S., Vega, J. M., & Soria, J. (2017). Higher order dynamic mode decomposition of noisy experimental data: The flow structure of a zero-net-mass-flux jet. *Experimental Thermal and Fluid Science*, 88, 336–353.
- Lefebvre, A. H., & McDonell, V. G. (2017). *Atomization and sprays*. CRC Press.
- Ling, Y., Fuster, D., Tryggvason, G., & Zaleski, S. (2019). A two-phase mixing layer between parallel gas and liquid streams: multiphase turbulence statistics and influence of interfacial instability. *Journal of Fluid Mechanics*, 859, 268–307.
- Weller, H. G., Tabor, G., Jasak, H., & Fureby, C. (1998). A tensorial approach to computational continuum mechanics using object-oriented techniques. *Computers in Physics*, 12(6), 620–631.

Installation of a Ram Air Turbine in a Fixed-Wing UAV



María Expósito Turbak, Xin Chen , and Andreu Carbó Molina

1 Introduction

Unmanned air vehicles (UAV) had been used generally for all missions considered “dull, dirty and dangerous” (Gundlach, 2014). However, from 5 to 10 years ago, the first projects to carry passengers on UAV are starting to appear, making it compulsory to improve the safety requirements of these vehicles (Morby, 2017). The idea of UAV for dispensable, risky missions must be reviewed, using technology coming from manned aircrafts to increase its safety margins in emergency conditions.

Ram air turbines (RAT) are small wind turbines used as an emergency power source when there is a generalized failure of the electric system in aircrafts (Zhang et al., 2018). These RAT were first implemented in military aircraft during WWII, and in the 1960s they were also installed in civil aircrafts. Since then, several major incidents have been avoided, thanks to the application of this small turbine (Valencia Torres et al., 2020).

The RAT is connected to the aircraft electrical system or to a hydraulic pump and, thanks to the rotation of its blades caused by the incident wind, allows to generate enough power to run the essential avionic systems to approach and land (Saad et al., 2017). In normal aircraft operation, the RAT is retracted below the wings or the fuselage, and it is only depleted in emergency occasions. It is normally built in aluminum or titanium and due to its high rotational speeds is equipped with two to four blades.

The installation of a RAT into a UAV has not yet been studied in depth (Aliff, 2010; Valencia Torres et al., 2020). Those studies describe the process of fabrication, design, and testing of a small RAT for a micro-UAV system. The general idea is to use the extra energy provided by the RAT for extending the duration of the flight,

M. Expósito Turbak · X. Chen · A. Carbó Molina (✉)
Universidad Rey Juan Carlos, Fuenlabrada, Spain
e-mail: andreu.carbo@urjc.es

while it is not considered for an emergency procedure. Moreover, those studies only focus on generating the necessary power but not in the effect that the depletion of the RAT (and its extra drag force) would provoke in the flight characteristics of the UAV.

The objectives of the study are the following:

Recovery of UAV controllability in a complete loss of power situation.

Install a RAT in a fixed-wing UAV which can provide power to its avionics in a glide descent.

Study the effects of the deployment of the RAT on the flight qualities of the UAV.

2 Method

2.1 Drone Used for the Study

The UAV chosen as the benchmark is the Albatross multipurpose fixed-wing drone, developed by Applied Aeronautics (Applied Aeronautics, 2014). The basic specifications of the Albatross can be consulted in Table 1, along with the standard avionic package.

The sum of all component power accounts to 38.56 W. However, in an emergency, the CASIA I system could be switched off; therefore, the UAV could maintain the flight and proceed to an emergency landing with an electrical power of 28.56 W. This would be the necessary power delivered by the turbine. The RAT is placed under the UAV belly, and its maximum diameter is set at 180 mm to be able to retract it inside the fuselage (Fig. 1).

2.2 Flight Conditions

Using the flight mechanic equations (from Fig. 2), the flight speed V is determined for various angles of descent γ_d . As this angle is increased, wind speeds and the

Table 1 Basic specifications and avionic equipment of the Albatross UAV (Applied Aeronautics, 2014)

Specifications		Component	Power required
MTOW	10 kg	Camera FLIR	2.1 W
Max speed	129 km/h	Detect-and-avoid system CASIA I	10 W
Range	250 km	Autopilot Pixhawk V5X	20.56 W
Endurance	4 h	RFD900x Modem	0.6 W
Max payload	4 kg	Dragon Link 433 MHz Wi-Fi system	7 W
Power system	Electric	HS-5245MG Servo	1.5 W
Wingspan	3 m	LIDAR SF11	1 W

Fig. 1 Schematic size of the RAT in the Albatross UAV fuselage

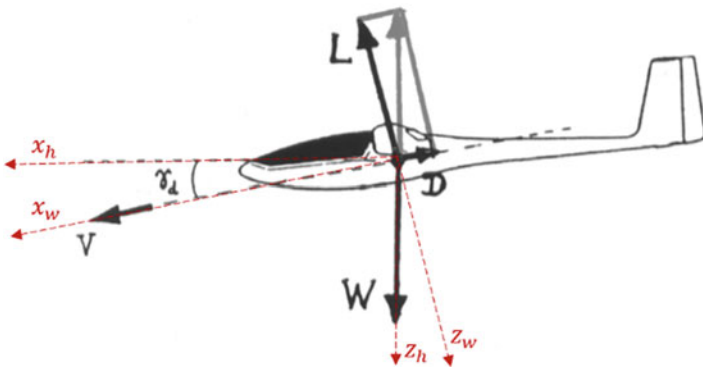


Fig. 2 Schematic representation of the flight dynamics of a glide maneuver

available power are increased, but the UAV loses efficiency. The power coefficient C_P is defined then as the power that the turbine extracts from the wind power available (Eq. 1):

Table 2 Required CP to power the avionics under different glide conditions

γ_d	Efficiency	Speed	Required CP
1.9°	30 (max)	16.3 m/s	0.42
2°	28.6	18.8 m/s	0.27
2.1°	27.3	20.2 m/s	0.22

Table 3 Characteristics of the optimized RAT

Airfoil	Number of blades	Rotational speed	Pitch angle
SG6043	3	5900 rpm	-10°

$$C_P = \frac{P_{\text{turbine}}}{\frac{1}{2}\rho AV^3} \quad (1)$$

Table 2 presents the necessary C_P for the RAT to be able to power the UAV avionics at different angles of descent. A $\gamma_d = 2^\circ$ is considered suitable for the study purposes, as it requires a feasible value of C_P according to wind energy literature, and the flight efficiency is not severely decreased.

2.3 QBlade Software

This open-source software for turbine calculation is used for the optimization of the blades. With the input of the blade airfoils, number of blades, and flow conditions, the software uses the blade element method (BEM) to generate optimal distribution of chord and blade twist for the desired rotor (Marten & Wendler, 2013).

The BEM calculates the forces in each section of the blade to provide both power extracted and thrust force. It comes at a low computational cost, though it must be noted that it takes several assumptions:

- No friction effects nor vorticity in the turbine wake
- Steady, incompressible flow without compressibility effects
- No 3D effects nor interactions between the different elements

3 Results and Discussion

Initializing the input parameters from consulted literature (Sudhamshu et al., 2016; Ramirez Gomez & Saavedra-Montes, 2012) and after a careful tuning of turbine solidity, pitch angle, and number of blades, the characteristics of the resulting turbine can be appreciated in Table 3. The criteria followed were to obtain the necessary power without creating too much thrust force (which would increase the drag of the UAV). Its geometry is presented in Fig. 3.

Fig. 3 Geometry and discretization of the optimized turbine blades obtained in the study

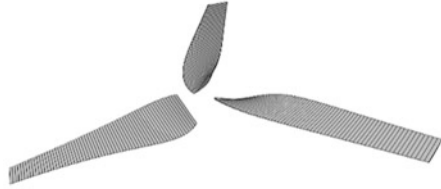


Fig. 4 Power coefficient curve of the optimized turbine

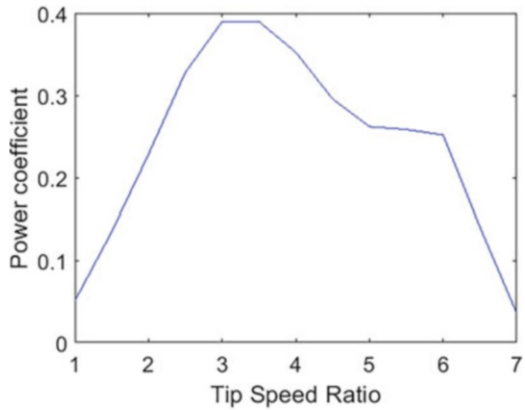
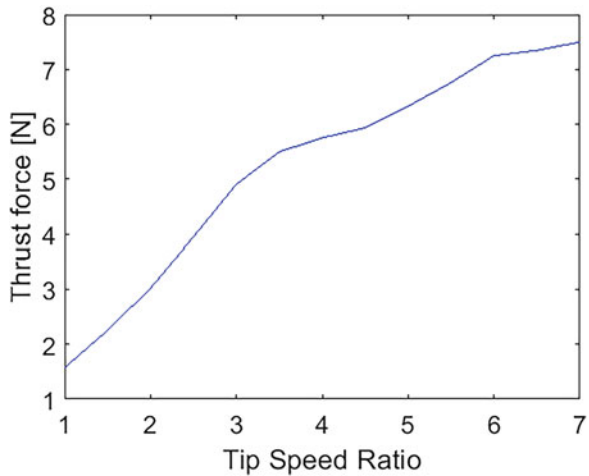


Fig. 5 Thrust force caused by the optimized turbine



The power and thrust curves obtained using the QBlade software are presented in Figs. 4 and 5, plotted against the tip-to-speed ratio (TSR) of the turbine (ratio between the speed of the rotating blade tip and the incoming wind speed). For an optimal TSR of 3, it can be seen how the turbine delivers enough power to feed the avionics while registering a thrust force of 3.5 N.

Table 4 Effect of the RAT deployment on the UAV aerodynamic efficiency

Without RAT			With RAT deployed		
Speed	Drag	Efficiency	Speed	Drag	Efficiency
18.8 m/s	1.8 N	28.6	19.2 m/s	5.3 N	9.8
Range	Endurance		Range	Endurance	
4295 m	228 s		1464 m	76 s	

Values of range and endurance are calculated from an initial height of 150 m

The deployment of the RAT causes a huge distress in the UAV aerodynamics. While 3.5 N may not seem a lot, for these small, very aerodynamic vehicles, the total drag values are in the same order of magnitude. Table 4 shows the effect of the RAT drag on the UAV aerodynamic efficiency. That large decrease will mean that when deflecting the RAT, even if the UAV will be controllable, the fall will be much more pronounced, resulting in a large loss of range and endurance.

4 Conclusion

The implementation of a RAT in the chosen UAV allows to perform a controlled descent in case of total failure of the electrical power supply. The drawback is a substantial decrease in aerodynamic efficiency. Due to this, it could be convenient to use the RAT in an intermittent manner, just in short phases of the descent in order to correct the course and attitude and do not lose most of the range and endurance. It is important to note that the chosen UAV has a rather reduced size, the effect on larger aircrafts would be smaller, therefore is a technology the most suitable the largest is the vehicle.

Aspects that have not been considered in this study that should be addressed in the future are the effect of the RAT depletion on flight stability, the structural stresses both in the turbine and transmitted to the UAV structure, and the aerodynamic interference between the RAT and other aircraft elements (landing gear, surface controls, or fuselage).

References

- Aliff, M. (2010). *Micro wind turbine as the power supply for micro unmanned aerial vehicle*. Bachelor degree thesis. Universiti Teknologi Petronas.
- Applied Aeronautics. (2014). *Meet Albatross, the first affordable, long range drone*. <https://www.appliedaeronautics.com/albatross-uav>
- Gundlach, J. (2014). *Designing unmanned aircraft systems: A comprehensive approach* (AIAA education series). American Institute of Aeronautics and Astronautics, Incorporated.
- Marten, D., & Wendler, J. (2013). *QBlade guidelines*. TU Berlin and Chair of Fluid Dynamics.

- Morby, M. (2017). *Dubai to begin flying world's first passenger drone*. Dezeen. <https://www.dezeen.com/2017/02/14/dubai-begin-flying-world-first-passenger-drone-transport-technology-news/>
- Ramirez Gomez, C., & Saavedra-Montes, A. (2012). Parameter calculation of a small wind turbine. *Circuits and Systems (CWCAS)*, 2012.
- Saad, M., Mohd, S., & Fadhli, M. (2017). A survey on the use of ram air turbine in aircraft. *AIP Conference Proceedings*, 1831, 020048.
- Sudhamshu, A., Pandey, M., Sunil, N., Satish, N., Mungundhan, V., & Velamati, R. (2016). Numerical study of effect of pitch angle on performance characteristics of a HAWT. *Engineering Science and Technology, an International Journal*, 19(1), 632–641.
- Valencia Torres, E., Berrazueta, M., Leines, D., Lema, H., Rodríguez, D., & Hidalgo Díaz, V. (2020). *Aerodynamic design and testing of a ram air turbine for small fixed-wing UAVs*. AIAA 2020-3957 Propulsion and Energy 2020 Forum.
- Zhang, X., Ding, S., Du, F., Ji, F., & Guo, S. (2018). Numerical simulation on aerodynamic performance of ram air turbine based on mixed flow field. In *Proceedings of the ASME 2018 international mechanical engineering congress and exposition. Volume 7: Fluids engineering*. Pittsburgh, Pennsylvania, USA. November 9–15, 2018. ASME.

Assessment of UAV Operators by Human Factor Analysis and Classification System (HFACS) Based on AHP



Omar Alharasees and Utku Kale

Nomenclature

AHP	Analytic hierarchy process
HFACS	Human factor analysis and classification system
UAV	Unmanned aeronautical vehicle
DOD	Department of Defense
UAS	Unmanned aircraft system

1 Introduction

Researchers' assessments aim to justify and understand the main reasons leading to failures in UAV operations, illustrate the leading cause, and improve system safety by presenting recommendations that can be used in the industry to reach a sustainable system. Even in unmanned aircraft systems (UAS) incidents and accidents, human error has been established as a primary component of many major aviation catastrophes. Human error frameworks such as HFACS and "Reason's Swiss cheese model" have been used to identify and evaluate contributing variables of accidents linked to human error in order to avoid future mishaps.

HFACS is one of the most extensively utilized technical models in the field to assess human factors among various accident analysis models. It was firstly created

O. Alharasees (✉) · U. Kale

Department of Aeronautics and Naval Architecture, Faculty of Transportation Engineering and Vehicle Engineering, Budapest University of Technology and Economics, Budapest, Hungary
e-mail: ooalharasees@edu.bme.hu

using the Swiss cheese model developed by James Reason (Reason, 1990). This conceptual framework has been applied to accidents and incidents in a variety of fields, including medical science (Diller et al., 2014), naval operations (Celik & Cebi, 2009), petroleum industry (Aas, 2008), construction (Xia et al., 2018), rail transport (Zhan et al., 2017), mining (Lenné et al., 2012), security and safety (Fu et al., 2020), and aviation (Li et al., 2008; Ancel & Shih, 2012).

For 10 years, the Department of Defense (DOD) has successfully employed the human factor analysis and classification system (HFACS) categorization to identify the human error in UAV incidents (Cotter & Yesilbas, 2014). It is critical not to overlook the undeniable human presence in UAVs and the potential human-related cause elements in UAV accidents to decrease and avoid such occurrences effectively. The HFACS framework has four primary categories and 19 subcategories. In this research, the present researchers consider 15 subcategories. The HFACS is beneficial for determining which variables have arisen historically and which ones should be prioritized. The HFACS originated from the “Swiss cheese model” reasons to explain the aviation system failure in this research.

On the other hand, the analytic hierarchy process (AHP) is a well-recognized “multicriteria decision-making (MCDM)” method for quantitative scoring techniques and an exceptional methodology for complex decision-making (Saaty, 2008). This method can help decision-makers classify significances and make the optimum selection (Saaty, 1990). An additional benefit of the AHP is to obtain mutually subjective and objective considerations by arranging complex opinions to a series of pairwise comparisons and then making the decisions.

Several previous researches employed AHP in UAV operations in the literature. Ting et al. used AHP to assess the UAV training system based on visual stimulation (Ting et al., 2018). Li, Xiaoyang, et al. developed a UAV route evaluation algorithm based on CSA-AHP and TOPSIS to solve the problem of UAV route evaluation (Li et al., 2017). Another significant usage in safety and security is creating a decision support model for UAV-aided disaster response using the AHP-TOPSIS method by Yildizbasi and Lütü (Makalesi et al., 2020).

This research aims to evaluate the elements that influence and affect the UAV operators based on the HFACS and investigate the human factor accident causation from the UAV operators’ point of view. The present study examines the preferences of the two operator categories, namely, (i) licensed UAV operators and (ii) non-licensed UAV operators, based on the primary criteria. In order to create a general hierarchical model, the analytic hierarchy process (AHP) is employed in this research. These decision-making models are primarily built on two layers in order to develop evaluator preference loads for (i) the assessment procedure, (ii) preventing complication, and (iii) lacking information from other AHP functions. In this study, the Saaty scale was utilized for scoring to depict lost data utilizing matrices that could be computed using a particular technique.

2 Method

Choosing the alternatives and sub-criteria should be determined or selected depending on their attributes, according to the MCDM technique. In MCDM scenarios, a specified number of options are constructed, sorted according to the evaluator’s priorities, and scored using the overall hierarchy.

The primary technique employed in the research is the analytic hierarchy process (AHP), a popular multicriteria decision-making (MCDM) technique to investigate the major and main characteristics of human factor accident causation in UAVs.

The present authors created a two-level hierarchy model generated from the HFACS with four main criteria extracted from the “Swiss cheese model” and reflected on the UAVs system, as shown in Fig. 1. The model categorizes the main types of aviation human factor accident causation factors from the HFACS model: (i) organizational influences, (ii) supervision, (iii) preconditions, and (iv) unsafe acts. Fifteen sub-criteria were considered in the research which suit the UAV system in this present research.

Figure 2 demonstrates the hierarchical model for the HFACS for UAVs with the components of each level.

Because the AHP utilizes the unique properties of pairwise comparison matrices (PCM), the choice of decision-makers between specific pairs of options illustrates the importance and priority of a particular aspect over another based on a scale (see Table 1). The matrix of pairwise comparisons (see Eq. 1) $A = [a_{ij}]$ represents the strength of the decision-makers’ preference between individual pairs of alternatives (A_i versus A_j , for all $i, j = 1, 2, \dots, n$). The pairwise comparison matrix can be given as follows (Eq. 1):

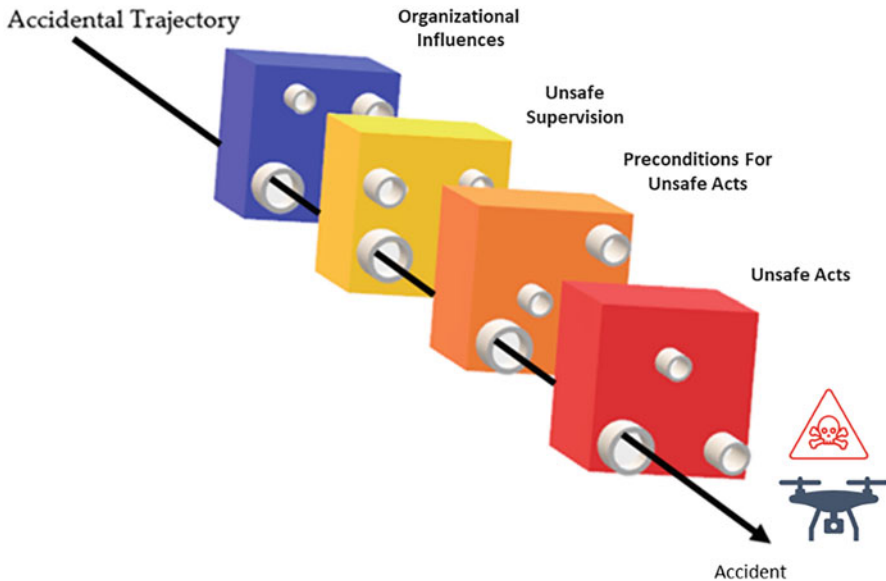


Fig. 1 Swiss cheese model based on HFACS for AUV

Fig. 2 The HFACS-AHP hierarchal model

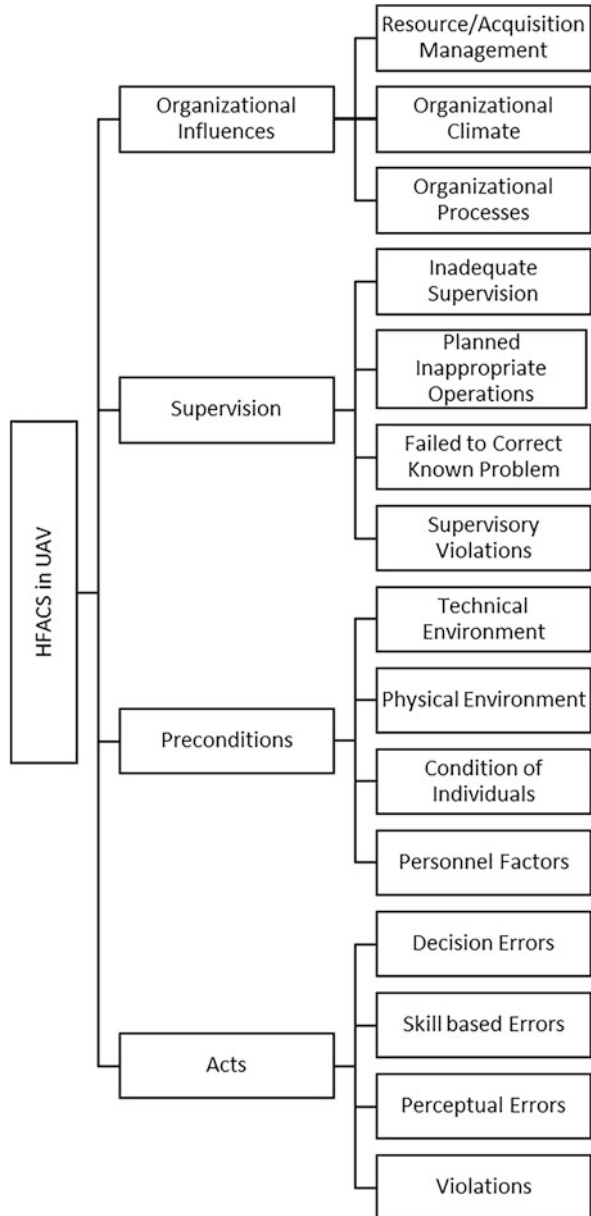


Table 1 Saaty fundamental scale

Numerical values	Verbal scale	Explanation
1	Equal importance of both elements	Two elements contribute equally
3	Moderate importance of one element over another	Experience and judgment favor one element over another
5	Strong importance of one element over another	An element is strongly favored
7	Very strong importance of one element over another	An element is very strongly dominant
9	Extreme importance of one element over another	An element is favored by at least an order of magnitude
2,4,6,8	Intermediate values	Used to compromise between two judgments

$$A = [a_{ij}] = \begin{bmatrix} 1 & a_{12} & \dots & a_{1j} & \dots & a_{1n} \\ \frac{1}{a_{12}} & 1 & \dots & a_{2j} & \dots & a_{2n} \\ \vdots & \vdots & \vdots & \vdots & \vdots & \vdots \\ \frac{1}{a_{1j}} & \frac{1}{a_{2j}} & \dots & a_{ij} & \dots & a_{in} \\ \vdots & \vdots & \vdots & \vdots & \vdots & \vdots \\ \frac{1}{a_{1n}} & \frac{1}{a_{2n}} & \dots & \frac{1}{a_{in}} & \dots & 1 \end{bmatrix} \tag{1}$$

The geometric mean of each group is calculated in the pairwise comparison matrices for prioritization proposes and to show the influence of each aspect in the model on each level. Because most experience matrices are unreliable, the matrix consistency ratio CR should be smaller than 0.1 for groups.

2.1 Questionnaire

An online AHP-based survey was designed and performed among UAV operators in this research. Sixteen UAV operators (average age 25 years) participated in a two-level hierarchal model grouped into two categories of UAV operators, namely, (i) licensed UAV operators (44%) and (ii) non-licensed UAV operators (56%) from 12 different countries as shown in Fig. 3 (right). Since the requirement to operate UAVs is different based on the field or the operation sector, it is essential to investigate the type of operation the participated operators are working on (Fig. 3, left).

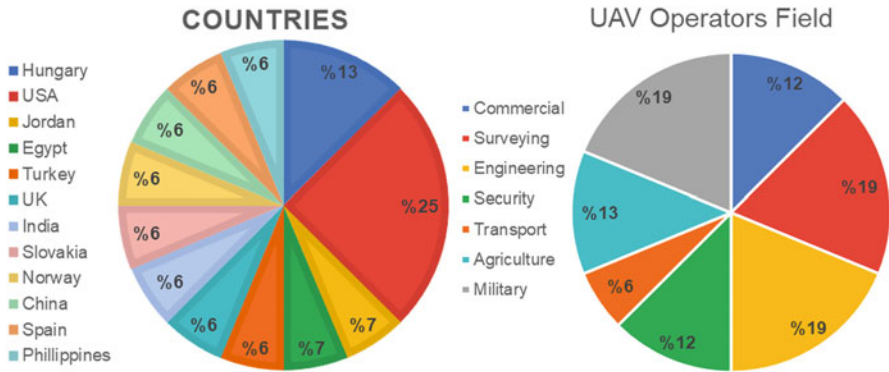


Fig. 3 Countries of the participants (right) and work sector of the participants (left)

Table 2 Licensed UAV operators PCM for the first level

Licensed UAV operators – first level					
HFACS	Organizational influences	Supervision	Preconditions	Acts	Weights (%)
Organizational influences	1.00	1.81	2.80	0.62	28.10
Supervision	0.55	1.00	0.71	0.36	13.29
Preconditions	0.36	1.40	1.00	0.20	12.23
Acts	1.62	2.75	5.03	1.00	46.37
CR = 0.0347	Sum=				100

3 Results and Discussions

The AHP method shows the variances between the groups’ overviews after evaluating and displaying the participants’ preferences in the model. Based on pairwise comparisons, the AHP approach will highlight the crucial features. The geometric mean has been used to gather and analyze the responses.

The following tables (Tables 2 and 3) show the aspects (weights, final score, and consistency ratio) that have been computed for the first level in the HFACS model characteristics from each group based on the collected responses of the two groups of UAV operators and by employing the AHP, evaluating and weighing the characteristics in each level individually.

The viewpoints of the two groups would reveal the differences between groups, which may increase related to expertise degree and work category. Comparing different groups of participants would make it easier to evaluate and weigh various individual aspects of UAV accident causation factors from other overviews. As shown in both groups’ overviews, unsafe acts would be the primary motive to cause the accidents, so investigating the subcategories of unsafe acts would give a more precise evaluation for the source of UAV mishaps.

Table 3 Non-licensed UAV operators PCM for the first level

Non-licensed UAV operators – first level					
HFACS	Organizational influences	Supervision	Preconditions	Acts	Weights (%)
Organizational influences	1.00	2.17	2.42	0.88	31.66
Supervision	0.46	1.00	2.72	0.28	18.10
Preconditions	0.41	0.37	1.00	0.52	12.18
Acts	1.14	3.51	1.94	1.00	38.06
CR = 0.08535	Sum=				100

Table 4 Licensed UAV operators PCM for the second level

Licensed UAV operators – second level					
Unsafe acts	Decision errors	Skill-based errors	Perceptual errors	Violations	Weights (%)
Decision errors	1.00	0.74	5.29	3.89	37.7
Skill-based errors	1.35	1.00	5.01	4.23	43.4
Perceptual errors	0.19	0.20	1.00	2.80	11.4
Violations	0.26	0.24	0.36	1.00	7.5
CR = 0.0804	Sum=				100

Table 5 Licensed UAV operators PCM for the second level

Non-licensed UAV operators – second level					
Unsafe acts	Decision errors	Skill-based errors	Perceptual errors	Violations	Weights (%)
Decision errors	1.00	0.72	1.83	4.82	33.0
Skill-based errors	1.39	1.00	1.88	3.51	36.8
Perceptual errors	0.55	0.53	1.00	4.88	23.1
Violations	0.21	0.28	0.21	1.00	7.1
CR = 0.0422	Sum=				100

The unsafe acts sub-criteria (weights, final score, and consistency ratio) that have been computed for the second level in the HFACS model characteristics from each group are shown in Tables 4 and 5 numerically and in Fig. 4 graphically.

Looking into the second level of the model (Fig. 4) for the sub-criteria of unsafe acts also provides a clear overview of the specific issue from the operators’ eyes. These are the decision errors that are directly linked to the inadequate training of UAV operators. In fact, combining both groups to compare the differences, as shown

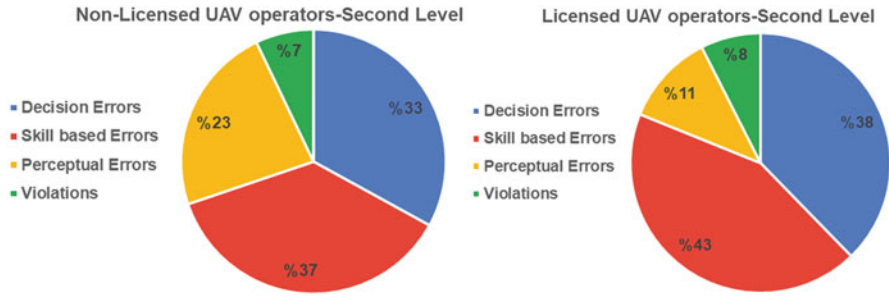


Fig. 4 Second level (unsafe acts) non-licensed (right) and licensed (left)

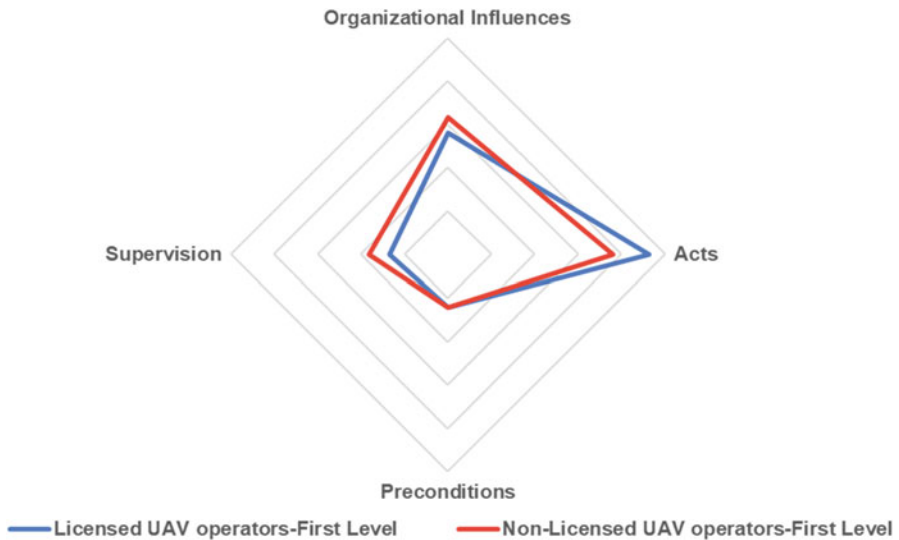


Fig. 5 HFACS model both groups comparison

in Fig. 5 in the first level, illustrates the importance of focusing on the training techniques. The authorization to use UAVs also going in the second level of the model would highlight the significance of framing bullet points in UAV operators’ training. As shown in Fig. 6, the decision- and skill-based errors are the crucial factors in accident causation from the participant’s point of view.

The comparison shows that the discrepancies become clear at every level when considering more groups and multiple levels.

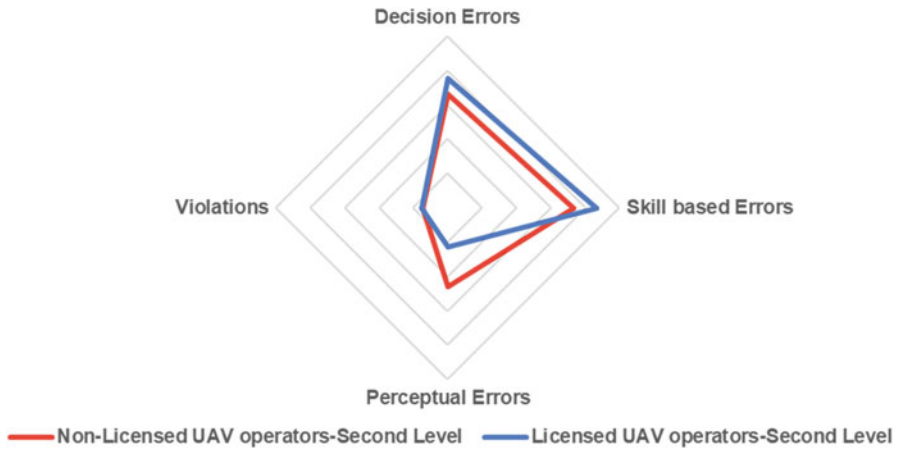


Fig. 6 Second level unsafe acts both groups comparison

4 Conclusion

The findings revealed a preference order and scaling for HFACS accident causation in UAV operations based on the participating operators’ responses to the AHP procedure, which shows the critical factors within each level and gives a reliable indicator of the important aspects. In order to assess essential features in a futuristic UAV environment and control critical human errors, multicriteria methods, especially AHP, played a crucial role. The discrepancies between the views are demonstrated using quantitative and qualitative criteria and the conventional, basic, and simple analytical hierarchical process (AHP) decision-making approach.

The results of this survey were based on a total of 16 UAV participated operators from two groups based on the minimum requirement of UAV license and different work sectors. The outcomes of this research highlighted the importance of operators’ skills and decisions in the system.

This research shows that the UAV operators’ unsafe act plays a dominant role in the HFACS model for all participants. The organizational influences follow this in the first level which could be dealt with in detail if there were a common image of the UAV operator’s license requirement. The second level of the model reflected the lack of training for UAV operators.

Acknowledgment The present researchers would like to thank the support given to this publication from KTI (Közlekedéstudományi Intézet Nonprofit Kft.) – BME (Budapest University of Technology and Economics) Project, proposal titled “Assessing Operators (Pilot, Air Traffic Controller) Total Loads and Evaluating Aeronautical Decision-Making.”

References

- Aas, A. L. (2008). The Human Factors Assessment and Classification System (HFACS) for the oil & gas industry. In *IPTC International Petroleum Technology Conference*. OnePetro. <https://doi.org/10.2523/IPTC-12694-MS>
- Ancel, E., & Shih, A. T. (2012). The analysis of the contribution of human factors to the in-flight loss of control accidents. In *12th AIAA Aviation Technology, Integration and Operations (ATIO) conference and 14th AIAA/ISSMO multidisciplinary analysis and optimization conference*. <https://doi.org/10.2514/6.2012-5548>
- Celik, M., & Cebi, S. (2009). Analytical HFACS for investigating human errors in shipping accidents. *Accident Analysis & Prevention*, 41(1), 66–75. <https://doi.org/10.1016/J.AAP.2008.09.004>. Pergamon.
- Cotter, T., & Yesilbas, V. (2014). Structural analysis of HFACS in unmanned and manned air vehicles. In *Proceedings of the American society for engineering management 2014 international annual conference*. American Society for Engineering Management (ASEM).
- Diller, T. W., et al. (2014). The Human Factors Analysis Classification System (HFACS) applied to health care. *American Journal of Medical Quality*, 29(3), 181–190. <https://doi.org/10.1177/1062860613491623>. SAGE.
- Fu, L., et al. (2020). Investigation into the role of human and organizational factors in security work against terrorism at large-scale events. *Safety Science*, 128, 104764. <https://doi.org/10.1016/J.SSCI.2020.104764>. Elsevier.
- Lenné, M. G., et al. (2012). A systems approach to accident causation in mining: An application of the HFACS method. *Accident Analysis & Prevention*, 48, 111–117. <https://doi.org/10.1016/J.AAP.2011.05.026>. Pergamon.
- Li, W. C., Harris, D., & Yu, C. S. (2008). Routes to failure: Analysis of 41 civil aviation accidents from the Republic of China using the human factors analysis and classification system. *Accident Analysis & Prevention*, 40(2), 426–434. <https://doi.org/10.1016/J.AAP.2007.07.011>. Pergamon.
- Li, X., et al. (2017). UAV route evaluation algorithm based on CSA-AHP and TOPSIS. In *2017 IEEE International Conference on Information and Automation, ICIA 2017* (pp. 915–920). Institute of Electrical and Electronics Engineers Inc. <https://doi.org/10.1109/ICINFA.2017.8079033>
- Makalesi, A., Yıldızbaşı, A., & Gür, L. (2020). A decision support model for unmanned aerial vehicles assisted disaster response using AHP-TOPSIS method. *European Journal of Science and Technology (Avrupa Bilim ve Teknoloji Dergisi)*, 20, 56–66. <https://doi.org/10.31590/EJOSAT.737764>
- Reason, J. (1990). Human error. *International Journal of Man-Machine Studies*, 39, 1051–1057. Cambridge University Press.
- Saaty, T. L. (1990). How to make a decision: The analytic hierarchy process. *European Journal of Operational Research*, 48(1). [https://doi.org/10.1016/0377-2217\(90\)90057-I](https://doi.org/10.1016/0377-2217(90)90057-I)
- Saaty, T. L. (2008). Decision making with the analytic hierarchy process. *International journal of services sciences*, 1(1), 83–98. <https://doi.org/10.1504/IJSSci.2008.01759>
- Ting, W. T., et al. (2018). Research on UAV simulation training system based on visual simulation. In *Proceedings of 2018 IEEE International Conference on Mechatronics and Automation, ICMA 2018* (pp. 1972–1977). Institute of Electrical and Electronics Engineers Inc. <https://doi.org/10.1109/ICMA.2018.8484640>
- Xia, N., et al. (2018). A hybrid BN-HFACS model for predicting safety performance in construction projects. *Safety Science*, 101, 332–343. <https://doi.org/10.1016/J.SSCI.2017.09.025>. Elsevier.
- Zhan, Q., Zheng, W., & Zhao, B. (2017). A hybrid human and organizational analysis method for railway accidents based on HFACS-Railway Accidents (HFACS-RAs). *Safety Science*, 91, 232–250. <https://doi.org/10.1016/J.SSCI.2016.08.017>. Elsevier.

WMLES of a Small-Scale Hovering Propeller



Jelena Svorcan and Christopher Ivey

Nomenclature

P Power
T Thrust

1 Introduction

Today, unmanned air vehicles (UAVs) are one of the fastest growing engineering fields, mostly due to their diverse applications as well as various shapes and sizes. Much work is being done on their development, improvement, and testing in both academia and industry (Delorme et al., 2021; HERNICZEK et al., 2019; RUSSELL & SEKULA, 2017). In most cases, small-scale UAVs, which can be used for surveillance, scientific measurements, deliveries, etc., are propelled by rotors. Since these rotors must remain operational, efficient, and reliable in numerous different operating regimes (including hover and vertical flight but also horizontal and forward/backward flight), they are mostly designed for particular aircraft, and special attention should be dedicated to their modeling and simulation (KELLY & JEMCOV, 2019; ZHAO & SHENG, 2022). This paper presents one such attempt, i.e., a detailed analysis of the flow structures appearing around a small-scale hovering propeller.

J. Svorcan (✉)

Faculty of Mechanical Engineering, University of Belgrade, Belgrade, Serbia
e-mail: jsvorcan@mas.bg.ac.rs

C. Ivey

Cascade Technologies Inc., Palo Alto, CA, USA
e-mail: civey@cascadetechnologies.com

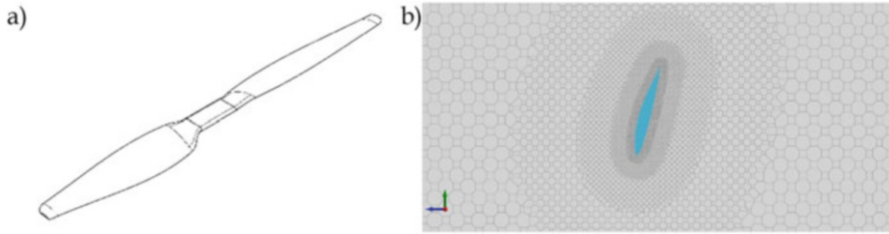


Fig. 1 (a) Propeller geometry, (b) detail of the computational grid

The tested rotor geometry, illustrated in Fig. 1a, was previously designed at the University of Belgrade, Faculty of Mechanical Engineering (UB-FME) (Kovačević et al., 2021). Its diameter is $D = 0.762$ m, and nominal rotational frequency $\nu = 54.817$ Hz resulting in Reynolds number $Re = 300,000$ at 0.75 blade span. It was defined through aerodynamic optimization and flow simulations that ranged from simple (corrected potential flow) to more complex ones involving the solution of Reynolds-averaged Navier-Stokes (RANS) equations.

However, if a more accurate estimation of aerodynamic performances is to be obtained, the unsteadiness and complexity of the propeller flow, particularly of the shedding vortices, require more advanced computational approaches that resolve some portion of the flow scales (since it is still not viable to resolve all of them). One such approach is wall-modeled large eddy simulation (WMLES) where larger-scale turbulent motion is resolved, while subgrid-scale motion (appearing in the wall vicinity) is considered more isotropic and can then be modeled (Moin et al., 2016). Here, the objective is to estimate the possibilities of LES in flows around small-scale hovering rotors/propellers under different operating regimes.

2 Method

The performed numerical study is validated through a comparison with experimental data also obtained at UB-FME.

2.1 *Experimental Measurement*

While more details and illustrations of experimental setup may be found in Kovačević et al. (2021), here, just the most important aspects are repeated. Five different quantities (rotor thrust in hover T , rotor frequency, voltage, current, and vibrations) were measured, while the rotor torque and power P were implicitly determined. A serious drawback of the performed experiment is that most part of the measuring equipment as well as the rigid support stand is located in the propeller

wake, which affects the measured aerodynamic performances but in a favorable way. Namely, the wake is being dispersed in a similar way as if it were in the ground vicinity (which happens in takeoff and landing phases). In such peculiar operating conditions, it is possible to generate higher levels of thrust for the same power (or vice versa, achieve the same thrust at lower required power) which, at least partially, explains the high levels of thrust that were documented.

2.2 Numerical Computation

Outer, stationary computational domain is a large cylinder surrounding the propeller, extending 2 m, 8 m, and 5 m in upstream, downstream, and radial directions, respectively. To assure that grid features do not affect the final results, computational meshes of different levels of refinement were generated and tested. The coarse, medium (whose detail is illustrated in Fig. 1b), and fine meshes contain approximately 2, 7, and 16 million hexagonal control volumes, respectively. All meshes are generated by building Voronoi diagrams and smoothing the point distribution by Lloyd iterative process in a mesh generator called Stitch (which is native to charLES).

Finite-volume-based compressible flow solver charLES developed by Cascade Technologies, Inc., is used to compute the investigated flow fields. The basic idea behind LES approach is to solve the spatially filtered Navier-Stokes equations governing the flow. The subgrid-scale stresses resulting from the filtering process should be modeled. Here, the Vreman model is used to model the subgrid-scale stresses. A no-penetration stress-based algebraic equilibrium wall model is used to obtain the velocity profiles in the wall vicinity.

Two different versions of the charLES solver are available: low-Mach (Helmholtz) and compressible formulation. The former, which approximates the flow as isentropic, achieves a coupling between pressure and density fields and preserves a finite speed of sound thus admitting lower frequency acoustic waves at acceptable time steps, is more appropriate for lower velocity flows (Ambo et al., 2017), while the latter solves the fully compressible Navier-Stokes equations using the ideal gas law for the equation of state. It can be used in all flow cases, although it is computationally more expensive (<https://support.cascadetechnologies.com/posts/2265-charles-low-mach>). Here, the compressible formulation alongside the moving mesh option was employed since blade tip Mach number is approximately 0.4.

Standard values of air properties are assumed. Flow is initialized from rest. In this compressible formulation, the effects of rotation are incorporated by actually moving (i.e., rotating) the inner portion of the mesh in every time step. The moving/rotating region is also shaped like a cylinder closely encompassing the propeller (extending 0.2 m and 0.6 m in axial and radial directions, respectively). Zero velocity is defined along all the outer boundaries, while an interface surface separates the inner rotor

from the outer stator. Walls are rotating, with algebraic equilibrium wall model boundary condition (which assumes velocity profiles used for the computation of wall stresses).

Time step (on the medium mesh) corresponds to an angular increment of 0.025° , while 25 rotations in total are computed, until achieving the convergence of aerodynamic force and moment (their fluctuations remain below 1%). Flow statistics is collected during the last five rotations.

3 Results and Discussion

Figure 2 presents the measured and computed thrust and power curves with respect to rotor rotational frequency. As may be observed, the expected second and third power-law dependencies for the thrust and power, respectively, are nicely captured. Numerical curves are generally in good agreement with experimental data, although the thrust seems slightly underestimated. This is probably due to the previously mentioned insufficiently clean experimental setup. Computed points are obtained by averaging the instantaneous values of thrust and power over the last five rotations.

Wakes aft of the rotor at nominal frequency are depicted in Fig. 3a by the averaged induced velocity field. As could be expected, the wake contracts in the downstream direction. It is also possible to illustrate various instantaneous flow scales and vortical flow features appearing around the rotor, Fig. 3b. They are mostly noticeable near the blade tips, i.e., in the blade region that mostly contributes to the rotor aerodynamics, and they vacillate as the propeller rotates.

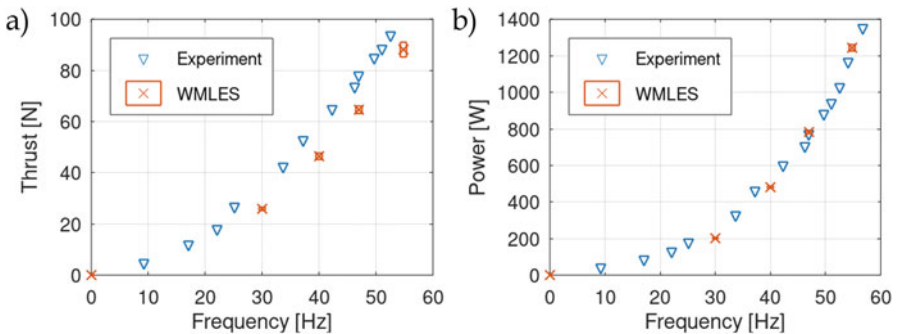


Fig. 2 (a) Thrust curve and (b) power curve

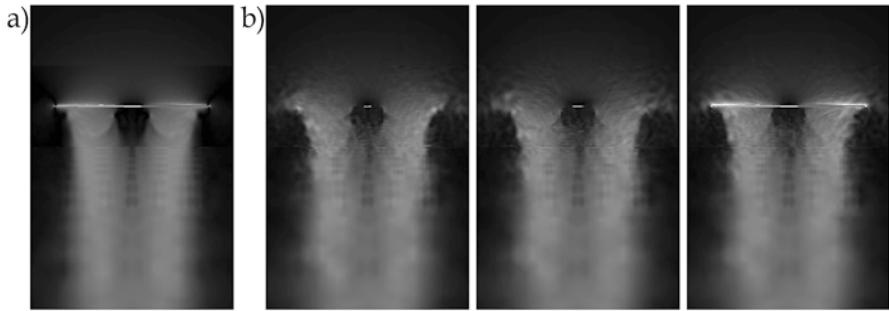


Fig. 3 (a) Averaged induced velocities and (b) instantaneous induced velocities (corresponding to different propeller azimuth angles)

4 Conclusion

It has been demonstrated that a relatively computationally economic LES can provide usable results (estimate rotor aerodynamic performances with sufficient accuracy, in addition to providing extremely vivid visualizations of instantaneous flow fields which are quite important for urban air vehicles). Satisfactory agreement with experimental data is achieved. To achieve better correspondence to experimental data, future studies will include the:

- Improved (higher fidelity) geometries and refined computational meshes
- Consideration of ground effect
- Investigation of other vertical flight regimes

Acknowledgment J. S. conducted this research during a Fulbright Fellowship at Stanford University, Center for Turbulence Research from November 2021. J. S. is also supported by the Ministry of Education, Science, and Technological Development of Republic of Serbia through contract no. 451-03-68/2022-14/200105.

The GPU-accelerated simulations in this paper were performed using “Chapman” at the Center for Turbulence Research.


References

- Ambo, K., Yoshino, T., Kawamura, T., Teramura, M., Philips, D., Bres, G., & Bose, S. (2017). *Comparison between wall-modeled and wall-resolved large eddy simulations for the prediction of boundary-layer separation around the side mirror of a full-scale vehicle*. AIAA SciTech Forum 2017, AIAA, AIAA 2017-1661.
- Delorme, Y., Stanly, R., Frankel, S. H., & Greenblatt, D. (2021). Application of actuator line model for large eddy simulation of rotor noise control. *Aerospace Science and Technology*, 108, 106405.
- Herniczek, M. K., Jee, D., Sanders, B., & Feszty, R. (2019). Rotor blade optimization and flight testing of a small UAV rotorcraft. *Journal of Unmanned Vehicle Systems*, 7(4), 325–344.

- Kelly, R., & Jemcov, A. (2019). *Very large eddy simulation of a UH-60 rotor in hover*. AIAA SciTech Forum 2019, AIAA, AIAA 2019-1885.
- Kovačević, A., Svorcan, J., Hasan, M. S., Ivanov, T., & Jovanović, M. (2021). Optimal propeller blade design, computation, manufacturing and experimental testing. *Aircraft Engineering and Aerospace Technology*, 93(8), 1323–1332.
- Moin, P., Bodart, J., Bose, S., & Park, G. I. (2016). Wall-modeling in complex turbulent flows. *Notes on Numerical Fluid Mechanics and Multidisciplinary Design*, 133, 207–219.
- Russell, C. R., & Sekula, M. K. (2017). Comprehensive analysis modeling of small-scale UAS rotors. In *Annual forum proceedings – AHS international, American Helicopter Society*, pp. 2865–2880.
- Zhao, Q., & Sheng, C. (2022). *Predictions of HVAB rotor in hover using hybrid RANS/LES methods-II*. AIAA SciTech Forum 2022, AIAA, AIAA 2022-1550.

A Review on Fishbone Active Camber Morphing Wing Surfaces



Emre Özbek, Selcuk Ekici, and T. Hikmet Karakoc 

Nomenclature

EMC	Elastomeric matrix composite
FEM	Finite element method
FISHBAC	Fishbone active camber
UAV	Unmanned aerial vehicle

1 Introduction

With the entry of the second century in aircraft design, the prominent issues are increasing the efficiency of designs. Issues such as reducing fuel consumption, reducing greenhouse gas emissions, increasing the rate of alternative fuels, and reducing noise have begun to come to the fore.

Morphing technologies are the subjects that serve this productivity increase expectation. When we look at flying creatures in nature, we see morphing technologies. It is accepted that the beginning of people's dream of flying was formed by watching birds. In this context, it is a continuation of the same school to be inspired

E. Özbek (✉)
Eskisehir Technical University, Eskisehir, Türkiye
e-mail: emreozbek@eskisehir.edu.tr

S. Ekici
Department of Aviation, Iğdır University, Iğdır, Türkiye

T. H. Karakoc
Eskisehir Technical University, Eskisehir, Türkiye
Information Technology Research and Application Center, Istanbul Ticaret University,
Istanbul, Türkiye

Table 1 Focal points of morphing wing studies

2D parameters	3D parameters
Leading edge control (Vasista et al., 2019)	Wing span control (Bae et al., 2005)
Trailing edge control (Soneda et al., 2021)	Wing chord control (Thill et al., 2010)
Thickness change control (Gamboa et al., 2007)	Dihedral angle control (Wu et al., 2017)
Camber change (Yokozeki et al., 2014)	Wing sweep angle control (de Marmier & Wereley, 2003)

by flying animals in developing our aircraft technologies and in applications that will increase efficiency.

The word morphing derives from the root “morph,” meaning to change shape (Rodriguez, 2007). Considering this origin, actually pulling the landing gear into the fuselage, which has been one of the features in our aircraft for a long time, is a morphing act. Vectored thrust applications are a morphing feature that can be evaluated in this context with the ability to create a significant shape change on the plane. Despite these origins and well-established practices, the standard view is to call the changes seen in various quantities of wing morphing.

There are no rules regarding which studies should be included in the scope of morphing in the literature. Nevertheless, some preliminary information can guide the researchers who will enter this study area. As it is known, the wings of birds take various forms during flight, and we try to create similar force differences with control surfaces in the wings of our present aircraft. That’s why the wings of our planes are called “fixed wings.” The wings of birds can be conceived as “morphing wings” (Taylor et al., 2012). Bird’s wings are responsible for thrust generation and transport generation, unlike our fixed-wing aircraft (Ghommem et al., 2014). Studies to understand the flight dynamics of birds are still in full swing. However, their ability to switch to stable and unstable states during the flight (Harvey et al., 2022), to create continuous and discontinuous structures using their feathers (Wissa et al., 2015), and to make trade-offs between performance components such as maneuverability, handling, and speed throughout the flight is undoubtedly above the point we can reach in our aircraft (Harvey, 2018).

Many unmanned aerial vehicles (UAVs) have been developed with the bio-inspired studies guided by these studies, and various performance advantages have been tried to be obtained from one or more of these movements (Budholiya et al., 2021). Morphing wing applications have emerged as a branch of these studies. With morphing wing studies, components such as lift, drag, and moment on the wings can be changed, and angle values such as dihedral and sweep of the wing planform that affect flight mechanics can be changed. In this way, the performance of aircraft can be changed, and aircraft that can take on more roles and perform a broader range of operations emerge. Essentially, morphing wing studies aim to reduce the disadvantage of designing aircraft for a single phase of flight. Unmanned aerial vehicles (UAVs) are generally used as test platforms for these studies due to their size, accessibility, and cost (Özel et al., 2021). If it is desired to make a

classification in morphing wing studies, it can be divided into studies on three-dimensional or two-dimensional parameters of wings as in Table 1.

2 Fishbone Active Wing Camber Literature

Fishbone active wing camber morphing studies, which are the subject of the study, focus on 2D parameters such as trailing edge control and camber control areas from the areas given in Table 1. In this study area, abbreviated as FishBAC, it is aimed that the control surfaces on the wing are placed under the wing cover without any seams.

The first study that mentioned the FISHBAC concept was a published conference paper by Benjamin King Sutton Woods and Michael Ian Friswell from the UK in 2012 (Woods & Friswell, 2012). The study was held as a preliminary investigation of the concept. In this study, actuators mounted inside a D-shaped wing spar induced bending moments on the spine through an antagonistic pair of tendons like natural musculature systems. The researchers employed a pretension-loaded elastomeric matrix composite (EMC) as wing skin. A small pulley with a driving shaft was also used to provide the required actuations.

As the founding fathers of this concept, researchers defined three criteria for the guidance:

- Control authority.
- Simplicity.
- Reliability.

Their research has employed a highly anisotropic and compliant structure with EMC skin. The fishbone-inspired spine provided the required anisotropy for the core. Pretensioning of the EMC was performed to get rid of buckling that may cause over the wing skin. Apart from the previous school of using smart materials as actuators and skin, they've excluded the smart structure approach in their concept. Maintainability, vulnerability to fatigue, and the cost basis of smart structures were provided as the main reasons for exclusion. In the research, NACA 0012 airfoil was selected, and XFOIL analyses were performed with flapped and unflapped settings to understand the aerodynamic features of the resultant geometry. Analysis performed by the researchers brought promising results with an increase in lift coefficient. Also, a prototype manufactured within this study was provided with the capability of significant camber changes with low actuation effort.

In 2013, the FishBAC concept design was developed further by employing coated corrugated skin (Dayyani et al., 2013). Composite corrugated panels, with their stiffness along the corrugation direction and flexibility in the transverse direction, have been used in previous morphing wing studies (Ge et al., 2010). In this conference paper, their advantages have been combined with the FishBAC concept. Finite element method (FEM) analyses were performed to select the most advantageous corrugation for the application, and coated trapezoidal configuration was

selected. Although a model of FishBAC geometry with corrugated skin was provided, however a prototype or experimental study was not provided.

In 2014, Benjamin King Sutton Woods and Michael Ian Friswell came up with a new prototype for the FISHBAC concept (Woods & Friswell, 2014). The new test model was based on an OA212 airfoil. The tendon-shaped area has been moved and narrowed to a 75–90% chord that differs from the first proposed concept. A series of benchtop tests and laser displacement sensor scans were performed to validate the analytical results. Tendon-shaped core coupled with the proposed mechanism and the intended concept was experimentally validated for the first time.

A test piece was manufactured during the study. The rigid part of the wing/rotor section was manufactured from nylon using selective laser sintering. The core section of the FISHBAC was printed using ABS material on a 3D printer, along with the tendon activator pulley and the mounting bracket. Stainless steel and aluminum were the driveshaft, bearings, and assembly hardware materials. The skin material used in the test article was pure silicone elastomer. Researchers then, performed tests to provide actuation energy requirement and displacement data for the design. Test data showed good agreement with the analyses.

In 2017, a composite FishBAC prototype was developed (Rivero et al., 2017). In previous FishBAC wing designs, isotropic polymers were used, and advantages can be achieved from anisotropic were not utilized. In this study, a composite spine FishBAC has been designed for wind tunnel testing. A modular leading edge and trailing edge model was employed, and the FishBAC section was adopted from the previous design.

In 2019, a modification to the previous actuation mechanisms was presented. The modification integrated the spiral pulley negative stiffness mechanism (Wang et al., 2019). The mechanism was integrated to lessen the actuation energy cost. The NACA 23012 airfoil was selected for the research. Wind tunnel experiments were not provided in this conference paper. Still, the spiral pulley mechanism provided a negative stiffness against the structural stiffness and was found to be a promising articulation mechanism for FISHBAC studies.

In 2020, a wind tunnel comparison between a conventionally flapped wing and a FishBAC wing was performed with a reported at least 16% aerodynamical efficiency increase (Rivero et al., 2020). Also, a wind tunnel test article was manufactured and was used in experiments.

In 2022, a novel 3D printed skin was used in a FishBAC design (Rivero et al., 2022). These skin panels were manufactured using two different thermoplastic polyurethanes. Additionally, modularity between actuation and installation was employed in the designed prototype within the study. 9. A wing part with a 1-meter span, 0.27 m chord, and %25 FishBAC area was built and used for experiments. Benchtop proof load tests were also performed to provide robustness of the design. The new design also provided a change in pitching moment, and the lift coefficient increased around 0.55, thus showing potential for FishBAC technology as a promising control surface substitute.

3 Conclusions

FishBAC technology is an up-and-coming research field that has been developed by a narrow group of researchers, as shown in this literature survey. Reaching a wider research pool may provide different points of view on this topic. The present FishBAC technology could be upgraded more in materials, design, and mechanisms with more perspectives involved. It is a promising branch of morphing wing/tail design that could be integrated with rotor blades, UAV wings, and general aviation aircraft surfaces.

As stated by the founding fathers of this concept, future studies should focus on keeping the simplicity, reliability, and control authority. The main drawbacks of morphing research are actuation costs, complexities, and costs. There's an ingrained prejudice against morphing applications about added weight and unnecessary complexity. The FishBAC technology can overcome these issues and provide feasible wing camber control, and trailing edge deflections can replace ailerons and flaps in the future.

The present literature lacks experimental data. Although there is wind tunnel involvement in some published articles, there are no flight tests. UAVs can provide feasible testbeds for these studies.

Developments in three-dimensional printing technologies are also crucial in using different materials and printing techniques to improve FishBAC designs.

Future research on this topic should offer different approaches feasible in terms of added weight and manufacturing costs. These can be achieved by aiming for low actuation force and being lightweight in design. Extra mechanisms and parts must be avoided to overcome the prejudice against morphing designs.

Acknowledgments The research was funded by the Eskisehir Technical University with a project code of 21DRP049.

References

- Bae, J. S., Seigler, T. M., & Inman, D. J. (2005). Aerodynamic and static aeroelastic characteristics of a variable-span morphing wing. *Journal of Aircraft*, 42(2), 528–534.
- Budholiya, S., Bhat, A., Raj, S. A., Hameed Sultan, M. T., Md Shah, A. U., & Basri, A. (2021). State of the art review about bio-inspired design and applications: An aerospace perspective. *Applied Sciences*, 11(11), 5054.
- Dayyani, I., Woods, B. K., Friswell, M. I., & Khodaparast, H. H. (2013, October). The optimal design of a coated corrugated skin for the FishBAC morphing wing. In *24th international conference on adaptive structures and technologies*.
- de Marmier, P., & Wereley, N. M. (2003). Morphing wings of a small scale UAV using inflatable actuators- sweep control. In *44th AIAA/ASME/ASCE/AHS/ASC structures, structural dynamics, and materials conference*.
- Gamboa, P., Aleixo, P., Vale, J., Lau, F., & Suleman, A. (2007). *Design and testing of a morphing wing for an experimental UAV*. University of Beira Interior Covilha (Portugal).

- Ge, R., Wang, B., Mou, C., & Zhou, Y. (2010). Deformation characteristics of corrugated composites for morphing wings. *Frontiers of Mechanical Engineering in China*, 5(1), 73–78.
- Ghommam, M., Hajj, M. R., Beran, P. S., & Puri, I. K. (2014). Role of wing morphing in thrust generation. *Theoretical and Applied Mechanics Letters*, 4(3), 032003.
- Harvey, C. (2018). *Gull wing morphing allows active control of tradeoffs in efficiency, maneuverability and stability*. Doctoral dissertation, University of British Columbia.
- Harvey, C., Baliga, V. B., Wong, J. C. M., Altshuler, D. L., & Inman, D. J. (2022). Birds can transition between stable and unstable states via wing morphing. *Nature*, 603(7902), 648–653.
- Özel, C., Özbek, E., & Ekici, S. (2021). A review on applications and effects of morphing wing technology on UAVs. *International Journal of Aviation Science and Technology*, 1(01), 30–40.
- Rivero, A. E., Weaver, P. M., Cooper, J. E., & Woods, B. K. (2017, October). Progress on the design, analysis and experimental testing of a composite fish bone active camber morphing wing. In *ICAST 2017: 28th international conference on adaptive structures and technologies* (pp. 1–11). ICAST.
- Rivero, A. E., Fournier, S., Manolesos, M., Cooper, J. E., & Woods, B. (2020). Wind tunnel comparison of flapped and FishBAC camber variation for lift control. In *AIAA SciTech 2020 forum* (p. 1300).
- Rivero, A. E., Fournier, S., Heeb, R. M., & Woods, B. K. (2022). Design, manufacture and wind tunnel test of a modular FishBAC wing with novel 3D printed skins. *Applied Sciences*, 12(2), 652.
- Rodriguez, A. (2007, January). Morphing aircraft technology survey. In *45th AIAA aerospace sciences meeting and exhibit* (p. 1258).
- Soneda, K., Yokozeki, T., Imamura, T., & Tsushima, N. (2021). Multi-fidelity aeroelastic simulation of a morphing wing trailing edge. In *AIAA Scitech 2021 forum* (p. 0953).
- Taylor, G., Carruthers, A., Hubel, T., & Walker, S. M. (2012). Wing morphing in insects, birds and bats: Mechanism and function. *Morphing Aerospace Vehicles and Structures*, 13–40.
- Thill, C., Etches, J. A., Bond, I. P., Potter, K. D., & Weaver, P. M. (2010). Composite corrugated structures for morphing wing skin applications. *Smart Materials and Structures*, 19(12), 124009.
- Vasista, S., Riemenschneider, J., Monner, H. P., Nolte, F., & Horst, P. (2019). Manufacture and testing of a large-displacement droop-nose morphing wing leading edge. In *AIAA Scitech 2019 forum* (p. 1858).
- Wang, C., Zhang, J., Shaw, A. D., Amoozgar, M., Friswell, M. I., & Woods, B. K. (2019). Integration of the spiral pulley negative stiffness mechanism into the FishBAC morphing wing. In *9th ECCOMAS thematic conference on smart structures and materials (SMART 2019)*.
- Wissa, A., Han, A. K., & Cutkosky, M. R. (2015, July). Wings of a feather stick together: Morphing wings with barbule-inspired latching. In *Conference on biomimetic and biohybrid systems* (pp. 123–134). Springer.
- Woods, B. K. S., & Friswell, M. I. (2012, September). Preliminary investigation of a fishbone active camber concept. In *Smart materials, adaptive structures and intelligent systems* (Vol. 45103, pp. 555–563). American Society of Mechanical Engineers.
- Woods, B. K., & Friswell, M. I. (2014). Structural characterization of the fish bone active camber morphing airfoil. In *22nd AIAA/ASME/AHS adaptive structures conference* (p. 1122).
- Wu, M., Xiao, T., Ang, H., & Li, H. (2017). Investigation of a morphing wing solar-powered unmanned aircraft with enlarged flight latitude. *Journal of Aircraft*, 54(5), 1996–2004.
- Yokozeki, T., Sugiura, A., & Hirano, Y. (2014). Development and wind tunnel test of variable camber morphing wing. In *22nd AIAA/ASME/AHS adaptive structures conference* (p. 1261).

Reliable Aircraft Trajectory Prediction Using Autoencoder Secured with P2P Blockchain



Seyed Mohammad Hashemi, Seyed Ali Hashemi,
and Ruxandra Mihaela Botez

Nomenclature

- i Number of steps for future trajectory prediction
- j Number of executed transactions
- N Number of associated with a block in the chain
- T_n Time during which the aircraft is as step n

1 Introduction

Air traffic management (ATM) is the most critical issue in aviation transportation (Tomlin et al., 1998). Weakness in the ATM system can increase expenses (Gagné et al., 2013), and mistakes can result in aerial collisions (Hashemi & Botez, 2022a, b). Artificial intelligence has proved its extraordinary ability for ATM (Hashemi et al., 2023) and control (Kuitche et al., 2022).

The ATM system mainly works based on “future trajectories.” Hence, the advancement of trajectory prediction algorithm can significantly improve ATM efficiency. In this paper, a novel algorithm is designed to construct a highly reliable and accurate aircraft trajectory prediction (ATP) model. A large number of

S. M. Hashemi (✉) · R. M. Botez

Laboratory of Applied Research in Active Controls, Avionics and AeroServoElasticity
LARCASE, ÉTS—École de Technologie Supérieure, Université de Québec,
Montréal, QC, Canada

e-mail: seyed-mohammad.hashemi.1@ens.etsmtl.ca; ruxandra.botez@etsmtl.ca

S. A. Hashemi

Department of Electrical and Computer Engineering, University of Tehran, Tehran, Iran

deterministic and probabilistic approaches were designed for aircraft trajectory prediction (ATP) (Ghazi et al., 2020).

Among all proposed methodologies, data-driven algorithms have shown until now the best performance when a rich dataset was provided (Hashemi et al., 2020). Thus, for the ATP task, the autoencoder algorithm is utilized in this paper due to its excellent functionality and results obtained even in case of deficient data (Ivanovic et al., 2020). Since the autoencoder is sensitive against adversarial attacks, the peer-to-peer (P2P) confirmation strategy (Alladi et al., 2020) is used to ensure predicted trajectories. Nowadays, blockchain technology can support P2P strategies, and it is significantly improving their security and reliability (Miglanı et al., 2020).

The paper is organized as explained in the next sections. Methodology (Sect. 2) explains trajectory prediction using the autoencoder and securing using P2P blockchain. Section 3 is devoted to Results, where the ATP accuracy is represented under data failures and adversarial attack, which are finally concluded in Sect. 4.

2 Method

A flight zone is assumed that contains several aircraft which are flying in their air corridors as shown in Fig. 1. By using the GPS data at time $= T_n$ (including latitude, longitude, altitude, heading, speed, and time), the model predicts data at the next i steps.

The autoencoder was utilized as benchmarking algorithm for the ATP due to the strong dependency among training data and to its excellent performance when data is deficient. Figure 2 shows autoencoder architecture (Nguyen & Quanz, 2021).

As shown in Fig. 2, the GPS data (latitude, longitude, altitude, heading, speed, time) is applied to the input layer and fully propagates through the Encoder layer that compresses the input dimensionality. The latent layer in the middle of architecture produces the code, which is fully passed to the decoder layer that is the mirror of the encoder layer and is used to enlarge the code dimension. Finally, the decoder layer prepares the full dimension data for the output layer.

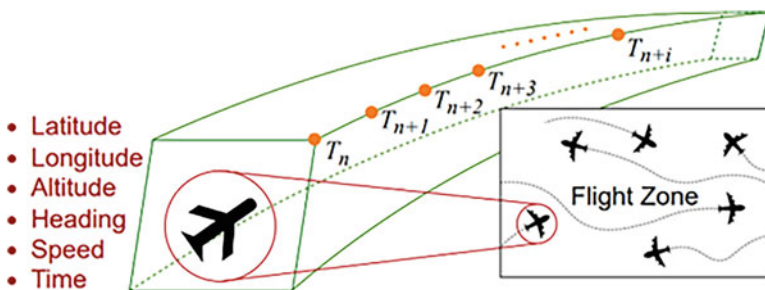


Fig. 1 Aircraft trajectory prediction used for air traffic management

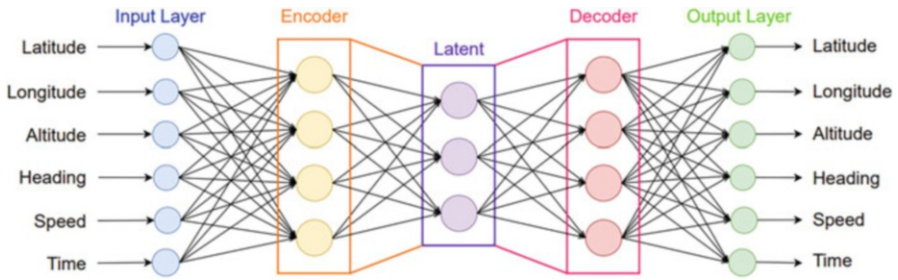


Fig. 2 The trained autoencoder architecture for aircraft trajectory prediction

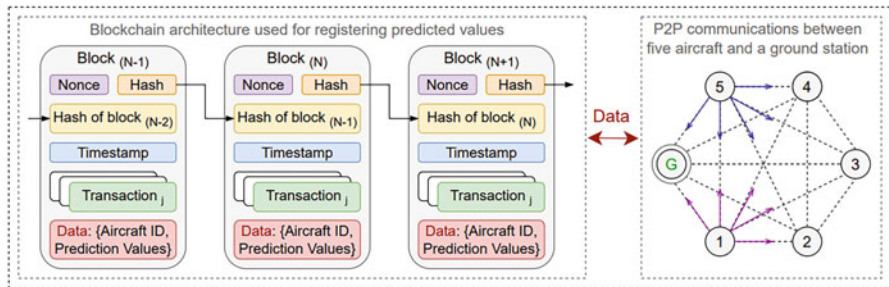


Fig. 3 The P2P blockchain architecture for confirming truth of predicted trajectories

Although the autoencoder is robust when it approaches deficient data, it may be attacked by the adversarial data (Hashemi et al., 2020). Hence, peer-to-peer (P2P) blockchain (Alladi et al., 2020), shown in Fig. 3, was used as a decentralized supervisory multi-agent system to confirm predicted trajectories by the autoencoder.

We assume a ground station and five aircraft that are fully communicated together and construct a P2P topology. Each aircraft (as an agent) is equipped with an autoencoder and can predict its and other aircraft’s future trajectories. The ATP is performed decentralized, and predicted values are transferred to be registered on the blockchain. Each block is executed if all agents confirm the predicted trajectory for a specific aircraft. Secured data mainly contains aircraft ID (1–5) and predicted values that are stored in the block. This process is done on-chain relying on the hash of the previous block, added number to the hash (nonce), exact execution moment (timestamp), and j trajectory predictions (transactions).

3 Results and Discussion

For validation studies, the utilized dataset in Hashemi et al. (2020) was used for training, testing, and validation of the designed autoencoder. Weighing vectors were initialized, and then batch normalization was done by recentering and rescaling input

Table 1 Aircraft trajectory prediction accuracy using autoencoder and LSTM under a variety of failures

Data failures	LSTM (%)	Autoencoder (%)
No failures	99.5	98.7
Latitude	91.6	98.1
Latitude and heading	83.2	95.3
Latitude, altitude, and speed	58.7	91.2

Table 2 Aircraft trajectory prediction accuracy using secured autoencoder under a variety of failures while adversarial attacks are imposed

Data failures	Secured autoencoder	
	Adversarial retraining (%)	P2P blockchain (%)
No failure	65.3	97.7
Latitude	45.1	97.2
Latitude and heading	31.7	94.4
Latitude, altitude, and speed	24.1	90.1

data in order to fast and stable trajectory prediction. Regularization was also done to reduce magnitude in the trajectory regression phase. Hyperparameters were tuned such that the code size was 3×1 to be tolerant in case of missing three elements in input vector $[latitude, longitude, altitude, heading, speed, time]_{6 \times 1}$ due to the GPS data failures. The number of nodes for the encoder and decoder must be less than input and more than latent (we considered four nodes which showed a better performance compared to five nodes). Mean square error (MSE) was determined as the loss function. Table 1 represents the prediction accuracy for autoencoder and long short-term memory (LSTM) under a variety of data failures.

According to Table 1, the LSTM shows slightly better performance than autoencoder only for no failure cases. But when these methods used deficient (failure) data (e.g., latitude, altitude, and speed failure), the autoencoder showed good prediction accuracy (91.2%), while the LSTM performance dramatically degraded (58.7%). Therefore, the autoencoder gives better results for deficient data than the LSTM.

Not surprisingly, experiments showed that both the autoencoder and LSTM are sensitive against adversarial attacks. Hence, both adversarial retraining and P2P blockchain were used to secure the autoencoder. For the adversarial retraining, we used 25% of total available adversarial samples. For securing with P2P blockchain, we utilized a private chain constructed by “consensus layer” and “contract layer” that works based on proof of stake and smart contract, respectively. Table 2 represents the prediction accuracy for autoencoder under a variety of failure cases, while it is secured using adversarial retraining and P2P blockchain.

In accordance with Table 2, although adversarial retraining could make the autoencoder robust against adversarial attacks, its prediction accuracy was very poor in case of data failure. For instance, under adversarial attacks and missed data (e.g., latitude and heading), the prediction accuracy was 31.7%, despite that

the autoencoder was adversarially retrained. In contrast, P2P private blockchain secured autoencoder such that it provided 94.4% prediction accuracy (in case of adversarial attack and data failures related to latitude and heading).

4 Conclusion

A reliable aircraft trajectory prediction model was designed based on autoencoder architecture. It showed excellent prediction accuracy when it was approached with deficient data obtained from the GPS. The autoencoder was examined by adversarial attacks. The adversarial retraining technique could not provide both high robustness and prediction accuracies. The decentralized private P2P blockchain secured the ATP model based on multi-agent confirmations, in which the autoencoder prediction accuracy was higher than 90% despite adversarial attack on the supposed agent and deficient input vector due to the lack of GPS data.

References

- Alladi, T., Chamola, V., & Sahu, N. (2020). Applications of blockchain in unmanned aerial vehicles: A review. *Vehicular Communications*, 23, 100249.
- Gagné, J., Murrieta, A., Botez, R. M., & Labour, D. (2013). New method for aircraft fuel saving using Flight Management System and its validation on the L-1011 aircraft. In *2013 Aviation technology, integration, and operations conference* (p. 4290).
- Ghazi, G., Botez, R. M., & Maniette, N. (2020). Cessna Citation X takeoff and departure trajectories prediction in presence of winds. *Journal of Aerospace Information Systems*, 17(12), 659–681.
- Hashemi, S. M., & Botez, R. M. (2022a). Lyapunov-based robust adaptive configuration of the UAS-S4 flight dynamics fuzzy controller. *The Aeronautical Journal*, 1–23.
- Hashemi, S. M., & Botez, R. M. (2022b). Support vector regression application for the flight dynamics new modelling of the UAS-S4. In *AIAA SCITECH 2022 forum* (p. 2576).
- Hashemi, S. M., Botez, R. M., & Grigorie, T. L. (2020). New reliability studies of data-driven aircraft trajectory prediction. *Aerospace*, 7(10), 145.
- Hashemi, S. M., Hashemi, S. A., Botez, R. M., & Ghazi, G. (2023). A novel fault-tolerant air traffic management methodology using autoencoder and P2P blockchain consensus protocol. *Aerospace*, 10(4), 357.
- Ivanovic, B., Leung, K., Schmerling, E., & Pavone, M. (2020). Multimodal deep generative models for trajectory prediction: A conditional variational autoencoder approach. *IEEE Robotics and Automation Letters*, 6(2), 295–302.
- Kuitche, M. A. J., Yañez-Badillo, H., Botez, R. M., & Hashemi, S. M. (2022). Stabilisation, tracking and disturbance rejection control design for the UAS-S45 Balaam. *The Aeronautical Journal*, 1–23.
- Miglani, A., Kumar, N., Chamola, V., & Zeadally, S. (2020). Blockchain for Internet of Energy management: Review, solutions, and challenges. *Computer Communications*, 151, 395–418.
- Nguyen, N., & Quanz, B. (2021, January). Temporal latent auto-encoder: A method for probabilistic multivariate time series forecasting. In *Proceedings of the AAAI conference on artificial intelligence* (Vol. 35, No. 10, pp. 9117–9125).
- Tomlin, C., Pappas, G. J., & Sastry, S. (1998). Conflict resolution for air traffic management: A study in multiagent hybrid systems. *IEEE Transactions on Automatic Control*, 43(4), 509–521.

Sensor Hybridization Through Neural Networks for Terminal Guidance



Raul de Celis, P. Solano-Lopez, and Luis Cadarso

1 Introduction

Navigation signals from global navigation satellite systems (GNSS) are commonly used nowadays in aerospace applications. Unfortunately, reliability decreases inversely proportional to the requirement of the application for which it is designed. Note that attenuation and loss of the GNSS signal result in reduced signal-noise relationship. To lessen these effects and defend against jamming, independent sources of navigation information are needed. Although inertial navigation systems (INS), such as inertial measurement units (IMUs), are independent of external perturbations, they present important deficiencies. However, INS are excellent source of navigation information when combined with GNSS receivers, which can minimize errors in INS (de Celis et al., 2017). The benefits of integrated data fusion has been shown in many antisubmarine, strategic air, and land warfare applications (Waltz & Buede, 1986). Data fusion algorithms for six-degree-of-freedom (DOF) missiles are described in Nguyen et al. (2016). The advantages and issues in utilizing diverse sorts of INS expanded with GNSS updates have been considered by Schmidt and Phillips (2011). In addition to INS/GNSS hybridization, a group of nonlinear observers are described by Bryne et al. (2017). On the off chance that different sensors are accessible, they might be extra contributions to a filter, e.g., the Kalman filter (de Celis et al., 2017). Modern laser-guided ballistic rockets are integrating IMU, GPS, and laser guidance capability, offering high precision and all-weather attack capability (de Celis & Cadarso, 2019), especially during the last phases of the trajectory. Sensor hybridization methodologies and algorithms which aim at proposing effective and robust GNC are a present need. The use of ML methods for the

R. de Celis (✉) · P. Solano-Lopez · L. Cadarso
Aerospace Systems and Transport Research Group, Rey Juan Carlos University, Fuenlabrada,
Spain
e-mail: raul.decelis@urjc.es; pablo.solano@urjc.es; luis.cadarso@urjc.es

estimation of parameters based on the dynamics of aerospace vehicles presents the advantage that once the algorithm is trained or calibrated, it is not necessary to know the physical-mathematical foundations that govern dynamics, but it is the algorithm that, for the input data, returns the information that can later be used within the GNC algorithm (Solano-Lopez et al., 2019).

The objective of this paper is to obtain an accurate vector between rocket and target to be employed on a terminal guidance and control system from a combination of different sensor measurements hybridized by neural networks.

2 System Modeling

The proposed guidance, navigation, and control approach is applied to a 140 mm axis symmetric rotary rocket with wraparound stabilizing fins. Launch speed is supersonic, and initial spin rate is approximately 150 Hz. The maneuvering mechanism consists of a roll-decoupled fuse attached to the tip of the rocket. The fuse is made up of four canard surfaces, decoupled 2 by 2, to generate control force modulus and argument in an orthogonal plane to the rocket section, and its associated moment (de Celis et al., 2017).

To construct the flight dynamics model, two-axis systems are defined: conventional aerospace body-fixed axes (b) and inertial north-east-down axes (e). The following expression (1) defines the forces and moments, respectively. \vec{D} , \vec{L} , \vec{M} , \vec{P} , \vec{T} , \vec{W} , \vec{C} , and \vec{CF} are drag, lift, Magnus, pitch damping, thrust, weight, Coriolis, and actuator control forces, respectively, and \vec{O} , \vec{P}_M , \vec{M}_M , \vec{S} , and \vec{CM} are overturn, pitch damping, Magnus, spin damping, and actuator control moments, respectively:

$$\left[\vec{F}_{\text{ext}}, \vec{M}_{\text{ext}} \right] = \left[\vec{D} + \vec{L} + \vec{M} + \vec{P} + \vec{T} + \vec{W} + \vec{C} + \vec{CF}, \quad \vec{O} + \vec{P}_M + \vec{M}_M + \vec{S} + \vec{CM} \right] \quad (1)$$

Rocket aerodynamic forces in body axes are described in (2):

$$\begin{bmatrix} \vec{D} \\ \vec{M} \\ \vec{CF} \end{bmatrix} \begin{bmatrix} \vec{L} \\ \vec{P} \end{bmatrix} = -\frac{\pi}{8} d^2 \rho \begin{bmatrix} \left(c_{D_0}(M) + c_{D_{a^2}}(M) \alpha^2 \right) \|\vec{v}_b\| \|\vec{v}_b\| & \left(c_{L_a}(M) \alpha + c_{L_{a^3}}(M) \alpha^3 \right) \left(\|\vec{v}_b\|^2 \vec{x}_b - (\vec{x}_b \cdot \vec{v}_b) \vec{v}_b \right) \\ d \frac{C_{mf}(M)}{I_x} \left(\vec{L}_b \cdot \vec{x}_b \right) \left(\vec{x}_b \times \vec{v}_b \right) & -d \frac{C_{Nq}(M)}{I_y} \|\vec{v}_b\|^2 \left(\vec{L}_b \times \vec{x}_b \right) \\ \sum_{i=1}^{i=4} \left(C_{N\delta}(M) \delta_i \vec{n}_{b\delta_i} \right) & \end{bmatrix} \quad (2)$$

where d is caliber, ρ is air density, \vec{L}_b is angular momentum, I_x and I_y are inertia moments, \vec{x}_b is rocket nose pointing vector, δ_i is the deflection angle for each canard i , $\vec{n}_{b\delta_i}$ is the normal vector to each canard i , and \vec{v}_b is rocket velocity. Rocket moments, which include overturning, pitch damping, Magnus, spin damping, and control, are shown in (3):

$$\begin{bmatrix} \dot{\vec{O}} \\ \vec{M}_M \\ \vec{CM} \end{bmatrix} \begin{bmatrix} \vec{P}_M \\ \vec{s} \end{bmatrix} = \frac{\pi}{8} d^3 \rho \begin{bmatrix} (C_{Ma}(M) + C_{M\alpha^2}(M)\alpha^2) \|\vec{v}_b\|^2 (\vec{v}_b \times \vec{x}_b) & , & \frac{1}{I_y} C_{Mq}(M) \|\vec{v}_b\| \left(\vec{L}_b - (\vec{L}_b \cdot \vec{x}_b) \vec{x}_b \right) \\ -\frac{d}{I_x} C_{mm}(M) \left((\vec{L}_b \cdot \vec{x}_b) ((\vec{v}_b \cdot \vec{x}_b) \vec{x}_b) - \vec{v}_b \right) & , & \frac{d}{I_x} C_{spin}(M) \|\vec{v}_b\| (\vec{L}_b \cdot \vec{x}_b) \vec{x}_b \\ \sum_{i=1}^{i=4} \left(C_{N\delta}(M) \frac{C_{L\alpha}(M)}{C_{Ma}(M)} \delta_i \cdot (\vec{i}_b \times \vec{n}_{b\delta_i}) \right) & & \end{bmatrix} \quad (3)$$

Two different sensor sets are introduced: a GNSS/IMU system and a semi-active laser quadrant photo detector. The GNSS/IMU system is modeled to permit good performance for intermediate trajectories. A bias and a random noise are added to the calculated position and attitude. To calculate laser footprint centroid coordinates, the electric intensities generated in the photo diodes are used. The combination of these sensors may provide an accurate definition of the line-of-sight vector if their signals are correctly hybridized.

3 Navigation, Guidance, and Control

Navigation The aim is to obtain the line of sight between rocket and target which can be obtained from hybridized signals of GNSS/IMU and semi-active laser kit sensors. The hybridization algorithm, based in neural networks, is to recover a high accuracy on the line of sight determination process by combining the measurements from the quadrant detector, the IMU/GNSS, and the potential offered by NNs. Two neural networks are utilized to estimate x_c and y_c , which are the real spot center coordinates. They both are employed in the proposed hybridization approach. They feature two layers with 100 standard sigmoid hidden neurons and a linear output neuron. The input vector is composed of three components, the signals from the GNSS/IMU and SAL, and a binary signal which is 1 if SAL receives data and 0 otherwise. The target is the line of sight. Consequently, NNs are trained replicating the flight dynamics. As it is shown in Fig. 1, the GNSS/IMU measurements (black line) degrade during the last stages of flight, while the hybridized solution (red line) keeps fidelity to the real line of sight (blue line) during the whole trajectory.

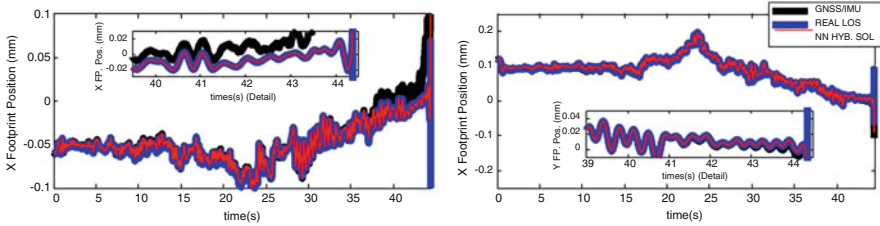


Fig. 1 Results for the hybridization algorithm: x and y coordinates

Guidance and Control Guidance is provided in two phases. The first one consists of a constant angle glide trajectory defined. The second phase consists of a modified proportional law. The control law is integrated in the present system. Two control parameters are introduced in the actuation system: the angle and the modulus for the rotating force. Control is processed by a double-loop feedback system. The inner loop is only used as a system of stability augmentation.

4 Numerical Simulations

The previous nonlinear equations of motion are integrated forward in time using a fixed time step Runge-Kutta scheme of fourth order to obtain a single flight trajectory. The approach in de Celis et al. (2017) features a control based on a GNSS/IMU system, while the one in de Celis and Cadarso (2018) features a Kalman-based hybridization of a GNSS/IMU system and a semi-active laser quadrant photodetector. MATLAB/Simulink R2020a on a desktop is employed in the simulations. To test the algorithms developed, three nominal trajectories will be employed. They differ in their initial pitch angle: 20° , 30° , and 45° . Impact points are at 18790 m, 23,007 m, and 26,979 m, respectively. Monte Carlo analysis is conducted to determine closed-loop performance across a full spectrum of uncertainty at initial conditions, sensor data acquisition, atmospheric conditions, and thrust properties. A set of 2000 shots is performed for each of the following combinations: ballistic shots, Kalman hybridization guidance, neural network hybridization guidance, and ideal shots. Results for ballistic trajectories and comparisons between different approaches are shown in Fig. 2. As a general remark, controlled flights exhibit tighter impact groupings, getting similar results for both hybridizations and ideal controller.

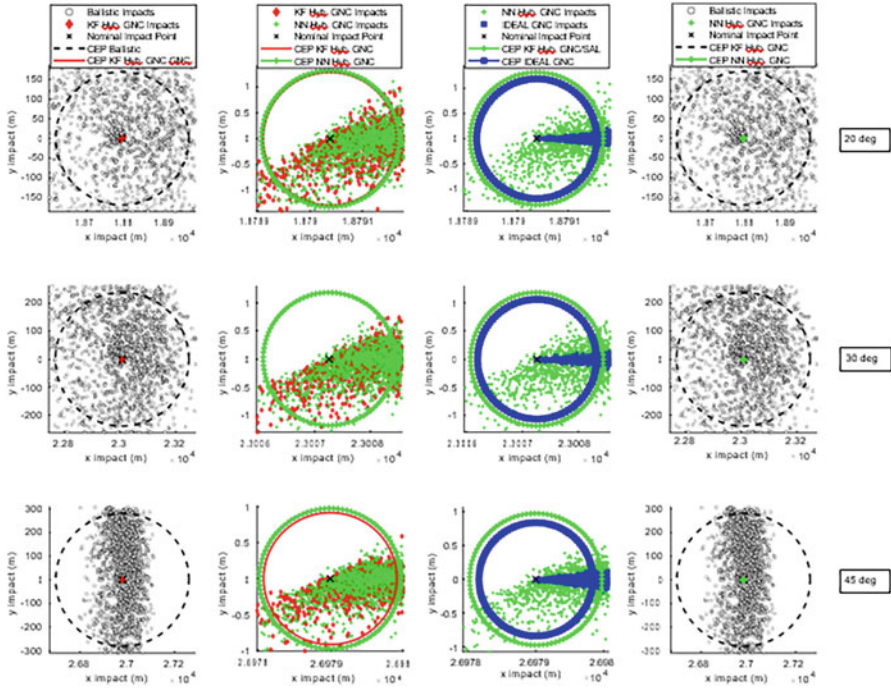


Fig. 2 Detailed shots for different algorithms

5 Conclusions

A novel approach, which is based on an innovative hybridization between GNSS/IMU and semi-active laser quadrant photodetectors, has been developed. Small errors of 1 m in GNSS/IMU systems may induce significant errors in line of sight vector calculation. The proposed approach can improve the precision of line of sight determination during the terminal guidance, therefore ameliorating the precision on impact point. A two-phase guidance algorithm and a novel control technique for high-rate spinning rockets are proposed. The guidance algorithm is based on a constant angle glide and on a modified proportional law, while the control algorithm is based on a simple but effective and robust double-input double-output controller. Several algorithms are proposed for fusing signals of different sensors in the terminal trajectory. The novel proposed approach shows that levels of accuracy can be improved or matched as compared against other methodologies.

References

- Bryne, T. H., Hansen, J. M., Rogne, R. H., Sokolova, N., Fossen, T. I., & Johansen, T. A. (2017). Nonlinear observers for integrated INS/GNSS navigation: Implementation aspects. *IEEE Control Systems Magazine*, 37(3), 59–86.
- de Celis, R., & Cadarso, L. (2018). GNSS/IMU laser quadrant detector hybridization techniques for artillery rocket guidance. *Nonlinear Dynamics*, 91(4), 2683–2698.
- de Celis, R., & Cadarso, L. (2019). Spot-centroid determination algorithms in semiactive laser photodiodes for artillery applications. *Journal of Sensors*, 2019.
- de Celis, R., Cadarso, L., & Sa'nchez, J. (2017). Guidance and control for high dynamic rotating artillery rockets. *Aerospace Science and Technology*, 64, 204–212.
- Nguyen, N. V., Tyan, M., & Lee, J.-W. (2016). Efficient framework for missile design and 6DoF simulation using multi-fidelity analysis and data fusion. In *17th AIAA/ISSMO multidisciplinary analysis and optimization conference*. 13–17 June, p. 3365.
- Schmidt, G. T., & Phillips, R. E. (2011). *INS/GPS integration architecture performance comparisons*. NATO RTO lecture series, low-cost navigation sensors and integration technology RTO-EN-SET-116.
- Solano-Lopez, P., de Celis, R., Fuentes, M., Cadarso, L., & Barea, A. (2019). Strategies for high performance GNSS/IMU guidance, navigation and control of rocketry. In *Eighth European conference for aeronautics and space sciences*, 1–3 July.
- Waltz, E. L., & Buede, D. M. (1986). Data fusion and decision support for command and control. *IEEE Transactions on Systems, Man, and Cybernetics*, 16(6), 865–879.

Performance Improvement of a Fixed-Wing UAV Using Model Predictive Control



Abdurrahman Talha Yildiz and Kemal Keskin

1 Introduction

The use of unmanned aerial vehicles (UAVs) has become widespread in recent years. While UAVs were first used for reconnaissance and surveillance, with the development and spread of unmanned technologies, it is now seen that they are also used in transportation and military fields by being armed. This increasing interest in UAVs and the problem of improving the performance of the flight control system attracts great attention. When we look at the studies dealing with performance improvement problems in the literature, it is seen that the PID controller, which is easy to develop and implement, is often preferred (Win et al., 2018; Kada & Ghazzawi, 2011; Moreira & Shiroma, 2017; Miranda et al., 2018). There have been cases where the performance of the PID controller is insufficient against the instantaneously changing external factors such as winds, and the use of more advanced control methods for these cases has begun to be investigated. Furthermore, the PID controller can be applied in single-input, single-output systems. Some modifications are required for multiple-input, multiple-output (MIMO) systems (Bidikli, 2018). Various studies have been conducted in this regard to improve PID performance (Kada & Ghazzawi, 2011; Moreira & Shiroma, 2017; Bidikli, 2018; Mobarez et al., 2019). LQR controller is one of the frequently used methods for controlling MIMO systems. The parsing control of multiple-input, multiple-output (MIMO) operations is not a simple problem (Keviczky & Bányász, 2011).

A. T. Yildiz (✉)

Eskişehir Osmangazi University, Eskişehir, Türkiye

Turkish Aerospace Industries, Ankara, Türkiye

e-mail: talhayildiz@outlook.com.tr

K. Keskin

Eskişehir Osmangazi University, Eskişehir, Türkiye

e-mail: kkeskin@ogu.edu.tr

Although it has a simple structure, the LQR controller has wide application areas and performs well. In the literature, to improve the performance of fixed-wing UAVs, besides the LQR controller (Ashari et al., 2019; Ingabire & Sklyarov, 2019), integral sliding mode control (ISMC) (Haridas & Vivek, 2016), backstepping controller (Kumar et al., 2019), multi-model controller (Kong et al., 2014), dynamic inversion control techniques (Lungu, 2022), model reference adaptive control (Lu et al., 2016), and H_∞ control (Bao et al., 2021) methods have also been successfully applied.

In this study, model predictive control (MPC) method is proposed for the control of longitudinal axis motion in fixed-wing UAVs. Tests have been carried out to improve speed, reliability, and robustness. The effectiveness of the proposed method has been demonstrated by comparing the results with the results obtained by the LQR method.

2 Method

In this section, firstly, the mathematical model of the UAV will be obtained, and then short information about the control methods MPC and LQR to be used in solving the problem will be given.

2.1 Mathematical Model of UAV

The aircraft model to be used in this study is GTM (generic transport model) published by NASA Technology Transfer Program. For the aircraft in the model used, a 5.5% scale version of a general passenger aircraft was prepared. The scaled aircraft is a fixed-wing unmanned aerial vehicle. The flights were carried out to validate and finalize the model.

The dynamics of a fixed-wing UAV can be modeled with six degrees of freedom. This model consists of two components, longitudinal and lateral. In this study, the longitudinal dynamics of the fixed-wing UAV will be studied. The longitudinal dynamics equations:

$$\dot{V} = \frac{T \cos(\alpha) + D - mg \sin(\gamma)}{m} \quad (1)$$

$$\dot{\alpha} = q - \frac{T \cos(\alpha) + L - mg \sin(\gamma)}{mV} \quad (2)$$

$$\dot{q} = \frac{M}{I_{yy}} \quad (3)$$

$$\dot{\theta} = q \quad (4)$$

where V is the aircraft relative velocity; m is the aircraft mass; q is the pitch rate; θ is the pitch angle; α is the angle of attack; M is the pitching moment; I_{yy} is the moment of inertia in pitch axis; and T , D , and L are the thrust, drag, and lift forces, respectively. The aerodynamic forces in equation and aerodynamic coefficients are described as:

$$M = \frac{1}{2} \rho V^2 S c C_M \quad (5)$$

$$L = \frac{1}{2} \rho V^2 S C_L \quad (6)$$

$$D = \frac{1}{2} \rho V^2 S C_D \quad (7)$$

$$\dot{T} = \tau_t (\delta_t T_{\max} - T) \quad (8)$$

$$C_L = C_{L_0} + C_{L_\alpha} \alpha \quad (9)$$

$$C_D = C_{D_0} + K C_L^2 \quad (10)$$

$$C_M = C_{M_0} + C_{M_\alpha} \alpha + C_{M_{\delta_e}} \delta_e + C_{M_q} \frac{qc}{V} \quad (11)$$

The nonlinear model of the UAV was used by linearizing it under the conditions of 0-degree gamma and 80 kt speed at 800 ft altitude.

Discrete-time state-space model of a linearized and linear time-invariant system:

$$x_{k+1} = Ax_k + Bu_k \quad (12)$$

$$\dot{x} = Ax + Bu \quad (13)$$

$$\begin{bmatrix} \dot{V} \\ \dot{\alpha} \\ \dot{q} \\ \dot{\theta} \end{bmatrix} = A \begin{bmatrix} V \\ \alpha \\ q \\ \theta \end{bmatrix} + B \begin{bmatrix} \delta_e \\ \delta_t \end{bmatrix} \quad (14)$$

$$A = \begin{bmatrix} 0.9997 & -0.05415 & 7.283 \times 10^{-5} & -0.1608 \\ -1.695 \times 10^{-5} & 0.987 & 0.004691 & 1.363 \times 10^{-6} \\ -4.217 \times 10^{-5} & -0.2213 & 0.982 & 3.453 \times 10^{-6} \\ -1.073 \times 10^{-7} & -0.0005561 & 0.004955 & 1 \end{bmatrix} \quad (15)$$

$$B = \begin{bmatrix} -0.000218 & 0.0003562 \\ -3.096 \times 10^{-5} & -1.947 \times 10^{-7} \\ -0.003885 & 4.762 \times 10^{-5} \\ -9.744 \times 10^{-6} & 1.194 \times 10^{-7} \end{bmatrix} \quad (16)$$

$$C = \begin{bmatrix} 1 & 0 & 0 & 0 \\ 0 & 0 & 0 & 1 \end{bmatrix} \quad (17)$$

The given model defines a MIMO system. The inputs in the model are elevator and throttle, and the outputs are speed and pitch angle.

2.2 *Model Predictive Control and LQR*

MPC is a control method based on the solution of the optimal control problem on the finite horizon in each control cycle. LQR, on the other hand, is a control method that tries to minimize the cost function in the infinite horizon and to obtain a stable system. Expressing system constraints in the control rule and working on a limited horizon are the biggest advantages of MPC.

Q and R weight matrices for the MPC method were adjusted in accordance with the Bryson normalization method. The state-space model has been updated so that the system's states can follow the reference without steady-state error. It can be used as an example for the MPC method (Dursun et al., 2018).

In the LQR method, the Q and R weight matrices are considered to be the same as the matrices used in the MPC method for comparison. Because LQR is doing regulation, the system output does not follow the applied reference. Pre-compensator scaling factor was used for reference tracking.

3 Results and Discussion

The two reference signals, step and sinus, were applied to the controllers designed using two different methods. The reference signals used in the simulations were applied to the trim condition of the UAV. The UAV has two control channels, namely, two inputs, where the speed and theta angle are controlled.

When step reference was applied to both channels in the first second of the simulation, it was observed that the MPC method did not overshoot and peak in the velocity channel. In addition, the reference value was reached in 1.75 s. In the LQR method, it was observed that it made reverse peak before the reference was applied and reached the reference in 7.852 s. It was observed that the MPC method did 1.0415% overshoot and 1.465 s peak response time in the theta channel. In addition, the reference value was reached in 4.274 s. In the LQR method, it was observed that it made reverse peak before the reference was applied and reached the reference in 10.519 s (Fig. 1).

When step reference was applied to theta channel in the first second of the simulation, 10 dB and 0.25 Hz sinus reference was applied to velocity channel. In the velocity channel, the MPC method followed the reference with an error of 0.4% and a phase difference of 16.38°. It was observed that the LQR method followed the reference with an error of 7.65% and a phase difference of 65.79°. In the theta channel, it was observed that the MPC method had a higher resistance to the sine reference applied to the velocity channel than the LQR method and followed the reference with less error (Fig. 2).

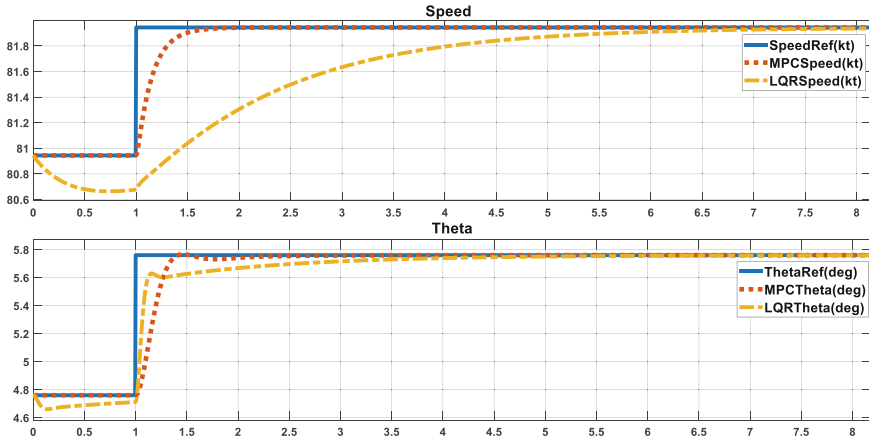


Fig. 1 Response of speed and theta versus time considering step reference signal

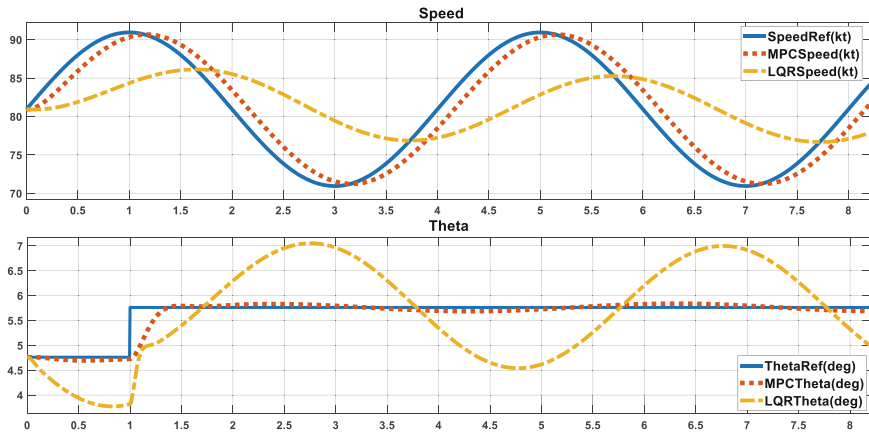


Fig. 2 Response of speed versus time considering sinus reference and theta versus time considering step reference signal

A 10 dB and 0.25 Hz sinus reference was applied to both channels. In the velocity channel, the MPC method followed the reference with an error of 0.4% and a phase difference of 16.38°. It was observed that the LQR method followed the reference with an error of 7.65% and a phase difference of 65.79° in the velocity channel. In the theta channel, the MPC method followed the reference with an error of 6.21% and a phase difference of 15.84°. It was observed that the LQR method followed the reference with an error of 21.55% and a phase difference of 7.29° in the theta channel (Fig. 3).

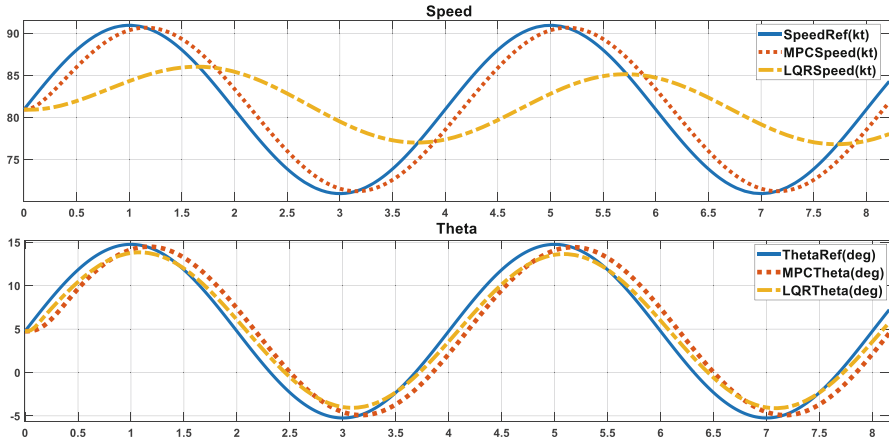


Fig. 3 Response of speed and theta versus time considering sinus reference signal

4 Conclusion

In this study, an MPC-based control approach is proposed for the longitudinal motion control of a fixed-wing unmanned aerial vehicle. The problem is defined as a multi-input, multi-output system, and velocity and theta angle are selected as inputs. First of all, the fixed-wing unmanned aerial vehicle was modeled in Simulink/MATLAB environment, and then it was controlled with the proposed control method. In order to show the efficiency of the proposed method, the system response obtained for different reference signals is compared with the results obtained by applying the LQR control method. As a result, it was observed that the MPC method performed better than the LQR method and was less affected by the decoupling effect. The controller designed with MPC has robust, reliable, and fast response features.

Acknowledgment This work has been supported by Eskisehir Osmangazi University Scientific Research Projects Coordination Unit under grant number FYL-2022-2282.

References

- Ashari, A., Dharmawan, A., Fadhi, H. A., & Handayani, A. M. (2019). Flight trajectory control system on fixed wing UAV using linear quadratic regulator. *International Journal of Engineering Research and Technology (IJERT)*, 8(8), 345–352. <https://doi.org/10.17577/IJERTV8IS080135>
- Bao, C., Guo, Y., Luo, L., & Su, G. (2021). Design of a fixed-wing UAV controller based on adaptive backstepping sliding mode control method. *IEEE Access*, 9, 157825–157841. <https://doi.org/10.1109/ACCESS.2021.3130296>

- Bidikli, B. (2018). A self-tuning PID control method for multi-input-multi-output nonlinear systems. *Electrica*, 18(2), 218–226.
- Dursun, U., Ustoğlu, I., & Tascikaraoglu, F. Y. (2018). Hidrolik test sisteminin model öngörülü kontrolü. *Pamukkale Üniversitesi Mühendislik Bilimleri Dergisi*, 24(8), 1443–1449.
- Haridas, V., & Vivek, A. (2016). Longitudinal guidance of unmanned aerial vehicle using integral sliding mode control. *Procedia Technology*, 25, 36–43. <https://doi.org/10.1016/j.protecy.2016.08.078>
- Ingabire, A., & Sklyarov, A. A. (2019). Control of longitudinal flight dynamics of a fixedwing UAV using LQR, LQG and nonlinear control. *E3S Web of Conferences*, 104, 02001. <https://doi.org/10.1051/e3sconf/201910402001>
- Kada, B., & Ghazzawi, Y. (2011). Robust PID controller design for an UAV flight control system. In *Proceedings of the world congress on engineering and computer science* (Vol. 2, pp. 945–950).
- Keviczky, L., & Bányász, C. (2011). MIMO controller design for decoupling aircraft lateral dynamics. In *9th IEEE international conference on control and automation (ICCA)* (pp. 1079–1084). <https://doi.org/10.1109/ICCA.2011.6137900>
- Kong, D., Geng, Q., Hu, Q., & Shao, J. (2014). Longitudinal control law design for fixed-wing UAV based on multi-model technique. In *Fifth international conference on intelligent control and information processing* (pp. 48–52). <https://doi.org/10.1109/ICICIP.2014.7010312>
- Kumar, K. K. S., Arya, H., & Joshi, A. (2019). Longitudinal control of agile fixed-wing UAV using backstepping. In *IEEE aerospace conference* (pp. 1–11). <https://doi.org/10.1109/AERO.2019.8742162>
- Lu, X., Geng, Q., & Mo, R. (2016). New composite MRAC with modification for fixed-wing UAV. In *Chinese Control and Decision Conference (CCDC)* (pp. 479–484). <https://doi.org/10.1109/CCDC.2016.7531032>
- Lungu, M. (2022). Backstepping and dynamic inversion control techniques for automatic landing of fixed wing unmanned aerial vehicles. *Aerospace Science and Technology*, 120, 107261. <https://doi.org/10.1016/j.ast.2021.107261>
- Miranda, D. V., Gil-Martínez, M., & Rico-Azagra, J. (2018). Longitudinal control of a fixed wing UAV. *Jornadas de Automática*, XXXIX, 598–604. <https://doi.org/10.17979/spudc.9788497497565.0598>
- Mobarez, E., Sarhan, N., & Mohamed, A. M. (2019). Modeling of fixed wing UAV and design of multivariable flight controller using PID tuned by local optimal control. In *18th international conference on aerospace sciences & aviation technology* (Vol. 610, p. 012016). <https://doi.org/10.1088/1757-899X/610/1/012016>
- Moreira, E. I., & Shiroma, P. M. (2017). Design of fractional PID controller in time-domain for a fixed-wing unmanned aerial vehicle. In *Latin American Robotics Symposium (LARS) and Brazilian Symposium on Robotics (SBR)* (pp. 1–6). <https://doi.org/10.1109/SBR-LARS-R.2017.8215335>
- Win, T., Tun, H. M., & Nyunt, H. T. C. (2018). Modelling and PID Control System for Fixed-Wing Unmanned Aerial Vehicle. *International Journal of Electrical, Electronics and Data Communication (IJEEDC)*, 6(6, Part 2), 8–11.

Deep Q Network-Based Controller for Vertical Takeoff and Landing System



Şerefcan Helvacıoğlu, Mehmet Uğur Soydemir, Alkım Gökçen,
and Savaş Şahin

1 Introduction

Deep reinforcement learning (DRL) is a recent technology that combines deep learning and reinforcement learning (François-Lavet et al., 2018). The traditional control algorithms such as proportional-integral-derivative (PID) controller are insufficient to perform against the possible environmental effects. The DRL algorithms can solve complex tasks in disturbances and possible environmental effects that traditional control algorithms suffer from. The main objective of the DRL algorithm is to maximize the reward function by using an agent and an environment. The first DRL algorithm, called Deep Q Network (DQN), was developed by the Google DeepMind team in 2015 (Liu et al., 2019). The works on DQN algorithms show that human-level performance is possible for complex physical control tasks (Mnih et al., 2015). The performance of the nonlinear controller is compared to the reinforcement learning algorithm implemented by Markov decision process (MDP)-based fitted value iteration (FVI) controller model (Bou-Ammar et al., 2010). A self-balancing robot model is controlled using Q-learning and DQN algorithms to compare reference tracking and reward scaling factors (Rahman et al., 2018). Chen et al. developed a DQN algorithm to control the speed of the servo-based system and compared the DQN algorithm with the PID control algorithm according to different velocity commands and inertia under the circumstances (Chen et al., 2018). The works show that DQN algorithm is successful in the real-life systems. Huang et al. worked on a DQN-based design which is used to navigate UAVs through the MIMO technique, and this technique is compared with different learning rates and speeds (Huang et al., 2019).

Ş. Helvacıoğlu (✉) · M. U. Soydemir · A. Gökçen · S. Şahin
İzmir Katip Çelebi University, İzmir, Türkiye
e-mail: savas.sahin@ikc.edu.tr

In this study, the pitch angle of the vertical takeoff and landing (VTOL) system is controlled by a DQN-based controller algorithm. The DQN-based controller algorithm is trained through MATLAB/Simulink environment. Simulation processes determine the parameters of the controller. The DQN-based controller algorithm is tested for both sinusoidal and constant reference signals. The performance of the DQN-based controller is compared with traditional PID controller algorithm by mean square error (MSE), integral absolute error (IAE), and integral square error (ISE).

2 Method

The VTOL system model can be used to perform different control algorithms or different flight mechanics such as vertical takeoff (Goossen, 2012). The free-body diagram of the VTOL system is shown in Fig. 1. The VTOL system consists of a body rope, variable speed fan motor, and a weight. It can be simulated through the transfer function shown in Eq. 1. $Y(s)$ refers to the system’s output, which is called pitch angle, and $U(s)$ refers to the system’s input voltage (Quanser Inc, 2011).

$$\frac{Y(s)}{U(s)} = \frac{3.11}{s^2 + 0.576s + 10.7} \tag{1}$$

DQN algorithm might be considered as deep reinforcement learning version of Q-learning algorithm (Mnih et al., 2013). In this algorithm, deep neural networks are used as representation for Q-table with their approximation property. This representation maps states (s) to action (a). DQN uses to train this representation to estimate future rewards by aiming to maximize future reward. s_t, a_t, r_t, s_{t+1} are states at time t , action at time t , reward at time t , and states at time $t + 1$, respectively, while experiences $e_t = (s_t, a_t, r_t, s_{t+1})$ are stored using experience replay technique.

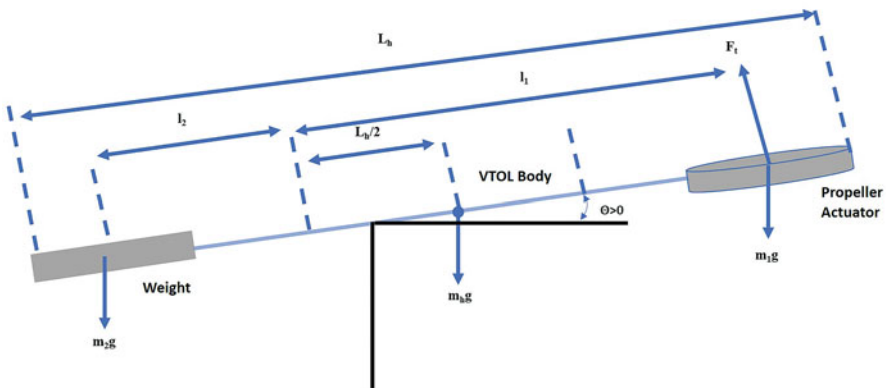


Fig. 1 Free-body diagram of VTOL system

These experiences are stored in the $R = e_1, e_2, \dots, e_N$ dataset which is called replay memory, and herein N denotes capacity of replay memory R (Mnih et al., 2013). Besides, a network copy (target) of actual network Q-table is created for training stability purposes so in this algorithm we have two network targets which are named as actual and target network. Algorithm is as follows; replay memory R with capacity N , actual Q network with weights q , and target Q' network with q' (initially, same weight in actual network but normally q') are initialized. In each episode, for every time step, the agent is chosen as a_t using epsilon-greedy algorithm with ϵ value. After applying a_t at s_t , r_t and s_{t+1} are observed. Then, storing process for R is realized using (s_t, a_t, r_t, s_{t+1}) tuple. A random minibatch of R is chosen and for every j th experience of minibatch at time j is evaluated at loss function $L = (r + \gamma \max_{a'} Q'(s', a', q') - Q(s, a, q))^2$ where r, s', s, a are r_j, s_{j+1}, s_j, a_j with a related time j in random minibatch, γ is gamma discount factor, and a' is best action among all actions which can be taken at s_{j+1} . For the minimization process of loss function, gradient descent algorithm is used according to actual network weights q , and for every C steps, actual network weights q are equalized to target network weights q' .

3 Results and Discussion

The DQN control algorithm was implemented in MATLAB/Simulink environment by using Reinforcement Learning Toolbox. The mathematical model of the VTOL system was used as a plant. The controller algorithms were run in the Windows 10 PRO operating system, NVIDIA Quadro P2000 as GPU, and 32 GB as RAM. The observations for DQN algorithms were selected as integral of tracking error, the derivative of tracking error, and tracking error, itself. The reward function is used $r(t) = -e^2(t)$ where $e(t)$ refers to the tracking error of the pitch angle. Discrete action space is increased equally with 0.5 in the range $[-0.8, 0.8]$. The Q-table actual network structure is shown in Fig. 2.

The sinusoidal reference $0.2 \sin(\frac{\pi}{2}t)$ was trained for 21 h, and the best agent for the trained sinusoidal reference was obtained in the 157th agent, and the episode reward of the 157th agent was -0.8223 . For this training process, 20 s of sinusoidal and constant reference responses for both PID and DQN algorithms is shown in Fig. 3, respectively. MATLAB PID Tuner obtained the parameters of the PID controller as $K_p = 29.599$, $K_i = 34.108$, and $K_d = 4.607$ (Taşören et al., 2020). The tracking performance errors were compared in terms of MSE, ISE, and IAE. The mathematical formulas of the MSE, ISE, and IAE are shown in Eq. 2, respectively (Hussain et al., 2014):

$$\text{MSE} = \frac{1}{S} \sum_{i=1}^S e^2(i), \text{ISE} = \int_{t_o}^{t_f} e^2(i) dt \approx \sum_{k=k_o}^{k_j} e^2(k) \text{IAE} = \int_{t_o}^{t_f} |e(i)| dt \approx \sum_{k=k_o}^{k_j} |e(k)| \quad (2)$$

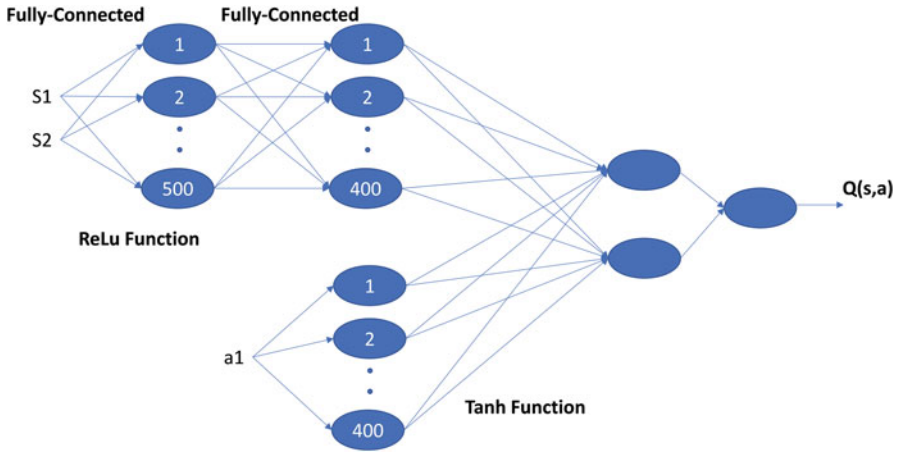


Fig. 2 Deep network structure for $Q(s, a)$

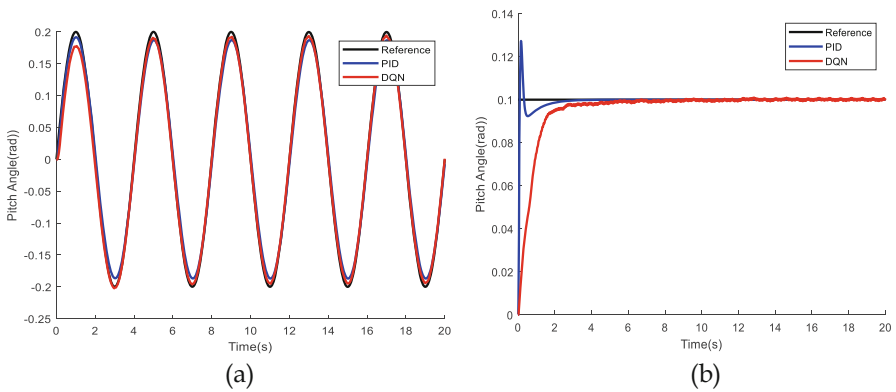


Fig. 3 The tracking performances of DQN and PID controller for sinusoidal reference (a) and constant reference (b)

where S represents the number of observations, $e(i)$ represents the difference between the observed value and predicted value, k_o and t_o represent initial observation, and k_f and t_f represent a final observation. The performance of the DQN algorithm is better than the PID algorithm in terms of error metrics and overshoot in sinusoidal reference. In terms of overshoot performances, the DQN algorithm outperforms the PID algorithm. However, the settling time of the PID algorithm is better than DQN algorithm in the constant reference (Tables 1, 2, and 3).

Table 1 Result of PID and DQN algorithms in terms of IAE, MSE, and ISE for sinusoidal reference

	MSE	ISE	IAE
DQN	7.241×10^{-5}	0.14489	12.2884
PID	10.902×10^{-5}	0.21815	18.6957

Table 2 Result of PID and DQN algorithms in terms of IAE, MSE, and ISE for constant reference

	MSE	ISE	IAE
DQN	0.000201	0.40275	8.3533
PID	2.7871×10^{-5}	0.055769	1.7301

Table 3 Result of PID and DQN algorithms in terms of settling time and overshoot for constant reference

	Overshoot (%)	Settling time (s)
DQN	0.508	9.083
PID	27.56	3.279

4 Conclusion

In this study, the pitch angle of the VTOL system is controlled by the DQN algorithm in MATLAB/Simulink. The DQN algorithm is compared with the traditional PID algorithm, in which parameters are found by MATLAB PID Tuner in terms of MSE, ISE, and IAE. According to the sinusoidal reference, the DQN algorithm performs better than the PID algorithm in terms of error metrics and overshoot. The performance of the DQN algorithm is better than PID algorithm in terms of overshoot. However, the settling time and error metrics of the PID algorithm performance are better than DQN algorithm in the constant reference. In the future studies, other reinforcement learning algorithms that have continuous action space can be used to control pitch angle of the VTOL system.

Acknowledgments This work is supported by the Scientific and Technical Research Council of Turkey (TUBITAK) under 2209A – Research Project Support Programme for Undergraduate Students with project number 1919B011901769.

References

Bou-Ammar, H., Voos, H., & Ertel, W. (2010). *Controller design for quadrotor uavs using reinforcement learning*. In 2010 IEEE international conference on control applications (pp. 2130–2135). IEEE.

Chen, P., He, Z., Chen, C., & Xu, J. J. A. (2018). Control strategy of speed servo systems based on deep reinforcement learning. *Algorithms*, 11, 65.

- François-Lavet, V., Henderson, P., Islam, R., Bellemare, M. G., & Pineau, J. J. A. P. (2018). An introduction to deep reinforcement learning. *Foundations and Trends® in Machine Learning*, 11(3–4), 219–354.
- Goossen, E. (2012). *Vertical take off and landing unmanned aerial vehicle airframe structure*. Google Patents.
- Huang, H., Yang, Y., Wang, H., Ding, Z., Sari, H., & Adachi, F. (2019). Deep reinforcement learning for UAV navigation through massive MIMO technique. *IEEE Transactions on Vehicular Technology*, 69, 1117–1121.
- Hussain, K. M., Zepherin, R. A. R., & Shantha, M. J. C. (2014). Comparison of PID controller tuning methods with genetic algorithm for FOPTD system. *Criterion*, 16, 17.
- Liu, W., Si, P., Sun, E., Li, M., Fang, C., & Zhang, Y. (2019). *Green mobility management in UAV-assisted IoT based on dueling DQN*. In ICC 2019–2019 IEEE International Conference on Communications (ICC) (pp. 1–6). IEEE.
- Mnih, V., Kavukcuoglu, K., Silver, D., Graves, A., Antonoglou, I., Wierstra, D., & Riedmiller, M. (2013). Playing atari with deep reinforcement learning. arXiv preprint arXiv:1312.5602.
- Mnih, V., Kavukcuoglu, K., Silver, D., Rusu, A. A., Veness, J., Bellemare, M. G., Graves, A., Riedmiller, M., Fidjeland, A. K., Ostrovski, G., & Petersen, S. (2015). Human-level control through deep reinforcement learning. *Nature*, 518, 529–533.
- Quanser Inc. (2011). QNET VTOL instructor workbook.
- Rahman, M. M., Rashid, S. H., & Hossain, M. M. (2018). Implementation of Q learning and deep Q network for controlling a self balancing robot model. *Robotics and Biomimetics*, 5, 1–6.
- Taşören, A. E., Gökçen, A., Soydemir, M. U., & Şahin, S. (2020). Artificial neural network based adaptive PID controller design for vertical takeoff and landing model. *Avrupa Bilim ve Teknoloji Dergisi*, 2020, 87–93.

Process and Measurement Noise Covariance Tuning in Kalman-Based Estimator Aided by SVD



Chingiz Hajiyev and Demet Cilden-Guler

1 Introduction

A Kalman filtering-based estimator can be used for attitude and angular velocity estimation purposes in a spacecraft. One way is to use the nonlinear measurements (magnetometer, sun sensor, etc.) directly in the filter (Hajiyev & Cilden-Guler, 2017; Ivanov et al., 2018; Mashtakov et al., 2020; Springmann & Cutler, 2014), while another way is to use processed linear measurements. The attitude angles can be processed in a single-frame attitude determination method (Hajiyev & Cilden-Guler, 2017; Mimasu & Van der Ha, 2009). The attitude angles can be used as measurement inputs for an attitude filter such as extended Kalman filter (EKF). This approach makes the filter robust against measurement faults inherently (Cilden et al., 2017; Hajiyev & Cilden-Guler, 2017). In conventional filters, the tuning in terms of the process noise covariance might be challenging. Since, an adaptive EKF (AEKF) algorithm that tunes the process noise covariance matrix can be used in the linear measurement-based filtering (Hajiyev, 2007; Hajiyev & Cilden-Guler, 2021; Kang et al., 2014).

In this study, a covariance tuning is implemented for the Q matrix in addition to the measurement noise covariance tuning rule. The rest of the paper reads as follows. In Sect. 2, the extended Kalman-based estimator aided by SVD is given. In Sect. 3, the results and discussion of the simulations are given. Section 4 finally summarizes the study.

C. Hajiyev (✉) · D. Cilden-Guler
Istanbul Technical University, Istanbul, Türkiye
e-mail: cingiz@itu.edu.tr; cilden@itu.edu.tr

2 Extended Kalman Filter-Based Estimator Aided by SVD

Two or more vector observations can be used in singular value decomposition method. In this study, we use two vector observations from magnetometer and sun sensor by minimizing Wahba's loss function (Wahba, 1965) in order to obtain the attitude measurements. \mathbf{A}_{opt} is the optimal attitude matrix determined by SVD, and \mathbf{P}_{svd} is the error covariance matrix of the attitude measurements. The state vector (\mathbf{x}) is composed of attitude angles and angular rates in the filter as:

$$\mathbf{x} = [\phi \ \theta \ \psi \ \omega_x \ \omega_y \ \omega_z]^T \quad (1)$$

The process and measurement models are expressed in the discrete form as:

$$\hat{\mathbf{x}}(j+1) = \mathbf{f}[\hat{\mathbf{x}}(j), j] + \mathbf{w}(j), \mathbf{z}(j) = \mathbf{H} \hat{\mathbf{x}}(j) + \mathbf{v}(j) \quad (2)$$

where $\mathbf{f}[\cdot]$ is the process function, \mathbf{w} is the zero-mean Gaussian noise of the process, \mathbf{z} is the measurement vector, \mathbf{H} is the measurement matrix, and \mathbf{v} is the zero-mean Gaussian noise of the measurements. The measurement vector is composed of attitude measurements processed under SVD:

$$z_\phi(j) = \phi_{svd}(j) + v_\phi(j), z_\theta(j) = \theta_{svd}(j) + v_\theta(j), z_\psi(j) = \psi_{svd}(j) + v_\psi(j) \quad (3)$$

where $v_{(\cdot)}(j)$ is the measurement noise of the attitude angles. The rate gyros are also used in the measurement input to the filter as:

$$\mathbf{z}_\omega(j) = \boldsymbol{\omega}_{Bl}(j) + \mathbf{v}_\omega(j) \quad (4)$$

where $\boldsymbol{\omega}_{Bl}$ is the body angular rate with respect to the inertial frame and \mathbf{v}_ω is the zero-mean Gaussian noise of the measurements of $\mathbf{z}_\omega = [z_{\omega_x} \ z_{\omega_y} \ z_{\omega_z}]^T$. The estimation of the state vector is formulated as:

$$\hat{\mathbf{x}}(j+1) = \hat{\mathbf{x}}(j+1/j) + \mathbf{K}(j+1) \times \{\mathbf{z}(j) - \mathbf{H} \hat{\mathbf{x}}(j+1/j)\} \quad (5)$$

where $\mathbf{z}(j) = [\mathbf{z}_\phi(j) \ \mathbf{z}_\omega(j)]^T$ is the measurement vector and \mathbf{H} is the measurement matrix. The measurement matrix is a unit matrix in our case. The prediction and filter gain are, respectively,

$$\hat{\mathbf{x}}(j+1/j) = \mathbf{f}[\hat{\mathbf{x}}(j), j] \quad (6)$$

$$\mathbf{K}(j+1) = \mathbf{P}(j+1/j) \mathbf{H}^T \times [\mathbf{H} \mathbf{P}(j+1/j) \mathbf{H}^T + \mathbf{R}(j)]^{-1} \quad (7)$$

where \mathbf{R} is the measurement noise covariance matrix that is obtained from SVD. The covariance matrix of the prediction error is:

$$\mathbf{P}(j+1/j) = \frac{\partial \mathbf{f}[\hat{\mathbf{x}}(j), j]}{\partial \hat{\mathbf{x}}(j)} \mathbf{P}(j/j) \frac{\partial \mathbf{f}^T[\hat{\mathbf{x}}(j), j]}{\partial \hat{\mathbf{x}}(j)} + \mathbf{Q}(j) \quad (8)$$

where \mathbf{Q} is the process noise covariance matrix. Finally, the covariance matrix of the estimation error is:

$$\mathbf{P}(j+1/j+1) = [\mathbf{I} - \mathbf{K}(j+1)\mathbf{H}]\mathbf{P}(j+1/j) \quad (9)$$

The measurement noise covariance matrix is tuned by using the SVD's covariance by $\mathbf{R}(j) = \mathbf{P}_{\text{svd}}(j)$. The extended Kalman-based Q-adaptive estimator aided by SVD (SVD-aided AEKF) algorithm includes the process noise covariance tuning in addition to the SVD-aided EKF algorithm. The tuning of the process noise covariance matrix \mathbf{Q} is performed in the filtering stage based on a single scale factor. The covariance tuning is based on the equalization of the real and theoretical values of the innovation covariance. The innovation process of the filter is defined as:

$$\tilde{\mathbf{e}}(j) = \mathbf{z}(j) - \mathbf{H}\hat{\mathbf{x}}(j+1/j) = \mathbf{z}(j) - \mathbf{H}\mathbf{f}[\hat{\mathbf{x}}(j), j] \quad (10)$$

Tuning of the covariance can be applied by using single measurement noise scale factor. The tuning factor (Λ) is implemented into the algorithm as:

$$\mathbf{P}(j+1/j) = \frac{\partial \mathbf{f}[\hat{\mathbf{x}}(j), j]}{\partial \hat{\mathbf{x}}(j)} \mathbf{P}(j/j) \frac{\partial \mathbf{f}^T[\hat{\mathbf{x}}(j), j]}{\partial \hat{\mathbf{x}}(j)} + \Lambda(j)\mathbf{Q}(j) \quad (11)$$

and determined from:

$$\text{tr} \left[\frac{1}{\mu} \sum_{k=j-\mu+1}^j \tilde{\mathbf{e}}(k)\tilde{\mathbf{e}}^T(k) \right] \approx \text{tr}[\mathbf{P}(j+1/j)] + \text{tr}[\mathbf{R}(j)] \quad (12)$$

where $\text{tr}[\cdot]$ is the trace of the matrix and μ is the width of the sliding window. The tuning factor can be found as:

$$\Lambda(j) = \frac{\text{tr} \left[\frac{1}{\mu} \sum_{k=j-\mu+1}^j \tilde{\mathbf{e}}(k)\tilde{\mathbf{e}}^T(k) \right] - \text{tr} \left[\frac{\partial \mathbf{f}[\hat{\mathbf{x}}(j), j]}{\partial \hat{\mathbf{x}}(j)} \mathbf{P}(j/j) \frac{\partial \mathbf{f}^T[\hat{\mathbf{x}}(j), j]}{\partial \hat{\mathbf{x}}(j)} \right] - \text{tr}[\mathbf{R}(j)]}{\text{tr}[\mathbf{Q}(j)]} \quad (13)$$

3 Results and Discussion

A spacecraft is considered in the simulations that orbits in low Earth almost-circular orbit at around 600 km altitude. The orbit of the nanosatellite includes an eclipse period between 4000 and 4500 s; therefore, there is a zero-output failure on the sun sensors. A noise increment is applied on the process for analyzing the proposed covariance tuning mechanism. The process noise increment has a standard deviation of $\sigma_{1,2,3}^{\text{process}} = 0.01$ rad and $\sigma_{4,5,6}^{\text{process}} = 0.001$ rad/s between 1500 and 3000 s.

In Fig. 1, the eclipse period and process noise increment are presented for SVD-aided EKF and SVD-aided AEKF. The noise increment on the process worsens the estimations of the SVD-aided EKF that does not include the second covariance tuning for the process noise. Figure 2 presents the scalar scale factor that compensates the process noise increment in the SVD-aided AKEF. The improved estimations using this tuning rule can be seen in Fig. 1 during the process noise increment period applied to the simulations.

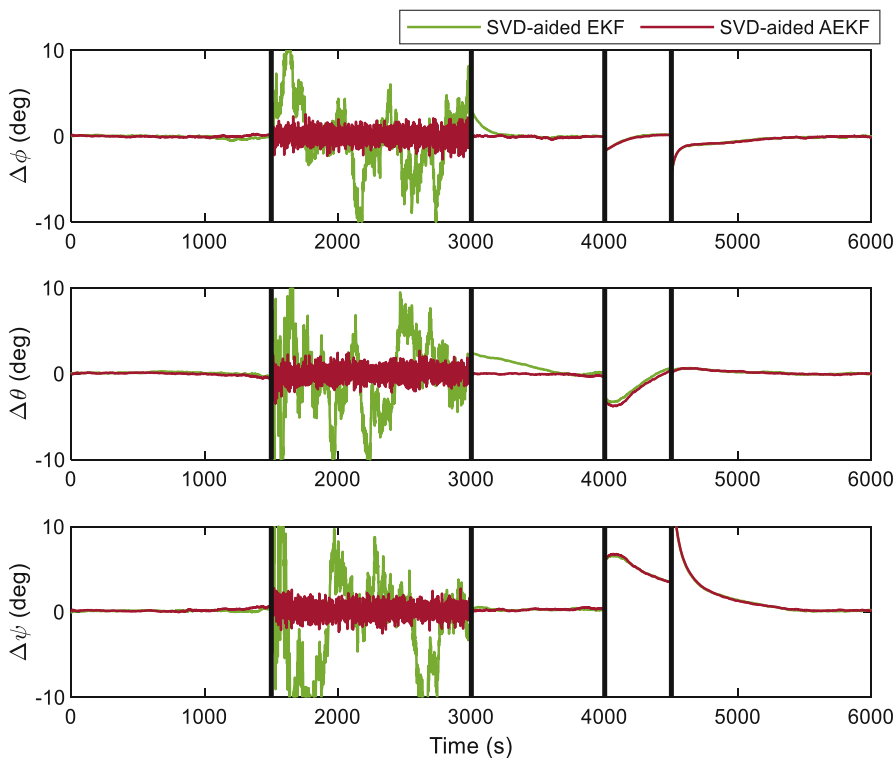


Fig. 1 The errors of the attitude estimations in case of eclipse (4000–4500) and process noise increment (1500–3000 s)

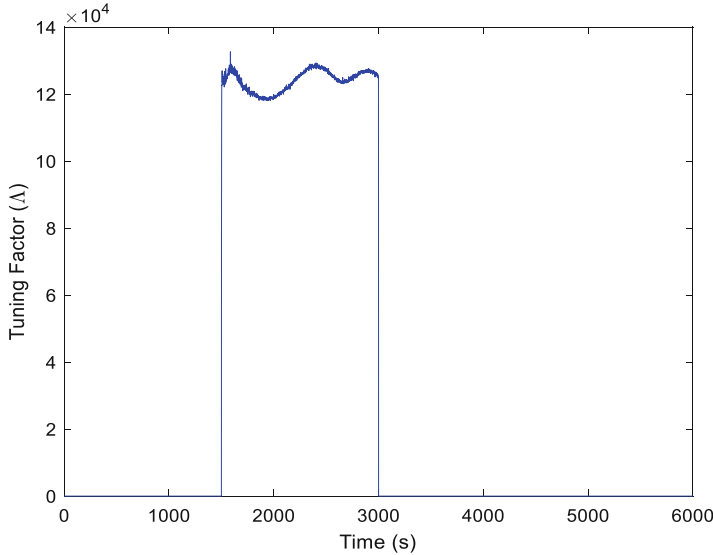


Fig. 2 The tuning factor of the SVD-aided AEKF

4 Conclusion

Simultaneous process and measurement noise covariance tuning is introduced in this study for a Kalman-based estimator that is aided by SVD method. The measurement noise covariance is tuned directly by the SVD, while the process noise covariance is tuned in the filtering stage. By this way, there are two covariance tuning rules in one filter design without any external filter necessity. The results show that the tuning algorithm that includes two separate adaptations copes well with the measurement or process noise increments.

References

- Cilden, D., Soken, H. E., & Hajiyev, C. (2017). Nanosatellite attitude estimation from vector measurements using SVD-AIDED UKF algorithm. *Metrology and Measurement Systems*, 24(1), 113–125.
- Hajiyev, C. (2007). Adaptive filtration algorithm with the filter gain correction applied to integrated INS/radar altimeter. *Proceedings of the Institution of Mechanical Engineers, Part G: Journal of Aerospace Engineering*, 221(5), 847–885.
- Hajiyev, C., & Cilden-Guler, D. (2017). Review on gyroless attitude determination methods for small satellites. *Progress in Aerospace Science*, 90, 54–66.
- Hajiyev, C., & Cilden-Guler, D. (2021). Satellite attitude estimation using SVD-aided EKF with simultaneous process and measurement covariance adaptation. *Advances in Space Research*, 68(9), 3875–3890.

- Ivanov, D., Ovchinnikov, M., & Roldugin, D. (2018). Three-axis attitude determination using magnetorquers. *Journal of Guidance, Control, and Dynamics*, *41*(11), 2455–2462. <https://doi.org/10.2514/1.G003698>
- Kang, C. H., Kim, S. Y., & Park, C. G. (2014). A GNSS interference identification and tracking based on adaptive fading Kalman filter. *IFAC Proceedings*, *47*(3), 3250–3255.
- Mashtakov, Y., Ovchinnikov, M., Wöske, F., Rievers, B., & List, M. (2020). Attitude determination & control system design for gravity recovery missions like GRACE. *Acta Astronautica*, *173*, 172–182.
- Mimasu, B. Y., & Van der Ha, J. C. (2009). Attitude determination concept for QSAT. *Transactions of the Japan Society for Aeronautical and Space Sciences, Space Technology Japan*, *7*, 63–68.
- Springmann, J. C., & Cutler, J. W. (2014). Flight results of a low-cost attitude determination systems. *Acta Astronautica*, *99*, 201–214.
- Wahba, G. (1965). Problem 65-1: A least squares estimate of satellite attitude. *Society for Industrial and Applied Mathematics Review*, *7*(3), 409.

Fault-Tolerant Attitude Estimation for a Nanosatellite Using Adaptive Fading Kalman Filter



Hasan Kinatas and Chingiz Hajiyev

Nomenclature

AFKF Adaptive fading Kalman filter
EKF Extended Kalman filter
RMSE Root-mean-square error

1 Introduction

In order to fulfill the pointing accuracy requirement of a satellite, it is important to estimate the attitude accurately. Although a conventional extended Kalman filter (EKF) provides good enough attitude estimations for a nanosatellite under normal operational conditions, it gives erroneous results and diverges with time when measurements become unreliable due to any malfunction in attitude sensors. A nanosatellite, whose sensors are usually low cost, is inherently more prone to these malfunctions than larger satellites. Therefore, it is important to design an attitude estimation system which is capable of maintaining the estimation accuracy even if the sensor measurements are not reliable.

Traditional approaches to satellite attitude estimation algorithm design include applications of extended or unscented Kalman filters using direct input of nonlinear measurement models to the filter (Lefferts et al., 1982). On the other hand, in nontraditional approaches, measurements are first preprocessed via a static attitude determination method, and a coarse estimation is obtained. Then, this estimation is fed to the filter (Hajiyev et al., 2015). In this approach, where the attitude estimation

H. Kinatas (✉) · C. Hajiyev
Istanbul Technical University, Istanbul, Türkiye
e-mail: kinatas16@itu.edu.tr; cingiz@itu.edu.tr

is directly given to the filter, the measurement model becomes linear, unlike traditional approaches, thus reducing the computational burden.

One of the biggest challenges encountered while using conventional Kalman filtering for satellite attitude estimation is that the conventional filter is not capable of maintaining the estimation accuracy in case of any malfunction in the attitude sensors. To cope with this problem, adaptive filters have been developed that can adapt to changing conditions and compensate for the faults. There are different techniques in the literature to make the Kalman filter adaptive, and in Hajiyev and Soken (2021), they are explained in great detail.

In this study, a nontraditional attitude estimation system is proposed for a nanosatellite which combines the TRIAD algorithm, a static attitude determination algorithm, with an adaptive fading Kalman filter (AFKF). The TRIAD algorithm is preferred because of its simple and fast algorithm, and the adaptive filter is based on the covariance matching technique. Specifically, the performance of the AFKF in case of sudden noise increments in the attitude sensors is investigated.

2 Method

2.1 TRIAD Algorithm

TRIAD algorithm, also known as the “two-vector algorithm” or “algebraic method,” uses reference direction vectors and measurement of these vectors in order to determine the three-dimensional attitude of a spacecraft. For nanosatellites, these reference direction vectors are generally unit vectors in the direction of the Sun and Earth’s magnetic field. Measurement of these vectors, on the other hand, is obtained using Sun sensors and magnetometers.

Given two vectors in the reference frame $\hat{\mathbf{V}}_1$ and $\hat{\mathbf{V}}_2$ and representations of these vectors in the body frame $\hat{\mathbf{Y}}_1$ and $\hat{\mathbf{Y}}_2$, the goal is to find an orthogonal attitude matrix A such that (Shuster & Oh, 1981):

$$A\hat{\mathbf{V}}_1 = \hat{\mathbf{Y}}_1, \quad A\hat{\mathbf{V}}_2 = \hat{\mathbf{Y}}_2 \quad (1)$$

where $\hat{\cdot}$ indicates that related vector is a unit vector. Matrix A is known to be overdetermined; therefore, two triads of orthonormal reference and measurement vectors are constructed according to:

$$\hat{\mathbf{r}}_1 = \hat{\mathbf{V}}_1 \quad (2)$$

$$\hat{\mathbf{r}}_2 = \left(\hat{\mathbf{V}}_1 \times \hat{\mathbf{V}}_2 \right) / \left| \hat{\mathbf{V}}_1 \times \hat{\mathbf{V}}_2 \right| \quad (3)$$

$$\hat{\mathbf{r}}_3 = \hat{\mathbf{r}}_1 \times \hat{\mathbf{r}}_2 \quad (4)$$

and

$$\hat{\mathbf{s}}_1 = \hat{\mathbf{Y}}_1 \tag{5}$$

$$\hat{\mathbf{s}}_2 = \left(\hat{\mathbf{Y}}_1 \times \hat{\mathbf{Y}}_2 \right) / \left| \hat{\mathbf{Y}}_1 \times \hat{\mathbf{Y}}_2 \right| \tag{6}$$

$$\hat{\mathbf{s}}_3 = \hat{\mathbf{s}}_1 \times \hat{\mathbf{s}}_2 \tag{7}$$

where there is a unique orthogonal matrix A which satisfies

$$A\hat{r}_i = \hat{\mathbf{s}}_i \quad (i = 1, 2, 3) \tag{8}$$

Equation (8) is known as the TRIAD solution, and a necessary and sufficient condition for the TRIAD solution to give the attitude matrix is:

$$\hat{\mathbf{V}}_1 \cdot \hat{\mathbf{V}}_2 = \hat{\mathbf{Y}}_1 \cdot \hat{\mathbf{Y}}_2 \tag{9}$$

2.2 Adaptive Fading Kalman Filter

The conventional EKF estimation routine is well documented elsewhere (Lefferts et al., 1982) and will not be repeated for the sake of brevity. However, EKF-based adaptive filters differ from the conventional EKF at several points. The main idea behind the AFKF is that it rescales the Kalman gain with fading factors to maintain the tracking performance of the filter. The fading factors are calculated based on the relation between the estimated and calculated innovation covariances. The calculated innovation covariance can be given as (Kim et al., 2015):

$$C_k = E \left[(\mathbf{z}_k - \hat{\mathbf{z}}_k^-) (\mathbf{z}_k - \hat{\mathbf{z}}_k^-)^T \right] = \mathbf{H}_k \mathbf{P}_k^- \mathbf{H}_k^T + \mathbf{R}_k \tag{10}$$

where C_k is the calculated innovation covariance and $(\mathbf{z}_k - \hat{\mathbf{z}}_k^-)$ is the measurement innovation. On the other hand, estimated innovation covariance is calculated as:

$$\hat{C}_k = \frac{1}{\xi - 1} \sum_{i=k-\xi+1}^k (\mathbf{z}_k - \hat{\mathbf{z}}_k^-) (\mathbf{z}_k - \hat{\mathbf{z}}_k^-)^T \tag{11}$$

where \hat{C}_k is the estimated innovation covariance and ξ is the window size which is the number of measurements that will be considered. After calculating the two different innovation covariances, fading factors can be found using the relationship:

$$\alpha_k = \begin{bmatrix} \alpha_k(1) \\ \alpha_k(2) \\ \vdots \\ \alpha_k(N) \end{bmatrix} = \max \left(1, \frac{\text{diag}(\widehat{C}_k)}{\text{diag}(C_k)} \right) \quad (12)$$

where $\text{diag}(\cdot)$ is the diagonal elements of the corresponding matrix and $\max(\cdot)$ function gives the highest value inside. After finding the fading factors, the Kalman gain is readjusted as:

$$\bar{K}_k = \begin{bmatrix} \frac{1}{\alpha_k(1)} K_{11} & \frac{1}{\alpha_k(2)} K_{12} & \cdots & \frac{1}{\alpha_k(N)} K_{1N} \\ \vdots & \vdots & \ddots & \vdots \\ \frac{1}{\alpha_k(1)} K_{M1} & \frac{1}{\alpha_k(2)} K_{M2} & \cdots & \frac{1}{\alpha_k(N)} K_{MN} \end{bmatrix} \quad (13)$$

where \bar{K}_k is the rescaled Kalman gain. In case of a sensor malfunction, the corresponding diagonal element of the estimated covariance matrix will be larger than the calculated which results in a ratio greater than one; thus, the fading factor for that state will be larger than one. Looking at Eq. (13), it can be seen that a high fading factor will reduce the effect of the corresponding columns of the Kalman gain matrix which means reducing the effect of the corresponding faulty measurement.

3 Results and Discussion

In order to verify the performance of the TRIAD/AFKF estimation algorithm, two simulations are performed. In the first simulation, the x-axis magnetometer noise value is increased 25 times at the 3500th second of the simulation, and this effect is maintained for 50 s, whereas in the second simulation, the y-axis Sun sensor noise value is increased 150 times at the 4100th second, and again the effect is maintained for 50 s. Figures 1 and 2 show the obtained results. As can be seen from Figs. 1 and 2, with the introduction of noise increment, the conventional EKF algorithm starts to give unreliable attitude estimations, whereas the AFKF algorithm continues to follow the ground truth closely.

Apart from the figures, Tables 1 and 2 show the RMSE values of both conventional EKF and AFKF during the noise increments. Looking at the tables, it can be said that AFKF successfully maintains the tracking performance unlike conventional EKF in case of a noise increment.

AFKF vs conventional EKF attitude estimations (Euler angles)

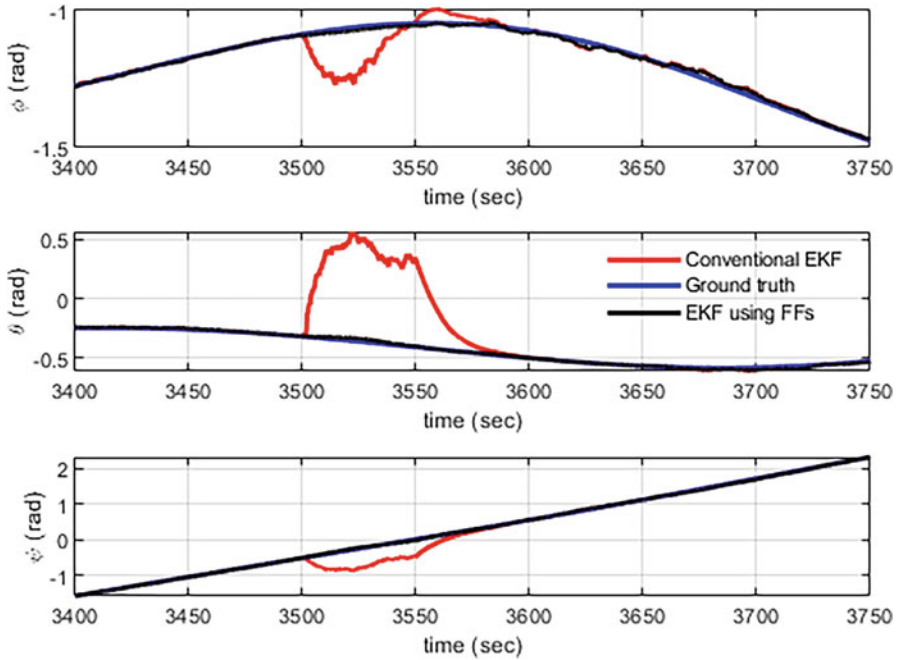


Fig. 1 Attitude estimation results in case of x-axis magnetometer noise increment

4 Conclusion

In this study, a nontraditional satellite attitude estimation algorithm based on an adaptive fading Kalman filter was proposed. In the first step of the algorithm, the TRIAD provides a coarse initial attitude estimation, and then this estimation is given to the adaptive filter. In order to verify the performance of the algorithm, two simulations are performed where the magnetometer and Sun sensor measurement noises are increased, respectively. Simulation results show that while the tracking performance of the conventional EKF decreases significantly in case of a sensor fault, the proposed AFKF maintains its tracking performance.

AFKF vs conventional EKF attitude estimations (Euler angles)

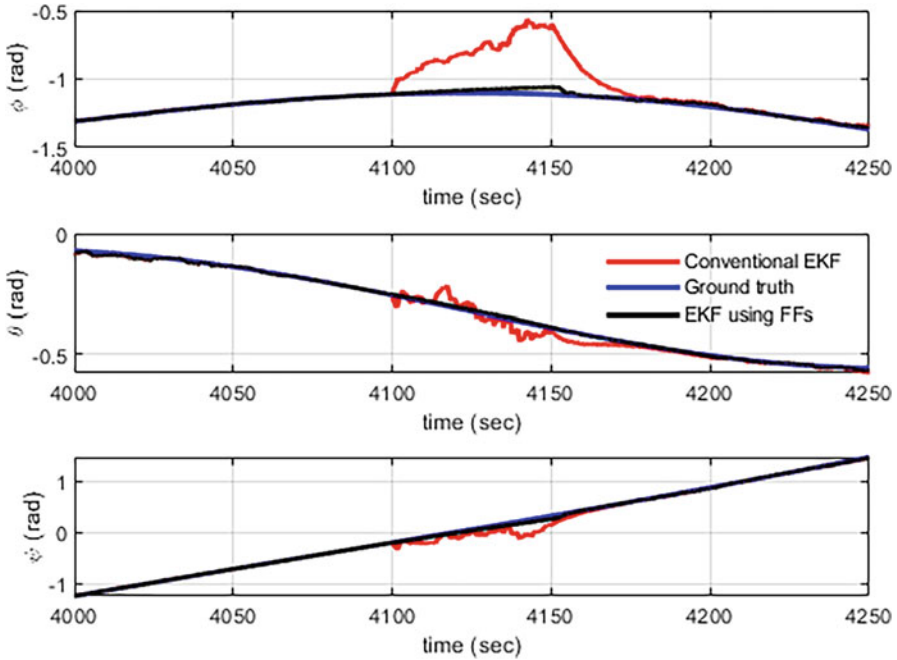


Fig. 2 Attitude estimation results in case of y-axis Sun sensor noise increment

Table 1 RMSE values of EKF and AFKF during x-axis magnetometer noise increment

Euler angle	Standard EKF	AFKF
ϕ (roll)	0.1149 rad	0.0130 rad
θ (pitch)	0.7196 rad	0.0108 rad
ψ (yaw)	0.4532 rad	0.0162 rad

Table 2 RMSE values of EKF and AFKF during y-axis Sun sensor noise increment

Euler angle	Standard EKF	AFKF
ϕ (roll)	0.3351 rad	0.0257 rad
θ (pitch)	0.0248 rad	0.0011 rad
ψ (yaw)	0.1763 rad	0.0310 rad

References

Hajjiev, C., & Soken, H. E. (2021). *Fault tolerant attitude estimation for small satellites*. CRC Press.

Hajjiev, C., Cilden, D., & Somov, Y. (2015). Integrated SVD/EKF for small satellite attitude determination and rate gyro bias estimation. *IFAC-PapersOnLine*, 48(9), 233–238. <https://doi.org/10.1016/j.ifacol.2015.08.089>

- Kim, S. Y., Kang, C. H., & Park, C. G. (2015). *A fault detection algorithm using an adaptive fading kalman filter for various types of GNSS fault*. In 2015 6th international conference on intelligent systems, modelling and simulation (pp. 113–117). <https://doi.org/10.1109/ISMS.2015.18>.
- Lefferts, E. J., Markley, F. L., & Shuster, M. D. (1982). Kalman filtering for spacecraft attitude estimation. *Journal of Guidance, Control, and Dynamics*, 5(5), 417–429. <https://doi.org/10.2514/3.56190>
- Shuster, M. D., & Oh, S. D. (1981). Three-axis attitude determination from vector observations. *Journal of Guidance, Control, and Dynamics*, 4(1), 70–77. <https://doi.org/10.2514/3.19717>

On the Number of Monte Carlo Runs for Stochastic Processes



Alvaro Arroyo Cebeira and Mariano Asensio Vicente

Nomenclature

ACAS	Airborne collision avoidance system
ME	Margin of error
MC	Monte Carlo
SDE	Stochastic dynamic equation
UAV	Unmanned aerial vehicle

1 Introduction

UAV applications in defense industry may include different types of algorithms such as collision avoidance, trajectory estimation, target tracking, or sensor fusion. These algorithms are usually complex, and they try to estimate variables which are governed by stochastic dynamic equations (SDEs); hence, its theoretical analysis is cumbersome, and they are suitable to be simulated via the Monte Carlo method as in Deaton and Owen (2020) or Jenie et al. (2018).

However, there is no agreement on the number of MC runs that should be simulated to have accurate results, and even some papers about MC simulation do not provide the rationale of the number of MC runs used (Hu et al., 2015). In the following sections, an analysis of advantages and disadvantages of the number of MC runs is presented, and a strategy to select a number to obtain valid results is defined.

A. A. Cebeira (✉) · M. A. Vicente
Universidad Politécnica de Madrid, Madrid, Spain
e-mail: alvaro.arroyo.cebeira@alumnos.upm.es; mariano.asensio@upm.es

One of these algorithms that are useful for UAV applications in defense industry is collision avoidance; the state of the art of collision avoidance systems is ACAS Xu (RTCA, 2020). During this research, the tracking module of ACAS Xu logic, which is used for estimating the intruder UAV trajectory, has been coded in MATLAB, and then a MC simulator based on the noise models depicted in Stroeve et al. (2019) has been implemented as well.

2 Method

As a first idea, MC simulator users may think that the accuracy of the sample parameters, such as the sample mean, could define the number of MC runs; however, the accuracy of the sample mean cannot be defined since there is not a true sample mean, or the true sample mean and the estimated sample mean are always the same, since the sample mean depends only on the sample data collected. Another idea could be to analyze when the sample mean converges to a steady value, but that strategy does not provide information about the accuracy of the system.

In order to assess the performance of the system, parameters about the population (and not the sample) shall be inferred. During this investigation, the first and second moments of the population will be inferred by means of the mean and standard deviation confidence intervals.

According to the central limit theorem, the distribution of the means of each MC run is a normal distribution, so the Student's t -distribution-based confidence interval is used. The following equations define the lower and upper endpoints of the confidence interval:

$$CI_{\text{lowerEndpoint}} = \underline{x} - t_{\frac{\alpha}{2}} \cdot \frac{s}{\sqrt{N}} \quad (1)$$

$$CI_{\text{upperEndpoint}} = \underline{x} + t_{\frac{\alpha}{2}} \cdot \frac{s}{\sqrt{N}} \quad (2)$$

where \underline{x} is representing the estimated mean (sample mean in this case), $t_{\frac{\alpha}{2}}$ is the t -score, which follows the Student's t -distribution with $N-1$ degrees of freedom, α is the significance level, s is the sample standard deviation, and N is the sample size (i.e., number of MC runs).

Based on the previous formula, the estimated margin of error (ME) of the confidence interval can be determined:

$$ME = \frac{t_{\frac{\alpha}{2}}}{\sqrt{N}} \cdot s$$

Therefore, the number of MC runs is

$$N \geq \left(\frac{t_{\frac{\alpha}{2}}}{ME} \right)^2 \cdot s^2$$

The problem is that the *t*-score depends on the degrees of freedom of the Student’s *t*-distribution, which is *N*-1, and *N* is the parameter to be estimated; in order to solve this catch-22 situation, an iterative method will be used.

On the other hand, the execution time of running the *N* Monte Carlo runs is assessed as well by means of the MATLAB profiler.

3 Results and Discussion

For the results’ discussion, MC simulation of the ACAS X tracking logic has been done for different MC runs, and the results are presented in the Table 1:

On the other hand, an initial estimate of the number of MC runs can be obtained if the equation is solved iteratively. In the first iteration, the *z*-score (from a Gaussian), instead of the *t*-score, can be used, and the sample standard deviation is approximately 140 ft (Fig. 1):

$$N \geq \left(\frac{z_{0.025}}{ME} \right)^2 \cdot \sigma^2 = \left(\frac{1.96}{2.5} \right)^2 \cdot 140^2 = 12048$$

$$N = \left(\frac{t_{12047, 0.025}}{5} \right)^2 \cdot 140^2 = 12049 \text{ MC runs}$$

Regarding the execution time, in the analyzed range it increases linearly, and for all the MC runs that have been simulated, the results were obtained in a reasonable time (within 40 min) (Fig. 2).

Table 1 Dependency of the statistical properties and execution time with the MC runs

MC runs	UE (ft)	LE (ft)	ME (ft)	RMSE mean (ft)	Change (%)	Time (s)
1	–	–	–	680.7	–	15.2
5	614.82	436.84	177.98	525.8	–29.5	16.74
10	781.24	542.72	238.52	661.98	+25.9	19
50	717.26	626.63	90.63	671.95	+1.5	25.77
100	685.38	629.75	55.63	657.56	–2.1	32.76
500	673.16	647.43	25.73	660.3	+0.4	95.17
1000	675.68	657.1	18.58	666.3	+0.9	176.27
2500	661.62	650.35	11.27	660	–0.95	382
5000	670.58	662.41	8.17	666.1	+0.92	797
10,000	663.36	657.63	5.73	660.5	–0.84	2000
12,500	666.6	661.5	5.1	664	+0.53	2283

Source: Results of the MC simulations performed during this research

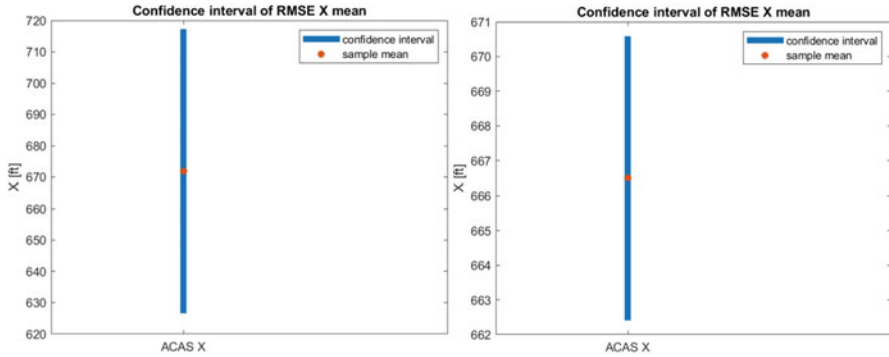


Fig. 1 Confidence intervals of the RMSE x mean for 50 and 5000 MC runs

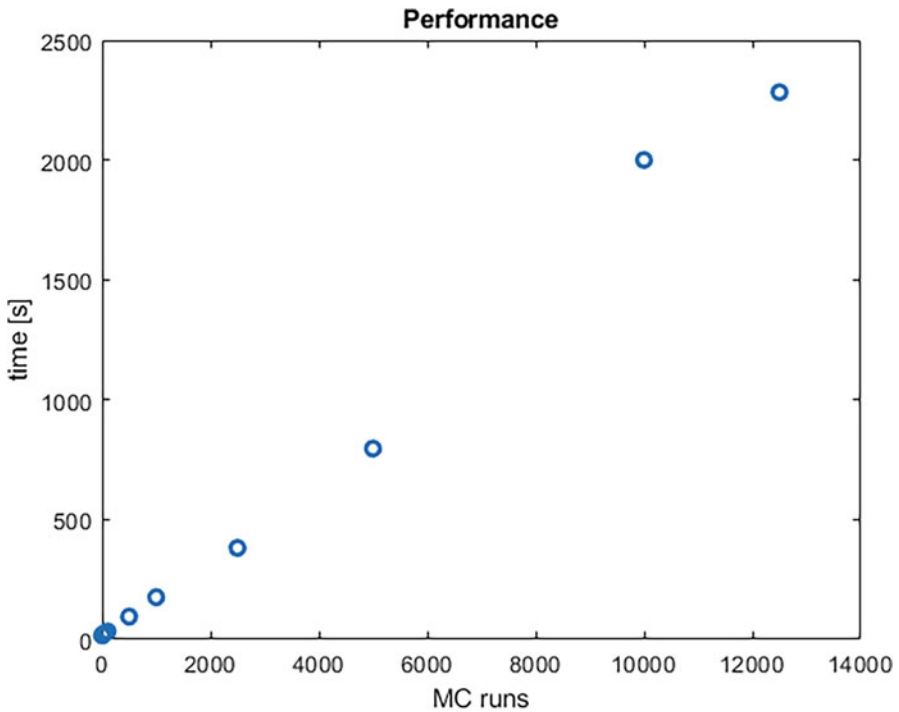


Fig. 2 Relation between number of MC runs and execution time

4 Conclusion

An increase in the number of Monte Carlos runs has an effect on the accuracy of the results, but it is important to analyze the impact on the right metric, and sample parameters such as sample mean are quite dependable on the sample obtained from

the MC runs, so it is more robust to analyze the impact on population parameters. Confidence intervals are used to infer the values of the population parameters from a sample. The sample mean converges at 500 MC runs; however, the accuracy of the results is not enough since the width of the mean confidence interval is greater than 25 ft.

On the other hand, as the number of MC runs increases, the more computational load is needed for the simulations, so the execution time of the simulator is analyzed as well. And a specific analysis on this topic shall be performed for each specific algorithm or logic which is going to be simulated. For the ACAS Xu tracking logic example 10,000 MC runs is a good trade-off between the execution time (simulation results can be obtained within 40 min) and the required accuracy is achieved (margin of error is 5 ft).

References

- Deaton, J., & Owen, M. P. (2020). Evaluating collision avoidance for small UAS using ACAS X. *AIAA Scitech 2020 Forum*.
- Hu, G., Gao, S., Zhong, Y., Gao, B., & Subic, A. (2015). Modified strong tracking unscented Kalman filter for nonlinear state estimation with process model uncertainty. *International Journal of Adaptive Control and Signal Processing*, 29, 1561.
- Jenie, Y. I., van Kampen, E.-J., Ellerbroek, J., & Hoekstra, J. M. (2018). Safety assessment of a UAV CD&R system in high density airspace using Monte Carlo simulations. *IEEE Transactions on Intelligent Transportation Systems*, 19(8), 2686–2695.
- RTCA. (2020). *DO-386, Minimum operational performance standards for airborne collision avoidance system Xu (ACAS Xu)*.
- Stroeve, S., Blom, H., Medel, C. H., Daroca, C. G., Cebeira, Á. A., & Drozdowski, S. (2019). Development of a Collision Avoidance Validation and Evaluation Tool (CAVEAT): Addressing the intrinsic uncertainty in TCAS II and ACAS X. *13th USA/Europe air traffic management research and development seminar*.

Index

A

ABL, 126
ACAS Xu, 312, 315
Accidents, 209, 249–251, 254, 256, 257
Active, 56, 58, 59, 67, 132, 152, 159, 215, 267–268
Adaptive, 284, 297, 303–307
Adaptive filtering, 304, 305, 307
Additive manufacturing, 10–14, 29–31, 194
Adversarial attacks, 272, 274, 275
Aerodynamic coefficients, 125, 153–155, 285
Aerodynamic efficiency, 37, 93, 94, 97, 231, 233, 246
Aerodynamics, 21, 37–47, 61, 93, 94, 97, 98, 106, 151, 152, 156, 163, 164, 187, 188, 191, 196, 229–233, 246, 260–263, 267, 278, 285
Aerospace, 30, 31, 61, 93, 105–109, 132, 188, 205, 277, 278
Airfoils, 21–25, 37, 38, 196, 229–233, 244, 267, 268
Analysis, 12, 13, 25, 26, 33, 38, 43, 56, 63, 76, 95, 100, 105, 106, 132, 133, 135, 139, 142–149, 156–162, 166, 169, 175, 176, 179, 183, 201–203, 205, 230, 267, 311, 315
Analytic hierarchy process (AHP), 249–257
Arboreal terrain, 38
Artificial neural networks (ANNs), 100–103, 187–191
Attitude, 17, 49–53, 67–73, 82, 140, 246, 279, 297, 298, 300, 303–307
Attitude control, 67–73

Attitude estimation, 49–53, 82, 300, 303–308
Autoencoders, 132, 134, 135, 271–275
Autonomous technologies, 139, 141
Autonomous weapons, 137–142
Avionics, 241, 242, 244, 245

B

Ballistic rocket, 277
Ballistics, 187, 188, 280
Big data, 175–179
Biomimetic, 93–98, 144
Blockchain, 271–275

C

Camber, 265–269
Canopy flow, 61, 63
Coherent structures, 64, 202
Computational fluid dynamics (CFD), 94, 125, 169
Computer fluid dynamics (CFD), 13
Consensus control, 224
Control, 9, 15, 22, 38, 49, 56, 67, 81, 106, 113, 132, 141, 143, 159, 193, 201, 209, 215, 221, 246, 257, 261, 266, 271, 278, 283
Convolutional neural networks (CNNs), 108, 163–167
Cooling, 152, 215, 216, 219
CubeSat, 157–162

D

Data-driven methods, 105–109, 133, 203, 205
 Deep learning, 76, 77, 100, 101, 105, 167, 169, 291
 Deep Q Network (DQN), 291–295
 Defect detection, 124
 Defense, 9, 10, 14, 30, 207–214, 250
 Deployable mast (DM), 181–183
 Deployable structures, 181
 Design, 10, 13, 14, 17–18, 21–25, 29–36, 49, 58, 97, 100, 106, 122, 125, 139–141, 151, 157–160, 162, 181–185, 201, 215, 229, 241, 265, 267–269, 301, 303
 Disaster analysis, 175, 176
 Docking, 81–92
 Double acting hydropneumatic suspension, 112–117
 Drones, 31–35, 38, 193–195, 208–211, 213, 242
 Dynamic mode decomposition (DMD), 62, 106, 108, 133, 135, 156, 164, 165, 202–205, 237, 239
 Dynamic modelling, 113, 115

E

Electric aircraft, 1, 2, 4, 5
 Energy sources, 1, 2, 215
 Ethics, 138, 139, 141, 142

F

Fault, 297, 304, 307
 FFD control points, 21–26
 Fishbone, 265–269
 Fishbone active camber (FishBAC), 265–269
 Fixed-wing UAV, 214, 241–246, 284
 Flexure modulus, 57–59
 Fluid dynamics, 79, 105, 106, 125
 Fluid-structure interaction (FSI), 43, 45–47
 Flutter, 163–167
 Formation control, 221–226
 Free-form deformation (FFD), 21–26
 Fused filament fabrication (FFF), 10–13, 29–36

G

Gain optimization, 67, 69–71
 Gaussian mixture (GM), 169–172
 Global navigation satellite system (GNSS), 82–84, 86, 88–92, 277, 279–281
 Gradient-based optimization, 22, 24

Graph theory, 226

Grids, 57, 62, 63, 76, 77, 93–98, 107, 133, 201, 204, 231, 237, 238, 260, 261
 Guidance navigation and control (GNC), 277, 278
 Gyroscope, 49–53

H

Heat transfer, 152, 215–219
 Higher-order dynamic mode decomposition (HODMD), 62–64, 75, 106–109, 132–134, 163–167, 236–239
 High-order discontinuous Galerkin, 171
 Honeybees, 143–149
 Hover, 259, 260
 Human factor, 175, 249–251
 Human factors analysis and classification system (HFACS), 249–257
 Hybrid aircraft, 1–5
 Hybrid UAV, 194, 199

I

Insect flapping wing, 43–47
 Insect flight, 143–149
 Interpolation, 105, 125–128, 146, 217, 218

J

Just war, 138–142

K

Kalman filter, 50, 85–86, 88, 277, 297, 303–307

L

Launch vehicle, 157–162
 LES, 170, 171, 260, 261, 263
 Linear matrix inequality (LMI), 15–19
 Linear-quadratic control, 82
 Longitudinal control, 284, 288

M

Machine learning (ML), 75–79, 135, 139, 167, 169–172, 176, 277
 Magnetometer, 49, 50, 52, 297, 298, 304, 306–308
 Martian UAV, 230

- MATLAB, 70, 90, 117, 145, 188, 189, 280, 288, 292, 293, 295
- Medical transportation, 15
- Model predictive control (MPC), 82, 283–288
- Monte Carlo (MC) simulation, 280, 311–313
- Morality, 138
- Morphing wing, 21, 55, 265–269
- Multi-input, multi-output system, 288
- Multiphase, 235–240
- Multiphase flows, 235–240
- N**
- Nanosatellite, 49–53, 300, 303–307
- Natural language processing, 175, 177
- Navigation, 82–84, 143, 144, 190, 277–279
- Neural networks (NNs), 77–79, 100–103, 108, 125–128, 188–191, 235–240, 277–281, 292
- Non-destructive testing, 124
- O**
- Obstacle avoidance, 143, 144, 146, 149
- P**
- Payload vibration suppression, 15–19
- PD controller, 17, 67, 69, 73
- Planar synthetic jets, 132–136
- Polyethylene terephthalate glycol (PET-G), 9–14
- Projectile, 187–191
- Propeller, 29–36, 95, 106, 259–263
- Proper orthogonal decomposition (POD), 76, 77, 100, 156, 158, 202–205
- Proportional-integral-derivative (PID), 283, 291–295
- Python, 22, 171
- Q**
- Quarter car for rough terrain vehicles, 112–117
- R**
- Ram air turbines (RAT), 241–244, 246
- Rapid prototyping, 29, 193
- Reacting flows, 75–79
- Reduced order model (ROM), 75, 76, 79, 100, 134, 156, 201, 238, 239
- Reinforcement learning, 291–293, 295
- Rendezvous, 81–92
- Resolvent analysis, 202, 203, 205
- Reynolds number (Re), 62, 95, 107, 152, 203, 229–231, 260
- Robust, 21, 63, 79, 106, 119, 143, 167, 201, 205, 273, 274, 277, 281, 288, 297, 315
- Rocket, 157–162, 277–279, 281
- Rotating circular cylinder, 151–156
- S**
- Satellite components, 183
- Sectional area, 59
- Security, 12, 31, 207, 210–213, 250, 272
- Shape memory alloy (SMA), 55–59
- Simulink, 117, 188, 189, 280, 288, 292, 293, 295
- Singular value decomposition (SVD), 50, 63, 76, 77, 100, 103, 106, 126–128, 202, 203, 205, 237, 297–301
- Smart city, 179
- Soft actuator, 55
- Stochastic processes, 311–315
- Stratosphere, 157, 158, 162
- Sun sensor, 49, 50, 52, 297, 298, 300, 306
- Surveillance, 31, 38, 207, 210, 211, 213, 259, 283
- SVD-aided EKF, 299, 300
- T**
- Tandem airfoil configuration (TAC), 108, 229–233
- Terminal guidance, 277–281
- Tethered UAV, 208–210, 213
- Text classification, 175
- Thermal sensors, 215–219
- Thrust, 33–35, 86, 87, 132, 244, 245, 260–262, 266, 278, 280, 285
- Topological derivative, 119–124
- Tracking, 82, 222, 223, 225, 226, 286, 291, 293, 305–307, 311–313, 315
- Trajectory prediction, 271–275
- Transonic flow, 151–156, 229–233
- Turbulence, 12, 65, 103, 164, 169, 230, 231
- Turbulent flow, 12, 100–103, 107, 109, 171, 201
- Two-body, 81
- U**
- UAS-S45, 21–26
- Ultra-high-altitude micro-aerial vehicles (UHAMAV), 230

Unmanned aerial vehicles (UAVs), 15, 21, 30, 93, 106, 126, 149, 193, 207, 215, 230, 241, 249, 259, 266, 283
Unmanned aircraft system (UAS), 208, 213, 249
Unmanned surface vehicle (USV), 12–14

V

Vacuum infusion, 196

Vector quantization principal component analysis (VQPCA), 132, 133, 135
Vertical take-off and landing (VTOL), 193, 194, 292, 293, 295
Volume of fluid, 236

W

Welding joint inspection, 119–124
Wind energy, 105, 244
Wingtip, 45, 97